Axial Performance of Self-tapping Screws in Mass Timber Products Under Moisture Content Variation

by

Mehsam Tanzim Khan

A thesis submitted in partial fulfillment of the requirements for the degree of

Master of Science

in

Structural Engineering

Department of Civil and Environmental Engineering
University of Alberta

ABSTRACT

Self-tapping screws (STS) are widely used in wood-to-wood and wood-to-steel connections in timber structures. The premature failure of STS during the construction phase has been recently reported by structural engineers and contractors of several mass timber projects in North America due to the increase of the wood's surrounding moisture content. This type of STS failure is suspected of having been precipitated by additional axial stress exerted on the STS from moisture swelling of the wood. This research investigates the axial performance of STS installed in two mass timber products, CLT and glulam, under axial loading conditions and moisture content change of the wood to understand this failure mechanism. This research emphasizes the case of moisture content increase (wood wetting) of CLT and glulam. A moisture transport model for predicting the moisture content variation distribution in CLT and glulam during moisture adsorption has been presented here. Then, a method to determine the swelling of the CLT and glulam from the moisture content variation distribution has been proposed. The properties of self-tapping screws under axial loading conditions, such as tensile and withdrawal properties, have been investigated. Subsequently, an analytical model to predict the stress distribution along the length of the screw has been developed. The analytical model has been verified with a numerical (finite element) model with the input properties from material properties tests conducted on the self-tapping screws, CLT and glulam. The numerical model results and the analytical model predictions of the screw stress distributions showed good agreement for the wood wetting cases. Finally, the stress distribution model of the screw has been linked to the stress distribution in self-tapping screws in wood-to-wood and wood-to-steel connections. The database and the methods developed in this thesis lays the foundation for developing failure criteria and guidelines to prevent the premature failure of self-tapping screw connections under moisture content variation.

PREFACE

This thesis is an original work by Mehsam Tanzim Khan. The research conducted for this thesis forms part of a research collaboration led by Dr. Ying Hei Chui at the University of Alberta, Dr. Dorian P. Tung, Dr. Chun Ni and Jieying Wang at FPInnovations. The test program for the research was conducted at the FPInnovations facility in Vancouver, British Columbia. All the experimental works of this research have been carried out by Mehsam Tanzim Khan, with help from FPInnovations technologists Paul Symons, Gordon Chow and Philip Eng. The data analysis and modelling of the thesis are Mehsam Tanzim Khan's original work with review and feedback from Dr. Ying Hei Chui, Dr. Chun Ni and Jieying Wang.

Parts of Chapters 1, 2, 3, 4, 5 and 6 have been published as a technical report by Mehsam Tanzim Khan and Chun Ni, "Expanding wood use towards 2025. Developing design guidelines to prevent failure of self-tapping screw due to wetting, year 2" online in the FPInnovations Research Library (https://library.fpinnovations.ca/en/permalink/fpipub8691). The manuscript was prepared by Mehsam Tanzim Khan and reviewed by Dr. Chun Ni and Dr. Zhiyong Chen at FPInnovations.

ACKNOWLEDGEMENTS

I want to take this opportunity to express my sincere gratitude to the wonderful people who have supported me during my master's studies.

First, I would like to express my most profound appreciation for my supervisor, Dr. Ying Hei Chui, for his extraordinary academic guidance, above and beyond mental support, and outstanding supervision.

I also want to extend my sincere gratitude to Dr. Chun Ni and Dr. Dorian P. Tung for allowing me to work at FPInnovations, their valuable feedback and their continued support despite their busy schedules.

I cannot thank the FPInnovations technologists Paul Symons, Gordon Chow and Philip Eng enough for helping me in preparing my specimens, conducting tests and giving me moral support after a long day of work. The experimental part of this thesis would not have been possible without them.

I am grateful to my wonderful colleagues at FPInnovations and the ARTS research group at the University of Alberta. I shall always cherish their encouragement and friendship.

Finally, I would like to express my indebtedness to my light, Shababa Tasneem Hossain, my parents, Dr. Masum Kamal Khan and Tahera Tabassum, my uncle and aunt, Asif Zaman and Shaila Anjuman, my cousins Tasnia, Shehzad and Afraaz, and my friend and landlord, Jo Anne for the love, encouragement and support during my graduate studies and my life in Canada. I also would like to take a moment to remember my late grandfather, Nawab Ali Khan, the most enlightened human being in my life, who inspired me to come to Canada for my graduate studies and to dream big.

TABLE OF CONTENTS

LIST OF TABLES

LIST OF FIGURES

1 INTRODUCTION

1.1 Background

The introduction of a relatively new category of engineered wood products called mass timber panels (MTP) has made it possible to construct tall and complex timber structures. This type of construction utilizing MTP is called mass timber construction. Some common types of mass timber products are cross-laminated timber (CLT), nail laminated timber (NLT), structural composite lumber (SCL) and glued-laminated timber (glulam) (Zhou et al., 2017). Mass timber construction is making headway in the construction industry of North America. Self-tapping screws (STS) have become the proprietary fastener of choice in mass timber construction. Due to its ease of installation, stiffer resulting connections, and large length and diameter availability, STS is ideal for use in mass timber products (e.g., cross-laminated timber, glulam, nail laminated timber, etc.) (Dietsch & Brandner, 2015). STS are preferably used in wood members at an angle to the grain direction of the main wood member. In recent times, the load-carrying capacity of screws in tension (load acting along the screw axis) has been a focus compared to the lateral load-carrying capacity of the screw (load acting perpendicular to the screw axis). When the screw is subjected to tension load, the condition can be considered the axial loading condition of the screw.

The premature failure of STS during the construction phase has been recently reported by structural engineers and contractors (source: personal communication) of several projects in North America due to the increase of the surrounding moisture content (MC) of timber members made with mass timber products. This type of STS failure is suspected of having been precipitated by additional axial stress exerted on the STS from moisture swelling of the wood. It can be categorized as an axial failure of the STS. STS failure can compromise the structural integrity of mass timber structures as connections formed with STS are the main contributors to the strength and stiffness of the structure. The detection and replacement of failed STS are onerous and costly. To avoid this type of failure, designers need to consider the effect of MC variation on the performance of STS in the design stage. However, limited information is available to reliably predict the behaviour and performance of STS under MC variation. For example, the current CSA O86 (Canadian Standards Association, 2019) standard does not have any provision for addressing this issue.

Considering the current state of knowledge, this research is focused on investigating the performance of axially loaded STS inserted into two kinds of mass timber products, glulam and

CLT, under varying moisture conditions, especially during wood-wetting (increasing moisture content). The study was conducted at the FPInnovations facility in Vancouver, British Columbia. Fully threaded STS of different lengths and diameters and two kinds of Canadian mass timber products, CLT (Spruce-Pine-Fir) and glulam (Douglas Fir-Larch), were investigated in the test program.

1.2 Objectives

The main broad objective of this thesis is to improve the understanding of the axial behaviour of STS inserted into mass timber products under MC variation of wood, emphasizing the increase of MC of wood (wood-wetting). For a better understanding of the behaviour of STS, the thesis first looks into the material properties of STS and the mass timber products. It then investigates the properties of the STS-mass timber composite system. The following goals were set for the research:

- Determination and documentation of the relevant material properties of STS and mass timber products to understand the axial behaviour of STS inserted into mass timber products under MC variation of wood
- Development of a method to predict the actual moisture content distribution and moisture change distribution inside large mass timber products
- Development of a stress distribution model along the length of STS in mass timber products due to moisture content change and application of an axial load from the material properties of the mass timber products and STS

Additionally, recommendations for some future work have been made at the end of this thesis. This thesis lays the foundation for developing guidelines for addressing the recently identified premature failure mechanism of STS inserted into mass timber products like CLT and glulam. The guidelines can be included in the "Connections" clause of the CSA O86 (Canadian Standards Association, 2019) standard and can be readily used by structural designers.

1.3 Methodology

This research aims to investigate factors that affect the performance of STS due to moisture content variation of CLT and glulam so that the mechanical behaviour of STS can be estimated accurately and the premature failure of STS can be averted. The wood-wetting case (an increase of moisture

content) is emphasized here, as the premature STS failure has been reported due to a rise in the surrounding moisture content of the wood. This research consists of the following chronological steps:

- Determination and documentation of the tensile properties of STS
- Determination of moisture transport properties and numerical modelling of the moisture transport process of mass timber products
- Determination of the swelling properties of mass timber products and analytical modelling of the swelling behaviour
- Determination and modelling of the withdrawal properties of STS in mass timber products under varying moisture conditions
- Analytical modelling to predict the stress distribution of axially loaded STS during moisture content change
- Numerical modelling, validation and implementation of the analytical model

At first, STS of different configurations were subjected to uniaxial tensile tests, and their tensile properties were documented. The tensile properties of STS are hypothesized to be critical under varying moisture conditions, as suggested by a relevant study (Naderer et al., 2016). Documenting tensile properties of different STS configurations will help create guidelines for the screw failure criteria based on the axially loaded screw's mechanical behaviour during moisture content variation.

Then, the moisture transport properties of the mass timber products used in this study, glulam and CLT, were determined. A method was developed to predict the temporal and spatial variation of moisture content inside the mass timber products from the determined properties. Determining moisture content distribution of the mass timber products is necessary to estimate the additional stress exerted on the STS from the wood swelling and shrinkage.

Thirdly, the wood swelling and shrinkage deformations can be predicted if the moisture content change distribution in the wood is known. As this thesis primarily focuses on the wood-wetting case, the dimensional changes of CLT and glulam due to an increase in moisture content of the wood were investigated from swelling tests. An analytical method was developed to predict the dimensional changes and strain from moisture swelling. The method relies on the properties of the individual laminates of CLT and glulam.

Fourthly, the withdrawal properties of STS in the STS-mass timber composite system were determined at different moisture conditions from withdrawal tests. The withdrawal properties are pivotal for modelling the stress distribution inside the screw under axial load and change in moisture conditions. For the withdrawal properties determination, screws of two diameters were used from the screw configurations used in the tensile tests. The screws were installed perpendicular to the wood's grain direction inside CLT and glulam specimens.

Fifthly, an analytical model was developed to predict the stress distribution along the length of the screw from the withdrawal properties of the screw and the swelling properties of the mass timber products. The moisture content change throughout the mass timber product was considered uniform in the analytical model. With the moisture transport modelling method presented here, the analytical model can be improved in the future to include the non-uniform moisture content change throughout the mass timber product. The proposed analytical model can form the basis for critical failure criteria determination for self-tapping screws.

Finally, a numerical model of the screw-mass timber composite system was developed to verify the proposed analytical model. Since it was not feasible to experimentally determine the screw stress distribution, the analytical model could only be verified with the numerical model. The input properties of the numerical model were taken from the tensile, withdrawal and swelling tests.

1.4 Thesis Structure

The thesis begins with a literature review necessary for understanding the behaviour of STS in glulam and CLT under moisture content variation. The following three chapters investigate the STS, glulam, and CLT properties. In the subsequent chapter, an analytical model for predicting the stress distribution in the STS is put forward. Then, the STS-mass timber composite system is analyzed using a numerical model, and the analytical model is validated using the results from the numerical model. Finally, the thesis ends with conclusions and recommendations for future research. The contents of the chapters of the thesis are encapsulated below:

- Chapter 2 reviews the previous studies and codes on the moisture transport properties, shrinkage and swelling behaviour of mass timber products and the axial behaviour of self-tapping screws. These areas are deemed necessary in understanding the axial behaviour of STS in CLT and glulam under moisture content variation.

- Chapter 3 describes a test program of the tensile properties of self-tapping screws from two manufacturers. This chapter begins with a brief discussion on the geometry and features of self-tapping screws. Screws of various configurations from two manufacturers were tested in axial tension until failure to generate a database of the tensile properties of self-tapping screws. The load-deformation behaviour of the screws was recorded, and they were used to determine tensile properties such as the yield strength, Young's modulus, tensile strength, strain at failure etc. This information can be fundamental in developing screw failure criteria based on the axially loaded screw's mechanical behaviour during moisture content variation.
- Chapter 4 describes modelling the moisture transport process inside CLT and glulam and determining the required diffusion coefficients of the model described in this chapter. With this method, the moisture content distribution inside the multi-layered mass timber products like CLT and glulam can easily be predicted under different moisture conditions at any time interval from the beginning of the moisture diffusion process. Thus, the moisture content change gradient inside CLT and glulam can be predicted to determine the swelling and shrinkage deformations of the mass timber product, which affect the behaviour of the self-tapping screw due to moisture content change.
- In chapter 5, the swelling behaviour of CLT and glulam have been experimentally and numerically investigated. A prediction model for estimating the swelling strain of CLT and glulam is proposed, and the predicted strains from the prediction model are compared with the experimental and numerical results. The prediction model relies on the laminate properties as input parameters and is suitable for hand calculations in practical engineering settings. The prediction model can determine the average effective swelling strain and the swelling strain of the individual layers of CLT and glulam in the out-of-plane direction.
- Chapter 6 investigates the withdrawal properties of self-tapping screws of 8 mm and 13 mm outer nominal diameters inserted into CLT and glulam. All the preceding chapters were concerned with the properties of wood and screw individually. The individual properties of the screw and wood and the properties of the wood-screw composite system are essential to predict the behaviour of self-tapping screws due to moisture content changes in the wood. Moreover, the properties presented here are the first attempt at

documenting the withdrawal properties of self-tapping screws in Canadian CLT and glulam products under varying moisture conditions.

- In chapter 7, an analytical model to predict the stress distribution in an axially loaded self-tapping screw inserted into mass timber products like CLT and glulam under moisture content change is proposed. The analytical model considers uniform moisture content change in the CLT and glulam. This model can also be used for screws inserted into other wood members like GLT and solid lumber. This analytical model can form the basis for developing screw failure criteria and guidelines for self-tapping screw connections under moisture content variation and axial loading conditions.
- Chapter 8 describes the finite element modelling technique to find the stress distribution in self-tapping screws under moisture content change and axial load application. The input parameters of the finite element models came from the previous screw tensile tests, CLT and glulam swelling tests, and withdrawal tests. The finite element model was calibrated and verified with experimental withdrawal test results. The screw stress distributions from the finite element models were compared with the screw stress distributions from the analytical model. The finite element model results and the analytical model predictions of the screw stress distributions showed good agreement for the wood wetting cases. Finally, in this chapter, the stress distribution model of the screw has been linked to the stress distribution in self-tapping screws in wood-to-wood and wood-to-steel connections.
- Chapter 9 provides conclusions and recommendations for further research. The database and the methods developed in this thesis can be used in future research to develop failure criteria and guidelines to prevent the premature failure of self-tapping screws in mass timber member connections under moisture content variation.

2 LITERATURE REVIEW

2.1 Introduction

This research focuses on predicting the axial behaviour of STS inserted into common mass timber products such as cross-laminated timber (CLT) and glulam under MC variation. With a better understanding of the axial performance of STS under MC variation, premature STS failure can be avoided. To predict the axial performance of STS due to MC change of the mass timber members, it is necessary to understand the (a) process of moisture transport inside mass timber, (b) process of shrinkage and swelling of mass timber due to MC change (c) axial behaviour of STS in mass timber products under MC change (d) modelling the stress distribution in the STS-mass timber composite system. This chapter reviews the relevant research conducted in these four areas. Finally, a summary of the literature review is presented at the end.

2.2 Moisture Transport in Mass Timber Products

The surrounding environment of timber structures, such as temperature, relative humidity, and the presence or absence of liquid water, constantly fluctuate. This results in the variation of wood's equilibrium moisture content (EMC) and triggers moisture movement inside the wood. The moisture movement leads to variation in temporal and spatial moisture content inside wood products. The presence of varying moisture content along the geometric directions of the wood product is called moisture gradient. The presence of moisture gradient induces hygroscopic deformation and affects the structural performance of wood. It is necessary to determine the moisture gradient to predict the hygroscopic deformation. For this purpose, a proper description of the physical moisture transport process inside the wood product is needed. As part of the wood-wetting, if the moisture transport process during moisture adsorption can be modelled appropriately, mass timber products' internal moisture content distribution can be predicted.

Under varying ambient conditions, the moisture transport inside wood can be categorized as an unsteady-state diffusion process. Fick's second law of mass diffusion provides a simplified mathematical description of this process. Though Fick's second law only simplifies several parallel moisture flow processes inside the wood, for practical purposes, it gives relatively accurate results below the fibre saturation point (Angst & Malo, 2012b).

The challenge of describing the moisture diffusion process using Fick's law lies in determining the effective diffusion coefficient. Extensive research has been conducted to measure the effective diffusion coefficient of different wood species. However, the majority of the studies investigated the diffusion coefficient of only individual pieces of lumber (Arends et al., 2018) (Kain et al., 2018) (Hukka, 1999) (Rosenkilde & Arfvidsson, 1997). Moreover, most research has focused on determining the diffusion coefficient during moisture desorption (wood-drying) (Hukka, 1999) (Rosenkilde & Arfvidsson, 1997) (Plumb et al., 1985). Limited research has been conducted on the effective diffusion coefficient of mass timber products during moisture adsorption. Chiniforush et al. (Chiniforush, Valipour, et al., 2019) investigated the effective diffusion coefficient of some glulam, CLT and laminated veneer lumber products manufactured from timber species native to Australia. Nevertheless, the experimental methods adopted in the study (Chiniforush, Valipour, et al., 2019) for determining the diffusion coefficient are relatively complex and might not always be feasible. Numerical methods coupled with simple experimental measurements offer a convenient alternative.

Below the fibre saturation point, moisture exists in two states inside wood: as bound water inside the cell wall (liquid phase) and as water vapour in the cell lumen space (gaseous phase) (Plumb et al., 1985). The change in surrounding moisture conditions creates spatial moisture concentration variation inside the wood and acts as the primary driving force for moisture diffusion. For practical purposes, it is not imperative to differentiate between water's liquid and gaseous phases to describe the moisture diffusion process. To this end, Fick's second law adequately describes this process. Fick's second law of mass diffusion is given by equation 2-1. Equation 2-1 represents a one-dimensional mass transport model under unsteady-state conditions.

Equation 2-1

$$\frac{\delta u}{\delta t} = \frac{\delta}{\delta x}\left(D\frac{\delta u}{\delta x}\right)$$

In equation 2-1, u is the moisture content at a point inside the wood at any instant of time, D is the effective moisture diffusion coefficient, which is a function of the moisture content, t is the time from the start of the moisture diffusion process, and x represents the coordinate system in the direction of moisture transport. The moisture diffusion coefficient is referred to as the effective diffusion coefficient as several parallel moisture transport processes occurring inside the wood

have been simplified to one mass diffusion process described by Fick's law. Determining the diffusion coefficient poses a challenge due to the unsteady-state condition and the presence of a second-order derivative in equation 2-1.

The one-dimensional mass transport model considers wood as a continuous and homogenous medium. However, there is a breach of this continuity at the outer surface of the wood. An implicit assumption required to make equation 2-1 valid is that all the evaporation/condensation of water occurs at the wood surface. There has been evidence that the surface of the wood can impart some resistance to the moisture flow (Salin, 1996). However, in the case of moisture adsorption, the surface resistance is meagre and can be ignored (Shi, 2007).

Due to the orthotropic nature of wood, the diffusion coefficient value is different along the three orthotropic directions of wood. Moisture movement in the longitudinal direction of wood is typically 10-15 times faster than that in the transverse direction (Avramidis & Siau, 1987). In wood structures, it is often customary to take adequate measures to reduce moisture movement in the longitudinal direction to minimize wood splitting and checking (Ross & USDA Forest Service., 2010). Previously, the diffusion coefficient along the radial and tangential directions were found to be approximately equal (Rosenkilde & Arfvidsson, 1997). Thus, the same value of diffusion coefficient along the radial and tangential directions can be considered.

2.3 Shrinkage and Swelling of Mass Timber Products

As mentioned in section 2.2, wood is a hygroscopic material, and moisture is absorbed or desorbed from wood depending on the surrounding air's relative humidity (RH) and temperature. This triggers moisture content variation in the wood and leads to dimensional changes. In general, moisture adsorption is accompanied by an increase in volume (swelling) and moisture desorption is accompanied by a decrease in volume (shrinkage). In designing high-rise buildings and complex structures with MTP, wood's swelling and shrinkage behaviour under varying RH conditions should be considered due to the potential significant cumulative dimensional changes.

Previous studies have investigated the dimensional changes of CLT and glulam under different moisture conditions (Angst & Malo, 2012b), (Lee et al., 2019), (Gereke et al., 2008) and (Gereke & Niemz, 2010). For measuring the dimensional changes, digital callipers, image analysis, and digital image correlation (DIC) have been employed (Pang & Jeong, 2020). DIC technique is the most precise, although it is not always feasible for its expensive and complicated instrumentation

requirements. On the other hand, using digital callipers to measure the dimensional changes is inexpensive and straightforward.

Dimensional changes of CLT and glulam can be expressed as the strain produced due to moisture shrinkage or swelling. The shrinkage and swelling coefficient quantify wood products' shrinkage and swelling rate, and the coefficient is defined as the strain produced due to a unit change in the moisture content of the wood. The strain produced due to moisture shrinkage or swelling is mainly governed by solid wood's radial and tangential shrinkage and swelling coefficients. The longitudinal coefficient is less critical since the strain produced in the longitudinal direction is usually a lot lower than in the transverse directions (Chiniforush, Akbarnezhad, et al., 2019).

For solid wood, the coefficients in only the anatomical orthotropic directions of wood are adequate to predict the shrinkage and swelling strain. For mass timber products like glulam and CLT, the interaction of the adjacent layers and the presence of glue between adjacent layers necessitates using an effective shrinkage and swelling coefficient or more sophisticated methods to predict the shrinkage and swelling strain. Glulam is composed of adjacent laminates of random growth ring patterns. Such random growth ring patterns lead to a discrepancy between glulam and solid wood's shrinkage and swelling behaviour. This effect is most prominent in the width and height direction of the glulam cross-section (Lee et al., 2019). The discrepancy between the shrinkage and swelling behaviour of CLT and solid wood is even more prominent. The cross-wise orientation of the laminates of adjacent layers of CLT influences the effective shrinkage and swelling coefficient in the in-plane directions, which differs significantly from that of the solid wood laminates that constitute the CLT. In the out-of-plane direction of CLT, the shrinkage and swelling behaviour is dominated by the radial shrinkage and swelling coefficient of the laminates of CLT (Pang & Jeong, 2020).

Though the shrinkage and the swelling coefficient are product-specific, in the standard BS EN 16351 (European Committee for Standardization, 2015), constant-coefficient values are given for the out-of-plane and in-plane directions of CLT. The limitation of this approach is that the shrinkage and swelling coefficients are influenced by the layer combinations and species of the laminates of CLT (Pang & Jeong, 2020), and the exact value of the coefficients might not be applicable for CLTs manufactured by different manufacturers. If prediction models for predicting the moisture shrinkage or swelling strain of CLT and glulam are developed based on the properties

of the laminates of the CLT and glulam, the dimensional changes of various configurations of CLT and glulam can be reliably estimated.

Due to the moisture adsorption of wood, swelling strain arises. This type of strain is also referred to as the hygro-expansion strain. This strain component mainly depends on the change of moisture content inside the wood and can be described by its linear relationship with the change in moisture content (Angst & Malo, 2012a):

Equation 2-2

$$\{\boldsymbol{\varepsilon_{mc}}\} = \{\boldsymbol{\alpha}\}\Delta u$$

Here, $\{\boldsymbol{\varepsilon_{mc}}\}$ is the swelling strain vector and $\{\boldsymbol{\alpha}\}$ is the swelling (or hygro-expansion) coefficient vector (given by equation 2-3), both along the primary orthotropic directions of wood. Δu is the change in moisture content inside the wood. The swelling strain and coefficient vector are defined as:

Equation 2-3

$$\{\boldsymbol{\varepsilon_{mc}}\} = \begin{bmatrix} \boldsymbol{\varepsilon_{mc,L}} \\ \boldsymbol{\varepsilon_{mc,R}} \\ \boldsymbol{\varepsilon_{mc,T}} \\ 0 \\ 0 \\ 0 \end{bmatrix}, \{\boldsymbol{\alpha}\} = \begin{bmatrix} \alpha_L \\ \alpha_R \\ \alpha_T \\ 0 \\ 0 \\ 0 \end{bmatrix}$$

For orthotropic materials like wood, moisture ingress generates only axial strain components in the three primary orthotropic directions. The three primary orthotropic directions of wood are the radial, tangential and longitudinal directions. The L, R and T subscripts in equation 2-3 refer to these three orthotropic directions - longitudinal, radial, and tangential. If the $\{\boldsymbol{\alpha}\}$ vector is known, the swelling strain arising from a change in moisture content can be easily computed using equation 2-2.

2.4 Axial Behaviour of Self-tapping Screws in Mass Timber Products

Depending on its intended application, STS can be considered active or passive. The purpose of a passive screw is to increase the load-carrying capacity of timber members by acting as structural reinforcement. On the other hand, active screws are used in connections. The thesis focuses on the active application of STS in different types of connections, e.g., wood-to-wood connections, wood-to-steel connections etc. Three possible failure modes can occur in connections involving STS

under axial loading conditions: (1) steel tensile failure of STS, (2) withdrawal failure of STS in the main member, and (3) head pull-through failure of the side member. As the steel tensile strength of STS is usually very high compared to the withdrawal capacity or the head pull-through resistance, failure mode (1) usually dominates only when the penetration length of the screw inside the main wood member is very high. The minimum penetration length of the screw inside the main wood member that causes screw tensile failure depends on the wood species (Gutknecht & MacDougall, 2019). The material properties of STS govern the steel tensile failure of STS. On the other hand, the withdrawal failure of STS depends on the length of penetration of the screw inside the main member, the density of the main member and the screw diameter (Mack, 1979). Finally, the head pull-through failure of STS is governed by the screw head size and the density of the side member (Chui & Craft, 2002).

The premature STS failure inside mass timber products, which is the concern of this thesis, is dictated by the withdrawal behaviour of the screw inside the mass timber and the tensile strength of the screw. Thus, a key to understanding the failure mechanism is the withdrawal of properties of the screw. Further, the stress distribution inside the screw can be predicted by numerical and analytical methods from the withdrawal properties. Also, a good understanding of the use of STS as reinforcement in mass timber products cannot be overlooked in understanding the premature STS failure mechanism in this study.

2.4.1 Withdrawal of Self-Tapping Screws in Mass Timber Products

Two parameters characterize the withdrawal properties of STS: (a) withdrawal strength and (b) withdrawal stiffness. The withdrawal strength of STS in solid lumber can be predicted by using available design standard provisions (e.g. EN 1995-1-1 (European Committee for Standardization, 2004), DIN 1052 (German Institute for Standardisation, 2008) etc.). However, the standards usually focus on withdrawal strength and not withdrawal stiffness (Stamatopoulos & Malo, 2016).

The basic equations to predict the characteristic withdrawal resistance (5^{th} percentile) according to EN 1995-1-1 (European Committee for Standardization, 2004) are given by:

Equation 2-4

$$R_{ax} = \frac{n_{ef} f_{ax} d L_{eff} k_d}{1.2(\cos\alpha)^2 + (\sin\alpha)^2}$$

Equation 2-5

$$n_{ef} = n^{0.9}$$

Equation 2-6

$$f_{ax} = 0.52 d^{-0.5} L_{eff}^{-0.1} \rho_k^{0.8}$$

Equation 2-7

$$k_d = min \begin{cases} \frac{d}{8} \text{ if } 6 \leq d \leq 8\, mm \\ 1 \text{ otherwise} \end{cases}$$

Here, R_{ax} is the withdrawal capacity, f_{ax} is the withdrawal strength, d is the outer thread diameter of the STS in mm, n_{ef} is a group effect factor which gives the effective number of screws among a group of n axially loaded screws, L_{eff} is the effective penetration length of the threaded part of the screw inside the wood member in mm, α is the angle between the screw axis and the grain direction of the main wood member into which the screw is inserted, k_d is a factor that reduces the withdrawal resistance of screws with nominal outer thread diameter between 6 and 8 mm, and ρ_k is the characteristic density (5th percentile) of the main wood member into which the screw is inserted in kg/m^3. Density is the only parameter that measures the anchoring capacity of the main wood member.

The equation to predict the characteristic withdrawal resistance according to DIN 1052 (German Institute for Standardisation, 2008) is given by:

Equation 2-8

$$R_{ax} = \frac{f_{1,k} d L_{eff}}{\frac{4}{3}(\cos\alpha)^2 + (\sin\alpha)^2}$$

Here, all the parameters are as explained before except the characteristic withdrawal parameter $f_{1,k}$ which depends on the load-carrying category of the main wood member (TFK). The characteristic withdrawal parameter of each category is given by DIN 1052 (German Institute for Standardisation, 2008):

$$\text{For TFK 1: } f_{1,k} = 60 \times 10^{-6} \rho_k^2$$

$$\text{For TFK 2: } f_{1,k} = 70 \times 10^{-6} \rho_k^2$$

For TFK 3: $f_{1,k} = 80 \times 10^{-6} \rho_k^2$

The design provisions for the STS are not covered in the current CSA O86 (Canadian Standards Association, 2019) standard. Provisions for wood screws and lag screws are present, but the properties, profile and behaviour of STS are quite different from wood and lag screws. Wood screws often require predrilled holes for high-density wood; lag screws require a lead hole for the threaded portion and a counterbore for the unthreaded portion. The installation procedure contributes to the difference in behaviour between STS, wood screws and lag screws.

The design provisions mentioned above do not include the effect of factors such as the variation of the surrounding moisture content, temperature, humidity and whether the screw hole is predrilled or not on the capacities of STS. Furthermore, the current provisions are applicable for STS inserted into single-layer products, like solid timber, not for layered mass timber products. The standardized test methods for experimental determination of the withdrawal strength of STS, like EN 1382 (European Committee for Standardization, 1999), specify stringent surrounding moisture content and loading conditions, thus limiting the scope for observing the effect of varying these parameters. It has been observed that the variation of the surrounding moisture content can significantly affect the physical properties of wood members (Silva et al., 2016). This, in turn, affects the structural performance and capacity of STS inserted into the wood members. From the recently identified failure mechanism of STS, it can be conjectured that the variation of the surrounding moisture content of wood exerts additional stress on the screw to cause failure. Usually, an equilibrium moisture content of about 15% is the maximum limit for the dry condition of wood members in the Canadian climate. Equilibrium moisture content higher than 15% is considered a wet condition and is suspected of harming the structural performance of STS.

Currently, minimal information is available on the influence of varying moisture content on the withdrawal behaviour of STS. Furthermore, information on the capacity of STS inserted into Canadian layered timber products like CLT and glulam is also limited. A few recent studies in related areas are summarised in the following paragraphs.

Uibel & Blaß (2007) studied the withdrawal strength of STS inserted on both the side face and the plane face of CLTs. They tested three and five-layered CLT made from European spruce lumber of strength grade C24. Screws of diameters 6, 8 and 12 mm were tested. They came up with the following equation from their test results to predict the withdrawal capacity:

Equation 2-9

$$R_{ax} = \frac{0.44 d^{0.8} L_{eff}^{0.9} \rho^{0.75}}{1.25(\cos\alpha)^2 + (\sin\alpha)^2}$$

Here, ρ is the average density of the whole CLT section, and all other terms are as explained before. In this equation, the actual average density of the tested CLT panel was used as an input parameter to predict the withdrawal capacity. The following equation was suggested to predict the withdrawal resistance from the characteristic density of the CLT:

Equation 2-10

$$R_{ax} = \frac{0.35 d^{0.8} L_{eff}^{0.9} \rho_k^{0.75}}{1.5(\cos\alpha)^2 + (\sin\alpha)^2}$$

Pirnbacher et al. (2009) investigated the effect of the following factors on the withdrawal strength of STS: (a) moisture content, (b) temperature during the installation of screws and during withdrawal tests, (c) the screw diameter, (d) the length of embedment of the threaded part of the screw, (e) the angle between the screw axis and the grain direction of the timber member into which the screw is inserted (inclination angle), and (f) presence of predrilled screw hole. This study used solid timber of strength class C24 and glue-laminated timber (glulam) of strength class GL28h, both made from Sitka spruce, as wood members. The influence of varying the concerned parameters was quantified by normalizing the test results with respect to some reference values. For normalization, the following values were taken as reference values from the test:

- 12% as the reference moisture content
- 20° C as the reference temperature
- 8 mm diameter as the reference diameter of screws
- Stress levels reached at 15 mm embedment length of the screw as the reference for investigating the effect of the effective embedment length of the screw
- 90° as the reference angle between the screw and the grain direction of the timber member

For investigating the effect of all parameters except the screw diameter, the screw diameter was kept constant at 8 mm. The planned equilibrium moisture content levels in Pirnbacher et al. (2009)'s study were 0%, 6%, 12% and 20%, while the actual mean values of moisture content levels were 0%, 9%, 14% and 19%. They found a constant withdrawal capacity of STS between

8% and 12% surrounding moisture content. On the other hand, a linear decrease of 0.65% per percent increase of moisture content was observed above 12% and within 20% surrounding moisture content. However, the effect of moisture content above the fibre saturation point was not investigated since there is usually no change in the withdrawal strength above that point.

Screws of 8, 10 and 12 mm diameters were tested to investigate the effect of the diameter of the screw. Pirnbacher et al. (2009) explored the impact of the diameter of screws with a constant slenderness ratio of 12. Taking the withdrawal capacity of STS with a diameter of 8 mm as the reference, they found the withdrawal capacity to decrease nonlinearly with the increase of screw diameter above 8 mm following a power law. The diameter of the tested screws ranged from 8 mm to 12 mm.

The withdrawal strength of screws installed with predrilled holes was on average 3.5% and 1.3% lower than that of screws inserted without predrilled holes at the mean and the 5th percentile levels, respectively. The presence of predrilling was postulated to have no significant effect on the withdrawal resistance of STS owing to this slight difference. Some STS manufacturers recommend not using predrilled holes as predrilling can reduce the withdrawal capacity of the screws if the holes are too large. Notwithstanding, predrilling may be required in some exceptional cases, e.g. in extremely dry or high-density wood, aged timbers, installation close to the edges of the wood members etc. (MTC Solutions, 2020).

The effect of the length of the tip of the screw on calculating the effective screw length was accounted for by using a factor expressed in terms of the screw diameter in this study. The effective penetration length of the screw considers the length of the tip of the screw, which is not fully effective in imparting withdrawal resistance. The following expression gives the corrected effective length of the screw (in mm) to predict the withdrawal resistance, according to Pirnbacher et al. (2009).

Equation 2-11

$$L_{eff} = l_{threaded} - (1.17d)d$$

Here, $l_{threaded}$ is the length of the threaded portion of the screw inserted into the timber member in mm. Some screw manufacturers specify the length of the screw tip in their design guides and suggest subtracting the tip length from the length of the threaded part of the screw to determine

the effective penetration length (MTC Solutions, 2020). Thus, $(1.17d)d$ in the previous equation, with d being the screw diameter in mm can be considered the length of the tip of the screw.

Pirnbacher et al. (2009) modelled the experimental values of the withdrawal strength (in MPa) using the following two equations, depending on the angle between the screw axis and the grain direction of the timber member. The effect of the diameter of the screws on the withdrawal resistance is reflected in these two equations.

Equation 2-12

$$f_{ax,90} = 0.01353\rho_{test} - 0.28147(2.44d^{0.572}) + 2.18888$$

Equation 2-13

$$f_{ax,0} = 0.00538\rho_{test} - 0.45875(2.44d^{0.572}) + 5.92460$$

Here, $f_{ax,90}$ is the predicted withdrawal strength of screws inserted perpendicular to the direction of the grains of the timber member and $f_{ax,0}$ is the predicted withdrawal strength of screws inserted parallel to the direction of the grains of the timber member. ρ_{test} is the average density of the laminates of the timber member (in kg/m^3) determined from tests. These two equations apply to STS of outer diameter 8-12 mm inserted into solid timber of strength class C24 and glulam of strength class GL28h.

Ringhofer et al. (2014) investigated the influence of varying moisture content on the withdrawal resistance of STS in solid timber and CLT made of Norway spruce. The screws were inserted at two angles for solid timber, perpendicular and parallel to the grain direction wood. For the parallel to grain direction insertion, the planned moisture levels were 0%, 6%, 9%, 12%, 15%, 18% and 21%, and for the perpendicular to grain direction insertion, the planned moisture levels were 0%, 7%, 9%, 12%, 15%,18% and 20%. The screws in CLT were all inserted perpendicular to the wood's grain direction. For screws inserted into CLT, only three moisture content levels were planned, viz, 8%, 12%, and 18%. The actual moisture contents achieved during testing were very close to the planned levels.

Ringhofer et al. (2014) prepared the test specimens of their study in the following order: conditioning the sample to 12% moisture content, installing the screw, and conditioning the sample to the target moisture content. After the target moisture content was achieved, the specimen was subjected to withdrawal tests. Ringhofer et al. (2014) adopted this procedure to simulate the

condition that the moisture content of timber members might change after the assembly of screws in practical settings. However, in their study, Ringhofer et al. (2014) also included a control group of solid lumber specimens conditioned to the final target of 18% moisture content before installing the screw, without any further conditioning afterward. Through the statistical analysis, it was found that the mean and median values of the withdrawal strength of the control group did not deviate significantly from those of the specimen, which was first conditioned to a 12% moisture content and subsequently to the final moisture content of 18% after installation of screws. This finding implies that the withdrawal strength of the screw inserted into solid timber does not depend on the intermediate moisture conditions, provided the final moisture content is the same.

Nonetheless, this finding is only valid for the target 18% moisture content for screws inserted into solid timber. For STS inserted into CLT, it was found that the withdrawal strength stayed constant between 8% and 12% moisture content, and between 12% and 18% moisture content, the withdrawal strength decreased with the increase in moisture content. However, the rate of decrease in the withdrawal strength with the increase in moisture content between 12% and 18% was lower for screw inserted into CLT than that inserted into solid timber.

Ringhofer et al. (2014) identified an inaccurate measurement procedure adopted in Pirnbacher et al. (2009)'s tests for measuring the maximum force reached by some specimens. This led to a reassessment and correction of Pirnbacher et al. (2009)'s test data using maximum likelihood estimation and assuming the lognormal distribution of the test data. After correction of the test data, it was found that, above 12% moisture content, the rate of decrease of withdrawal strength with the increase in moisture content was more scarped than the original rate in Pirnbacher et al. (2009)'s study.

Ringhofer et al. (2014) proposed two models to encapsulate the effect of moisture content on the screw withdrawal strength from the tests, viz, (a) a bilinear model and (b) a non-linear model with a continuous function. For both models, a factor, η_u was proposed to predict the withdrawal strength at a given moisture content. The mean value of the withdrawal strength determined at a moisture content of 12% was taken as the reference point for the factor. The following equation gives the bilinear model:

Equation 2-14

$$\eta_u = \frac{f_{ax,u}}{f_{ax,u=12}} = \begin{cases} 1.00 \text{ for } 8\% \leq u \leq 12\% \\ 1.00 - k_{MC}(u-12) \text{ for } 12\% < u \leq 20\% \end{cases}$$

Here, k_{MC} is a factor that scales the reference withdrawal resistance at 12% moisture content $(f_{ax,u=12})$ to predict the withdrawal resistance at a moisture content different than 12% $(f_{ax,u})$. u is the moisture content of the wood member. The k_{MC} values are given in Table 2-1.

Table 2-1: k_{MC} Values

k_{MC}	Screw Insertion Direction	Type of Wood Member
0.036	Parallel to wood's grain	Solid Timber
0.031	Perpendicular to wood's grain	Solid Timber
0.017	Perpendicular to wood's grain	CLT

The following equation gives the non-linear model in Ringhofer et al. (2014)'s study:

Equation 2-15

$$\eta_u = \frac{f_{ax,u}}{f_{ax,u=12}} = \eta_0 + \frac{u + k_1 u^N}{k_2 + k_3 u + k_4 u^N} \text{ for } 0\% \leq u \leq 20\%$$

The values of the constants ($\eta_0, k_1, k_2, k_3, k_4, N$) of the non-linear model are given in Table 2-2.

Table 2-2: Input parameters (dimensionless) for the non-linear model

Screw Insertion Direction	η_0	$k_1(\times 10^{-6})$	k_2	k_3	$k_4(\times 10^{-6})$	N
Parallel to wood's grain	0.96	-2.34	53.6	5.44	4.36	5.94
Perpendicular to wood's grain	0.88	-3.42	54.8	1.37	9.13	5.50
Both	0.92	-9.13	55.5	1.99	1.92	5.30

Ringhofer et al. (2014) compared the non-linear model with values from similar works. They suggested the non-linear model is a good predictor of the screw withdrawal strength throughout the moisture content range 0% - 32%.

Ringhofer et al. (2015) found that the number of layers penetrated by STS in layered timber products like glulam and CLT significantly influences the withdrawal resistance. Their study used CLT and glulam made of Norway spruce of strength grade C24 and two different density groups.

Screws of 8, 10 and 12 mm diameter were used, and the screws were inserted into the plane side of CLT and glulam perpendicular to the wood's grain direction. The moisture content was kept constant at 12 ± 2% during the tests. The orthogonal arrangement of laminates in CLT imparts higher withdrawal resistance to STS than the unidirectional arrangement of the laminates in glulam. On average, the withdrawal strength of STS inserted into CLT was 2.9% higher than that inserted into glulam made of the same type of laminates. Screws inserted into either CLT or glulam with predrilled holes had 3.1% lower withdrawal strength than screws inserted directly into CLT or glulam.

Compared to the effect of the orientation of each layer and the presence of predrilling, the number of layers penetrated by the screw had the most significant influence on the withdrawal resistance of screws. Ringhofer et al. (2015) mentioned that the effect of homogenization in layered timber products is not reflected in the withdrawal resistance of STS inserted into them in any current technical standards or approvals. Homogenization leads to reduced dispersion in the mechanical properties of layered timbered products compared to solid lumber. To consider the effect of homogenization of layered products and multiple numbers of layers penetrated by the screw, Ringhofer et al. (2015) proposed a stochastic model to predict the 5th percentile withdrawal resistance of STS.

Ringhofer et al. (2015) assumed a lognormal distribution for the experimental values of the withdrawal strength of STS. If the withdrawal resistance of STS is represented by the random variable $x_{1,N}$, then $y_{1,N} = ln(x_{1,N})$ is a normally distributed random variable with the parameters $\mu_{y1,N}$ and $\sigma_{y1,N}$. Here, the random variable $x_{1,N}$ applies to N number of layers of the timber product penetrated by the screw. The effect of the N number of layers on the withdrawal resistance is considered by the method proposed by Brandner & Schickhofer (2006), using the distribution characteristics (mean and standard deviation) of the single-layer lumber's density. The parameters $\mu_{y1,N}$ and $\sigma_{y1,N}$ of the normally distributed random variable $y_{1,N}$ can be determined from the distribution characteristics of the experimental values of the withdrawal strength and the single-layer density of lumber. Then, the following equation determines the characteristic withdrawal strength of the STS penetrated into N layers of the layered product.

Equation 2-16

$$f_{ax,N} = e^{(\mu_{y1,N} + \phi^{-1}(0.05)\sigma_{y1,N})}$$

Here, $\mu_{y1,N}$ and $\sigma_{y1,N}$ are the parameters of $y_{1,N}$ and $\phi^{-1}(0.05)$ is the inverse of the standard normal distribution for the 5th percentile. This equation applies to both CLT and glulam, as Ringhofer et al. (2015) considered the difference in withdrawal resistance of screws in CLT and glulam to be negligible.

To make the stochastic model more straightforward and suitable for design purposes, Ringhofer et al. (2015) suggested the following method to predict the withdrawal resistance of the screw:

Equation 2-17

$$f_{ax,N} = \left(\frac{\rho_{CXY}}{\rho_k}\right)^{0.8} . k_{sys,k} . f_{ax}$$

Here, ρ_k and f_{ax} are the characteristic density and withdrawal strength of STS inserted into a single layer of lumber as determined according to EN-1995-1-1 (European Committee for Standardization, 2004). ρ_{CXY} is the characteristic density of the layered timber product. $k_{sys,k}$ is a system effect factor that quantifies the homogenization effect, a function of the number of layers (N) penetrated by the screw (Table 2-3).

Table 2-3: $k_{sys,k}$ values

N (Number of layers)	2	3	4	5	6	7	8	9	10
$k_{sys,k}$	1.06	1.10	1.12	1.13	1.14	1.15	1.16	1.17	1.17

It is to be noted that Ringhofer et al. (2015) 's model is only valid for CLT or glulam, which constitute laminates of the same strength class for all the layers. This model's width of the CLT and glulam laminates is limited to 40 mm. The primary parameters forming the basis of the model are the number of layers penetrated by the screw, distribution characteristics of the density of the solid lumber which forms the layered timber product, and the single-layer withdrawal resistance of the screw.

Silva et al. (2016) studied the effects of different moisture contents, varying relative humidity cycles, and the gaps in CLT panels on the withdrawal resistance of STS inserted on the wide face of CLT panels. The CLT used in the test program was produced from spruce of strength class C24. Three planned moisture content levels of 8%, 12% and 18% were considered for studying the effect of moisture content. For observing the impact of continuous different relative humidity

cycles, test specimens were subjected to six months of humidity cycles, in which relative humidity was alternately varied between 30% RH and 90% RH at intervals of 21 days, followed by stabilization to approximately 14% equilibrium moisture content. This whole process of the relative humidity cycle took 324 days.

For the same configuration of CLT, with the application of the varying relative humidity cycle, no significant effect on the withdrawal resistance was observed compared to the case without the application of the varying relative humidity cycle. Compared to the withdrawal resistance at 12% moisture content, CLT specimens without gaps along the screw path and with 0 mm gaps exhibited no change in withdrawal resistance at 8% moisture content. In comparison, a slight decrease was observed at 18% moisture content. On the other hand, CLT specimens with 4 mm gaps significantly reduced withdrawal resistance at 8% moisture content, compared to the withdrawal resistance at 12% moisture content. However, the decrease became less pronounced at 18% moisture content, especially with the increase in the number of gaps.

Concerning the effect of gaps along the path of the screw, CLT specimens with no gap, and 1,2 and 3 number of gaps between adjacent laminates of the same layer of CLT along the path of the screw were studied by Silva et al. (2016). For CLTs with gaps along the path of the screw, the gap widths of 0 mm and 4 mm were used. Silva et al. (2016) used 3-layered CLT specimens for their study.

It was found that the withdrawal resistance of STS increased with the gradual increase of the number of gaps of width 0 mm along the screw path for all the moisture content levels tested. However, upon subjecting the CLT to the varying relative humidity cycle for the same configuration and the same gap width of 0 mm, the withdrawal resistance decreased with the increased number of gaps. Furthermore, for the rise of gap width to 4 mm, the withdrawal resistance also reduced with increasing the number of gaps. Subjecting the CLT with a gap width of 4 mm to the six-month varying relative humidity cycle led to an even higher decrease in withdrawal resistance with the increase of the number of gaps compared to the CLT with a 0 mm gap width.

Silva et al. (2016) proposed a bi-linear factor to quantify the effect of moisture content (η_{MC}) on the withdrawal resistance of STS from their test results.

Equation 2-18

$$\eta_{MC} = \frac{f_{ax,u}}{f_{ax,u=12}}$$

$$= \begin{cases} \text{1.00 for CLT with no gap and CLT with gap width = 0 mm, with } 8\% \leq u \leq 12\% \\ 1.00 - k_{MC}(u-12) \begin{cases} \text{for CLT with gap width = 4 mm and } 8\% \leq u \leq 18\% \\ \text{for CLT with no gap and CLT with gap width = 0 mm and with } 12\% < u \leq 18\% \end{cases} \end{cases}$$

In this equation, $f_{ax,u}$ is the withdrawal resistance of STS inserted in a given configuration of CLT with an equilibrium moisture content between 8% and 18% and $f_{ax,u=12}$ is the mean withdrawal resistance of STS in the same configuration of CLT at 12% equilibrium moisture content. k_{MC} is a weighting factor, which specifies the change in withdrawal resistance with the change in equilibrium moisture content to any value other than 12%. The k_{MC} values are given in Table 2-4. The appropriate sign of the values accounts for the increase or decrease in the withdrawal resistance.

Table 2-4: k_{MC} Values from Silva et al. (2016)

Surrounding Moisture Content-Range	CLT Gap Type			
	No-Gap	0 mm Gap	4 mm Gap (1 gap)	4 mm Gap (2-3 gaps)
8-12%	0.00	0.00	-0.02	-0.05
12-18%	0.02	-0.02	-0.01	0.00

Silva et al. (2016) found the withdrawal resistance of STS to decrease by approximately 1.8% with each percent increase of the equilibrium moisture content of CLT for moisture content levels between 12% and 18%. In contrast to CLT, Ringhofer et al. (2014) found 3.1% and 2.5% decrease for each percent increase of moisture content for solid timber and glulam respectively.

Silva et al. (2016) also compared the withdrawal resistance of STS inserted into glulam and CLT specimens (without gaps) to understand the effect of the orthogonal arrangement of the laminates on the withdrawal strength. STS inserted into glulam specimens had 7.8% higher withdrawal resistance than STS inserted into CLT specimens. However, subjected to varying relative humidity cycles, STS inserted into glulam specimens exhibited 7.6% lower withdrawal resistance than STS inserted into CLT specimens. Thus, the relative humidity cycle coupled with the cross-wise lamination of the CLT has a positive effect on the STS withdrawal resistance.

Gutknecht & MacDougall (2019) studied the withdrawal resistance of STS inserted parallel-to-grain in Canadian timber species. Though there has been extensive research on the withdrawal resistance of STS inserted into European timber species, only a few studies, e.g., Gehloff (2011), Abukari (2012), investigated the withdrawal resistance of STS inserted into Canadian timber and glulam. However, these studies were not concerned with the effect of changing moisture content on the withdrawal resistance. Though studying the impact of a range of moisture content was not a focus of Gutknecht & MacDougall (2019)'s study, they carried out withdrawal tests of STS under the dry and wet conditions of the timber specimen and after subjecting timber to a dry-wet-dry cycle. The moisture content for the dry condition was between 6% and 7% EMC, while it was 28% for the wet condition. Screws of diameters 10 mm and 12 mm, and Douglas fir (select structural grade) and eastern white Pine (ungraded) lumber were used in the test program.
Gutknecht & MacDougall (2019) found that the embedment length required to initiate tensile failure of the screw was approximately 17% longer in wet conditions than the dry condition. Screws inserted into wet Douglas fir samples exhibited 15% lower withdrawal strength than dry samples. Moreover, Douglas fir samples subjected to a dry-wet-dry cycle showed a 49% reduction in the withdrawal strength compared to the dry samples.

2.4.2 STS as Reinforcement in Timber Products

Though this research focuses on applying STS in connections as active screws, the knowledge of STS as a reinforcement to increase the load-carrying capacity of timber members can not be disregarded entirely.

Angst & Malo (2012a) examined the effects of using STS as perpendicular to grain reinforcement in glulam under wet and dry exposures. Their study used glulam made from Norway spruce, comparable to strength class GL30c, and screws with a diameter of 8 mm. For wet exposure, they subjected specimens to 90% relative humidity (RH) and for dry exposure, to 50% RH.

From the experimental results, the perpendicular to grain strain across the glulam specimen with STS reinforcement was lower than that in the unreinforced specimen. Furthermore, the difference in the strain between the reinforced and unreinforced specimens increased over time. For the drying case, the tensile stresses arising at the outer sides of the glulam were amplified due to STS reinforcement, which implies STS has a negative effect on the glulam during drying. In the wetting case, the overall perpendicular to grain tensile stress in the glulam was reduced by 30-70% due to

the STS reinforcement. The overall stress arising during drying was significantly lower than that during wetting. Angst & Malo (2012a) also indicated that the stress developed in the screw during wetting exposures might be very close to the tensile strength of the screws. However, their study did not explore the stress generated in the screws.

Dietsch (2017) studied the influence of STS reinforcement on the magnitude of moisture-induced stresses in solid timber members. The emphasis was drawn on the shrinkage process of timber members. For this purpose, experimental and numerical methods were adopted. The study results indicate that a reduction of timber moisture content of 3% around threaded steel rods positioned perpendicular to the wood's grain direction can lead to critical tensile stresses perpendicular to the grain. Dietsch (2017) recommended STS reinforcements be placed in the center of a timber cross-section.

2.4.3 Stress Distribution in Screw-Mass Timber Composite System

As mentioned earlier, the stress distribution inside the screw can be predicted by numerical and analytical methods from the withdrawal properties. The analytical treatment of the stress distribution is based on the well-known classical Volkersen theory (Volkerson, 1938). Jensen et al. (2001) first presented analytical models for predicting a dowel's pull-out capacity parallel to the grain direction of joined timber parts. In this model, the dowel and the wood member were assumed to be in a state of pure axial tension, and the bond-line (glue-line) was assumed to be under pure shear. The thickness of the bond line was considered negligible. Then, from linear elastic stress analysis, stress distribution functions for the wood, the dowel and the bond line in the direction parallel to the dowel axis were proposed.

Stamatopoulos & Malo (2015) extended the work of Jensen et al. (2001) to predict the withdrawal capacity of axially loaded threaded rods embedded in glulam. The core of the threaded rods is analogous to the dowel, and the glulam element can be considered the wood member. On the other hand, the thread-wood interaction zone was considered the bond line under pure shear. A bilinear constitutive law for the bond line was proposed in this study. With the same principles adopted in Jensen et al. (2001), Stamatopoulos & Malo (2015) predicted the withdrawal capacity of threaded rods of 20 mm outer diameter embedded in glulam. The predicted capacity was verified with experimental withdrawal test results, and a linear relationship between the rod penetration length

and withdrawal capacity was derived. Further, in this study, a post-elastic stress analysis was carried out to find the stress distribution of the bond line after reaching the withdrawal capacity.

Another accompanying paper (Stamatopoulos & Malo, 2016) studied the withdrawal stiffness of axially loaded threaded rods of 20 mm outer diameter embedded in glulam based on the same principles. A model to predict the withdrawal stiffness of the threaded rod was suggested and verified with numerical and experimental results. The withdrawal stiffness was found to increase with the rod penetration length. Also, the stress distribution in the threaded rod was modelled numerically and analytically. A close match between the stress distribution from the analytical and numerical models was observed.

2.5 Summary

This chapter has reviewed the previous studies and codes on the moisture transport properties, shrinkage and swelling behaviour of mass timber products and the axial behaviour of self-tapping screws. The swelling behaviour of mass timber products has been extensively investigated. However, the prediction of swelling behaviour from the laminate properties of the mass timber has not been focused. The moisture transport in mass timber products has been investigated in limited studies. Still, none focused on the moisture transport process in mass timber products during moisture adsorption. Most of the work hitherto on the effect of moisture content variation of mass timber products on the performance of STS has focused on the withdrawal resistance of STS when they are used as active screws in connections. A few studies focused on the passive application of STS during moisture content variation of mass timber products. No study has examined the stress distribution of the screw-mass timber product composite system under axial load and moisture content variation of mass timber products.

3 SELF-TAPPING SCREW TENSILE PROPERTIES

3.1 Introduction

This chapter aims to overview and establish a database of the tensile properties of self-tapping screws from two manufacturers used in the research program. This chapter begins with a brief discussion on the geometry and features of self-tapping screws. Screws of various configurations from two manufacturers were tested in axial tension until failure to generate systematic information on the tensile properties of self-tapping screws. The load-deformation behaviour of the screws was recorded and used to determine the yield strength in tension, Young's modulus and ultimate tensile strength. This information is fundamental to the prediction of their behaviour under axial load.

3.2 Self-tapping Screw Geometry and Features

The various parts of a self-tapping screw are exhibited in Figure 3-1. In terms of the length of the threaded portion of the screw, self-tapping screws can be either (a) partially threaded or (b) fully threaded. The screw at the top of Figure 3-1 is partially threaded, and the one at the bottom is a fully threaded screw. Partially threaded screws are often utilized in cases where screws are subjected to lateral loading, or head pull-through is a critical design consideration. In contrast, fully threaded screws are preferred in axial or near-axial loading conditions (MTC Solutions, 2020). The self-tapping tip at the nib of the screw facilitates the self-drilling capability of self-tapping screws and eliminates the need for predrilling holes to insert the self-tapping screws. The elimination of predrilled holes contributes to greater withdrawal resistance of the screws. The shank cutter, usually present in partially threaded screws, reduces the torque requirement for screw installation and makes the screw installation easier. It also allows the wood member to settle freely around the shank of the screw. The head of the screw can have different shapes depending on the intended use of the screw. The most common screw heads are countersunk, cylindrical, and washer heads, as shown in Figure 3-2.

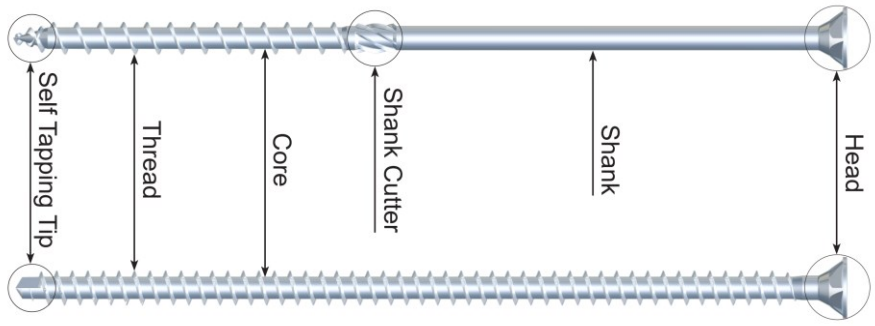

Figure 3-1: Parts of a self-tapping screw (MTC Solutions, 2020)

Figure 3-2: Different types of screw heads (MTC Solutions, 2020)

For defining the geometry of self-tapping screws, several parameters are of importance. Figure 3-3 shows the parameters used to determine the design properties of the screw. A partially threaded screw is shown here, though the exact parameters apply to a fully-threaded screw. D is the outer thread diameter of the screw, D_{core} is the core diameter of the screw, L_{Tip} is the length of the self-tapping tip, L_{Thread} is the length of the threaded part of the screw, and L is the total length of the screw.

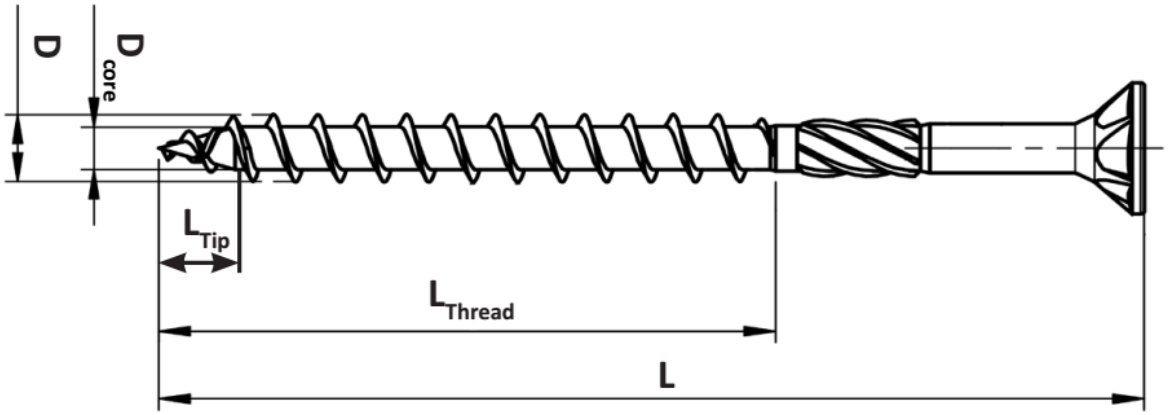

Figure 3-3: Screw geometry (MTC Solutions, 2020)

3.3 Uniaxial Tensile Test of Self-tapping Screws

The screw configurations shown in Table 3-1 were tested. The thread diameter in Table 3-1 is the outer diameter of the screw, including the threads and the root diameter is the diameter of the inner

core of the screw, as shown in Figure 3-3. Two manufacturers provided the screws. The number of samples tested for each screw configuration is also mentioned in the table. More samples were tested for screw configurations which produced less consistent load-deformation graphs. The screw samples were labelled according to the manufacturer/screw type, outer thread diameter and length. For example, the label "ASSY 6-200" means that the screw-type is ASSY, the outer thread diameter is 6 mm, and the length is 200 mm. In Figure 3-4, a few screw samples before the tensile test have been shown.

Table 3-1: Screw configurations tested

Screw Name	Screw Type	Head Type	Thread Diameter (mm)	Root Diameter (mm)	Length (mm)	Number of specimens
ASSY 6-200	ASSY	Cylindrical	6	3.8	200	6
ASSY 8-160	ASSY	Countersunk	8	5	160	6
ASSY 10-200	ASSY	Countersunk	10	6.2	200	8
ASSY 12-200	ASSY	Countersunk	12	7.1	200	6
VGS 9-360	VGS	Countersunk	9	5.9	360	8
VGS 11-200	VGS	Countersunk	11	6.6	200	9
VGS 13-200	VGS	Countersunk	13	9.6	200	11
VGZ 5-160	VGZ	Cylindrical	5.6	3.8	160	6
VGZ 11-250	VGZ	Cylindrical	11	6.5	250	6

Figure 3-4: A few screw samples before the tensile test

The screws were subjected to tensile tests using a universal testing machine. An ad-hoc adapter was prepared using a steel channel (HSS 5"×5"×0.5") section of length 88.9 mm, and a steel bearing plate was used to anchor the head of the screw inside the channel section. The adapter used is shown in Figure 3-5.

Figure 3-5: The adapter made from a steel channel section with a hole in the middle to accommodate the screw

Dies were used for gripping the thread of the ASSY screws, as shown in Figure 3-6. For the other screws, a gripping device was utilized to grip the screw thread. The complete test setup with the specimen fitted inside the test fixture is shown in Figure 3-7. In the figure, the gripping device is shown on the top. The elongation of the specimen was recorded with an extensometer attached to the thread of the screw. The applied load was measured by the load cell of the machine. Two different extensometers were used in the test program. For ASSY 6-200, ASSY 8-160, ASSY 12-200 and VGZ 5-160 screws, MTS model 632.11 extensometer with a gauge length of 1-inch was used. For the rest of the screws, Epsilon Model 3543 extensometer with a 2-inch gauge length was used. The load was applied to the specimen under displacement control at 0.5 inches/min. All the samples were loaded to failure.

The following section describes the mean tensile properties of each of the tested screw configurations. The data analysis was carried out using Origin 2022 (OriginLab Corporation, 2021) software. The screw samples that gave load-deformation graphs with a higher degree of non-linearity in the initial portion before the yielding and did not have any clear failure point were treated as outliers.

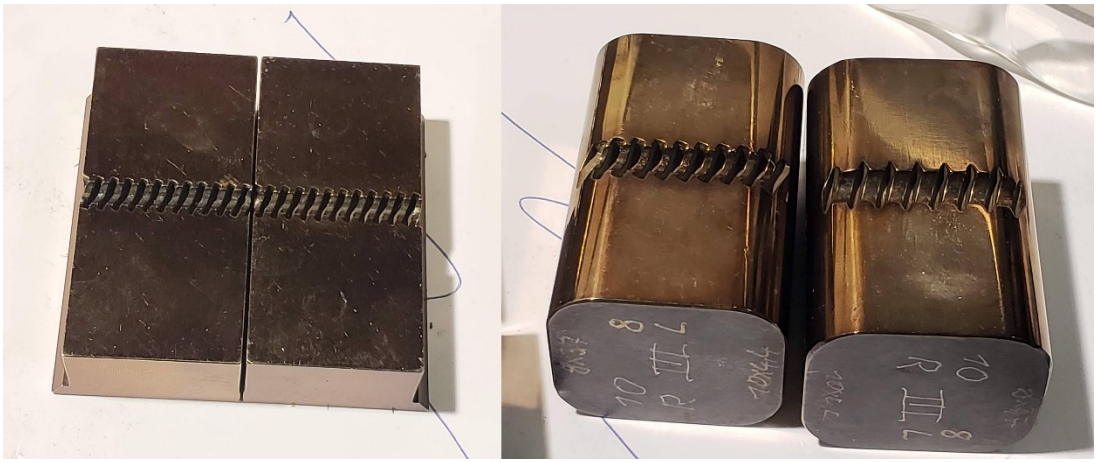

Figure 3-6: Two different types of dies used

Figure 3-7: Complete screw tensile test setup

3.4 Results and Discussion

3.4.1 Stress-strain Curve

The load-displacement curves were recorded at a rate of approximately 3 data points per second. The load-displacement curves were converted to stress-strain curves. The load at each data point was divided by the initial cross-sectional area of the root area (core part, excluding the threads) of the screw to calculate the stress. The change in length at each data point was divided by the gauge

length over which the displacement was measured to determine the strain. The effects of transverse strain and changing cross-section were ignored in calculating the axial stress in this test program. This can be justified by the negligible difference between the true stress-strain curve and the engineering stress-strain curve, as shown for one of the specimens in Figure 3-8. The engineering stress-strain curve does not consider the change in the cross-sectional area upon the action of axial stress. On the other hand, the true stress-strain curve considers the change in the cross-sectional area of the root area of the screw.

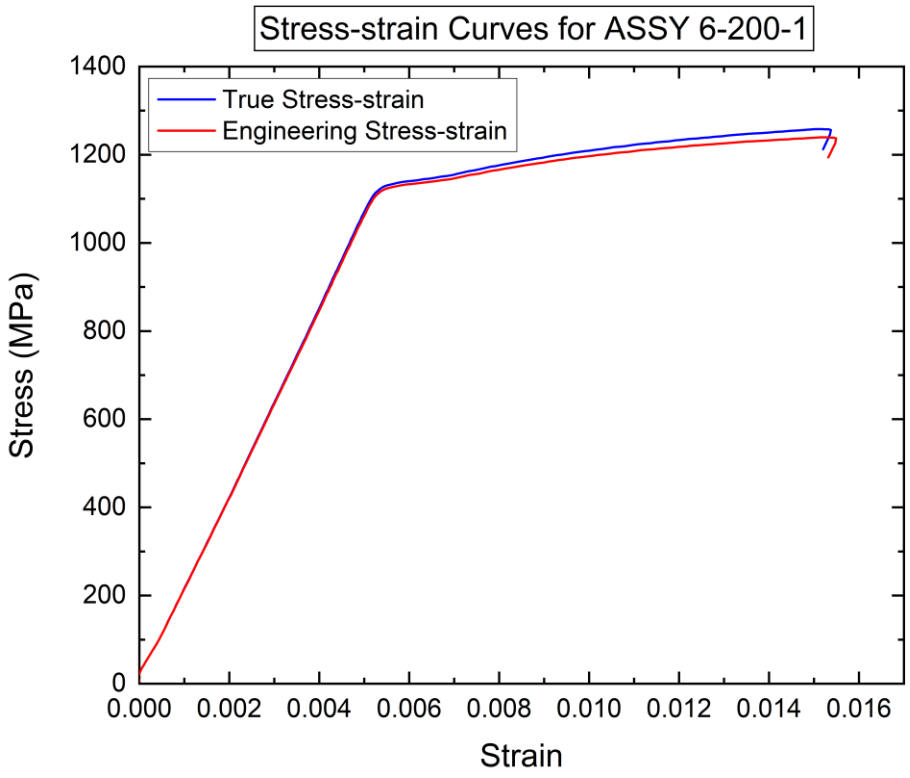

Figure 3-8: Engineering and true stress-strain curve

None of the samples exhibited any yield plateau or discrete yield points. Thus, the 0.2% offset method was used according to ASTM E8/E8M (ASTM International, 2021) to determine the yield strength. The stress-strain curve for the different configurations of the screw is exhibited in Figure 3-9. The samples with inconsistent stress-strain behaviour than the rest have been left out of the figure. The enlarged stress-strain curves can be found in Appendix A.

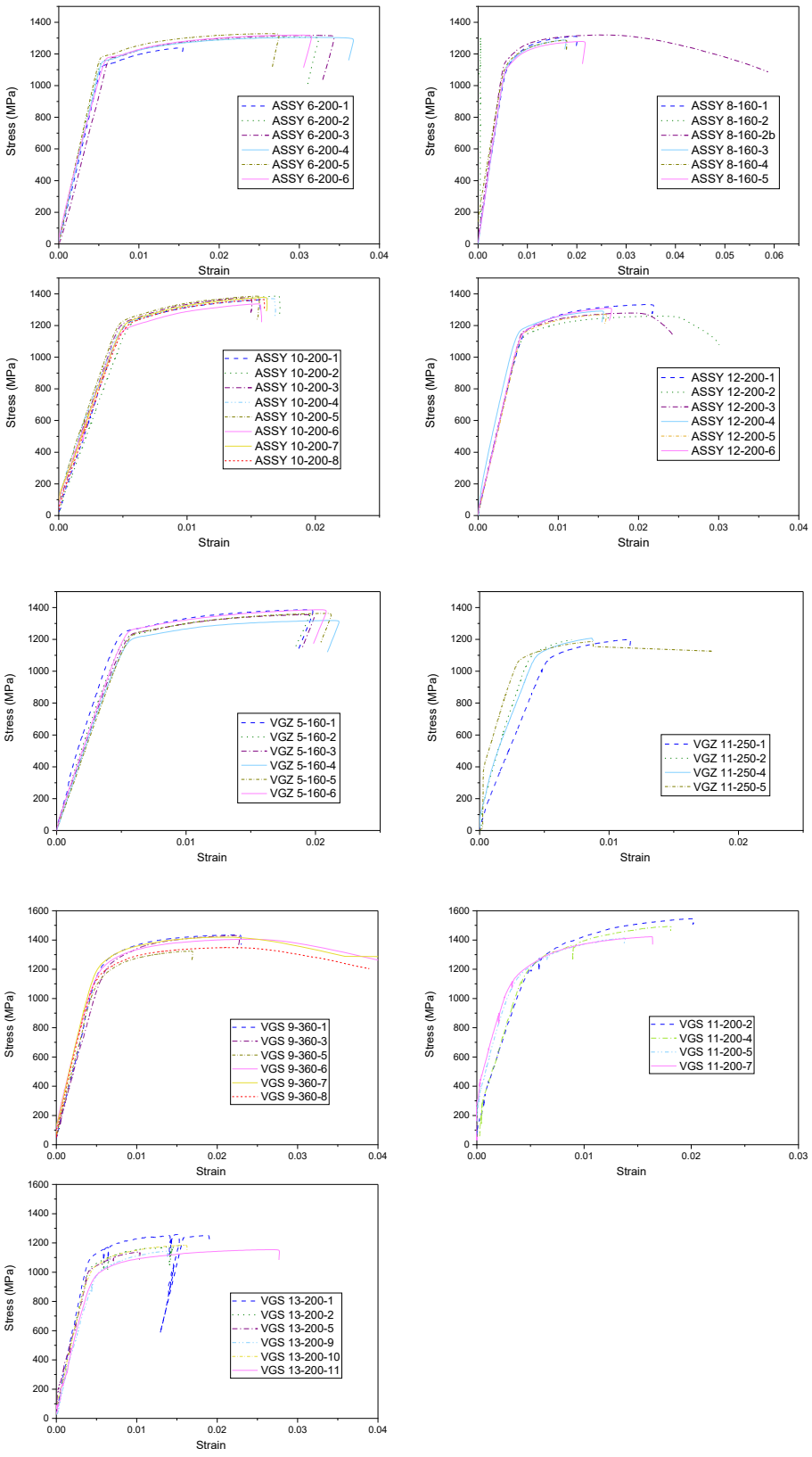

Figure 3-9: Stress-strain curves of different screw configurations

3.4.2 Young's Modulus

Young's modulus was determined by finding the slope of the fitted line of the initial linear portion of the stress-strain curve according to ASTM E111 (ASTM International, 2017). Table 3-2 lists the mean values of Young's modulus and coefficient of variation (a measure of variability) for each of the tested screw configurations.

Table 3-2: Young's modulus values

Screw Configuration	Mean Young's Modulus (GPa)	Coefficient of Variation (%)
ASSY 6-200	211.6	6.8
ASSY 8-160	208.2	3.8
ASSY 10-200	225.3	3.3
ASSY 12-200	217.8	3.2
VGS 9-360	216.5	6.4
VGS 11-200	253.8	12.1
VGS 13-200	226.6	11.8
VGZ 5-160	235.8	6.5
VGZ 11-250	226.3	11.1

3.4.3 Yield Strength

This test program determined yield strength using the 0.2% offset method according to ASTM E8/E8M (ASTM International, 2021). In this method, a straight line is drawn parallel to the initial linear portion of the stress-strain curve but is offset by 0.2% of the diameter of the screw along the x-axis, and the intersection point of this line with the stress-strain curve gives the value of the yield strength. The method for determining Young's modulus and the yield strength is illustrated in Figure 3-10. The mean yield strengths and coefficient of variation for each tested screw are given in Table 3-3.

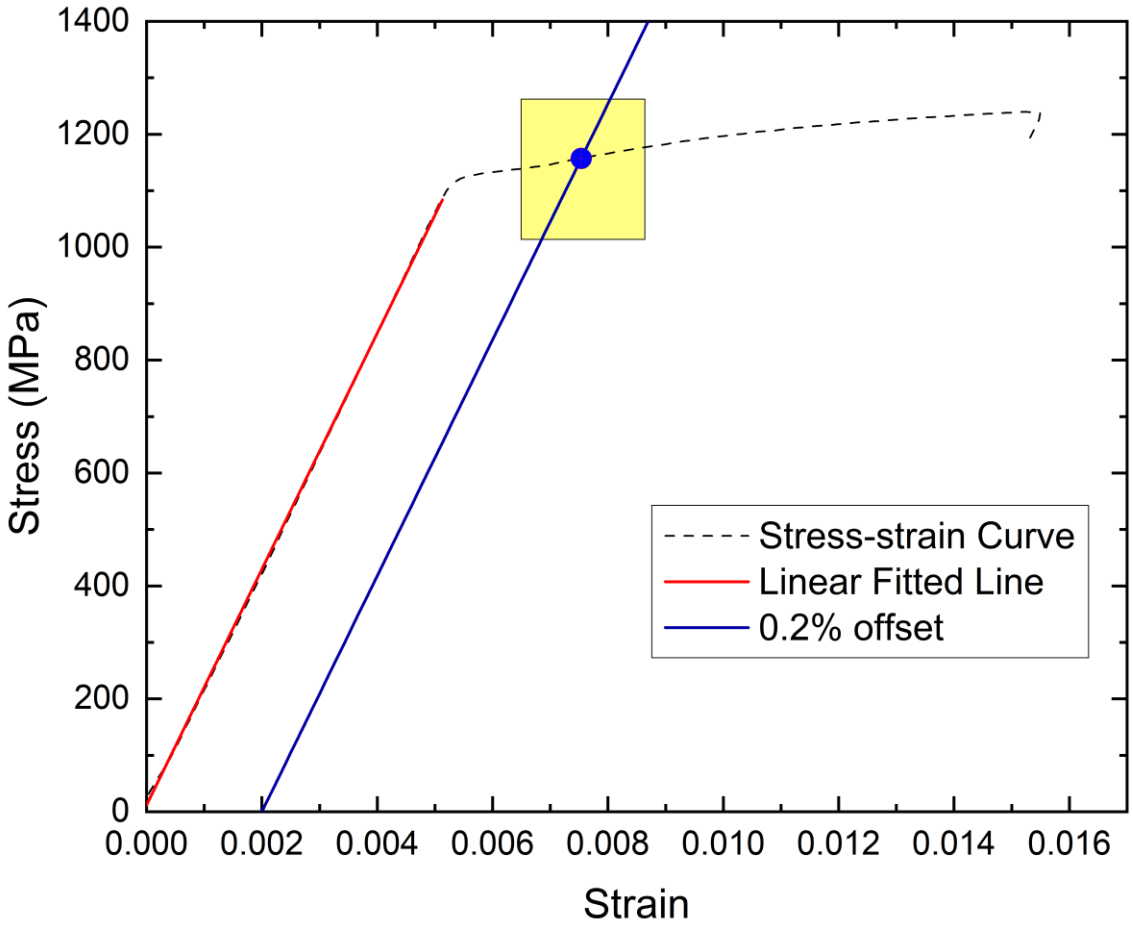

Figure 3-10: Yield point determination

Table 3-3: Yield strength values

Screw Configuration	Mean Yield Strength (MPa)	Coefficient of Variation (%)
ASSY 6-200	1186.5	1.5
ASSY 8-160	1192.7	1.3
ASSY 10-200	1277.0	1.4
ASSY 12-200	1203.0	1.3
VGS 9-360	1284.3	3.0
VGS 11-200	1335.4	2.5
VGS 13-200	1093.2	3.4
VGZ 5-160	1262.5	1.5
VGZ 11-250	1177.5	1.9

3.4.4 Ultimate Tensile Strength

The ultimate tensile strength was determined following ASTM E8/E8M (ASTM International, 2021). Table 3-4 summarizes the mean tensile strength and coefficient of variation for each tested screw. The self-tapping screws exhibited high tensile strength (>1100 MPa), with a small variability in the data.

Table 3-4: Tensile strength values

Screw Configuration	Mean Tensile Strength (MPa)	Coefficient of Variation (%)
ASSY 6-200	1302.4	2.5
ASSY 8-160	1296.8	1.4
ASSY 10-200	1369.6	1.2
ASSY 12-200	1290.3	2.1
VGS 9-360	1393.7	3.3
VGS 11-200	1469.4	3.7
VGS 13-200	1176.5	3.8
VGZ 5-160	1361.9	1.8
VGZ 11-250	1198.8	0.7

3.4.5 Strain at Ultimate Tensile Strength and Failure

Tables 3-5 and 3-6 show the mean strain at ultimate tensile strength and failure. It can be noticed that the coefficient of variation of the strain values is high compared to that of yield or ultimate strength values. In addition, test results show that the coefficient of variation of strain at failure is much higher than that of strain at ultimate tensile strength. The higher variability might be due to the failure region of the screw falling outside the bounds of the extensometer's gauge length. When failure occurs within the bounds of the extensometer's gauge length, the actual value of strain at failure is recorded. On the other hand, when the failure occurs outside the bounds of the gauge length, the recorded strain value is an under-estimate of the actual value. Since failure occurred outside the extensometer's gauge length for most tested screws, the measured strain at failure is smaller than the actual strain.

Table 3-5: Ultimate strain values

Screw Configuration	Mean Strain at Ultimate Tensile Strength (%)	Coefficient of Variation (%)
ASSY 6-200	2.72	22.7
ASSY 8-160	2.00	15.3
ASSY 10-200	1.58	4.3
ASSY 12-200	1.83	16.3
VGS 9-360	2.13	11.6
VGS 11-200	1.66	14.2
VGS 13-200	1.61	34.9
VGZ 5-160	1.99	3.5
VGZ 11-250	0.9	20.7

Table 3-6: Failure strain values

Screw Configuration	Mean Strain at Failure (%)	Coefficient of Variation (%)
ASSY 6-200	2.97	25.6
ASSY 8-160	2.73	64.7
ASSY 10-200	1.6	4.3
ASSY 12-200	2.08	27.7
VGS 9-360	2.4	17.6
VGS 11-200	1.68	14.3
VGS 13-200	1.71	34.6
VGZ 5-160	2.05	4.5
VGZ 11-250	1.14	41.9

Tables 3-5 and 3-6 show that the difference between the mean strain at ultimate tensile strength and mean strain at failure was minimal for all the screw configurations.

3.4.6 Necking

Most of the specimens failed without any significant necking, as shown in Figures 3-11 and 3-12. This can also be confirmed by the slight difference between the engineering and true stress-strain curves (Figure 3-8). Usually, necking causes a large discrepancy between the engineering and true

stress-strain curve before the failure point. Since the failure of the specimen occurred without necking, the failure mode was brittle. The failure modes for ASSY, VGS and VGZ screws were the same. Also, the screw failure region gradually moved closer to the head of the screw with the decrease of the screw diameter. This behaviour can be explained by the screw geometry, as the screw gradually tapers more sharply near the head of the screw for a screw with a larger outer diameter.

Figure 3-11: Failure in ASSY 6-200 (cylindrical head) screws

Figure 3-12: Failure in ASSY 8-160, ASSY 10-200, ASSY 12-200 (countersunk head) screws

3.5 Summary

The tensile properties of self-tapping screws of two different head types and from two manufacturers have been documented in this chapter. The screw properties are implemented in later chapters, and the properties can be helpful later in developing failure criteria and guidelines for preventing premature STS failure.

4 MASS TIMBER MOISTURE TRANSPORT PROPERTIES AND MODELLING

4.1 Introduction

Hygroscopic deformations from wetting and drying exert additional stress on the self-tapping screw in mass timber products. The internal moisture content distribution and its change with time should be known to predict the hygroscopic deformation along the length of the screw. Knowing the deformation can help to predict the stress distribution in the screw. The internal moisture content distribution can be modelled by an apt description of moisture transport (diffusion) through the wood. This chapter investigates the moisture diffusion process in glulam and cross-laminated timber (CLT). A numerical method to determine the moisture diffusion coefficient of the laminates of glulam and CLT has been presented. Then, the diffusion data is implemented in finite element analysis to numerically simulate the moisture content distribution inside these products.

The main objective of this chapter is to propose an efficient and convenient method to predict the internal moisture content distribution and moisture content change distribution of mass timber products. For this purpose, a test program with the following chronological steps was followed:

- Development of a computer program to numerically determine the effective diffusion coefficient
- Determination of the effective diffusion coefficient of the individual laminates of CLT and glulam from the moisture content readings during moisture adsorption (laminate phase)
- Measurement of moisture content of full-scale mass timber products at discrete locations (experimental multi-layer phase)
- Development of finite element models of the same products with the determined diffusion coefficients as input parameters and prediction of the moisture content distribution from finite element analysis (FEA) under appropriate boundary conditions (numerical multi-layer phase)
- Verification of the finite element model with the experimental multi-layer phase data
- Practical application of the finite element model

The test program in this chapter is comprised of the following phases:

- ❖ Laminate phase: In this phase of the test program, the moisture transport properties of the laminates of CLT and glulam during moisture adsorption are determined by experimental means
- ❖ Experimental multi-layer phase: The moisture content distribution of large-size CLT and glulam during moisture adsorption is experimentally investigated in this phase
- ❖ Numerical multi-layer phase: The moisture diffusion process of the same CLT and glulam specimens of the experimental multi-layer phase is numerically simulated in this phase and compared with the practical moisture content readings.

4.2 Finite-difference Formulation of Fick's Second Law

As discussed in chapter 2, Fick's second law adequately describes the moisture transport process in wood. A finite-difference formulation of Fick's second law using the forward finite-difference method can be implemented to solve for the effective diffusion coefficient from known moisture content values at discrete points of a specimen. This type of finite-difference formulation has been widely used in heat conduction problems (Chen et al., 1996). For the one-dimensional mass transport model using Fick's second law, symmetry conditions can be assumed across a specimen's thickness, length, and width. If moisture moves along any direction of the specimen with a dimension of $2a$, Fick's law can be written as:

Equation 4-1

$$\frac{\delta u}{\delta t} = \frac{\delta}{\delta x}\left(D\frac{\delta u}{\delta x}\right);\ 0 < x < a, t > 0$$

Here, the origin of the coordinate system is at the outer surface of the specimen ($x = 0$), a represents half of the specimen dimension along which moisture transport takes place. It is necessary to form a discretized finite-difference grid for the finite-difference approximation. The space domain is discretized with a width of Δx into a specified number of sub-intervals. In contrast, the time domain is discretized with a width of Δt, an open boundary, and an unspecified final value. The value of moisture content at the grid points (x_j, t_i) are assumed to be known. The notation represents the moisture content and diffusion coefficient at a grid point u_j^i and D_j^i. The superscript i represents the time domain ($i = 0,1,2 \ldots \ldots \ldots$), and the subscript j represents the space domain ($j = 0,1,2 \ldots \ldots \ldots n$). The basic building block of the finite-difference formulation is based on the stencil shown in Figure 4-1. Figure 4-1 shows that six grid points form one unit of the finite-

difference grid. This type of formulation may be categorized as a propagation formulation. Once the space domain's initial boundary conditions are defined, the time domain can propagate from the initial state.

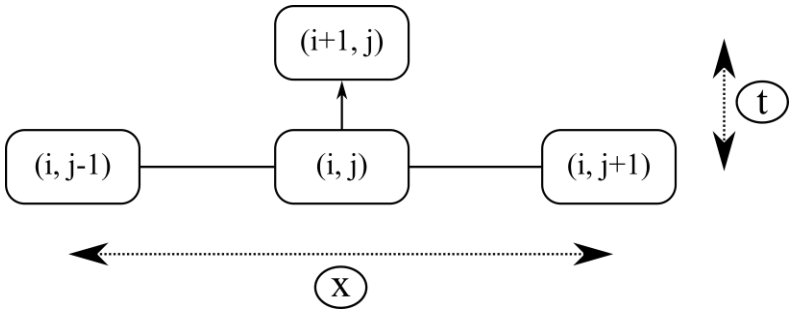

Figure 4-1: Finite-difference formulation stencil

The finite-difference approximation of Fick's law for a specimen is given by Liu et al. (Liu et al., 2001) as the following linear equations.

At the surface grid point ($j = 0, x = 0$) :

Equation 4-2

$$\frac{(\Delta x)^2}{\Delta t}\left(u_0^{i+1} - u_0^i\right) = D_0^i\left(u_2^i - 3u_1^i + 2u_0^i\right) + D_1^i\left(u_1^i - u_0^i\right)$$

At any internal grid point in the specimen ($0 < j < n, 0 < x < a$):

Equation 4-3

$$\frac{4(\Delta x)^2}{\Delta t}\left(u_j^{i+1} - u_j^i\right) = D_{j-1}^i\left(u_{j-1}^i - u_{j+1}^i\right) + 4D_j^i\left(u_{j+1}^i - 2u_j^i + u_{j-1}^i\right) + D_{j+1}^i\left(u_{j+1}^i - u_{j-1}^i\right)$$

At the centre of the specimen ($j = n, x = a$):

Equation 4-4

$$\frac{(\Delta x)^2}{\Delta t}\left(u_n^{i+1} - u_n^i\right) = 2D_n^i\left(u_{n-1}^i - u_n^i\right)$$

If the moisture content values at the grid points are known, this set of equations can be solved to get the value of the diffusion coefficient, D_j^i at each grid point. In equations 4-2, 4-3 and 4-4, at each time step, since D_j^i only appears in the initial ith time point, it can be represented by the subscript D_j alone.

4.3 Computer Software Implementation and Diffusion Coefficient Determination

The moisture content at discrete locations along the path of moisture transport was recorded for individual laminates of CLT and glulam. From the moisture content readings at the discrete locations, a continuous moisture content distribution along half of the width of the samples was modelled using the piecewise cubic Hermite interpolating polynomial in MATLAB (*MATLAB*, 2021) software. This interpolating polynomial was chosen for its computational efficiency and to avoid unnecessary oscillation of the recorded data. For the finite-difference formulation, the laminates were discretized in the space domain, as shown in Figure 4-2, and the width of the sub-intervals, Δx was set to 0.5 mm. From the stencil of Figure 4-1, it can be observed that a pair of time points form the basis of the finite-difference formulation. As the moisture content variation with time was slow, large time sub-intervals were used to measure moisture contents. The width of the time domain of the finite-difference formulation, Δt was varied for each pair of time points (each time step) and was set as the difference between the ith value of time point and $(i + 1)$th value of time point.

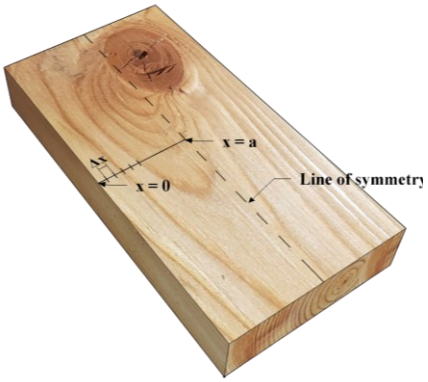

Figure 4-2: The finite-difference grid of the space domain of a laminate

Three arrays were defined to solve the linear set of equations 4-2, 4-3 and 4-4: A is a banded matrix, D is a column vector of the unknown diffusion coefficients, and B is another column vector.

Equation 4-5

$$A = \begin{bmatrix} a_{1,1} & a_{1,2} & 0 & 0 & 0 & 0 & 0 \\ a_{2,1} & a_{2,2} & a_{2,3} & 0 & 0 & 0 & 0 \\ 0 & . & . & . & 0 & 0 & 0 \\ 0 & 0 & . & . & . & 0 & 0 \\ 0 & 0 & 0 & . & . & . & 0 \\ 0 & 0 & 0 & 0 & a_{n-1,n-2} & a_{n-1,n-1} & a_{n-1,n} \\ 0 & 0 & 0 & 0 & 0 & 0 & a_{n,n} \end{bmatrix};$$

Equation 4-6

$$d = \begin{bmatrix} D_1 \\ D_2 \\ \vdots \\ D_n \end{bmatrix} \text{ and } b = \begin{bmatrix} b_1 \\ b_2 \\ \vdots \\ b_n \end{bmatrix}$$

The elements of the arrays A and b are defined as:

Equation 4-7

$$b_1 = K\left(u_0^{i+1} - u_0^i\right);$$

Equation 4-8

$$b_n = K\left(u_n^{i+1} - u_n^i\right);$$

Equation 4-9

$$b_m = 4K\left(u_{m-1}^{i+1} - u_{m-1}^i\right) \text{ for } 1 < m < n;$$

Equation 4-10

$$a_{1,1} = \left(u_2^i - 3u_1^i + 2u_0^i\right);$$

Equation 4-11

$$a_{1,2} = \left(u_1^i - u_0^i\right);$$

Equation 4-12

$$\left.\begin{aligned} a_{m,m-1} &= \left(u_{m-2}^i - u_m^i\right) \\ a_{m,m} &= 4\left(u_m^i - 2u_{m-1}^i + u_{m-2}^i\right) \\ a_{m,m+1} &= \left(u_m^i - u_{m-2}^i\right) \end{aligned}\right\} \text{ for } 1 < m < n;$$

Equation 4-13

$$a_{n,n} = 2\left(u_{n-1}^{i} - u_{n}^{i}\right)$$

Where u_j^i notation is defined in section 4.2 and $K = \frac{(\Delta x)^2}{\Delta t}$. The arrays A, d and b are related as:

Equation 4-14

$$Ad = b$$

Equation 4-14 can be easily solved in MATLAB (*MATLAB*, 2021) software for the unknown diffusion coefficient values. A program was developed in MATLAB software to model the continuous moisture content distribution and solve equation 4-14 for the diffusion coefficient values. Copies of the software can be obtained from the author.

4.4 Determination of the Effective Diffusion Coefficient of the Individual Laminates of CLT and Glulam (Laminate Phase)

Glulam made from Douglas Fir-Larch of stress grade 16c-E and Spruce-pine-fir (SPF) CLT of stress grade V2 were used in the test program. Glulam of two different sizes from the same manufacturer and CLT made from 2×4 laminates (CLT type A) and 2×6 laminates (CLT type B) from two different manufacturers were investigated. The two sizes of glulam and the two types of CLT used are shown in Figure 4-3. Individual laminates whose width direction aligned approximately with either the radial or tangential direction of the wood were cut out from the different layers of CLT and glulam (Figure 4-4). The dimensions of the individual laminates were recorded.

According to the technical specifications of the manufacturers of the CLT, the longitudinal (major) and the transverse (minor) layers of CLT were made from lumber of different grades and different sources. Thus, the laminates of the longitudinal and transverse layers might have different moisture transport properties, which were determined separately. Both sizes of glulam used in the test program were of the same grade and came from the same manufacturer. Furthermore, all the glulam used were of compression grade, and for compression grade glulam, laminates of all layers usually come from the same source and have similar properties. Thus, all the layers of both sizes of glulam were considered to have the same moisture transport properties. The properties of the laminates of the larger glulam (Figure 4-3 bottom right) were assumed to represent all the layers

of both glulam sizes. The number of specimens investigated for each laminate type of CLT and glulam is mentioned in Table 4-1.

This chapter proposes an efficient method to determine and model the moisture transport process in CLT and glulam as a preliminary investigation. The goal of this chapter is not to build a database of the diffusion coefficient values. Also, considering the significant time and effort required for instrumentation and monitoring of moisture content readings, a small sample size of two was employed (Table 4-1).

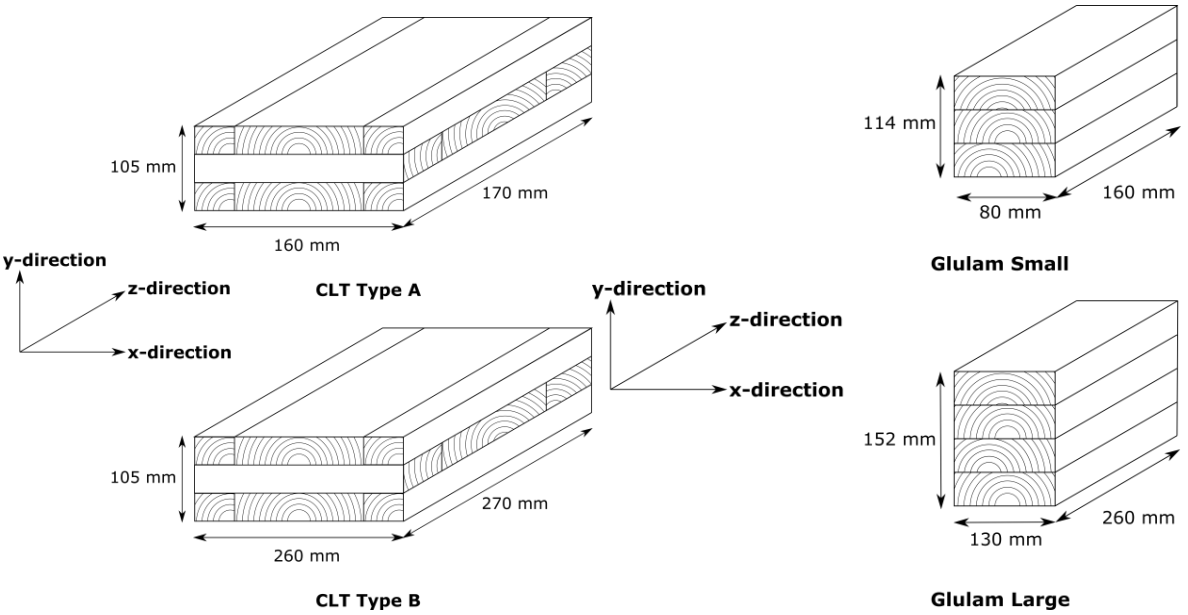

Figure 4-3: CLT and glulam products used in the test program

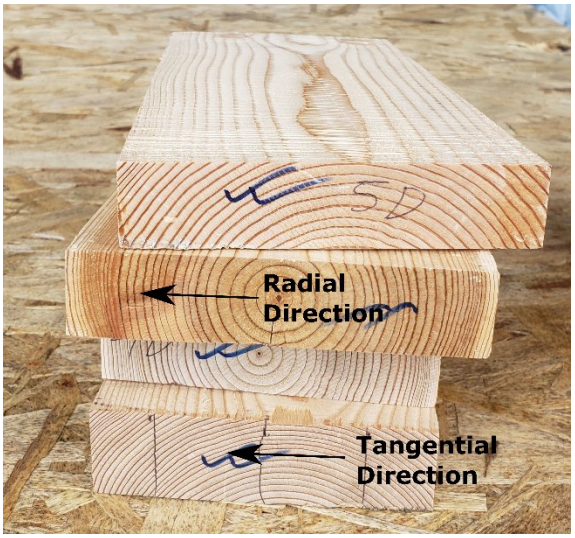

Figure 4-4: End grain of the laminates

Table 4-1: Number of specimens used in the laminate phase

Type of wood product	Layer type	Number of specimens
CLT Type A (2x4)	Longitudinal	2
	Transverse	2
CLT Type B (2x6)	Longitudinal	2
	Transverse	2
Glulam Small and Large	Same laminates for all layers	2

The laminates were coated with epoxy paint on four sides so that moisture could travel only along the width of the laminates (Figure 4-5). Thus, moisture diffusion was limited to the laminates' radial or tangential direction. Since the diffusion coefficient in only the transverse direction of wood is essential (Ross & USDA Forest Service., 2010), the diffusion coefficient values of the laminates along the radial and tangential directions were determined.

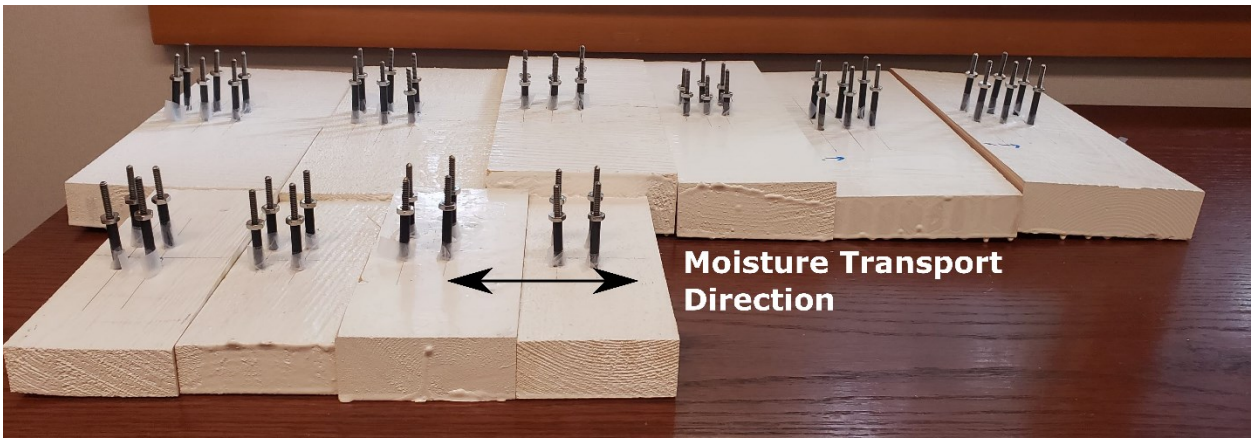

Figure 4-5: Moisture transport direction through the laminates

Insulated moisture pins were installed inside the laminates with the tip of the pins near the mid-height. Each pair of moisture pins measured the moisture content at each discrete location by connecting them to a resistance-based moisture meter. The accuracy of the moisture pins was ± 2% of the actual moisture content of the wood. Moisture pin-pairs were installed at discrete locations along the width of the laminates (Figure 4-6). Symmetry conditions were assumed across the width of the laminates, and moisture content readings in only one-half of the laminate width were recorded. The laminates were initially relatively dry (7-9% EMC) and placed in a

conditioning chamber with 89-92% RH and 20º C temperature (20-22% EMC). The initial moisture content at the discrete locations and the outer side surface was recorded. Then, continuous readings of the laminates during moisture adsorption in the conditioning chamber were taken for 1002.5 hours.

Figure 4-6: Moisture pin-pairs installed at discrete locations of epoxy-coated glulam sample

4.5 Measurement of Moisture Content of Full-scale CLT and Glulam (Experimental Multi-layer Phase)

The manufacturer provided 130x260 mm glulam (Glulam Large in Figure 4-3) had four layers, and 260x270 mm CLT (CLT Type B in Figure 4-3) was three-layered. A twelve-layered glulam and CLT sample was prepared to investigate the moisture transport in glulam and CLT members of large depths, as employed in structural members. For preparing the twelve-layered glulam and CLT, multiple glulam and CLTs were joined by gluing on the broad face (Figure 4-7). A single-component polyurethane glue with a glue spread rate of 160 g/m^2 was applied to the samples, and they were then pressed in a compression testing machine with a pressure of 110 psi for 2 hours. Insulated moisture pins were installed inside the glulam and CLT with the tip of the pins near the mid-width (along x-direction in Figure 4-7). Each moisture pin pair was installed at predetermined locations (Figure 4-8). The location coordinates of the pins along the z and y-direction were recorded. The samples were initially dry (7-9% EMC) and were put in a conditioning chamber with 89-92% RH and 20º C temperature (20-22% EMC). The initial moisture content at the discrete

locations and the top surface was recorded. Then, moisture content readings during moisture adsorption in the conditioning chamber were taken at 168, 336, 504, 671 and 837 hours from the start of the conditioning process for glulam. For CLT, the readings were taken at 167, 333, 693 and 816 hours from the beginning of the conditioning process.

The side faces of the top half on the z-plane and end-grains of the x-plane of CLT were sealed with moisture repellant tapes. On the other hand, the top half end-grains of the z-plane of glulam were sealed to prevent moisture transportation along the longitudinal direction (Figure 4-8). This sealing pattern was adopted to verify the experimental results with a 2D finite element model, as described in section 4.6.

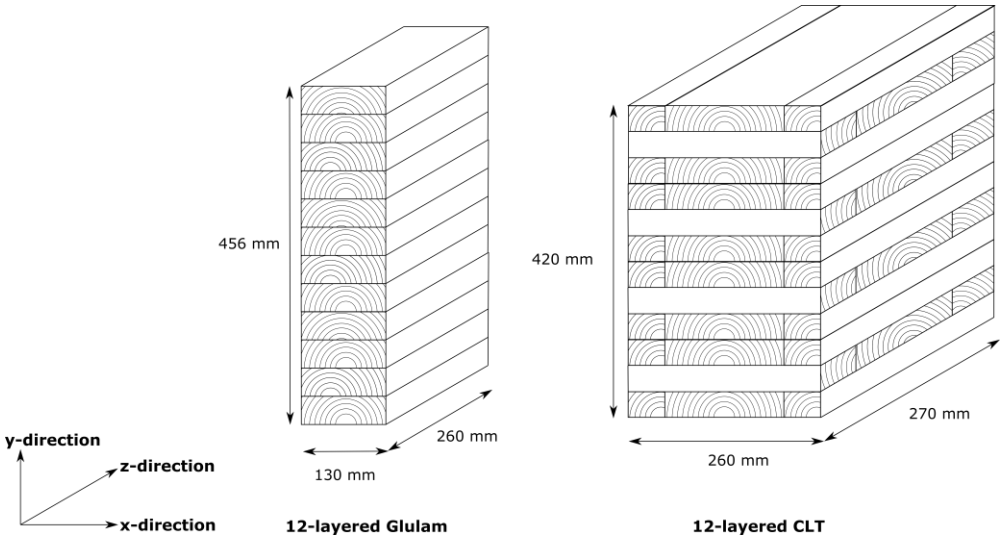

Figure 4-7: CLT and glulam samples for the experimental multi-layer phase

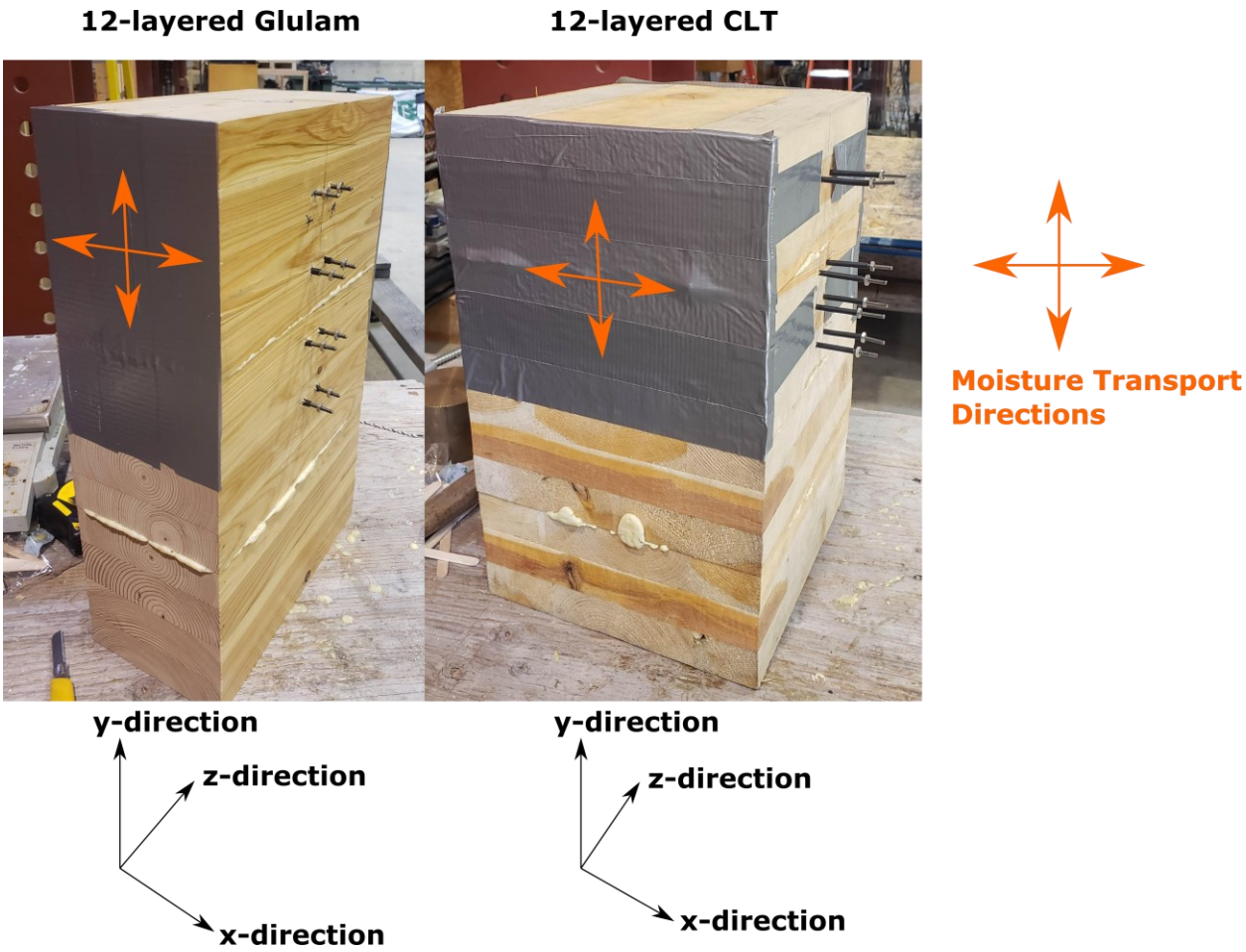

Figure 4-8: Large-scale Glulam (left) and CLT (right) samples with sealing

4.6 Finite Element Modelling of Full-scale CLT and Glulam (Numerical Multi-layer Phase)

The top half of the whole vertical cross-section of glulam and CLT was modelled using finite element analysis (FEA) software ABAQUS (Simulia, 2020). The purpose of the finite element model was to establish a numerical method to predict the moisture content distribution of glulam and CLT. The finite element model was verified with the moisture content readings from the experimental multi-layer phase. The sealing pattern of the samples of the experimental multi-layer phase (Figure 4-8) was adopted to carry out a 2D FEA in ABAQUS/CAE (Simulia, 2020) for its fast simulation time.

As seen in Figure 4-8, the end grains of the lower half of the samples were not sealed. The moisture transport in the longitudinal direction took place through the end-grain of laminates. It was assumed that the broad bottom face of the top half's lowermost layer instantaneously achieved the

wood's EMC in the conditioning chamber. This assumption is justified because moisture transport in the longitudinal direction for the non-end grain sealed layers is 10-15 times faster than that in the transverse direction (Avramidis & Siau, 1987). It was possible to model only the top half of the samples with this assumption.

2D finite element models of the top half of the samples were created in ABAQUS/CAE (Simulia, 2020), as shown in Figure 4-9. The CLT sample was modelled as a single part with a partitioned face, and the CLT part was partitioned into different layers to assign layer-specific material properties. On the other hand, the glulam was modelled as a single part without partitioning, and the same material properties were assigned to the whole glulam. Each layer of CLT and the glulam was modelled as a continuous homogeneous layer.

The three orthotropic grain directions of wood were assigned using local material orientations in ABAQUS/CAE. The longitudinal grain direction was assumed to be in the direction perpendicular to the plane of the 2D model, and the moisture transport properties in that direction were set as zero. Thus, the moisture content boundary conditions were assigned to the edges of the models through which moisture entered the samples, as shown in Figure 4-9. These edges were not sealed, as seen in Figure 4-8. The initial boundary condition in ABAQUS/CAE was set as the initial EMC of the samples, and the final boundary condition was set as the final EMC of the conditioning chamber. With the boundary conditions defined, the simulation was conducted over 837 hours for glulam and 816 hours for CLT, with a time increment of 1 hour at each time step.

The ABAQUS model was analyzed with transient mass diffusion analysis, with the appropriate diffusion coefficient values as the input material property of each layer (Figure 4-10). These values are found from the laminate phase and are discussed in section 4.7.1. In ABAQUS, heat transfer elements are used for heat transfer and mass diffusion analysis. Quadratic heat transfer (DC2D8) elements with an approximate mesh size of 4 mm for glulam and 1.5 mm for CLT were used. The moisture content distribution along the height of the samples (y-direction in Figure 4-7) was determined at the time intervals in which the moisture content readings of the experimental multi-layer phase were taken. Then, the finite element analysis results were compared with the actual moisture content readings of the samples to validate the diffusion coefficient determination method and to check the accuracy of the finite element model.

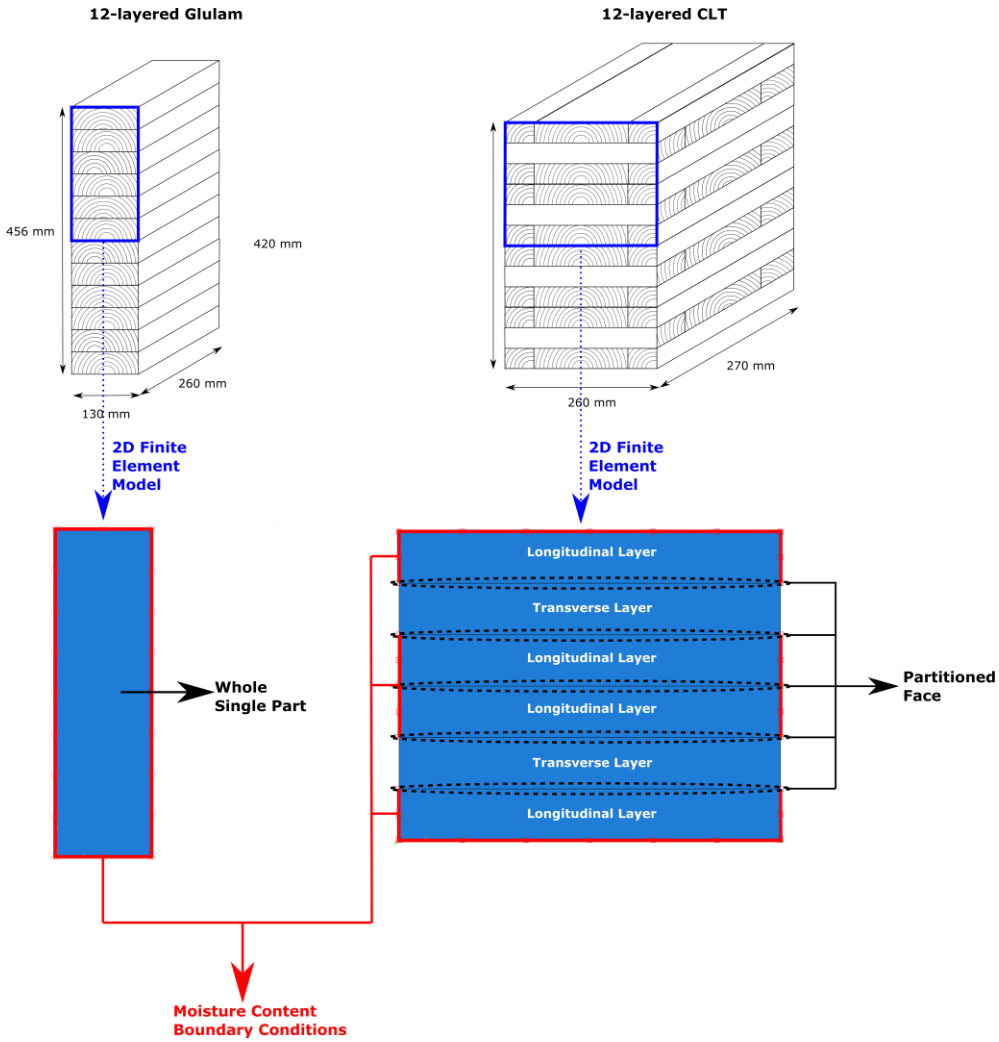

Figure 4-9:Finite element model geometry and boundary conditions in ABAQUS/CAE

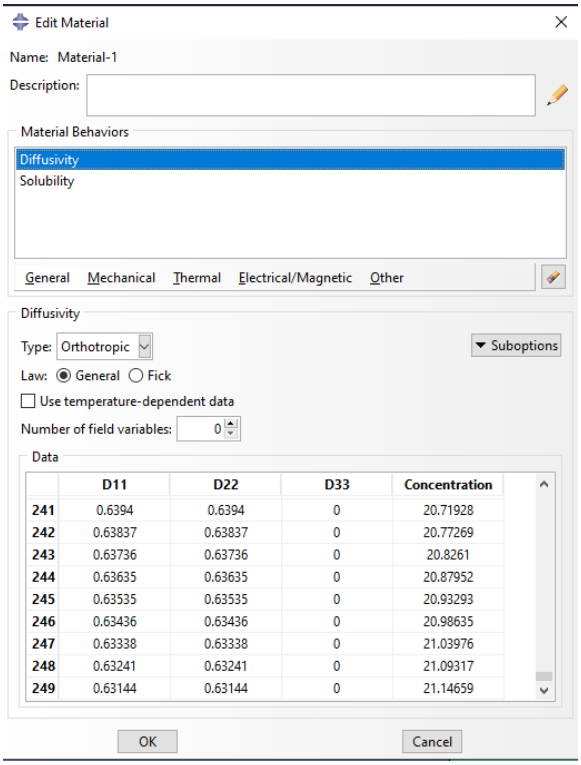

Figure 4-10: Diffusion coefficient values input in ABAQUS/CAE

4.7 Results and Discussion

4.7.1 Diffusion through Laminates

The moisture content of the laminate was modelled as a continuous function from the moisture content readings of the laminates mentioned in Table 4-1 (Figure 4-11). Figure 4-11 shows the moisture content variation along the width of a glulam laminate for t = 330.5 h (i-th time point) and 354.5 h (i+1-th time point). The piecewise cubic Hermite interpolating polynomial does not create any unwanted oscillation of the interpolated curve between the data points, as shown in Figure 4-11. Similar to Figure 4-11, all the laminates' moisture content distribution for every time step was modelled. Then, the diffusion coefficients along the radial and tangential (transverse) directions were determined for each time step using the program developed in MATLAB (*MATLAB*, 2021) software. The diffusion coefficient along the radial and tangential directions were approximately equal, and identical properties in radial and tangential directions were assumed. The diffusion coefficient values of CLT Type A and Type B were very similar. Therefore, the same diffusion coefficient values were used for the CLTs. However, the

longitudinal and transverse layers of CLT were found to have dissimilar diffusion coefficient values.

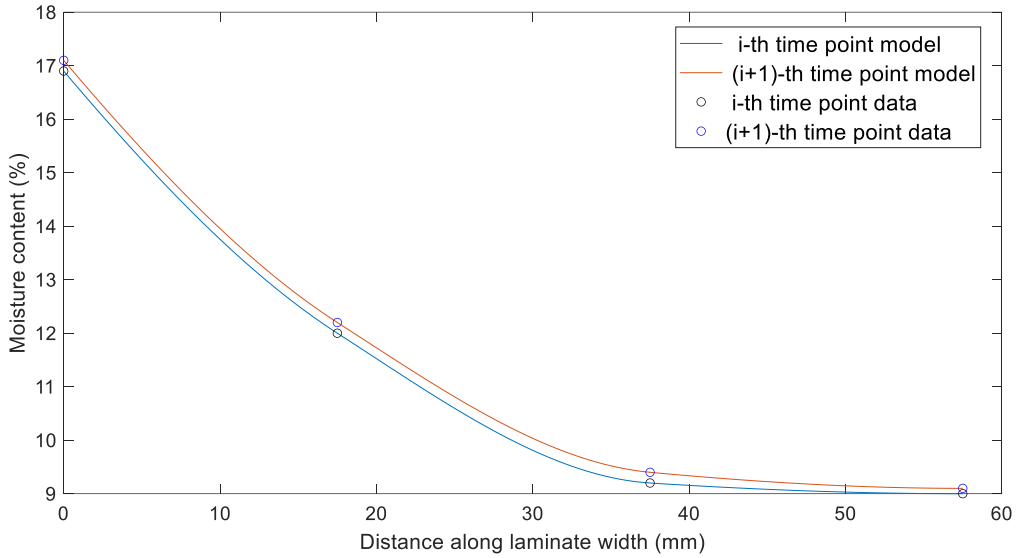

Figure 4-11: Moisture content variation along the width of a laminate

The variation of the transverse diffusion coefficient with the moisture content is shown in Figure 4-12. Non-linear curve fitting was used to express the diffusion coefficient as a function of the moisture content. Several studies have used exponential functions to describe the relationship between the effective diffusion coefficient and the moisture content (Hukka, 1999) (Avramidis et al., 1994). The non-linear curve fitting was conducted in OriginPro (OriginLab Corporation, 2016) software. Among the different exponential curve-fitting functions available in the software, the functions with the highest value of R-squared (coefficient of determination) was chosen. In Figure 4-12, it can be noted that only data at a few time steps are plotted. The data at these specific time sub-intervals were chosen since the data cover the typical range of moisture content in wood products, and these time steps yielded stable results.

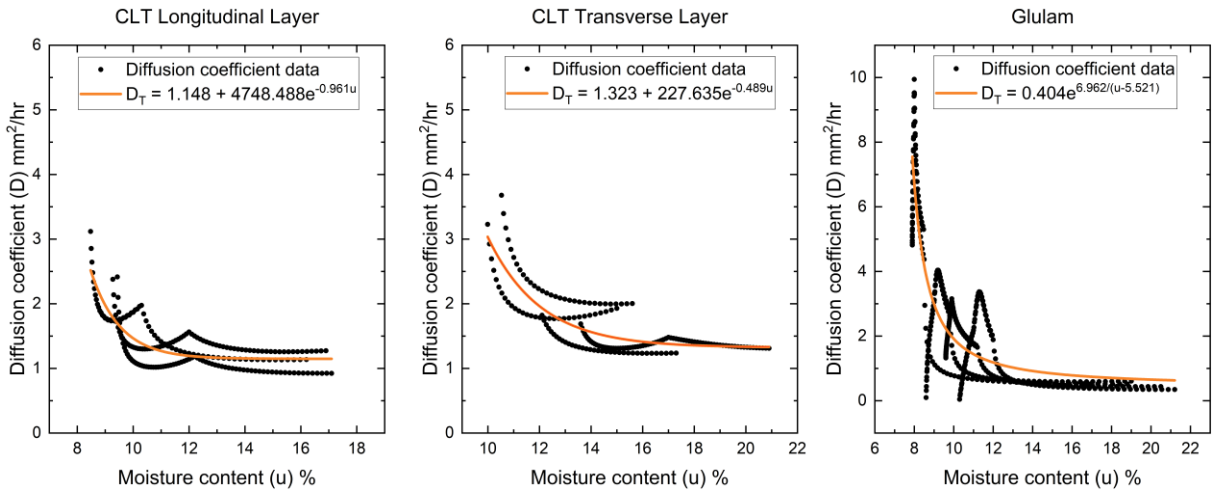

Figure 4-12: Variation of the diffusion coefficient with the moisture content, subscript T refers to diffusion in the transverse direction

The diffusion coefficient was found to decrease with the increase of moisture content during moisture adsorption, which agrees with Wu and Suchsland (Wu & Suchsland, 1996). This phenomenon occurs due to two reasons. As the moisture content inside wood gradually increases, moisture can only be transported as water vapour through the cell lumen space of wood. This reduces the moisture diffusion speed inside the wood; thereby, the diffusion coefficient decreases with increasing moisture content. Besides, the difference in partial vapour pressure of wood and the surrounding environment is a driving force for the moisture movement inside the wood. When the moisture content inside wood increases, the difference in partial vapour pressures decreases and the moisture movement becomes slower, decreasing the diffusion coefficient value.

If matrix A in section 4.3 is ill-conditioned, a slight change in the B vector can significantly change the value of the determined diffusion coefficients. To this end, the importance of accurate moisture content measurement cannot be overemphasized. A small amount of reliable data collected over a few time steps is more important than having a large amount of unreliable data covering a lot of time steps. Finally, although temperature affects the value of the diffusion coefficient (Avramidis & Siau, 1987), the effects of temperature were not investigated in this research. This is an aspect that can be explored in future research.

4.7.2 Modelling of Large-scale Samples and Verification with Experimental Measurements

The diffusion coefficient and moisture content relationship shown in Figure 4-12 was used to specify the diffusion material property in ABAQUS/CAE. The local 1 and 2 directions in

ABAQUS/CAE were used to represent the radial and tangential directions of the wood, respectively. Since the diffusion coefficients in the radial and tangential directions are approximately equal, the same value was used for both directions. The diffusion coefficient along the local 3 direction (wood longitudinal direction) was considered zero since moisture transport in the longitudinal direction was not considered in the 2D model. Further, the 2D model, without considering the longitudinal direction moisture transport property, was representative of the conditions of the experimental multi-layer phase samples (with the special sealing pattern). The moisture content was specified as concentration values in ABAQUS/CAE. The diffusivity of the adhesive between adjacent layers of the glulam and CLT was considered to be the same as that of wood, according to Srpčič et al. (Srpčič et al., 2009). In real-life scenarios, the diffusivity of the particular adhesive used in a timber product might not be known. Moreover, due to the project's limited time frame, the adhesive's diffusivity could not be investigated. Nevertheless, considering the diffusivity of the adhesive to be the same as that of the wood led to reasonably accurate predictions of moisture content distribution, as discussed in the following paragraphs.

A generalized version of Fick's law was used to describe the moisture transport process in ABAQUS/CAE. In the generalized version of Fick's law, the solubility of the base material (wood) was taken as 1 since a value of solubility other than 1 is usually observed in the diffusion of gas through metals. Temperature and pressure effects on moisture diffusion were ignored. The contour plots of the moisture content distribution from the finite element analysis at time t = 504 h for glulam and at t = 816 h for CLT are shown in Figure 4-13.

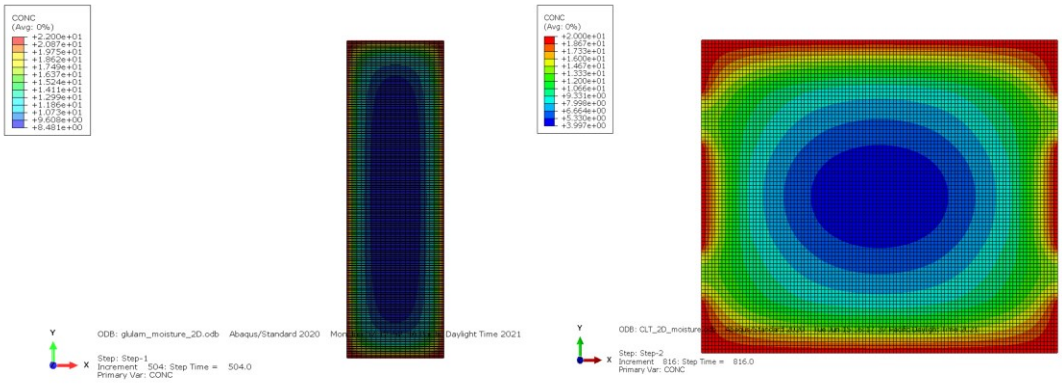

Glulam Moisture Contour Plot CLT Moisture Contour Plot

Figure 4-13: Moisture content contour plot from ABAQUS analysis, glulam (left) at t = 504 h and CLT (right) at t = 816 h

The 2D mass diffusion analysis is very quick as it requires minimum computational resources, and convergence issues usually do not arise. In practical engineering settings, 3D mass diffusion analysis might be necessary for complex structural members, which requires higher resources and computation time. The ABAQUS solver uses the backward Euler method, which is slightly different from the forward finite difference method used to derive the moisture diffusion coefficients. The backward Euler method is more accurate than the forward finite difference method.

As mentioned in section 4.5, the location coordinates of the moisture pins along the z and y-direction were recorded (Figure 4-8). The moisture content predictions at the location of the mid-point between the moisture pin pairs were found from the finite element analysis. Then, the experimental moisture content measurements on the sample at the location of the moisture pin pairs were compared with the finite element predictions. For the comparison, the locations of the moisture pin pairs were identified with the nomenclature shown in Figures 4-14 and 4-15. A comparison between the moisture content predictions from finite element analysis (FEA) and experimental measurement at different times and locations are given in Tables 4-2 and 4-3. In the tables, time recording was initiated when the sample was put inside the conditioning chamber. The percentage deviation between the predicted moisture content from FEA and the actual moisture content is given in the last four columns of the tables.

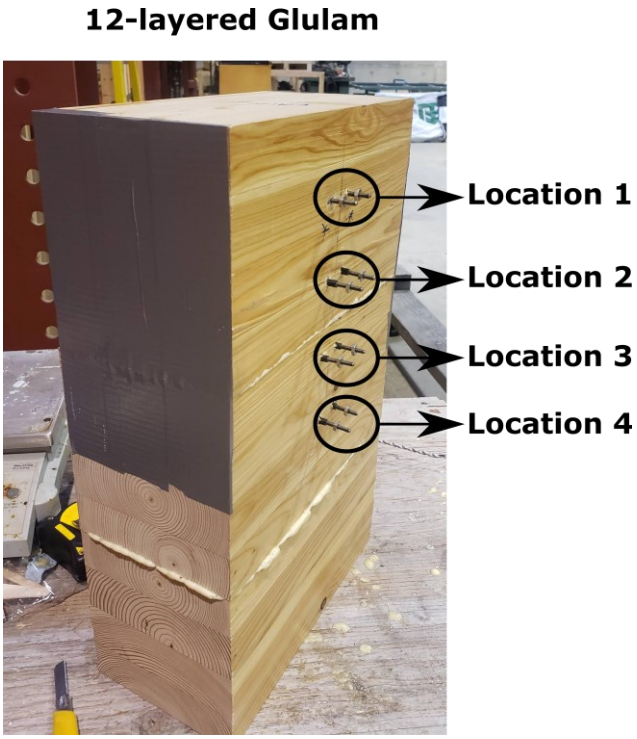

Figure 4-14: Location for moisture content probing of glulam

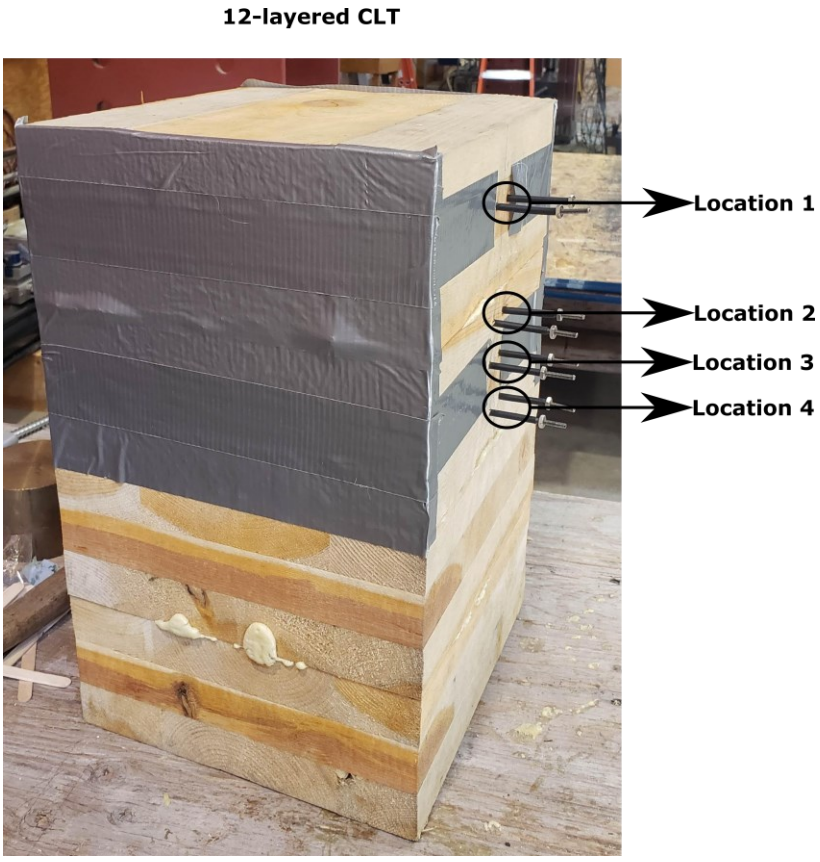

Figure 4-15: Location for moisture content probing of CLT

Table 4-2: Comparison of moisture contents for glulam

	Predicted Moisture content from FEA (%)				Experimental moisture content (%)				Percentage deviation			
	Location				**Location**				**Location**			
Time (hr)	**1**	**2**	**3**	**4**	**1**	**2**	**3**	**4**	**1**	**2**	**3**	**4**
168	15.79	13.77	13.39	13.18	16.8	13.8	13.9	13.1	6.0	0.2	3.7	0.6
336	18.35	17.06	16.61	16.38	18.5	16.6	16.8	16.2	0.8	2.8	1.1	1.1
504	19.56	18.26	17.91	17.68	19.5	18	17.9	17.7	0.3	1.5	0.1	0.1
671	20.63	19.13	18.76	18.53	19.8	18.5	18.7	18.5	4.2	3.4	0.3	0.2
837	21.61	19.92	19.53	19.30	20.5	19.2	19.4	18.9	5.4	7.7	0.7	2.1

Table 4-3: Comparison of moisture contents for CLT

	Predicted Moisture content from FEA (%)				Experimental moisture content (%)				Percentage deviation			
	Location				**Locaion**				**Location**			
Time (hr)	**1**	**2**	**3**	**4**	**1**	**2**	**3**	**4**	**1**	**2**	**3**	**4**
167	8.85	7.46	7.28	11.44	10	9	9.1	10.9	11.5	17.1	20.0	5.0
333	10.79	8.08	8.96	13.52	10.4	9.7	9.9	11.4	3.8	16.7	9.5	18.6
693	13.75	10.80	11.97	15.85	12.4	10.7	11.1	13.1	10.9	0.9	7.8	21.0
816	14.55	11.80	12.83	16.66	13	11.4	11.9	13.8	11.9	3.5	7.8	20.7

The maximum difference in the predicted and the actual (experimental) moisture content of glulam is only 6%. On the other hand, the maximum discrepancy in the predicted and the actual moisture content of CLT is 21%. The higher discrepancies between the predicted and the actual moisture content in CLT might be attributed to the presence of gaps and the difference in properties between adjacent laminates of the same layer of CLT due to the natural in-grade variation of lumber. It is to be noted that the CLT investigated in this study did not have any edge-gluing applied between adjacent laminates of the same layer. Nevertheless, the high difference in the predicted and the actual moisture content occurred only at a few time points. Thus, from the comparisons, it might be conjectured that the method of predicting moisture content distribution in CLT and glulam,

using finite element analysis, and considering the adhesives having the same diffusivity as the wood is reasonably accurate. Tables 4-2 and 4-3 are graphically depicted in Figures 4-16 and 4-17, respectively.

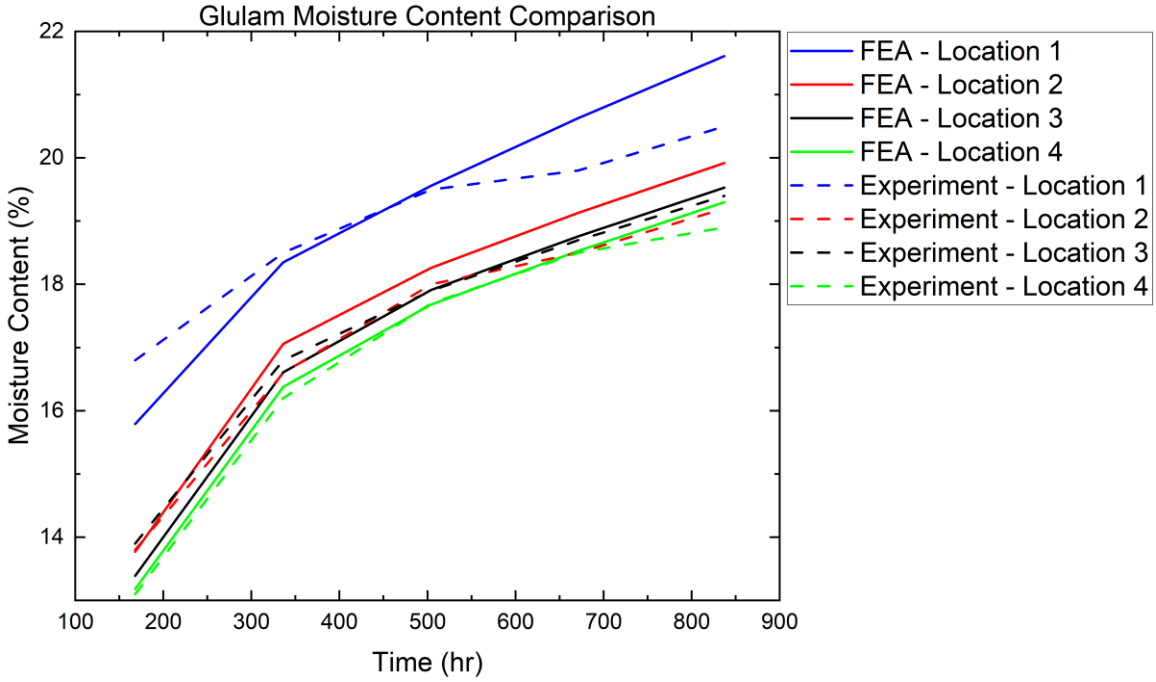

Figure 4-16: Comparison of moisture contents for glulam

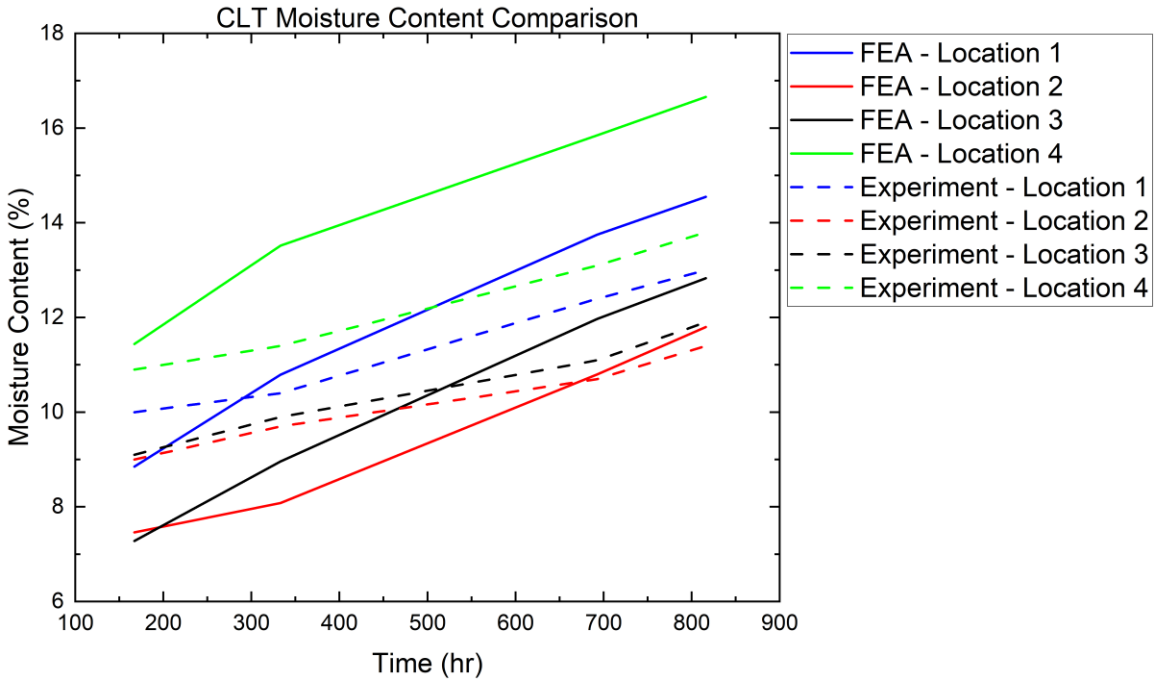

Figure 4-17: Comparison of moisture contents for CLT

The natural in-grade variation of lumber impacts the moisture content prediction of CLT, which might be overcome by statistically analyzing a large dataset of the diffusion coefficient of different lumber grades over a moisture content range. The presence of gaps between adjacent laminates of the same layer of CLT is also suspected to influence the moisture diffusion process significantly. This research aimed to develop and advocate a reliable method for moisture content prediction in CLT and glulam. The effects of in-grade variation of lumber grades and gaps between laminates of CLT were not investigated here.

4.7.3 Practical Application Example

In this section, a simple application of the diffusion coefficients determined for glulam and the modelling procedure described will be exhibited with the help of an example. A 4-layer glulam beam cross-section with 130 mm width and 152 mm height is considered (Figure 4-18). The glulam material's transverse (radial and tangential) direction is contained in the cross-section plane. In contrast, the longitudinal (grain) direction aligns with the beam's length direction perpendicular to the paper's plane. A self-tapping screw with a diameter of 8 mm is installed in the middle of the cross-section. The screw is installed perpendicular to the wood grain direction and penetrates 88 mm into the glulam. At the time of the installation of the screw, the EMC of the glulam is 10%. Due to variation in the surrounding relative humidity and temperature, the EMC of the glulam changes to 20%, which will trigger moisture adsorption in the glulam. The glulam will expand (swell) due to moisture adsorption. The swelling of wood in the longitudinal direction is very small compared to the swelling in the transverse direction (Angst & Malo, 2012a). The swelling of the glulam in the transverse direction will exert additional stress on the self-tapping screw. This stress might be critical to the performance of the screw. Now, the interior of the glulam will have a moisture gradient until the moisture content at every point inside the glulam becomes uniform. In the vicinity of the screw, the wood will have a moisture gradient in a direction parallel to the screw length, creating additional differential stress along the length of the screw. The stress distribution in the screw arising from the differential stress will depend on the moisture gradient in the glulam.

Suppose the initial EMC of 10% is considered to be uniform inside the glulam. In that case, the change in moisture content of the glulam along the length of the screw can be predicted from the finite element modelling method described in section 4.6. For this purpose, the whole glulam was modelled as a continuous section, and the part of the glulam where the screw was installed was

considered an empty hole (Figure 4-18). Since the final EMC of the glulam is 20%, the boundary condition was specified as the difference in the initial and final EMC, i.e., (20-10) = 10%.

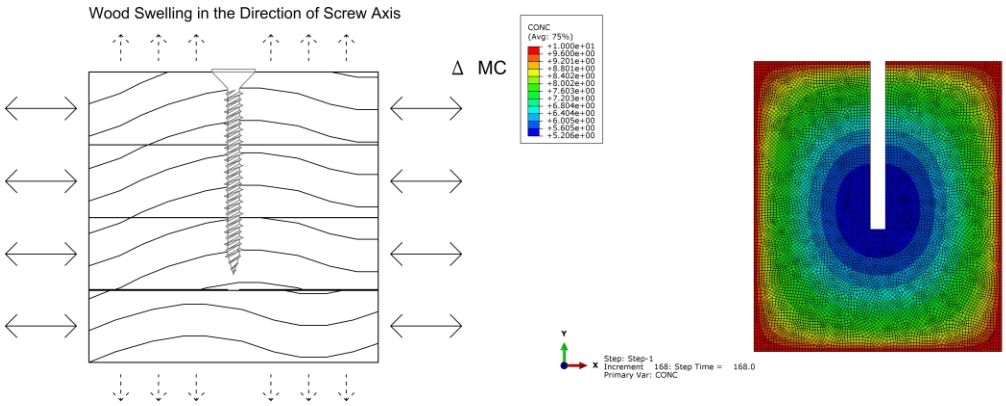

Figure 4-18: Glulam beam with self-tapping screw: schematic diagram (left), moisture content contour plot from ABAQUS analysis of the glulam (right)

The boundary condition was applied on the outer edges of the glulam as a mass concentration value. The contour plot from finite element analysis results is shown in Figure 4-18 after 7 days (168 hours) from the start of the moisture diffusion process. The edge of the hole represents the part of the glulam in the vicinity of the screw. The distribution of the moisture content change along the edge is shown in Figure 4-19. From this distribution, information on the additional differential stress exerted on the screw during moisture adsorption can be determined by an analytical treatment of wood and screw interaction. This example presents the issue recently reported by some mass timber practitioners in North America.

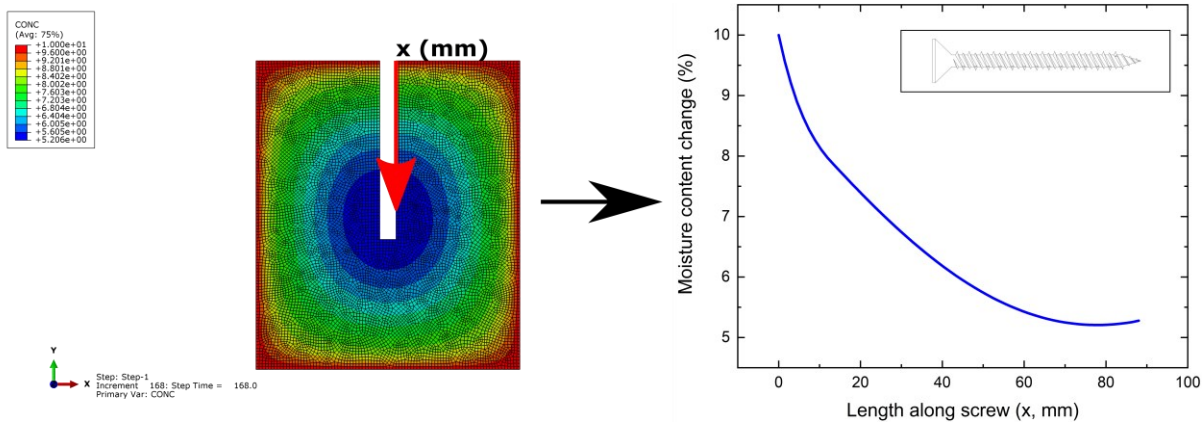

Figure 4-19: Moisture content change (Δu) of glulam in the vicinity of the screw and parallel to the length of the screw

4.8 Summary

A simple method to model the moisture transport process inside mass timber products and to determine the required diffusion coefficients of the model has been described in this chapter. With this method, the moisture content distribution inside the multi-layered mass timber products like CLT and glulam can easily be predicted under different moisture conditions at any time interval from the beginning of the moisture diffusion process. Also, this method can be used to model the moisture content change distribution along the screw axis in the CLT and glulam, which can be implemented in the analytical treatment of the case of non-uniform moisture content change in the CLT and glulam.

The diffusion coefficient of CLT and glulam laminates decreased with the increase of moisture content during moisture adsorption. Although the adhesive between adjacent layers of CLT and glulam have different diffusion coefficient values, assuming the same diffusivity value for the adhesive and the laminates gave reasonably accurate predictions of moisture content.

5 MASS TIMBER SWELLING PROPERTIES AND MODELLING

5.1 Introduction

In chapter 4, a method to predict the moisture content change distribution inside CLT and glulam under varying moisture conditions has been presented. This chapter presents an effective method for predicting the hygroscopic deformation arising from the change in moisture content from the laminate properties of the CLT and glulam. The hygroscopic deformation in only the thickness (out-of-plane) direction of CLT and glulam is investigated here. Moreover, the hygroscopic deformation due to moisture content increase has been focused on in this chapter. The hygroscopic deformation arising from moisture content increase (moisture adsorption) of wood cause an increase in volume, called wood swelling. On the other hand, hygroscopic deformation arising from moisture content decrease (moisture desorption) of wood cause wood shrinkage, which has not been investigated. This chapter has the following objectives:

- Determination of the swelling coefficient of the laminates of CLT and glulam
- The proposition of a prediction model for swelling of mass timber products from the laminate properties
- Determination of the effective swelling coefficient of the mass timber products
- Experimental and numerical verification of the prediction model

Similar to chapter 4, the test program in this chapter is composed of the following phases:

- Laminate phase: In this phase of the test program, the swelling strain and swelling coefficient of the laminates constituting the CLT and the glulam are determined by experimental means
- Experimental multi-layer phase: The swelling properties of large-size CLT and glulam are experimentally investigated in this phase
- Numerical multi-layer phase: The swelling process of the same CLT and glulam specimens of the experimental multi-layer phase is numerically simulated in this phase.

5.2 Determination of the Swelling Properties of the Individual Laminates of CLT and Glulam (Laminate Phase)

The test program included two mass timber products, glulam made from Douglas Fir-Larch of stress grade 16c-E and Spruce-pine-fir (SPF) CLT of stress grade V2. Glulam of two different sizes from the same manufacturer and CLT made from 2×4 laminates (CLT type A) and 2×6 laminates (CLT type B) from two different manufacturers were investigated. The two sizes of glulam and the two types of CLT used are shown in Figure 5-1. According to the technical specifications of the manufacturers of the CLT, the longitudinal (major) and the transverse (minor) layers of CLT were made from lumbers of different grades. Thus, the laminates of the longitudinal and transverse layers might have come from different sources, and the swelling properties of the longitudinal and the transverse layers of CLT were determined separately. Both sizes of glulam used in the test program were of the same grade and came from the same manufacturer. Furthermore, all the glulam used were of compression grade, and for the compression grade glulam, laminates of all layers came from the same source and had similar properties. Thus, all the layers of both sizes of glulam were considered to have the same swelling properties.

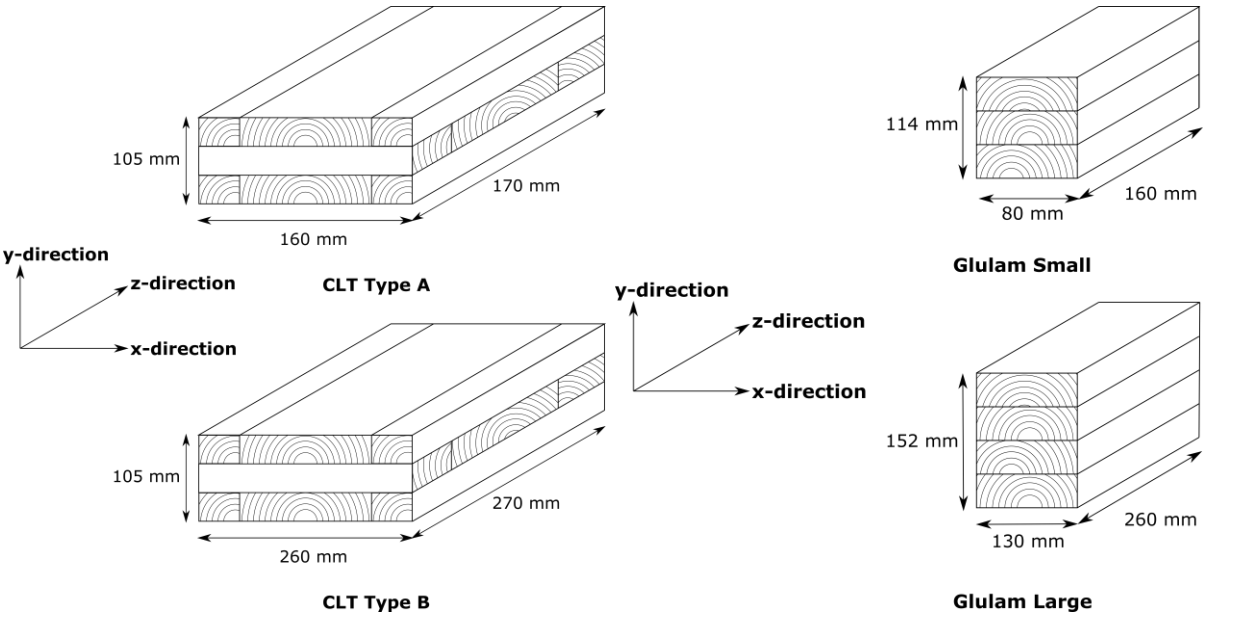

Figure 5-1: CLT and glulam products used in the test program

In the laminate phase, small-size samples of approximate dimensions of 80 (longitudinal) mm × 35 (radial) mm × 35 (tangential) mm were cut from the different layers of CLT and glulam. It was ensured that the samples of the laminate phase did not have any glue on any face. Three sample

groups were prepared in the laminate phase to investigate the dimensional changes with moisture content change. The number and type of specimens in each sample group are mentioned in Table 5-1.

Table 5-1: One sample group of laminate phase

Type of Wood Product	Layer type	Number of Specimens	Sample Label
CLT Type A (2x4)	Longitudinal	6	AO
	Transverse	6	AI
CLT Type B (2x6)	Longitudinal	6	BO
	Transverse	6	BI
Glulam Small and Large	Same laminates for all layers	6	C

The laminates of the longitudinal and transverse layers of CLT Type A and CLT Type B have different swelling properties. In contrast, all the laminates of both sizes of glulam have the same swelling properties. The sample group of Table 5-1 was adopted to determine the swelling coefficient following these premises.

Figure 5-2: One sample group

Each sample group was conditioned at constant relative humidity and temperature conditions in two stages. The conditioning time for each stage was two weeks. In the first stage, the samples

were kept in a conditioning chamber with 65 ± 2% relative humidity and 20 ºC temperature. In the second stage, the samples were kept in another conditioning chamber. The three sample groups were kept in three different conditioning chambers in the second stage, as shown in Table 5-2. The first conditioning stage was adopted to achieve an equilibrium moisture content (EMC) of 12% for all specimens. The second conditioning stage aimed to achieve EMCs of 6%, 16% and 21% (Table 5-2). All the samples reached a constant weight at the end of the two-week conditioning process, indicating uniform moisture content distribution inside the samples. After the two-stage conditioning, the samples were oven-dried at 105 ± 1 º C for two days.

Table 5-2: Relative humidity and temperature for conditioning and the corresponding equilibrium moisture content (EMC)

Conditioning Stage	Moisture Conditions Label	Relative Humidity (%)	Temperature (º C)	Target EMC
1st	EMC – 12	65 ± 2	20	12%
2nd	EMC – 6	42 ± 2	20	6%
	EMC – 16	80 ± 2	20	16%
	EMC – 21	92 ± 2	20	21%

A total of nine length measurements from each sample, three along each orthotropic direction, were taken (Figure 5-3). Each sample's length and weight measurements were taken at the end of the second-stage conditioning and after oven-drying. A digital balance with a sensitivity of 0.01 g was used to measure sample weight, and a digital calliper with a sensitivity of 0.01 mm was used to measure sample dimensions. The length measurements were later used to determine the swelling strains according to equation 5-1. The actual moisture content of each sample was determined using equation 5-2.

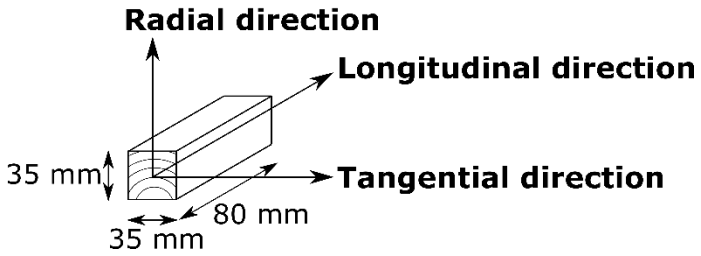

Figure 5-3: Laminate phase specimen along with the wood anatomical directions

The swelling coefficient can be determined by determining the slope of the swelling strain vs moisture content change graph. For this purpose, the strain values along the three orthotropic

directions should be recorded under different known moisture content changes. The strain value and the moisture content change of a sample can be determined using equations 5-1 and 5-2:

Equation 5-1

$$\varepsilon(t) = \frac{L(t) - L_0}{L_0}$$

Equation 5-2

$$MC(t) = \frac{w(t) - w_0}{w_0}$$

Here, L_0 and w_0 are the oven-dry length and weight of the sample, respectively, $L(t)$ and $w(t)$ are the length and weight at the end of the swelling process (at the end of the second conditioning stage) of the sample, $\varepsilon(t)$ is the generated shrinkage strain and $MC(t)$ is the moisture content inside the sample. The end point of the swelling process was identified as the point when a constant value of the weight of the sample, $w(t)$ was achieved.

5.3 Determination of the Swelling Properties of Full-size CLT and Glulam (Experimental Multi-layer Phase)

The dimensional changes due to moisture swelling of full-size glulam and CLT samples in the out-of-plane direction (y-direction in Figure 5-1) were investigated in the multi-layer phase. Two sample groups were used in the multi-layer phase, and each group consisted of two specimens of each type of glulam and CLT. One sample group of the multi-layer phase is shown in Table 5-3.

Table 5-3: One sample group of multi-layer phase

Type of Wood Product	Number of Specimens
CLT Type A	2
CLT Type B	2
Glulam Small	2
Glulam Large	2

The samples were subjected to the same two-stage conditioning process as described before. In the second conditioning stage, one sample group was conditioned under EMC – 16 conditions while another was conditioned under EMC – 21 conditions of Table 5-1. Each specimen's dimension in the y-direction and weight measurements were taken at the end of the second-stage conditioning and after oven-drying. For measuring the dimensions, two gauge points were marked near the top and bottom end of the specimen along the y-direction, and the distance between the gauge points was recorded. The strain in the out-of-plane direction was calculated from the dimension measurements, and actual moisture content was found from the weight measurements, using equations 5-1 and 5-2.

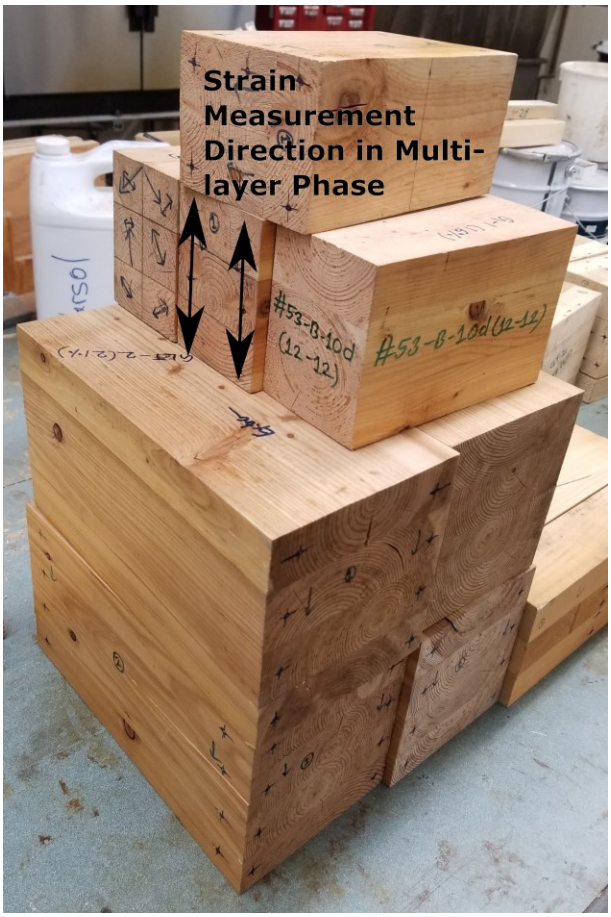

Figure 5-4: Multi-layer phase samples and strain measurements

5.4 Prediction of Swelling from Laminate Properties

If prediction equations for moisture swelling of CLT and glulam are developed based on the properties of the laminates, the dimensional changes of various CLT and glulam configurations due to moisture swelling can be reliably estimated.

Expressions 5-3, 5-4 and 5-5 are proposed to determine the effective swelling coefficient and swelling strain of the whole CLT and glulam panel in the out-of-plane direction (y-direction). The theoretical basis for these expressions comes from the concepts of transformation of plane strain found in mechanics of solid textbooks (Beer et al., 2012). Since the longitudinal direction of the wood undergoes minimal dimensional change under varying moisture content (Pang & Jeong, 2020), the strain in the longitudinal direction can be ignored, and plane strain conditions can be assumed. The shear strain component in the plane strain transformation equations was set to zero to get to equation 5-5. The zero shear strain comes from the premise that moisture ingress generates only axial strain components in the wood's three primary orthotropic directions.

Equation 5-3

$$\varepsilon_{eff,predicted} = \alpha_{eff,predicted}.\Delta u$$

Equation 5-4

$$\alpha_{eff,predicted} = \frac{\sum_{i=1}^{n} \alpha_{eff,i}}{n}$$

Equation 5-5

$$\alpha_{eff,i} = \alpha_{Ri} \cos^2 \theta_i + \alpha_{Ti} \sin^2 \theta_i$$

Here, $\varepsilon_{eff,predicted}$ is the average swelling strain in the out-of-plane direction, Δu is the change in moisture content, $\alpha_{eff,i}$ is the swelling coefficient of each layer of the CLT or glulam, which considers the annual ring orientation of the laminates in each layer. θ_i is the approximate angle between the horizontal-direction and the tangent to the annual rings at the location of strain measurement of the laminates of each layer (Figure 5-5). α_{Ri} is the value of the swelling coefficient of the laminates of each layer in the radial anatomic direction, whereas α_{Ti} is the swelling coefficient of the laminates of each layer in the tangential anatomic direction of the wood. The values of θ_i for each layer of the CLT and glulam used in the multi-layer phase were recorded manually by using a protractor. Equation 5-3 gives the average strain of all the layers of CLT and glulam, and the actual strain in each layer might be different from this average strain value. Equation 5-6 gives the swelling strain of the individual layers of CLT and glulam.

Equation 5-6

$$\varepsilon_{eff,predicted,i} = \alpha_{eff,i}.\Delta u$$

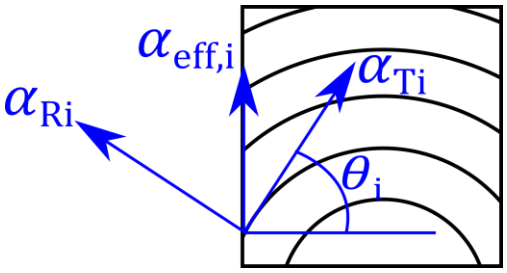

Figure 5-5: Nomenclature of the terms for the prediction model

5.5 Finite Element Modelling of Full-scale CLT and Glulam (Numerical Multi-layer Phase)

The full-size CLT and glulam samples used in the multi-layer phase were numerically investigated to test the validity of the prediction model. The commercial finite-element analysis software ABAQUS (Simulia, 2020) was used for the numerical investigation. The moisture swelling due to the two-stage conditioning process was simulated in ABAQUS. The thermal analysis formulation available in ABAQUS can best describe the process of moisture swelling and the strain arising from the moisture swelling. Thus, thermal analysis using the ABAQUS Standard solver was carried out to simulate the moisture swelling process in CLT and glulam.

The CLT and glulam layers were treated as continuous, and the edge gap between adjacent laminates in the same layer of CLT was disregarded. The different layers of CLT and glulam were created by partitioning the same part into the required number of layers in ABAQUS/CAE (Simulia, 2020). Local material orientation was assigned to each layer following the anatomical directions of the specimen, which was documented in the experimental multi-layer phase. The local material orientation directions used for modelling the specimens of the multi-layer phase are given in Tables 5-4, 5-5, 5-6 and 5-7. Figures 5-6 and 5-7 show the layer designations of the CLT and glulam used in Tables 5-4, 5-5, 5-6 and 5-7.

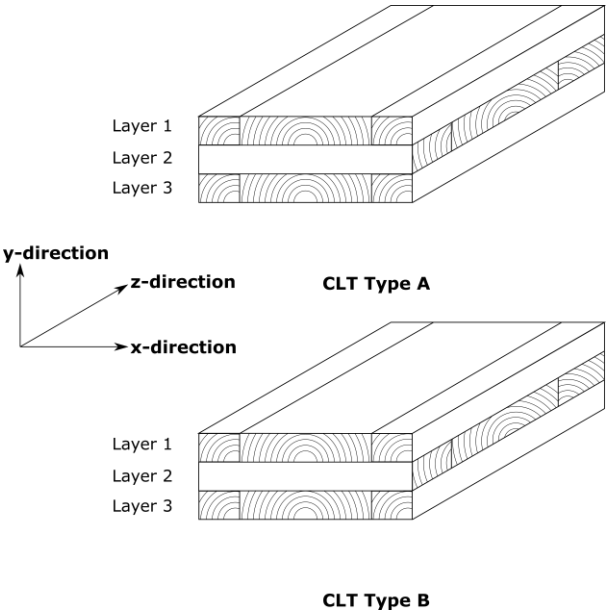

Figure 5-6: Layer designation of CLT for local material orientation definition

Table 5-4: CLT Type A local material orientation of different layers

CLT Type A	Sample Group 1 (EMC – 16%)		Sample Group 2 (EMC – 21%)	
	Specimen 1	Specimen 2	Specimen 1	Specimen 2
Layer 1	50º	30º	45º	50º
Layer 2	50º	20º	40º	60º
Layer 3	75º	30º	60º	80º

Table 5-5: CLT Type B local material orientation of different layers

CLT Type B	Sample Group 1 (EMC – 16%)		Sample Group 2 (EMC – 21%)	
	Specimen 1	Specimen 2	Specimen 1	Specimen 2
Layer 1	30º	15º	25º	30º
Layer 2	60º	30º	30º	25º
Layer 3	50º	35º	20º	55º

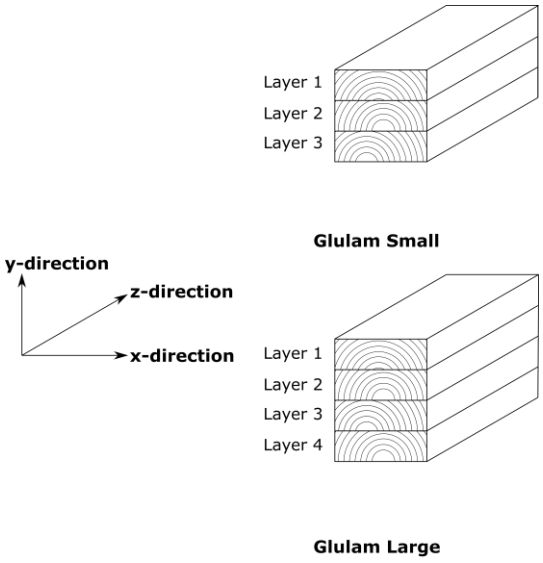

Figure 5-7: Layer designation of Glulam for local material orientation definition

Table 5-6: Glulam Small local material orientation of different layers

Glulam Small	Sample Group 1 (EMC – 16%)		Sample Group 2 (EMC – 21%)	
	Specimen 1	Specimen 2	Specimen 1	Specimen 2
Layer 1	40º	55º	45º	50º
Layer 2	60º	75º	75º	65º
Layer 3	45º	60º	30º	30º

Table 5-7: Glulam Large local material orientation of different layers

Glulam Large	Sample Group 1 (EMC – 16%)		Sample Group 2 (EMC – 21%)	
	Specimen 1	Specimen 2	Specimen 1	Specimen 2
Layer 1	80º	55º	35º	70º
Layer 2	85º	60º	75º	70º
Layer 3	75º	55º	80º	80º
Layer 4	50º	60º	65º	60º

The moisture content of the specimen is analogous to the specified temperature during thermal analysis in the ABAQUS environment. The test conditions were aimed to achieve a uniform moisture content distribution inside the specimen. Thus, the moisture content of each conditioning stage was specified as a uniform constant temperature field throughout the model in ABAQUS/CAE. The value of the uniform temperature field for each stage was specified as the equilibrium moisture content (EMC) corresponding to the conditioning chamber's relative humidity and temperature conditions, as shown in Table 5-2. The initial temperature boundary condition of the specimen was the EMC at the end of the first conditioning stage. In contrast, the EMC at the end of the second conditioning stage was the final temperature boundary condition. The temperature boundary conditions were specified in two distinct analysis steps in ABAQUS/CAE. The strain arising after the second stage of the conditioning was recorded as the swelling strain.

The two types of full-size CLT used in the multi-layer phase in this study were modelled in ABAQUS/CAE in three dimensions (3D) with C3D8 elements available in the ABAQUS library (Figure 5-8). The major direction of CLT (z-direction) was specified as the depth of the 3D section in ABAQUS/CAE. Input material properties used to model the two types of CLT, taken from the manufacturer's guide and the Wood handbook (Ross & USDA Forest Service., 2010), are given in Tables 5-8 and 5-9. The wood's elastic properties (Young’s Modulus, E and Shear Modulus, G) change with the moisture content (Gerhards, 1982). However, as this study only focuses on the strain values, the elastic properties did not influence the strain values and were kept constant at all moisture levels. On the other hand, stress analysis would require the change of elastic properties with moisture content change to be considered.

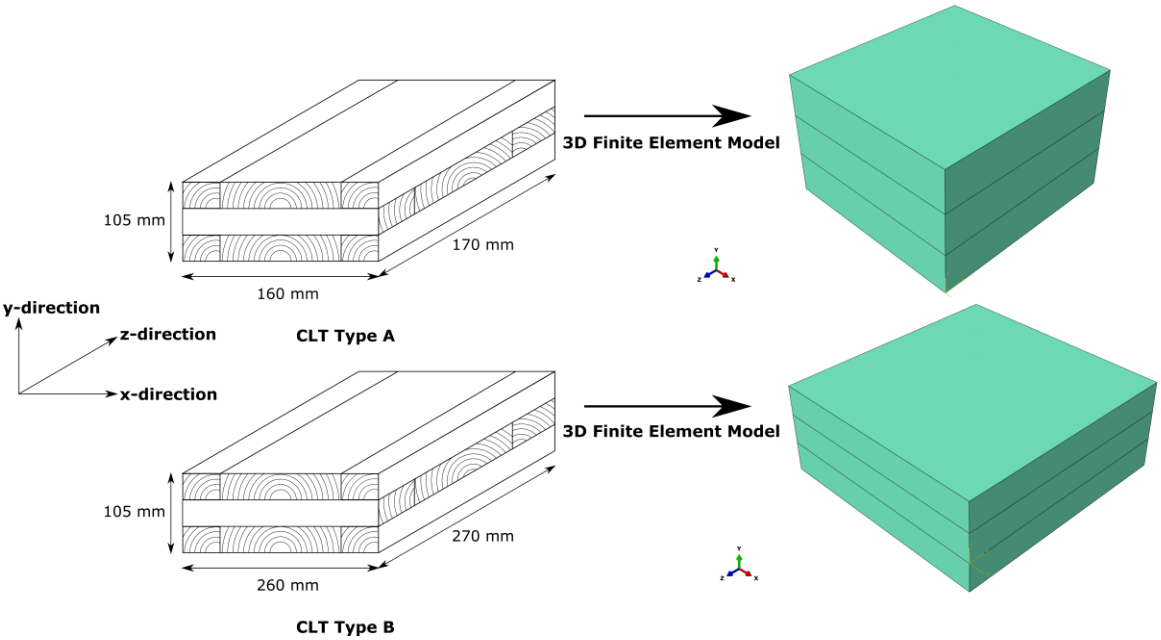

Figure 5-8: CLT modelling in ABAQUS/CAE

Table 5-8: CLT Type A Input Material Properties

Longitudinal Layers		Transverse Layers	
E_L	11700 MPa	E_L	9000 MPa
E_R	1193.4 MPa	E_R	918 MPa
E_T	631.8 MPa	E_T	486 MPa
G_{LR}	731 MPa	G_{LR}	563 MPa
G_{TL}	608.4 MPa	G_{TL}	468 MPa
G_{RT}	73.1 MPa	G_{RT}	56.3 MPa
υ_{LR}	0.032	υ_{LR}	0.032
υ_{TL}	0.024	υ_{TL}	0.024
υ_{RT}	0.381	υ_{RT}	0.381

Table 5-9: CLT Type B Input Material Properties

Longitudinal Layers		Transverse Layers	
E_L	9500 MPa	E_L	9500 MPa
E_R	969 MPa	E_R	969 MPa
E_T	513 MPa	E_T	513 MPa
G_{LR}	570 MPa	G_{LR}	570 MPa
G_{TL}	494 MPa	G_{TL}	494 MPa
G_{RT}	57 MPa	G_{RT}	57 MPa
υ_{LR}	0.032	υ_{LR}	0.032
υ_{TL}	0.024	υ_{TL}	0.024
υ_{RT}	0.381	υ_{RT}	0.381

The longitudinal direction of the wood undergoes minimal dimensional change under moisture content variation due to the small value of the swelling coefficient in the longitudinal direction (Pang & Jeong, 2020). In glulam, the longitudinal direction of all layers is aligned in the same direction. As the dimensional change in the longitudinal direction is minimal, the swelling in this direction was not investigated in the numerical model. Thus, only a two-dimensional (2D) model of the glulam containing the radial and tangential direction was created in ABAQUS (Figure 5-9). The local material orientation of two layers is shown in Figure 5-9. CPS4 plane stress elements available in the ABAQUS library were used for the two-dimensional model of the glulam. Material properties used to model the glulam are given in Table 5-10.

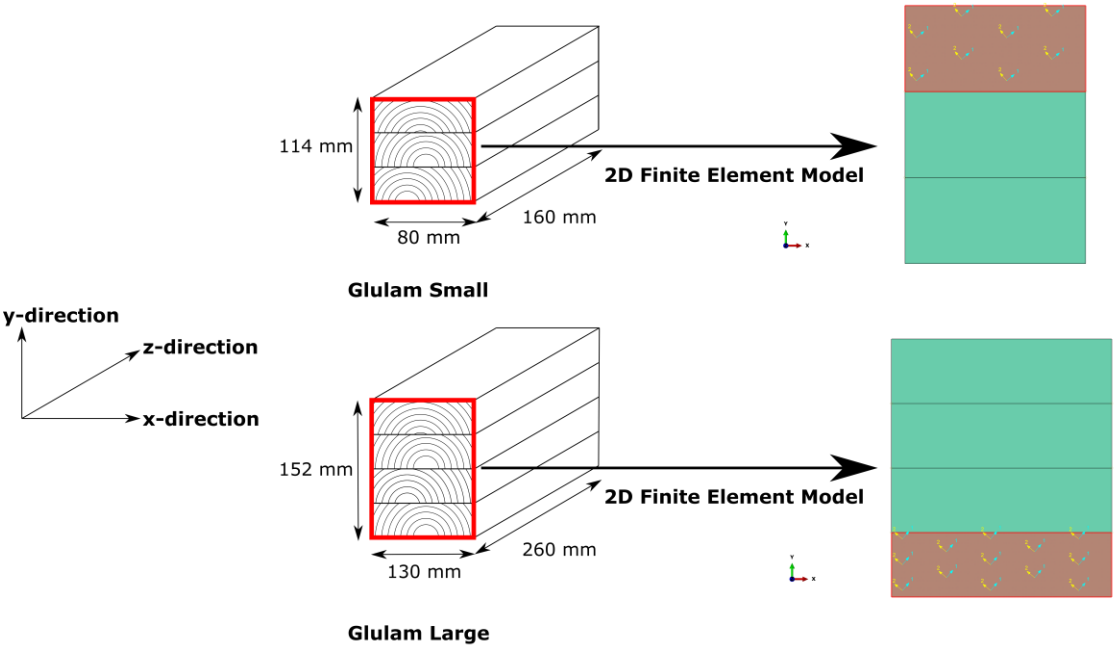

Figure 5-9: Glulam modelling in ABAQUS/CAE

Table 5-10: Glulam Input Material Properties

Longitudinal Layers	
E_L	12400 MPa
E_R	843.2 MPa
E_T	620 MPa
G_{LR}	793.6 MPa
G_{TL}	967.2 MPa
G_{RT}	86.8 MPa
υ_{LR}	0.036
υ_{TL}	0.029
υ_{RT}	0.39

For modelling the CLT and glulam, swelling coefficient values of the laminates of each layer are required. The swelling coefficient values are analogous to the expansion coefficients for thermal analysis in the ABAQUS environment. Following the orthotropic constitutive law adopted in this study outlined in section 2, the expansion coefficients were specified along the principal material

directions (primary orthotropic directions of the wood). The swelling coefficient values of the CLT and glulam laminates came from the laminate phase results in section 5.6.1.

5.6 Results and Discussion

5.6.1 Laminate Phase

The swelling strain vs. moisture content plot was made for each group of samples along the wood's radial, tangential, and longitudinal direction from each small-size sample's strain and moisture content data. The data points were fitted using a linear regression line. The slope of the regression line gives the value of the swelling coefficient (α). The swelling strain vs moisture content plot along the orthotropic directions of wood for CLT type A, CLT type B, and glulam are shown in Figures 5-10, 5-11 and 5-12.

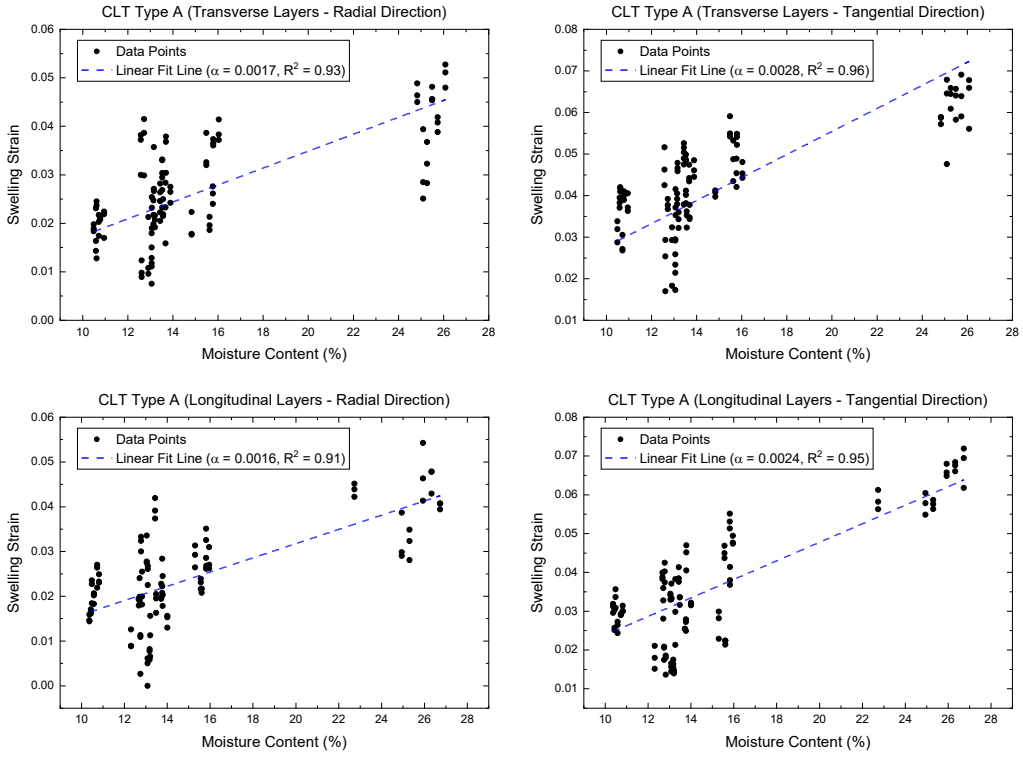

Figure 5-10: Swelling strain vs moisture content plot of CLT type A

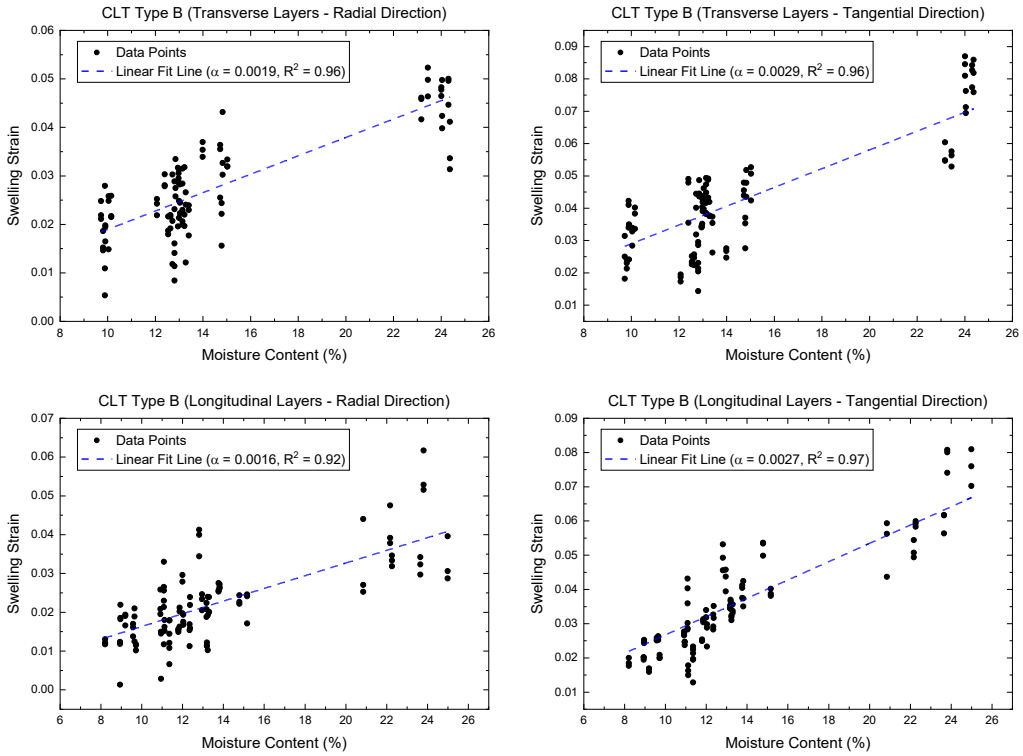

Figure 5-11: Swelling strain vs moisture content plot of CLT type B

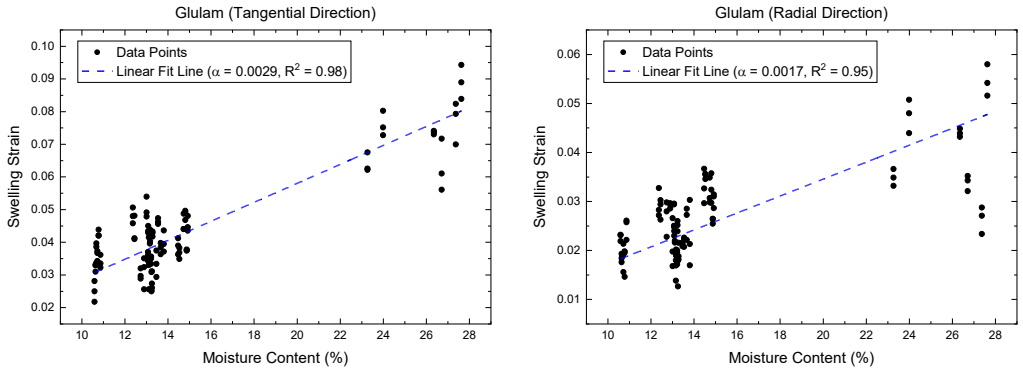

Figure 5-12: Swelling strain vs moisture content plot of Glulam

The swelling strain vs. moisture content plot along the longitudinal direction is not shown since the linear regression lines were almost horizontal and the swelling coefficient was very close to zero, consistent with values reported in similar studies, e.g., Angst & Malo (2012b). Also, swelling coefficient values along the tangential direction are the largest, as observed in other literature (Ross & USDA Forest Service., 2010). The swelling coefficient of all the wood products is summarised in Table 5-11. The swelling coefficient was used as input parameters for the numerical and analytical prediction models.

Table 5-11: Swelling coefficients

Type of wood product	Layer type	α_L	Standard error	α_R	Standard error	α_T	Standard error
CLT Type A	Longitudinal	0	-	0.0016	4.76×10^{-5}	0.0024	5.33×10^{-5}
	Transverse	0.0001	-	0.0017	4.63×10^{-5}	0.0028	5.31×10^{-5}
CLT Type B	Longitudinal	0	-	0.0016	4.64×10^{-5}	0.0027	4.77×10^{-5}
	Transverse	0.0002	-	0.0019	4×10^{-5}	0.0029	6.17×10^{-5}
Glulam Small and Large	-	0.0001	-	0.0017	3.98×10^{-5}	0.0029	4.36×10^{-5}

5.6.2 Multi-layer Phase

5.6.2.1 Comparison between measured and analytically predicted strains

The dimensional changes of each full-size CLT and glulam sample were recorded in the y-direction using digital callipers. These measurements were used to determine the strain by equation 5-1. It is to be noted that the strain determined in this process gives the average strain of all the layers of CLT and glulam in the y-direction, and the actual strain in each layer might be different from this average strain value. The moisture content of each sample was also found with equation 5-2. Then average swelling strain vs moisture content plots of CLT and glulam was made and shown in Figure 5-13. For the y-direction strain, the slope of the linear fit line of the test data gives the value of the effective swelling coefficient of CLT and glulam in the out-of-plane direction. Table 5-12 lists the effective swelling coefficient of CLT and glulam in the out-of-plane direction from the test data. The effective swelling coefficient predicted using equations 5-4 and 5-5 is also given in Table 5-12. The angle value required for equation 5-5 is the approximate angle between the horizontal direction and tangent to the annual rings of the laminates of each layer of CLT and glulam. Angles were measured near the edge of each layer's laminates to match the samples' experimental strain measurement location.

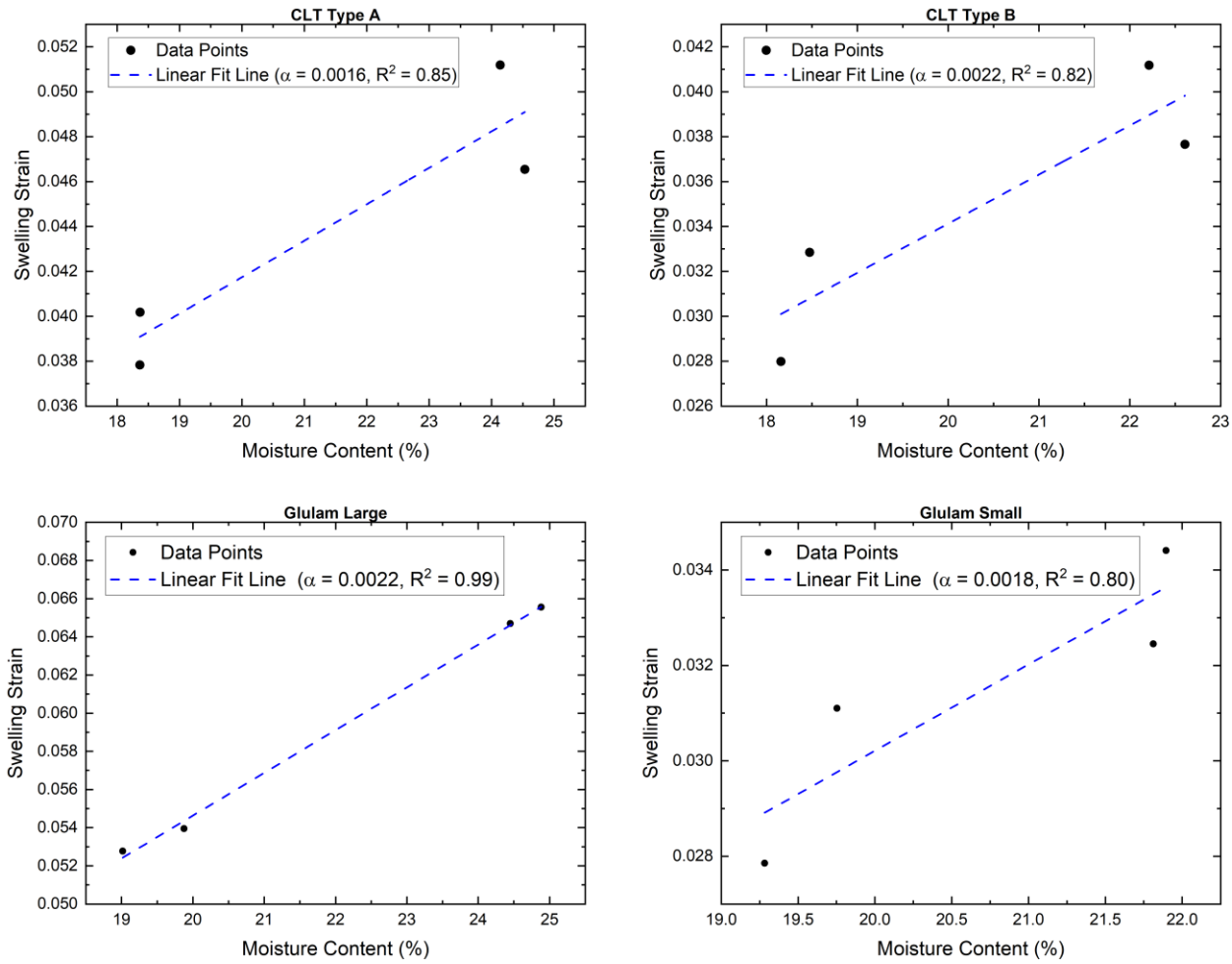

Figure 5-13: Average swelling strain vs moisture content plots of CLT and glulam

Table 5-12: Effective swelling coefficient of full-size CLT and glulam

Type of wood product	$\alpha_{eff,experimental}$	$\alpha_{eff,predicted}$	Percentage Difference
CLT Type A	0.0016	0.0021	31.25
CLT Type B	0.0022	0.0020	9.09
Glulam Small	0.0018	0.0024	33.33
Glulam Large	0.0022	0.0027	22.73

It can be seen from Table 5-12 that the percentage difference between the experimental and predicted values of the effective swelling coefficients ranged from 9 to 33%. The highest difference was observed for CLT Type A and small glulam samples. A possible reason for the difference might be the approximate angle measurement by hand. Nevertheless, as the predicted values were higher than the experimental values, they were conservative.

5.6.2.2 Comparison between numerically simulated and analytically predicted strains

As discussed in section 5.5, the moisture swelling of the full-size CLT and glulam specimens were numerically simulated using finite element analysis. From the 3D finite element analysis of CLT and 2D analysis of glulam, contour plots of the strain of CLT and glulam (Figures 5-14 and 5-15) in the out-of-plane direction were made. These contour plots were used to determine the swelling of the individual layers and the strain distribution along the y-direction of CLT and glulam. Strain in each layer of CLT and glulam can be predicted using equation 5-6. The predicted strain values using equation 5-6 have been compared with the strain values from finite element analysis for two CLT and glulam samples in Figures 5-16 and 5-17. The dashed lines represent the strain distribution from finite element analysis, while the solid lines give the predicted values using equation 5-6. It should be mentioned that the strain in each layer of CLT and glulam were not determined experimentally, for which Figures 5-16 and 5-17 only compare strain determined from finite element analysis and the prediction equation 5-6.

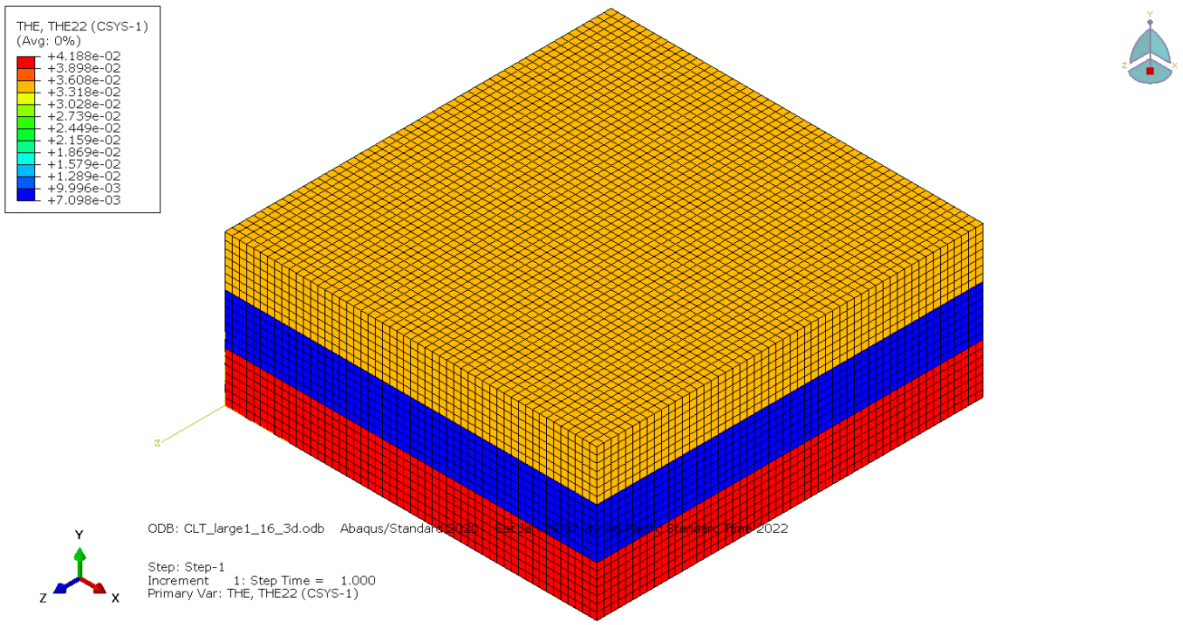

Figure 5-14: Strain distribution contour plot of CLT (3D analysis)

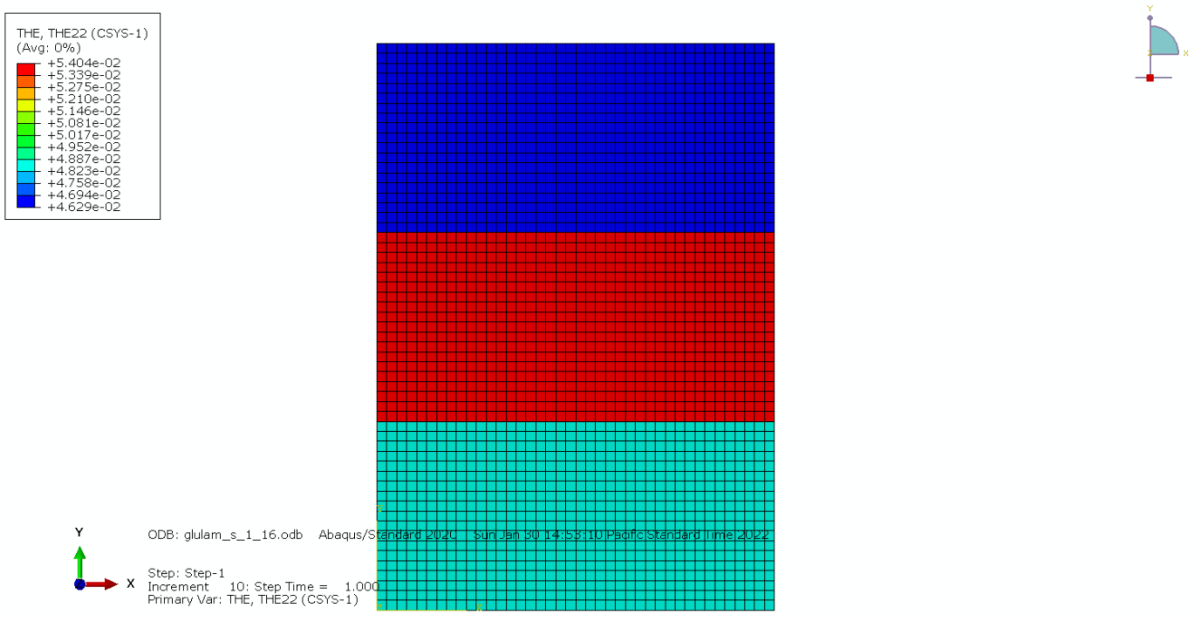

Figure 5-15: Strain distribution contour plot of Glulam (2D analysis)

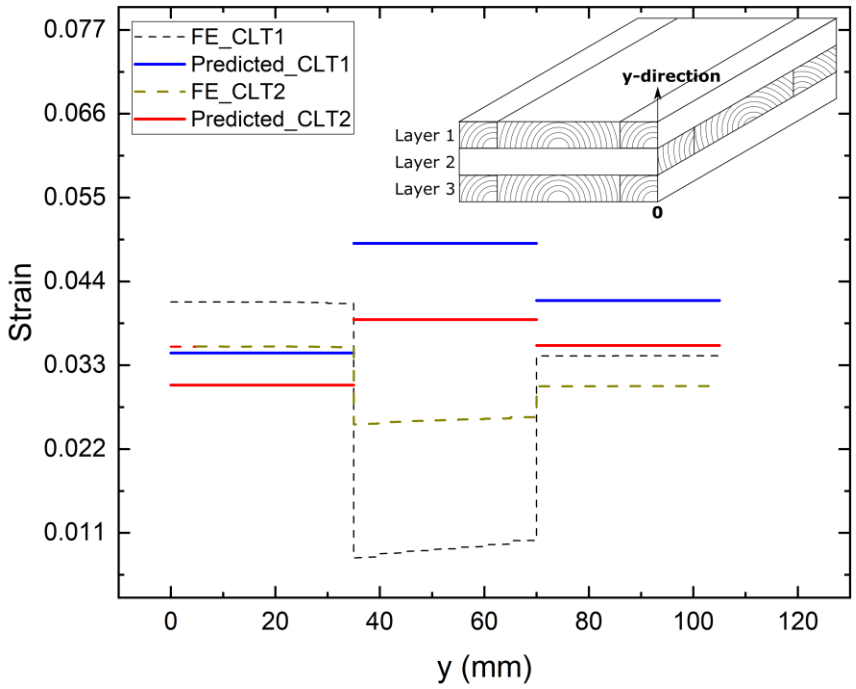

Figure 5-16: Strain distribution comparison between the predicted and finite element analysis values for CLT

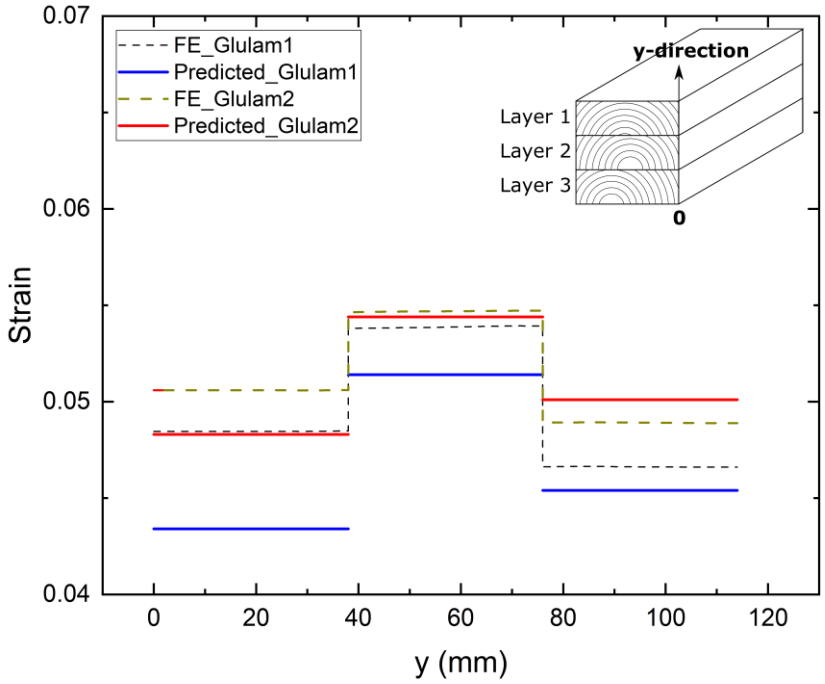

Figure 5-17: Strain distribution comparison between the predicted and finite element analysis values for Glulam

In Figure 5-16, the predicted strain in layer 2 for both CLT is overpredicted by equation 5-6, compared to the finite element analysis results. In contrast, the difference between the predicted and finite element strain for layers 1 and 3 for both CLT is minimal. In Figure 5-17, it can be observed that the predicted strains in almost all the layers of glulam are under-predicted compared to the finite element analysis strains. Nevertheless, the differences in the strains are pretty slight.

5.6.2.3 Comparison among measured, numerically simulated and analytically predicted strains

The strain contour plots from finite element analysis were averaged to find the CLT and glulam average strain (the average strain of all layers) in the y-direction. The average strain can also be predicted using equations 5-3, 5-4 and 5-5. The average strain determined from the experiment, finite element (numerical) analysis and prediction equations 5-3, 5-4 and 5-5 have been presented and compared in Tables 5-13 to 5-20. The percentage difference between the strains determined from these three methods does not exhibit any clear trend. The experimental strain measurement might be prone to measurement errors, while the numerically determined strain depends on the assumptions made during numerical modelling. The highest deviation of the experimental strain from the numerical and predicted strains was observed for small glulam samples, which might have been from experimental measurement errors. The percentage difference among the predicted, experimental and numerical strains for large glulam samples was only 9%, indicating all three

methods estimated nearly consistent strain values. The difference in predicted and experimentally determined strain for CLT Type A was limited to 12%, while the difference for CLT Type B was higher, with a maximum difference of 27%. On the other hand, the differences in experimental and numerical strain for CLT Type A were higher than those of CLT Type B.

The average difference between the strains determined using the three methods was calculated. The small glulam samples were excluded for possible measurement errors in calculating the average difference. The average difference between the predicted and experimental strains was approximately 11%. On the other hand, the predicted and numerical strains differed by approximately 13%. The average difference between the numerical and experimental strains, excluding the small glulam samples, was the lowest, at about 8%. Thus, the numerical method gave estimates of swelling strain closer to the experimental values. Nevertheless, numerical methods like finite element analysis might not always be feasible in practical engineering settings; in such cases, equations 5-3, 5-4 and 5-5 can be used to predict the average out-of-plane strain of CLT and glulam with reasonable accuracy.

Table 5-13: CLT Type A strain from different methods

CLT Type A Sample No.	$\varepsilon_{avg,experimental}$	$\varepsilon_{avg,numerical}$	$\varepsilon_{avg,predicted}$
1-16	0.0402	0.0327	0.0414
2-16	0.0378	0.0313	0.0332
1-21	0.0465	0.043	0.052
2-21	0.0512	0.042	0.0561

Table 5-14: CLT Type A strain from different methods comparison

CLT Type A Sample No.	Percentage difference between $\varepsilon_{avg,experimental}$ and $\varepsilon_{avg,numerical}$	Percentage difference between $\varepsilon_{avg,experimental}$ and $\varepsilon_{avg,predicted}$	Percentage difference between $\varepsilon_{avg,numerical}$ and $\varepsilon_{avg,predicted}$
1-16	18.66	2.99	26.61
2-16	17.20	12.17	6.07
1-21	7.53	11.83	20.93
2-21	17.97	9.57	33.57

Table 5-15: CLT Type B strain from different methods

CLT Type B Sample No.	$\varepsilon_{avg,experimental}$	$\varepsilon_{avg,numerical}$	$\varepsilon_{avg,predicted}$
1-16	0.0328	0.032	0.0417
2-16	0.028	0.0315	0.035
1-21	0.0377	0.0375	0.0428
2-21	0.0412	0.0436	0.0466

Table 5-16: CLT Type B strain from different methods comparison

CLT Type B Sample No.	Percentage difference between $\varepsilon_{avg,experimental}$ and $\varepsilon_{avg,numerical}$	Percentage difference between $\varepsilon_{avg,experimental}$ and $\varepsilon_{avg,predicted}$	Percentage difference between $\varepsilon_{avg,numerical}$ and $\varepsilon_{avg,predicted}$
1-16	2.44	27.13	30.31
2-16	12.50	25.00	11.11
1-21	0.53	13.53	14.13
2-21	5.83	13.11	6.88

Table 5-17: Glulam Large strain from different methods

Glulam Large Sample No.	$\varepsilon_{avg,experimental}$	$\varepsilon_{avg,numerical}$	$\varepsilon_{avg,predicted}$
1-16	0.0539	0.0552	0.0545
2-16	0.0528	0.0481	0.0485
1-21	0.0647	0.066	0.064
2-21	0.0655	0.0691	0.0683

Table 5-18: Glulam Large strain from different methods comparison

Glulam Large Sample No.	Percentage difference between $\varepsilon_{avg,experimental}$ and $\varepsilon_{avg,numerical}$	Percentage difference between $\varepsilon_{avg,experimental}$ and $\varepsilon_{avg,predicted}$	Percentage difference between $\varepsilon_{avg,numerical}$ and $\varepsilon_{avg,predicted}$
1-16	2.41	1.11	1.27
2-16	8.90	8.14	0.83
1-21	2.01	1.08	3.03
2-21	5.50	4.27	1.16

Table 5-19: Glulam Small strain from different methods

Glulam Small Sample No.	$\varepsilon_{avg,experimental}$	$\varepsilon_{avg,numerical}$	$\varepsilon_{avg,predicted}$
1-16	0.0311	0.0498	0.0467
2-16	0.0279	0.0515	0.0509
1-21	0.0344	0.0523	0.052
2-21	0.0324	0.0523	0.0515

Table 5-20: Glulam Small strain from different methods comparison

Glulam Small Sample No.	Percentage difference between $\varepsilon_{avg,experimental}$ and $\varepsilon_{avg,numerical}$	Percentage difference between $\varepsilon_{avg,experimental}$ and $\varepsilon_{avg,predicted}$	Percentage difference between $\varepsilon_{avg,numerical}$ and $\varepsilon_{avg,predicted}$
1-16	60.13	50.16	6.22
2-16	84.59	82.44	1.17
1-21	52.03	51.16	0.57
2-21	61.42	58.95	1.53

5.7 Summary

This chapter has experimentally and numerically investigated the swelling behaviour of CLT and glulam products made from Canadian lumber species. A prediction model for estimating the swelling strain of CLT and glulam is proposed, and the predicted strains from the prediction model are compared with the experimental and numerical results. The prediction model relies on the

laminate properties as input parameters and is suitable for hand calculations in practical engineering settings. The prediction model can determine the average effective swelling strain and the swelling strain of the individual layers of CLT and glulam in the out-of-plane direction with reasonable accuracy.

6 WITHDRAWAL PROPERTIES OF SELF-TAPPING SCREW IN MASS TIMBER PRODUCTS

6.1 Introduction

The axial behaviour of the screw inside a wood member is governed by: (a) the withdrawal properties of the wood-screw composite system and (b) the tensile properties of the screw. The tensile properties of self-tapping screws were discussed in chapter 3. This chapter deals with the withdrawal properties of self-tapping screws in a wood-screw composite system. All the preceding chapters were concerned with the properties of wood and screw individually. The individual properties of the screw and wood and the properties of the wood-screw composite system are essential to predict the behaviour of self-tapping screws due to moisture content changes in the wood.

Moisture content variations can change wood mechanical properties, such as shear strength and modulus. Consequently, these changes can alter the withdrawal strength and stiffness of self-tapping screws inserted in mass timber products, such as CLT and glulam. This chapter focuses on the withdrawal strength and stiffness of STS in CLT and glulam, inserted perpendicular to the wood's grain direction. The effect of CLT and glulam moisture content variation on the withdrawal strength and stiffness of STS was investigated. For this purpose, STS of two different diameters were inserted into two types of CLT and glulam products. The samples were then conditioned in different moisture conditions and tested in withdrawal under pull-push loading conditions. This chapter aims to characterize the withdrawal properties of STS under varying moisture contents of CLT and glulam, which will later help develop a model for predicting the stress distribution inside STS due to moisture content change of CLT and glulam. Also, the test results from the withdrawal tests will act as a database for the withdrawal properties of self-tapping screws inserted into Canadian CLT and glulam products under varying moisture conditions.

6.2 Withdrawal Test of Self-tapping Screws in CLT and Glulam

The test program used two kinds of mass timber products, Douglas Fir-Larch glulam of stress grade 16c-E and Spruce-Pine-Fir CLT of stress grade V2. Self-tapping screws of two diameters, 8 mm and 13 mm were utilized, and screws were inserted in the CLT and glulam at 10d penetration length. The 10d penetration length was chosen to achieve screw withdrawal failure instead of

screw failure in tension, based on the screw tensile strength and calculation of the withdrawal resistance of the screw from the screw manufacturer's guide. The two screws used in the test program are VGS 13x200 (13 mm nominal diameter) and ASSY VG 8x160 (8 mm nominal diameter). In the screw nomenclature, the letters indicate the type of screw used; the first number indicates the outer thread diameter in mm, and the last number indicates the length of the screw in mm. The test specimens are shown in Figure 6-1. 8 mm diameter screws were installed in 80x160 mm (width and length) glulam and 160x170 mm CLT, as shown in the top row of Figure 6-1. On the other hand, 13 mm diameter screws were installed in 130x260 mm glulam and 260x270 mm CLT, as seen in the bottom row of Figure 6-1.

The manufacturer provided 80x160 mm glulam was three-layered, while 130x260 mm glulam had four layers, and both the 160x170 mm and 260x270 mm CLT were three-layered. Two CLT samples were joined by gluing on the wide face to achieve the adequate thickness of the samples required for installing the 13 mm diameter screw at 10d penetration length in the 260x270 mm CLT. A single-component polyurethane glue with a glue rate of 160 g/m^2 was applied to the samples. The samples were then pressed in a compression testing machine with a pressure of 110 psi for 2 hours.

The CLT and glulam were conditioned in two separate stages. The two-stage conditioning was performed chronologically: achieving the initial target equilibrium moisture content (EMC) – screw installation – conditioning to reach the final EMC. The two-stage conditioning process was adopted to simulate the condition that the moisture content of timber members might change after screw installation in practical settings. In other words, the two-stage conditioning process was used to represent the condition that the moisture content of the timber during screw installation and pull-out of the screw might be different. The timber products were conditioned in three different conditioning chambers to achieve 12%, 16%, and 21% target EMC. On the other hand, the products were wholly immersed in water for three weeks to reach a fully saturated condition (fibre saturation point of wood). Though the actual moisture content in the fully saturated condition was not determined in the test program, the fully saturated condition moisture content is assumed to be close to 30% (Ross & USDA Forest Service., 2010).

The test matrix for the withdrawal test detailing the initial and final conditioning stage EMC (conditioning settings) and the type of timber product used for each test configuration is mentioned in Table 6-1. In Table 6-1, specimens of EMC condition no. 1-4 were conditioned under constant EMC before and after screw installation. On the other hand, the specimens of EMC condition no. 5-7 were conditioned at one EMC before screw installation and at a different EMC after screw installation. As discussed in chapter 8, the test results of the constant moisture content conditioning specimens (EMC conditions no. 1-3) are used as input properties in the numerical model. The screws were inserted perpendicular to the wood's grain direction on the samples' wide face (Figure 6-1). The screws were installed at the centre of the wide face of each glulam specimen. For CLT specimens, the screws were placed near the mid-point of each layer's middle laminate, which ensured the screws did not penetrate through the edge gaps between adjacent laminates of each layer. The minimum edge distance requirements for wood screws were satisfied according to the CSA O86-19 (Canadian Standards Association, 2019) standard. For each test configuration, six specimens were allocated.

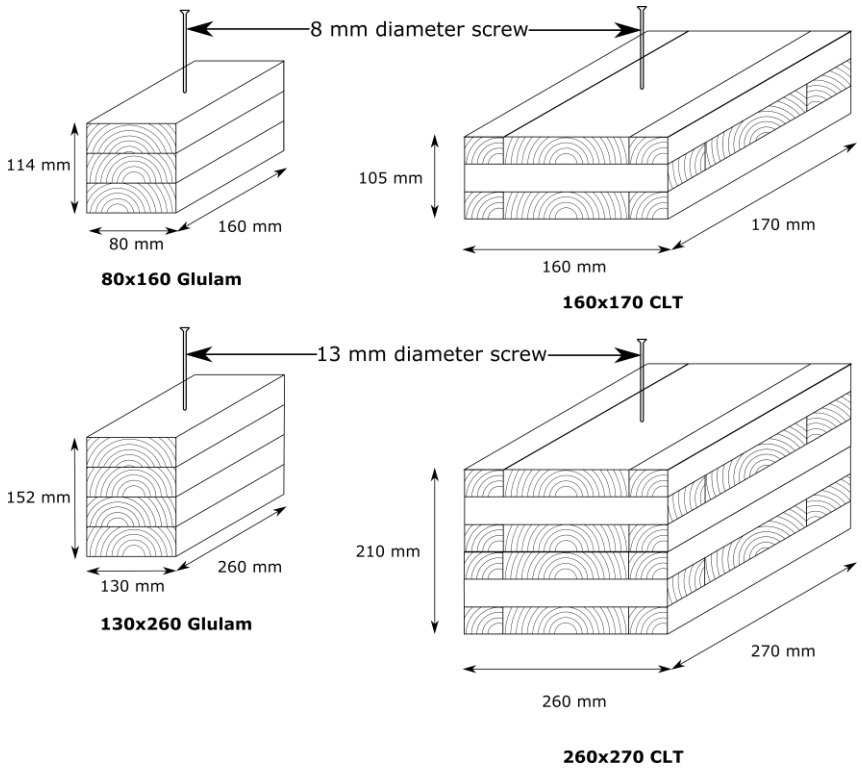

Figure 6-1: CLT and glulam samples with 8 mm screw (top row) and 13 mm screw (bottom row) – 10d penetration length (figure not to scale)

Table 6-1: Withdrawal test matrix

Screw Diameter	Mass Timber Product	EMC Condition No.	Initial Target EMC	Final Target EMC	Number of Specimens
8 mm	160 mm x 170 mm SPF CLT	1	12%	12%	6
		2	16%	16%	6
		3	21%	21%	6
		4	Saturation	Saturation	6
		5	12%	21%	6
		6	12%	Saturation	6
		7	21%	12%	6
	80 mm x 160 mm D.Fir Glulam	1	12%	12%	6
		2	16%	16%	6
		3	21%	21%	6
		4	Saturation	Saturation	6
		5	12%	21%	6
		6	12%	Saturation	6
		7	21%	12%	6
13 mm	260 mm x 270 mm SPF CLT	1	12%	12%	6
		2	16%	16%	6
		3	21%	21%	6
		4	Saturation	Saturation	6
		5	12%	21%	6
		6	12%	Saturation	6
		7	21%	12%	6
	130 mm x 260 mm D.Fir Glulam	1	12%	12%	6
		2	16%	16%	6
		3	21%	21%	6
		4	Saturation	Saturation	6
		5	12%	21%	6
		6	12%	Saturation	6
		7	21%	12%	6

The samples were conditioned in different conditioning chambers to achieve the target EMCs. The conditioning chambers' relative humidity and temperature settings to achieve the target EMCs are mentioned in Table 6-2. The specimens were conditioned for at least three months in each conditioning stage until a constant weight was achieved, indicating uniform moisture content distribution inside the sample.

Table 6-2: Conditioning chamber settings

Conditioning Chamber No.	Relative Humidity (%)	Temperature (ºC)	EMC
1	65 ± 2	20	12%
2	80 ± 2	20	16%
3	92 ± 2	20	21%

Screws were installed into the samples when they reached a constant weight in the first conditioning stage. For ease of installing screws, pilot holes of diameter 0.5d were drilled in the specimen before the actual screw installation (reducing the torque requirement for installation). The samples were quickly put back in the conditioning chamber for the second conditioning stage when the screw installation was complete to minimize moisture loss to the atmosphere. When the samples reached a constant weight in the second conditioning stage, they were taken out of the conditioning chambers and tested. The inside of a conditioning chamber with CLT and glulam samples is shown in Figure 6-2. It is to be noted that the actual moisture content of the specimens during withdrawal tests was not determined due to the large number of samples, and the target EMC of the conditioning chamber was taken as the moisture content of the specimens.

Figure 6-2: Conditioning of samples in a conditioning chamber

The test setup schematic used for the withdrawal test is exhibited in Figure 6-3. Figure 6-4 shows the test setup with a trial specimen. The pull-push loading condition of the withdrawal test was adopted. In this loading condition, support was provided by a half-inch thick steel counter plate on the screw entrant side of the sample. Two square-shaped steel hollow structural sections supported the counter plate (HSS 3"×3"×3/8") attached to the base plate by four fully threaded steel rods (Figures 6-3 and 6-4). An ad-hoc adapter was prepared using another square-shaped steel hollow structural section (HSS 5"×5"×0.5") of 88.9 mm length with extension arms to hold two LVDT transducers. The tips of the LVDT transducers were supported on the top surface of the steel counter plate. A small half-inch steel bearing plate was used to anchor the head of the screw inside the adapter. The top of the adapter was attached to the machine head, which pulled the screw in tension. The LVDT transducers measured the relative displacement between the top of the screw head and the steel counter plate. The steel counter plate was sufficiently rigid to counteract bending deflections due to the tensile load exerted by the machine head, which was verified by structural analysis.

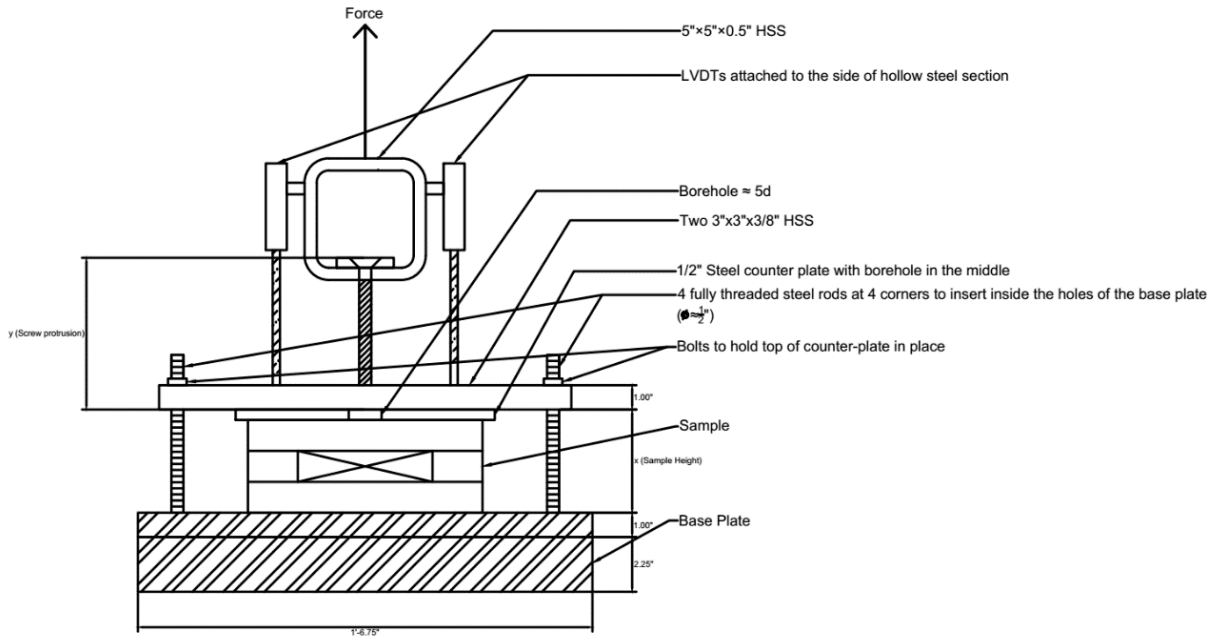

Figure 6-3: Withdrawal test setup schematic

The withdrawal tests were performed to reach the maximum load within 90 ± 30 s according to the standard BS EN 1382-99 (European Committee for Standardization, 1999). The withdrawal strength of the screws was determined with the following equation:

Equation 6-1

$$f_{ax} = \frac{F_{max}}{\pi d L_{eff}} \ [\mathrm{N/mm^2}]$$

Here, F_{max} is the maximum applied load as measured by the machine head, d is the outer thread diameter of the screw, L_{eff} is the effective penetration length of the screw inside the sample. The effective penetration length of the screw excludes the length of the tip of the screw, which is not fully effective in imparting withdrawal resistance. The effective penetration length was determined according to the screw manufacturer's guide.

Equations 6-2 and 6-3 determined the withdrawal displacement (w) of the screw. In equation 6-2, the elongation of the free part of the screw is subtracted to get the actual value of the withdrawal displacement of the screw inside the wood.

Equation 6-2

$$w = \frac{\delta_1 + \delta_2}{2} - \frac{\sigma_{core}}{E} l_{pro-screw}$$

Equation 6-3

$$\sigma_{core} = \frac{F_{applied}}{\frac{\pi}{4} {d_{core}}^2}$$

Here, δ_1 and δ_2 are the displacements recorded by the LVDT transducers, $l_{pro-screw}$ is the length of screw protrusion (Figure 6-3), E is Young's modulus of the material of the screw (determined in chapter 3), $F_{applied}$ is the applied load at each data point, d_{core} is the inner core diameter of the screw. The inner core diameter of the screw has been used here based on the premise that the screw core provides the axial rigidity of the protruded part. The effective length (based on screw manufacturers' guide) and the length of screw protrusion for the different screws used in the test program are given in Table 6-3.

Table 6-3: Self-tapping screw specifications

Product	Penetration Length (mm)	L_{eff} (mm)	$l_{pro-screw}$ (mm)
VGS 13x200	130 (10d)	120	55
ASSY VG 8x160	80 (10d)	72	72

The applied force and the corresponding withdrawal displacement using equation 6-2 were used to plot the load-displacement curve for each specimen. From the load-displacement curve, the withdrawal stiffness was calculated according to the following formula:

Equation 6-4

$$k_{ser} = \frac{K_{ser}}{\pi d L_{eff}} \ [\mathrm{N/mm^3}]$$

Here, K_{ser} is the slope of the linear fit-line between 10-40% of the maximum load of the load-displacement curve, and the other terms are as explained before.

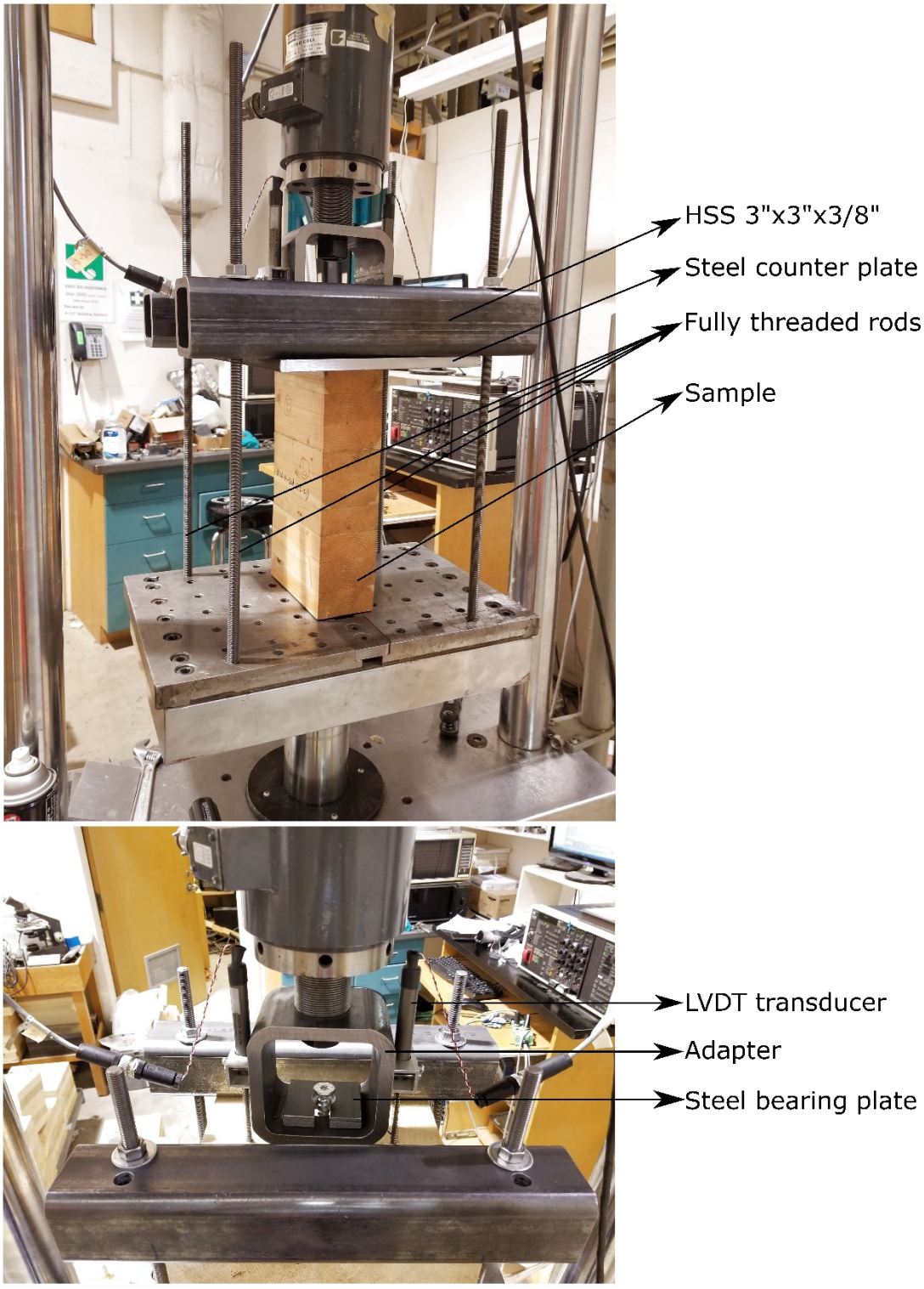

Figure 6-4: Withdrawal test setup

6.3 Results and Discussion

6.3.1 Typical Load-displacement Curves

The load-displacement data were recorded from the readings of the machine actuator, the LVDT transducers and the use of equation 6-2, as discussed in the previous section. A typical load-displacement curve from the withdrawal test is shown in Figure 6-5. The slope of the red line in the figure was determined to get the value of the initial linear portion of the load-displacement curve, which gives the value of K_{ser} in equation 6-4. The load-displacement curves of all tested specimens are included in Appendix B.

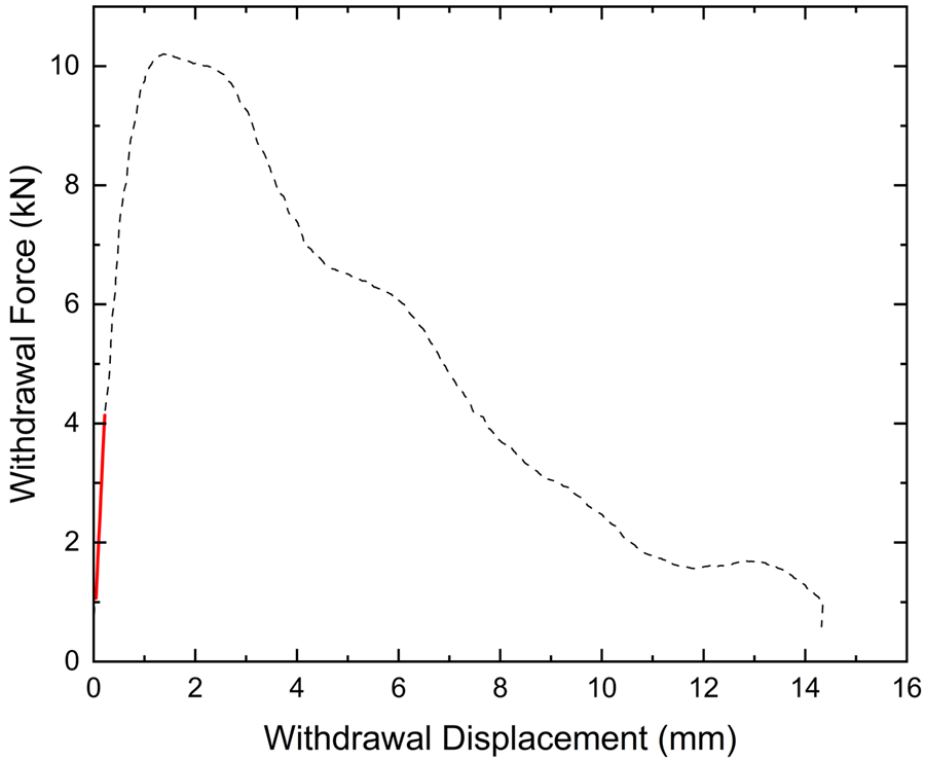

Figure 6-5: Typical load-displacement curve

6.3.2 Withdrawal Strength and Stiffness Trend

The withdrawal strength and stiffness were determined from the load-displacement data according to the methods outlined in section 6.2. The results of the withdrawal test are summarized in Table 6-4. The EMC of the CLT and glulam before and after screw installation is indicated in the 'Moisture Content Change' column. The constant moisture conditions suggest that the first and second stage conditioning moisture content was the same (EMC conditions no. 1-4). 'Sat' condition

in the table represents the fully saturated condition of the sample, which is usually higher than 21% moisture content. The test specimens with differing moisture contents in the two conditioning stages are indicated by the first and second stage conditioning moisture contents (EMC conditions no. 5-7).

The mean withdrawal stiffness and strength of the samples have been graphically compared in Figures 6-6 and 6-7. It was observed that the withdrawal stiffness of almost all the specimens with constant moisture content before and after screw installation decreased with the increase in the moisture content. The only exceptions were the glulam with 8 mm diameter screw at 16% moisture content and the glulam with 13 mm diameter screw at fully saturated moisture condition. The withdrawal stiffness also decreased with the increase in the difference between the moisture conditions between the two conditioning stages (12% - 21% and 12% - Sat), except for glulam with 8 mm diameter screw and 12% - Sat moisture conditions. Besides, from the withdrawal stiffness data trend, it was seen that wetting (12% - 21% and 12% - Sat) has an overall effect of a decrease of the withdrawal stiffness while drying (21% - 12%) increases the withdrawal stiffness.

Table 6-4: Withdrawal properties

Screw Diameter	Mass Timber Product	EMC Condition No.	Moisture Content Change	Withdrawal Stiffness (N/mm^3)		Withdrawal Strength (N/mm^2)	
				Mean	COV	Mean	COV
8 mm	160 mm x 170 mm SPF CLT	1	12% Constant	12.63	10.92	9.39	10.01
		2	16% Constant	10.33	38.35	7.19	13.81
		3	21% Constant	7.73	25.06	6.45	12.38
		4	Sat Constant	7.07	29.12	5.64	6.23
		5	12% → 21%	8.05	18.42	6.13	6.57
		6	12% → Sat	6.93	21.34	5.08	11.81
		7	21% → 12%	9.14	13.48	8.40	8.10
	80 mm x 160 mm D.Fir Glulam	1	12% Constant	10.73	24.67	9.31	13.84
		2	16% Constant	11.23	12.52	9.13	12.15
		3	21% Constant	9.62	10.82	7.71	11.97
		4	Sat Constant	8.46	18.32	5.67	12.51
		5	12% → 21%	7.40	12.44	6.26	4.89
		6	12% → Sat	8.20	9.59	6.49	18.85
		7	21% → 12%	10.15	28.82	8.50	8.36
13 mm	260 mm x 270 mm SPF CLT	1	12% Constant	4.51	23.18	6.18	11.55
		2	16% Constant	4.33	19.73	6.04	11.55
		3	21% Constant	3.17	10.29	4.72	11.06
		4	Sat Constant	2.77	19.91	4.04	9.61
		5	12% → 21%	2.71	17.88	4.74	11.83
		6	12% → Sat	2.29	26.13	3.68	16.00
		7	21% → 12%	3.55	21.86	5.60	9.65
	130 mm x 260 mm D.Fir Glulam	1	12% Constant	5.33	24.09	8.83	4.32
		2	16% Constant	4.60	22.10	7.13	5.75
		3	21% Constant	4.17	20.12	5.64	5.13
		4	Sat Constant	4.21	18.26	5.47	8.49
		5	12% → 21%	4.21	6.13	6.24	4.70
		6	12% → Sat	2.74	14.59	4.77	8.06
		7	21% → 12%	5.26	22.52	7.89	7.29

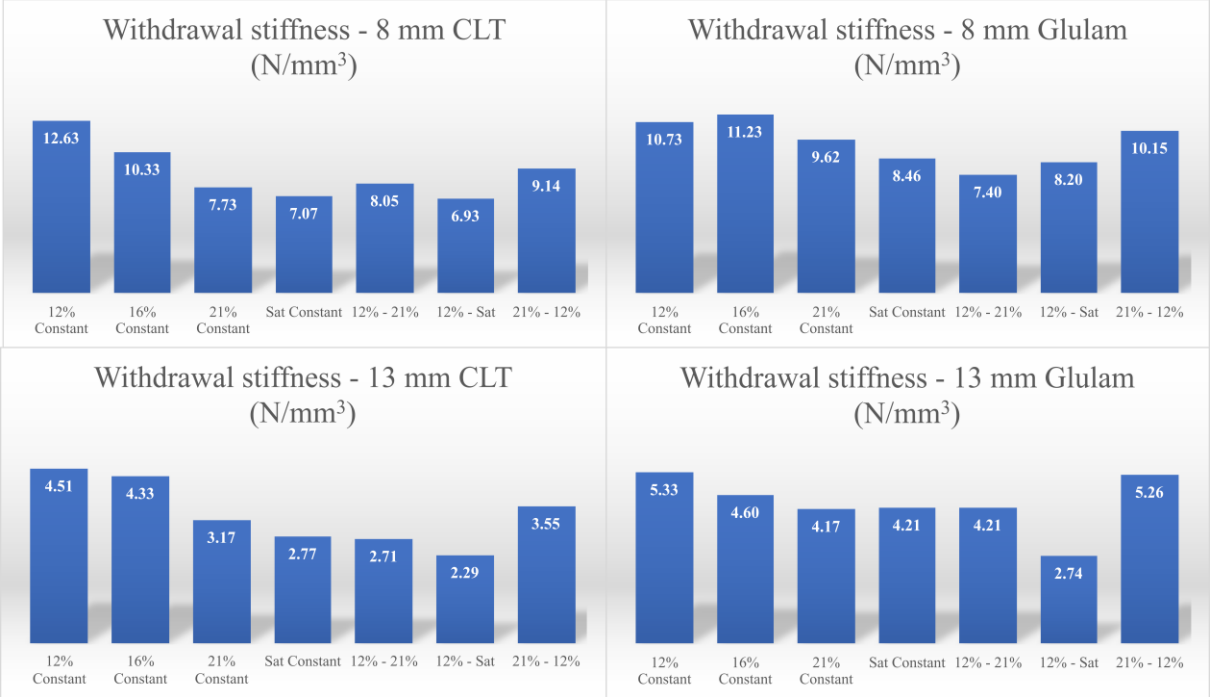

Figure 6-6: Average withdrawal stiffness comparison (6 samples in each condition)

The withdrawal strength of all samples with constant moisture content before and after screw installation decreased with the increase in the moisture content. The withdrawal strength also decreased with the increase in the difference between the moisture conditions between the two conditioning stages (12%-21% and 12%-Sat), except for glulam with 8 mm diameter screw and 12%-Sat moisture conditions. Like the withdrawal stiffness, wetting has an overall effect of decreasing the withdrawal strength, while drying increases the withdrawal strength. The variability (COV) of the withdrawal strength was lower than the withdrawal stiffness.

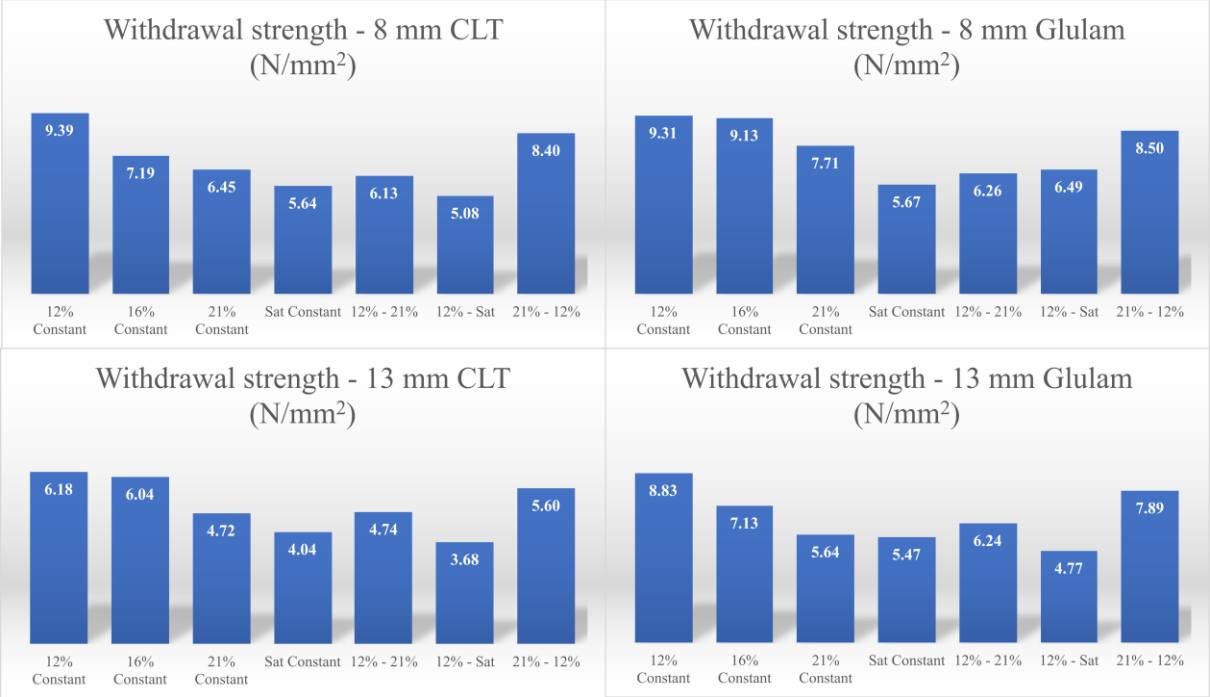

Figure 6-7: Average withdrawal strength comparison (6 samples in each condition)

6.3.3 Withdrawal Strength Modelling

A linear model describing the relationship between the withdrawal strength and moisture content was determined by the least-squares method, similar to the approach adopted by Ringhofer et al. (2014), which is shown in Figure 6-8. The withdrawal strength data of 12%, 16% and 21% constant EMC conditioning specimens (EMC conditions no. 1-3, Table 6-1) were utilized in deriving the relationship. The following equation gives the linear model:

Equation 6-5

$$f_{ax,mc} = f_{ax,12}\big(1 - k_{mc}(u - 12)\big) \text{ for } 12\% \leq u \leq 21\%$$

Here, $f_{ax,mc}$ is the withdrawal strength at a given moisture content, $f_{ax,12}$ is the withdrawal strength at 12% moisture content, which is the reference point. k_{mc} is an adjustment factor that accounts for the decrease in withdrawal strength at a moisture content between 12% and 21%, and u is the moisture content in the wood member. The moisture adjustment factor determined from the test is given in Table 6-5.

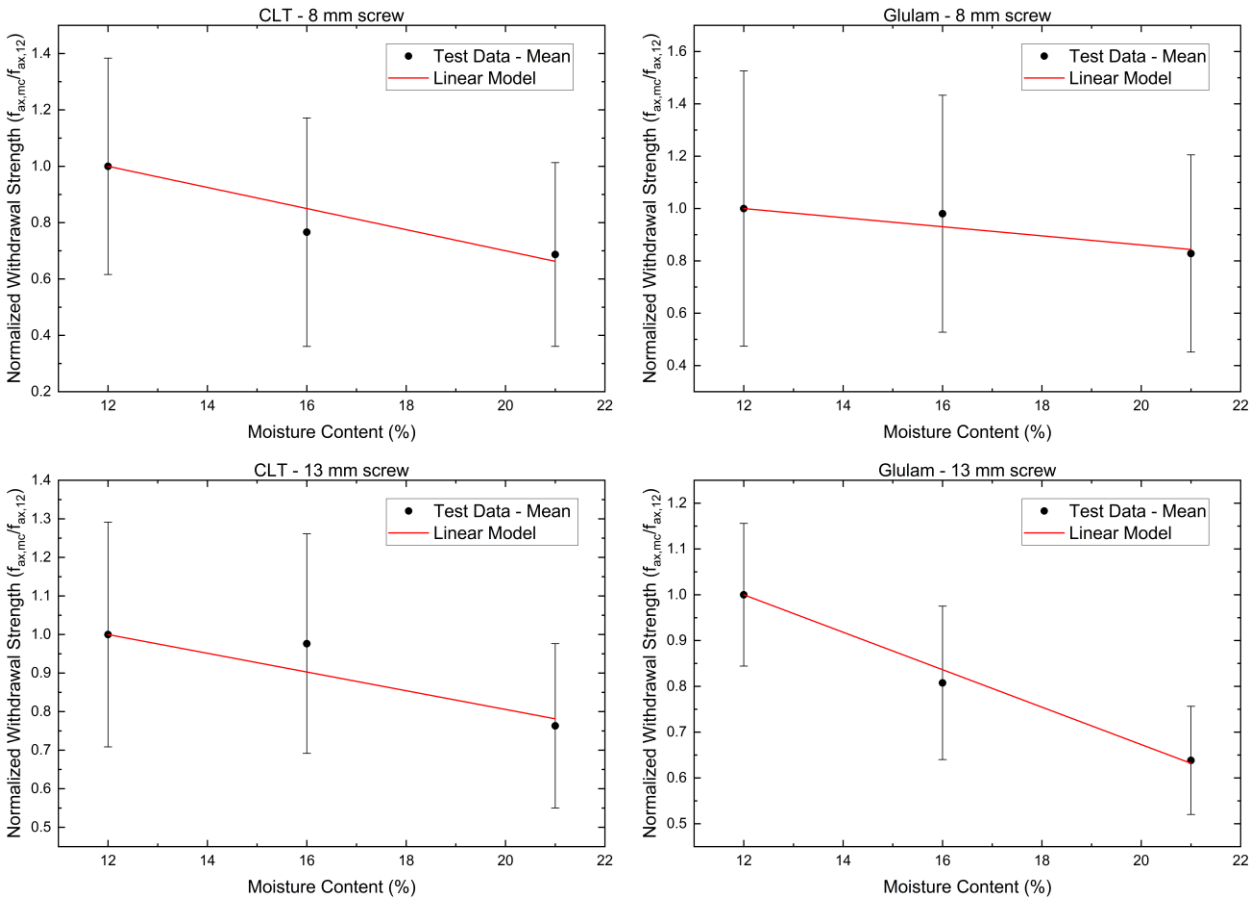

Figure 6-8: Linear model of the withdrawal strength and moisture content relationship

Table 6-5: Moisture adjustment factors

Screw diameter	Mass timber product	k_{mc}
8 mm	160 mm x 170 mm SPF CLT	0.038
	80 mm x 160 mm D.Fir Glulam	0.017
13 mm	260 mm x 270 mm SPF CLT	0.024
	130 mm x 260 mm D.Fir Glulam	0.041

The value of the moisture adjustment factor found for European CLTs for an 8 mm diameter self-tapping screw was 0.02 (Silva et al., 2016) and 0.017 (Ringhofer et al., 2014)., while for European glulam for an 8 mm diameter self-tapping screw was 0.0065 (Pirnbacher et al., 2009).

Pirnbacher et al. (2009) found that the withdrawal strength of self-tapping screws in European solid timber and glulam decreases by 5% on average when the moisture content of the wood increases from 12% to 20%. The average decrease in withdrawal strength for the different

specimen groups when the moisture content of the wood increased from 12% to 21% is shown in Table 6-6. The withdrawal strength decrease was found by comparing the withdrawal strength of specimen conditioned at a constant 12% EMC (EMC condition no. 1, Table 6-1) and a constant 21% EMC (EMC condition no. 3, Table 6-1). It can be seen that the decrease in withdrawal strengths of self-tapping screws in Canadian glulam and CLT are a lot higher than that of European solid timber and glulam.

Table 6-6: Decrease in withdrawal strength

Screw Diameter	Mass Timber Product	Moisture Content Change	Decrease in Withdrawal Strength (%)
8 mm	160 mm x 170 mm SPF CLT	12% → 21%	31.3
	80 mm x 160 mm D.Fir Glulam	12% → 21%	17.18
13 mm	260 mm x 270 mm SPF CLT	12% → 21%	23.68
	130 mm x 260 mm D.Fir Glulam	12% → 21%	36.16

In deriving the withdrawal strength and moisture content relationship, the withdrawal strength data at the saturated moisture condition was not utilized since the actual moisture content of the specimens at the saturated condition was not measured.

6.4 Summary

This chapter investigated the withdrawal properties (withdrawal strength and stiffness) of self-tapping screws of outer nominal diameters of 8 mm and 13 mm, inserted into two types of CLT and glulam products. The withdrawal properties will be the input parameters in the numerical and analytical models of self-tapping screw stress distribution under varying moisture conditions. Moreover, the properties presented here are the first attempt at documenting the withdrawal properties of self-tapping screws in Canadian CLT and glulam products under varying moisture conditions.

7 ANALYTICAL MODEL OF SELF-TAPPING SCREW STRESS DISTRIBUTION

7.1 Introduction

An analytical model to predict the stress distribution in a self-tapping screw installed in a wood member under the application of axial load and moisture swelling of wood is proposed in this chapter. The stress distribution arising from the two mechanisms, load application and wood swelling, are found separately and superimposed to get the overall stress distribution. The analytical model can predict the stress distribution along the axis of a self-tapping screw when loaded axially and the moisture content changes in the wood member, triggering swelling or shrinkage. A key to understanding the premature failure mechanism of self-tapping screws is to model the stress distribution of the screws analytically.

The moisture content change is considered uniform throughout the wood member in the proposed analytical model. The analytical model focuses on wood members made of glulam and CLT. This analytical model lays the foundation for developing a more sophisticated model for non-uniform moisture content change throughout the wood member. The principles of chapter 4 can be utilized to model the non-uniform moisture content change distribution in the wood member.

This chapter focuses on wood members made from CLT and glulam. However, the analytical model developed here also applies to wood members made of solid lumber and GLT.

The proposed analytical model falls under the domain of linear elastic stress analysis. The model described here is an extension of the work done by Taylor & Yuan (1962), Jensen et al. (2001) and Stamatopoulos & Malo (2016). These theories are based on applying the classical Volkerson (1938) theory to axially loaded fasteners.

An axially loaded self-tapping screw embedded in a wood member under pull-push loading conditions is presented on the left of Figure 7-1. The top of a wood member is held down in this loading condition while the screw is pulled in axial tension. The pull-push loading condition is analogous to a two-member wood-to-steel or wood-to-wood connection with a self-tapping screw, where the side member is sufficiently rigid to provide support at the top surface of the main wood member (Figure 7-2). Thus, if the stress distribution under the pull-push loading condition is

known, the stress distribution of the screw in a wood-to-steel or wood-to-wood connection can be determined.

In the analytical model proposed here, under the action of an axial load on the screw, it is assumed that pure axial stress arises in the screw and the wood surrounding the screw in the x-direction. Force transfer between the screw and the wood occurs through a shear layer of finite dimensions. The shear layer is situated in the interface between the wood and the outer threaded part of the screw. In reality, the shear layer and the wood overlap (Jensen et al., 2001). The shear layer is assumed to be in a state of pure shear. Considering the wood and the screw being under pure axial stress implies that they are more rigid to deformation than reality. This will result in the calculated value of shear stress of the shear layer being higher than the actual value. Thus, this value can be considered an upper limit and conservative during design situations.

7.2 Differential Equation Solution for Pull-push Withdrawal Load

A differential section of length dx of the wood-screw interaction zone is considered on the right of Figure 7-1. The coordinate system origin for the model is taken at the entrant side of the screw in the wood member.

When the screw is pulled in axial tension from the wood member, the whole length of the screw is not effective in imparting pull-out resistance to the screw due to the tapering geometry of the screw at the tip. The effective penetration length (Figure 7-1, L_{eff}) of the screw excludes the tip of the screw and is taken as the effective screw length that is effective in imparting pull-out resistance in the analytical model. The effective penetration length of the screw can be determined following the screw manufacturer's guide.

The displacement of the shear layer due to an axial load (P) is given by:

Equation 7-1

$$\delta(x) = \delta_s(x) - \delta_w(x)$$

Here, $\delta(x)$ is the displacement of the shear layer, $\delta_s(x)$ is the displacement of the screw and $\delta_w(x)$ is the displacement of the wood. The shear layer's geometric non-linearity is disregarded in the analytical model.

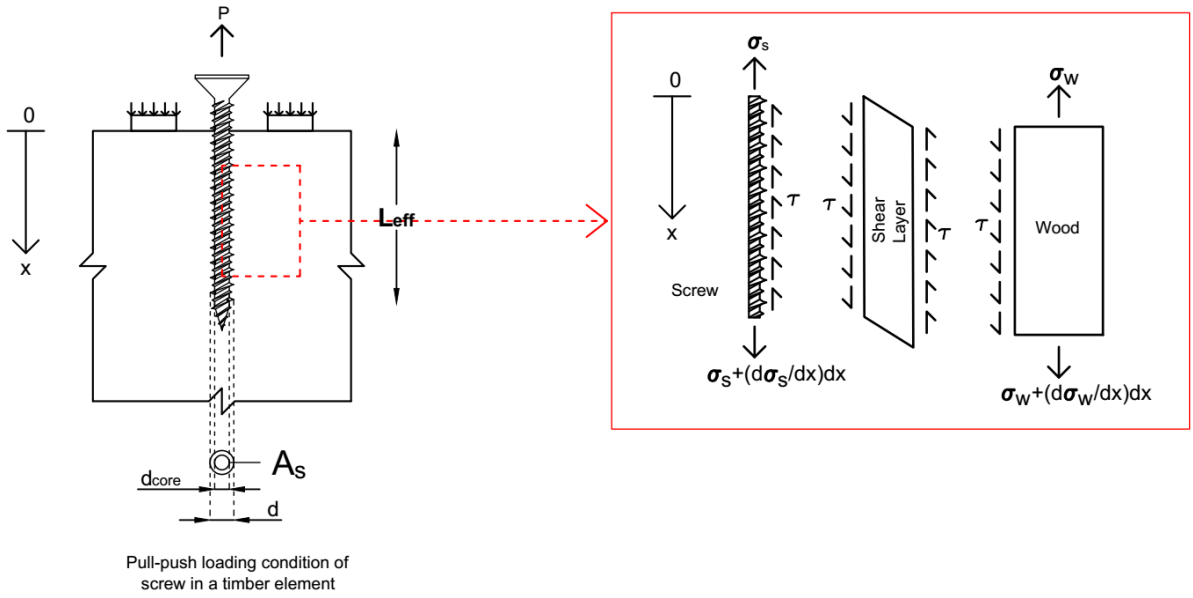

Figure 7-1: Wood-screw system and wood-screw interaction (only one critical section shown)

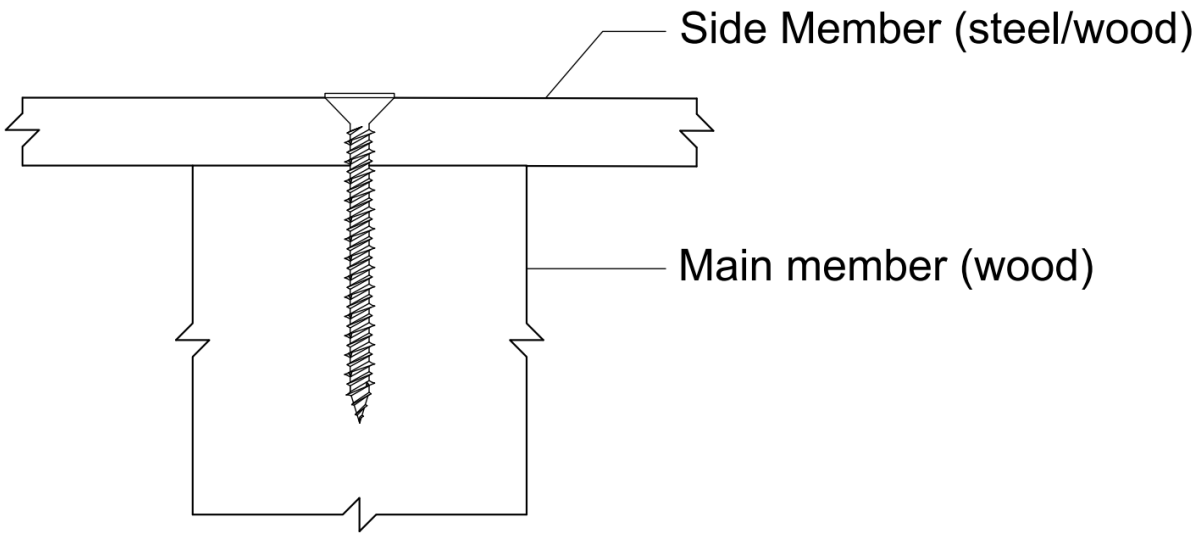

Figure 7-2: Two-member self-tapping screw connection

The thickness of the shear layer is neglected, and a linear model describes the constitutive relation of the shear layer:

Equation 7-2

$$\tau(x) = \Gamma_e \delta(x)$$

Here, $\tau(x)$ is the shear stress and Γ_e is the equivalent shear stiffness parameter of the shear layer. The 'e' subscript in the equivalent shear stiffness parameter signifies that the linear-elastic domain of the model is considered.

The static equilibrium conditions of the differential equation lead to the following equation for the screw and wood, respectively:

Equation 7-3

$$\frac{d\sigma_s(x)}{dx} = \frac{\pi d_{core} \tau(x)}{\pi \frac{{d_{core}}^2}{4}} = \frac{4}{d_{core}} \tau(x)$$

Equation 7-4

$$\frac{d\sigma_w(x)}{dx} = -\frac{\pi d_{core}}{A_{w,eff}} \tau(x)$$

Here, $\sigma_s(x)$ is the stress in the screw, $\sigma_w(x)$ is the stress in the wood, d_{core} is the inner core diameter of the screw (excluding screw thread), and $A_{w,eff}$ is the effective area of wood under pure axial stress under the pull-push loading conditions. The effective area of wood is given by Stamatopoulos & Malo (2016), assuming a 3:1 load distribution from the top surface of the wood member.

Equation 7-5

$$A_{w,eff} = 2b \left\{ s_s + min\left(e, \frac{L_{eff}}{6}\right) + min\left(\frac{s}{2}, \frac{L_{eff}}{6}\right) \right\}$$

Here, b is the width of the wood member, s_s is the length of the support at the top surface of the wood member, e is the edge distance from the end of the support, and s is the distance between the supports (Figure 7-3). For a wood-to-steel or wood-to-wood connection, as shown in Figure 7-2, $A_{w,eff}$ is the area of the whole top surface of the main wood member.

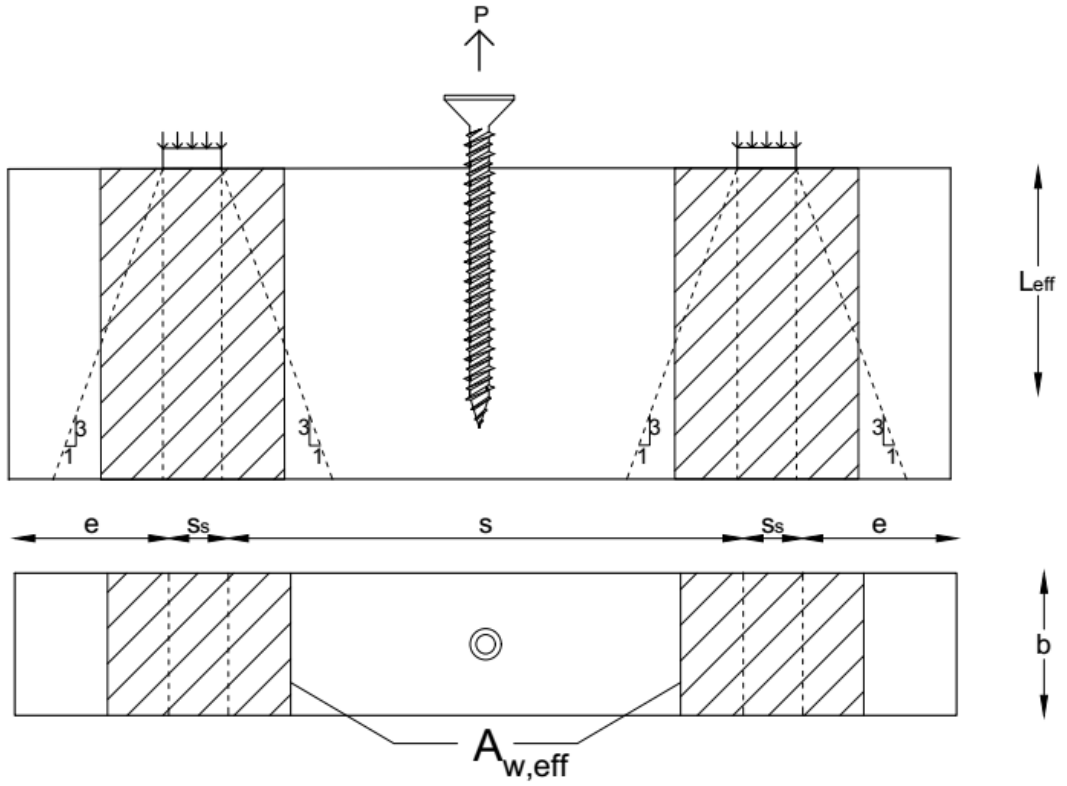

Figure 7-3: Determination of $A_{w,eff}$ (top) side view and (bottom) plan view

Successive differentiation of equation 7-1 lead to the following equations:

Equation 7-6

$$\frac{d\delta(x)}{dx} = \frac{d\delta_s(x)}{dx} - \frac{d\delta_w(x)}{dx} = \varepsilon_s(x) - \varepsilon_w(x)$$

Equation 7-7

$$\frac{d^2\delta(x)}{dx^2} = \frac{d\varepsilon_s(x)}{dx} - \frac{d\varepsilon_w(x)}{dx}$$

Here, $\varepsilon_s(x)$ and $\varepsilon_w(x)$ are the strains in the screw and wood respectively which are related to the stresses by Hooke's law as follows:

Equation 7-8

$$\varepsilon_s(x) = \frac{\sigma_s(x)}{E_s}$$

Equation 7-9

$$\varepsilon_w(x) = \frac{\sigma_w(x)}{E_w}$$

E_s and E_w are the Young's modulus of the screw and the wood in the x-direction. By proper substitutions and manipulations of equations 7-1 to 7-9, the following governing differential equation can be derived:

Equation 7-10

$$\frac{d^2\delta(x)}{dx^2} - \left(\frac{\omega}{L_{eff}}\right)^2 \delta(x) = 0$$

Here, the parameters ω and β are defined as (Stamatopoulos & Malo, 2016):

Equation 7-11

$$\omega = \sqrt{\pi d_{core} \Gamma_e \beta {L_{eff}}^2}$$

Equation 7-12

$$\beta = \frac{1}{A_s E_s} + \frac{1}{A_{w,eff} E_w}$$

$A_s = \left(\frac{\pi}{4} \times {d_{core}}^2\right)$ is the inner core area of the screw.

Now, the general solution of equation 7-10 is given by:

Equation 7-13

$$\delta(x) = c_1 e^{\frac{\omega x}{L_{eff}}} + c_2 e^{-\frac{\omega x}{L_{eff}}}$$

Differentiation of equation 7-13 and substitution from equation 7-6 leads to:

Equation 7-14

$$\frac{d\delta(x)}{dx} = \frac{\omega}{L_{eff}}\left(c_1 e^{\frac{\omega x}{L_{eff}}} - c_2 e^{-\frac{\omega x}{L_{eff}}}\right) = \varepsilon_s(x) - \varepsilon_w(x)$$

c_1 and c_2 are constants in the equation 7-14, which can be determined by proper boundary conditions.

Boundary conditions for the pull-push loading configuration are (Figure 7-4):

Equation 7-15

$$\text{At x} = 0, \varepsilon_s = \frac{P}{E_s A_s}\ (\text{Tension}), \varepsilon_w = -\frac{P}{E_w A_{w,eff}}\ (\text{Compression})$$

Equation 7-16

$$\text{At x} = L_{eff}, \varepsilon_s = 0, \varepsilon_w = 0$$

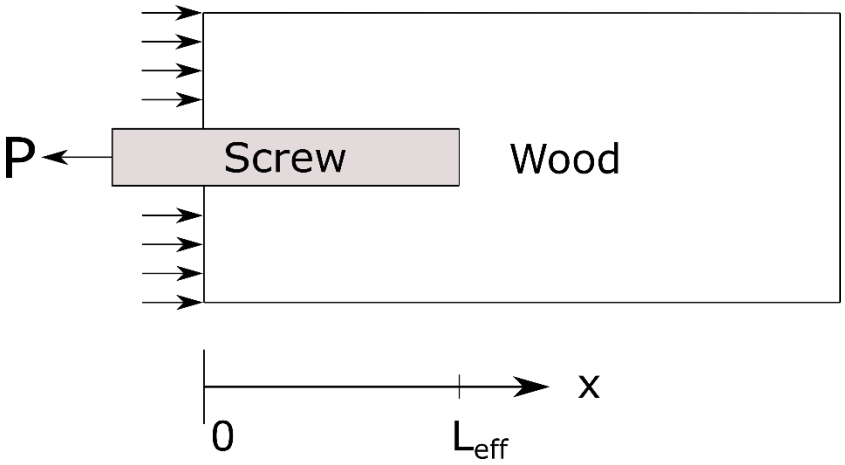

Figure 7-4: Pull-push boundary conditions

Using boundary conditions 7-15 and 7-16 in equation 7-14, the value of the constants c_1 and c_2 are determined as:

Equation 7-17

$$c_1 = \frac{P\beta L_{eff} e^{-\omega}}{\omega(e^{-\omega} - e^{\omega})}, c_2 = \frac{P\beta L_{eff} e^{\omega}}{\omega(e^{-\omega} - e^{\omega})}$$

Substituting the values of the constants in equation 7-13 gives the displacement function of the shear layer:

Equation 7-18

$$\delta_1(x) = \frac{-P}{\pi d_{core} L_{eff} \Gamma_e} \frac{\omega}{\sinh \omega} \cosh\left(\omega\left(1 - \frac{x}{L_{eff}}\right)\right)$$

The shear stress of the shear layer is given by:

Equation 7-19

$$\tau_1(x) = \Gamma_e \delta_1(x) = \frac{-P}{\pi d_{core} L_{eff}} \frac{\omega}{\sinh \omega} \cosh\left(\omega\left(1 - \frac{x}{L_{eff}}\right)\right)$$

The differential equation for screw stress distribution is given by equation 7-3:

Equation 7-3

$$\frac{d\sigma_{s_1}(x)}{dx} = \frac{4}{d_{core}} \tau_1(x)$$

The stress distribution in the screw at point x is given by rearrangement and integration of equation 7-3:

Equation 7-20

$$\sigma_{s_1}(x) = \int_0^x \frac{4}{d_{core}} \tau_1(x) dx = \frac{4P}{\pi {d_{core}}^2} \frac{\sinh\left(\omega\left(1 - \frac{x}{L_{eff}}\right)\right)}{\sinh \omega}$$

Equation 7-20 gives the stress distribution model inside the screw due to applying a load P on the screw under the pull-push loading condition. The "1" subscript in equations 7-18, 7-19 and 7-20 only signify the screw stress distribution under axial load. Equation 7-20 is a hyperbolic monotonic function whose maximum value occurs at x = 0.

7.3 Differential Equation Solution for Wood-swelling

The stress distribution of the screw due to a change of moisture content inside the wood member is proposed henceforth. An increase in moisture content will lead to wood swelling and contribute to the wood's total stress.

The material of the screw, steel, does not undergo any dimensional changes due to moisture content changes in wood. Though steel expands/contracts significantly due to changes in the temperature (Dietsch, 2017), the effect of temperature change is not a focus of this research.

Wood can deform freely in unrestrained conditions due to changes in moisture content. However, a self-tapping screw inserted into a wood member acts as a restraint due to the composite action

between the wood material and the thread of the screw. This is considered a case of restrained swelling condition of the wood member. Here, the restraint is provided by the screw and acts throughout its length. In the restrained swelling state, the additional contribution to the total stress in the wood member will lead to further stress distribution in the screw due to the composite action of the wood and screw.

Chen & Nelson (1979) conducted a study to determine the stress distribution in bonded materials induced by thermal expansion of the materials, which is analogous to the wood-screw composite system under moisture swelling. In light of this study, the shear stress distribution in the shear layer along the length of the screw will be symmetric about the mid-point along the length of the screw. For the analytical treatment of screw stress distribution due to wood swelling, the coordinate system of Figure 7-5 is considered. Two independent variables define the coordinate system, x_1 and x_2 to take advantage of the symmetric shear stress distribution and to simplify the stress distribution expressions.

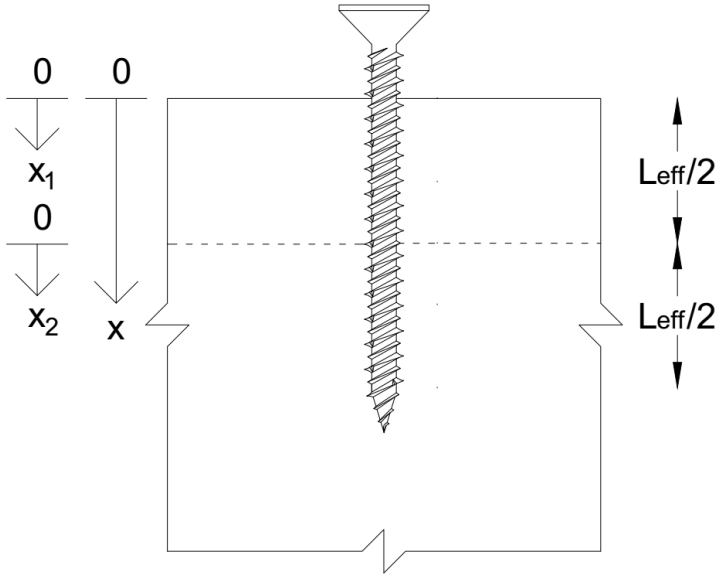

Figure 7-5: Coordinate system for wood swelling

The same assumption of pure axial stress in the screw and the wood surrounding the screw in the x-direction is considered (section 7-1). The moisture content change (Δu) is considered uniform throughout the wood member and along the length of the screw. If the swelling coefficient of

wood in the x-direction is α, under the uniform moisture content change, the strain of the shear layer is given by the following equation:

Equation 7-21

$$\frac{d\delta(x)}{dx} = \varepsilon_s(x) - \varepsilon_w(x) - \alpha\Delta u$$

Differentiation of equation 7-21 leads to:

Equation 7-22

$$\frac{d^2\delta(x)}{dx^2} = \frac{d\varepsilon_s(x)}{dx} - \frac{d\varepsilon_w(x)}{dx} = \frac{1}{E_s}\frac{d\sigma_s(x)}{dx} - \frac{1}{E_w}\frac{d\sigma_w(x)}{dx}$$

Now utilizing equations 7-2, 7-3 and 7-4, equation 7-22 can be rewritten as:

Equation 7-23

$$\frac{1}{\Gamma_e}\frac{d^2\tau(x)}{dx^2} = \left(\frac{4}{d_{core}E_s} + \frac{\pi d_{core}}{A_{w,eff2}E_w}\right)\tau(x)$$

Equation 7-24

$$\frac{d^2\tau(x)}{dx^2} - \left(\frac{4}{d_{core}E_s} + \frac{\pi d_{core}}{A_{w,eff2}E_w}\right)\Gamma_e\tau(x) = 0$$

Here, $A_{w,eff2}$ is the effective area of the wood under pure axial stress during wood swelling, which is different than the effective area of wood under pure axial stress under the pull-push loading conditions. The effective area represents the wood area that interacts with the screw thread during wood swelling. The additional stress exerted on the screw is assumed to be caused by the swelling stress of wood in this effective area. This area is given by taking a 3:1 stress distribution as in Stamatopoulos & Malo (2016), by equation 7-25 and Figure 7-6.

Equation 7-25

$$A_{w,eff2} = \frac{\pi}{2}\left(\left(\frac{L_{eff}}{6} + \frac{d}{2}\right)^2 - \left(\frac{d}{2}\right)^2\right)$$

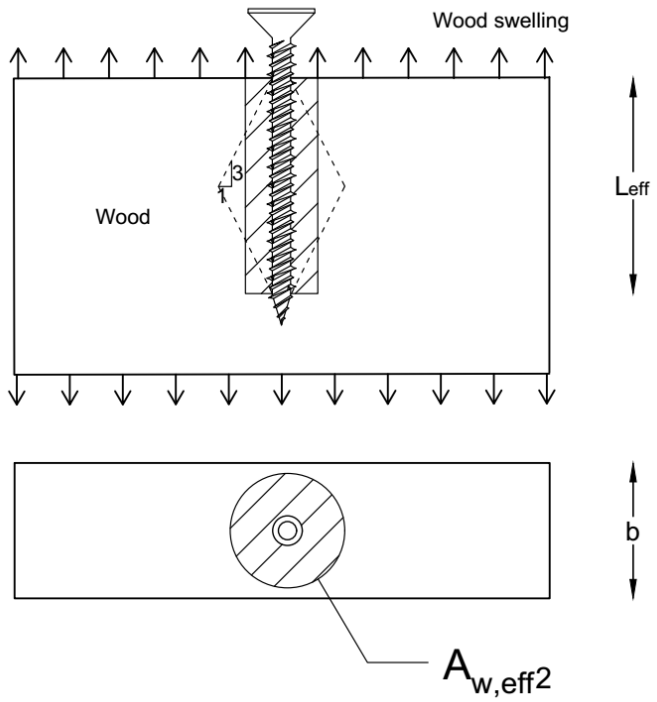

Figure 7-6: Determination of $A_{w,eff2}$ (top) side view and (bottom) plan view

Equation 7-24 is a second-order linear differential equation that can be simplified to :

Equation 7-26

$$\frac{d^2\tau(x)}{dx^2} - {K_s}^2\tau(x) = 0;\ \left[{K_s}^2 = \left(\frac{4}{d_{core}E_s} + \frac{\pi d_{core}}{A_{w,eff2}E_w}\right)\Gamma_e\right]$$

The highest shear stress will occur at the screw entrant side and near the end of the screw and will decrease exponentially to zero at the centre of the screw inside the wood member. The particular solution to equation 7-26, which describes this behaviour, is given by (Taylor & Yuan, 1962):

Equation 7-27

$$\tau_{1,swelling}(x_1) = c_3 e^{-K_s x_1};\ 0 \le x_1 \le \frac{L_{eff}}{2}$$

Equation 7-28

$$\tau_{2,swelling}(x_2) = c_4 e^{K_s(x_2 - L_{eff})};\ \frac{L_{eff}}{2} < x_2 \le L_{eff}$$

Here, c_3 and c_4 are constants that can be determined from the boundary conditions. Differentiation of equations 7-27 and 7-28 leads to:

Equation 7-29

$$\frac{d\tau_{1,swelling}(x_1)}{dx_1} = -K_s c_3 e^{-K_s x_1}$$

Equation 7-30

$$\frac{d\tau_{2,swelling}(x_2)}{dx_2} = K_s c_4 e^{K_s(x_2 - L_{eff})}$$

The boundary condition for the restrained wood swelling case are:

Equation 7-31

$$\text{At } x_1 = 0,\ \frac{d\tau_{1,swelling}(0)}{dx_1} = \Gamma_e \frac{d\delta_{1,swelling}(0)}{dx_1}$$

$$\Gamma_e \frac{d\delta_{1,swelling}(0)}{dx_1} = \Gamma_e(\varepsilon_s - \varepsilon_w - \alpha\Delta u) = \Gamma_e(0 - 0 - \alpha\Delta u) = -\alpha\Delta u\Gamma_e$$

Equation 7-32

$$\text{At } x_2 = L_{eff},\ \frac{d\tau_{2,swelling}(L_{eff})}{dx_2} = \Gamma_e \frac{d\delta_{2,swelling}(L_{eff})}{dx_2}$$

$$\Gamma_e \frac{d\delta_{2,swelling}(L_{eff})}{dx_2} = \Gamma_e(\varepsilon_s - \varepsilon_w - \alpha\Delta u) = \Gamma_e(0 - 0 - \alpha\Delta u) = -\alpha\Delta u\Gamma_e$$

Using boundary conditions 7-31 and 7-32 in equations 7-29 and 7-30, the values of the constants c_3 and c_4 are determined as:

Equation 7-33

$$c_3 = \frac{\alpha\Delta u\Gamma_e}{K_s}$$

Equation 7-34

$$c_4 = -\frac{\alpha\Delta u\Gamma_e}{K_s}$$

Substituting the values of the constants in equations 7-27 and 7-28 and using equation 7-2, the displacement and shear stress distribution function of the shear layer due to wood-swelling are:

Equation 7-35

$$\delta_{1,swelling}(x_1) = \frac{\alpha \Delta u}{K_s} e^{-K_s x_1}$$

Equation 7-36

$$\tau_{1,swelling}(x_1) = \frac{\alpha \Delta u \Gamma_e}{K_s} e^{-K_s x_1}$$

Equation 7-37

$$\delta_{2,swelling}(x_2) = -\frac{\alpha \Delta u}{K_s} e^{K_s(x_2 - L_{eff})}$$

Equation 7-38

$$\tau_{2,swelling}(x_2) = -\frac{\alpha \Delta u \Gamma_e}{K_s} e^{K_s(x_2 - L_{eff})}$$

Now, the differential equation for screw stress distribution is given by equation 7-3:

Equation 7-3

$$\frac{d\sigma_s(x)}{dx} = \frac{4}{d_{core}} \tau(x)$$

The stress distribution in the screw due to wood-swelling is given by re-organization and integration of equation 7-3:

Equation 7-39

$$\sigma_{s_{1,swelling}}(x_1) = \int \frac{4}{d_{core}} \tau_{1,swelling}(x_1) dx = -\frac{4\alpha \Delta u \Gamma_e}{d_{core} {K_s}^2} e^{-K_s x_1} + c_5$$

Equation 7-40

$$\sigma_{s_{2,swelling}}(x_2) = \int \frac{4}{d_{core}} \tau_{2,swelling}(x_2) dx = -\frac{4\alpha \Delta u \Gamma_e}{d_{core} {K_s}^2} e^{K_s(x_2 - L_{eff})} + c_6$$

Here, c_5 and c_6 are constants of integration which can be determined from the following boundary conditions:

Equation 7-41

$$\sigma_{s_{2,swelling}}(0) = 0 = -\frac{4\alpha\Delta u\Gamma_e}{d_{core}{K_s}^2} + c_5 = 0$$

Equation 7-42

$$c_5 = \frac{4\alpha\Delta u\Gamma_e}{d_{core}{K_s}^2}$$

Equation 7-43

$$\sigma_{s_{2,swelling}}(L_{eff}) = -\frac{4\alpha\Delta u\Gamma_e}{d_{core}{K_s}^2} + c_6 = 0$$

Equation 7-44

$$c_6 = \frac{4\alpha\Delta u\Gamma_e}{d_{core}{K_s}^2}$$

Thus the stress distribution in the screw is given by:

Equation 7-45

$$\sigma_{s_{1,swelling}}(x_1) = \frac{4\alpha\Delta u\Gamma_e}{d_{core}{K_s}^2}(1 - e^{-K_s x_1});\ 0 \le x_1 \le \frac{L_{eff}}{2}$$

Equation 7-46

$$\sigma_{s_{2,swelling}}(x_2) = \frac{4\alpha\Delta u\Gamma_e}{d_{core}{K_s}^2}\left(1 - e^{K_s(x_2 - L_{eff})}\right);\ \frac{L_{eff}}{2} < x_2 \le L_{eff}$$

7.4 Shear Stiffness Parameter Determination and Superposition of Stress Distribution

The unknown parameter in the model is the constant Γ_e, which is required to determine the constant ω given by equation 7-11

Equation 7-47

$$\omega = \sqrt{\pi d_{core} \Gamma_e \beta {L_{eff}}^2}$$

Setting $x = 0$ and ignoring the negative sign in equations 7-18 and 7-35 give the withdrawal displacements. The withdrawal displacement under withdrawal load is given by:

Equation 7-48

$$\delta_{withdrawal_1} = \frac{P\omega}{\pi d L_{eff} \Gamma_e} \frac{\cosh \omega}{\sinh \omega} = \frac{P}{\pi d L_{eff} \Gamma_e} \frac{\omega}{\tanh \omega}$$

The withdrawal displacement under wood swelling is given by:

Equation 7-49

$$\delta_{withdrawal_{1,swelling}} = \frac{\alpha \Delta u}{K_s} 1 = \frac{\alpha \Delta u}{K_s}$$

The withdrawal stiffness K_w is given by:

Equation 7-50

$$\mathrm{K}_w = \frac{P}{\delta_{withdrawal_1} + \delta_{withdrawal_{1,swelling}}}$$

Here, P is the axial load acting in the screw at $x = 0$.

$\delta_{withdrawal_1} \gg \delta_{withdrawal_{1,swelling}}$. Ignoring $\delta_{withdrawal_{1,swelling}}$ in equation 7-50, the withdrawal stiffness becomes,

Equation 7-51

$$\mathrm{K}_w = \frac{P}{\delta_{withdrawal_1}} = \pi d L_{eff} \Gamma_e \frac{\tanh \omega}{\omega}$$

The withdrawal stiffness K_w can be determined from the withdrawal test, and equation 7-51 can be solved to determine the value of Γ_e.

Finally, the stress distribution in the screw is given by the superimposition of equations 7-20, 7-45 and 7-46 as:

Equation 7-52

$$\sigma_s(x) = \sigma_{s_1}(x) + \sigma_{s_{1,swelling}}(x_1) = \frac{4P}{\pi {d_{core}}^2}\frac{\sinh\left(\omega\left(1-\frac{x}{L_{eff}}\right)\right)}{\sinh\omega} + \frac{4\alpha\Delta u\Gamma_e}{d_{core}{K_s}^2}(1-e^{-K_s x_1})$$

Equation 7-53

$$\sigma_s(x) = \sigma_{s_1}(x) + \sigma_{s_{2,swelling}}(x_2) = \frac{4P}{\pi {d_{core}}^2}\frac{\sinh\left(\omega\left(1-\frac{x}{L_{eff}}\right)\right)}{\sinh\omega} + \frac{4\alpha\Delta u\Gamma_e}{d_{core}{K_s}^2}\left(1-e^{K_s(x_2-L_{eff})}\right)$$

Where, $0 \le x_1 \le \frac{L_{eff}}{2}$, $\frac{L_{eff}}{2} < x_2 \le L_{eff}$ and $0 \le x \le L_{eff}$.

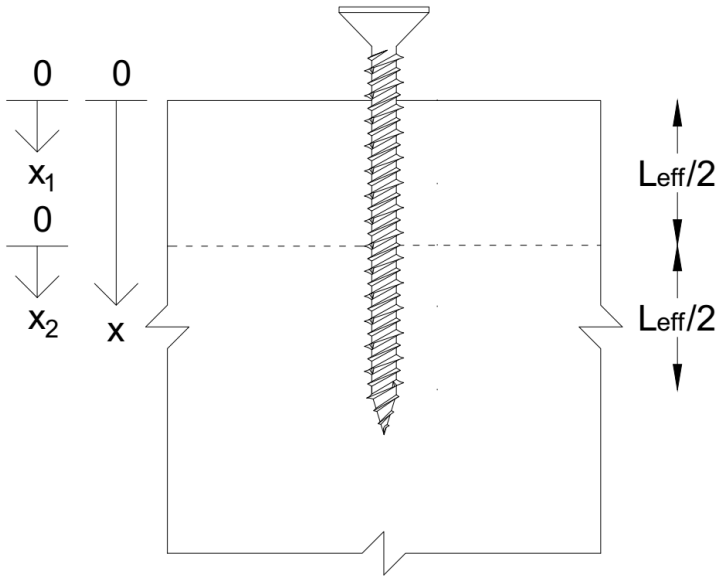

Figure 7-7: Coordinate system for analytical model

Equations 7-52 and 7-53 give the stress distribution in an axially loaded self-tapping screw under pull-push loading conditions due to moisture swelling of a wood member. The coordinate system for the analytical model is shown again in Figure 7-7.

In a two-member wood-to-steel or wood-to-wood connection with a self-tapping screw (Figure 7-2), if the screw is tightened with a torque more than that required to make the connection snug, an

axial load will be induced in the screw. Suppose the side member is assumed sufficiently rigid to provide support at the top surface of the main wood member. Then the axially loaded screw in the main wood member is similar to an axially loaded screw under pull-push loading conditions. In this over-torqued condition of the screw, if there is a change in moisture content in the main wood member, the total stress distribution in the screw is given by equations 7-52 and 7-53.

7.5 Notes on the Swelling Coefficient of Wood in the Analytical Model

The swelling coefficient used in the analytical model is used to quantify the swelling and shrinkage of the wood member in the x-direction (parallel to the screw axis). This research focuses on wood members made with mass timber products like CLT and glulam. For wood members involving mass timber products like CLT and glulam, the swelling and shrinkage of the wood member are governed by the swelling and shrinkage behaviour of the laminates of each layer of CLT and glulam. A simplified formula to predict the effective swelling coefficient of the whole CLT and glulam in the x-direction (parallel to the screw axis) from the properties of the laminates was developed in chapter 5. The prediction formulae are given by equations 7-54 and 7-55.

Equation 7-54

$$\alpha = \frac{\sum_{i=1}^{n} \alpha_{eff,i}}{n}$$

Equation 7-55

$$\alpha_{eff,i} = \alpha_{Ri} \cos^2 \theta_i + \alpha_{Ti} \sin^2 \theta_i$$

Here, $\alpha_{eff,i}$ is the swelling coefficient of each layer of the CLT or glulam, which considers the annual ring orientation of the laminates of each layer, θ_i is the approximate angle between the horizontal direction and the tangent to the annual rings of the end-grain of the laminates. The values of θ_i for each layer of the CLT and glulam can be determined manually by using a protractor. α_{Ri} is the value of the swelling coefficient of the laminates of each layer in the radial anatomic direction, whereas α_{Ti} is the swelling coefficient of the laminates of each layer in the tangential anatomic direction of the wood. These terms have been illustrated in Figure 7-8.

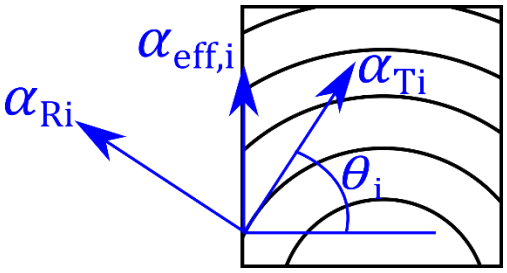

Figure 7-8: Nomenclature of the terms for effective swelling coefficient determination

In practical design situations, it is impractical to measure the angle θ_i and find the effective swelling coefficient of mass timber products by equations 7-54 and 7-55. In such cases, the most conservative approach is to consider the swelling coefficient of the laminates in the tangential direction of wood as the effective swelling coefficient of mass timber products. As seen in section 5.6.1, the swelling coefficient in the tangential direction of timber is the largest. For CLT and glulam consisting of laminates of each layer with different swelling coefficient values, the swelling coefficient of the layer with the highest value of swelling coefficient in the tangential direction can be considered the effective swelling coefficient.

7.6 Notes on the Elastic Constant of Wood in the Analytical Model

The mechanical properties of timber change significantly with the moisture content of the wood. A constant value of Young's modulus of wood was considered in the analytical model for simple forms of the analytical expressions. However, to slightly account for the effect of moisture content change on Young's modulus, the average value of Young's modulus of wood at the wood member's initial and final moisture content was used in the analytical model. For example, if the moisture content in the wood member changes from 12% to 21% EMC, the average of Young's modulus of wood at 12% and 21% EMC was taken as the input Young's modulus in the analytical model. Hankinson's formula (Stamatopoulos & Malo, 2016) was used to determine Young's modulus of wood along the x-direction (parallel to the screw axis) to consider the average end-grain angle of the laminates in each layer of CLT and glulam:

Equation 7-56

$$E_w = \frac{E_R E_T}{E_R \sin^2\theta + E_T \cos^2\theta}$$

Here, θ is the approximate average angle between the horizontal direction and the tangent to the annual rings of the end-grain of the laminates of CLT and glulam. E_R is the value of Young's

modulus of the laminates in the radial anatomic direction, whereas E_T is Young's modulus of the laminates in the tangential anatomic direction of the wood. A constant value of θ was used for the laminates of all layers of each CLT or glulam product for simplicity. For CLT and glulam with different properties of the laminates of the different layers, the elastic modulus of the whole CLT and glulam was determined by the following the formula:

Equation 7-57

$$E_w = \frac{\sum_{i=1}^{n} E_{wi}}{n}$$

Equation 7-58

$$E_{wi} = \frac{E_{Ri}E_{Ti}}{E_{Ri}\sin^2\theta + E_{Ti}\cos^2\theta}$$

Here, E_{wi} is Young's modulus along the x-direction of the laminates of each layer of CLT and glulam, E_{Ri} is the value of Young's modulus of the laminates of each layer in the radial anatomic direction, whereas E_{Ti} is Young's modulus of the laminates of each layer in the tangential anatomic direction of the wood. These terms have been illustrated in Figure 7-9.

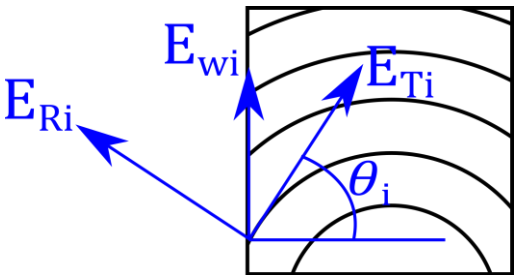

Figure 7-9: Nomenclature of the terms for Young's modulus determination

Similar to the case of swelling coefficient determination, in practical design situations, it is impractical to measure the angle θ and find Young's modulus of mass timber products by equations 7-56, 7-57 and 7-58. In place of any better estimate, it is suggested to use a value of 45° for θ.

7.7 Notes on the Shear Stiffness Parameter in the Analytical Model

The equivalent shear stiffness parameter, Γ_e also changes with the moisture content of the wood. Like Young's modulus, a constant value of the shear stiffness parameter was considered in the analytical model to get simple forms of the analytical expression. However, instead of taking an average value of the shear stiffness parameter, the shear stiffness parameter at the final moisture

content of the wood member was used to model the stress distribution in the screw during moisture content change. The value of the final moisture content was taken to achieve a better fit between the analytical and numerical prediction of the screw stress distribution.

7.8 Summary

An analytical model to predict the stress distribution in an axially loaded self-tapping screw inserted into mass timber products like CLT and glulam under moisture condition change is proposed in this chapter. The analytical model considers uniform moisture content change in the CLT and glulam. This model can also be used for screws inserted into other wood members like GLT and solid timber.

8 NUMERICAL MODEL OF SELF-TAPPING SCREW STRESS DISTRIBUTION, VERIFICATION, IMPLEMENTATION AND EXTENSION OF THE ANALYTICAL MODEL

8.1 Introduction

The stress distribution model proposed in chapter 7 could not be verified experimentally, and numerical finite element analysis was conducted to verify the proposed analytical model. Finite element (numerical) models for CLT and glulam specimens with self-tapping screws inserted perpendicular to the wood's grain direction were created in the commercial finite element analysis software ABAQUS (Simulia, 2020). The finite element analysis results were used to determine the stress distribution of the self-tapping screw under axial load and moisture swelling of the wood. The details of the finite element modelling techniques and the finite element analysis results are discussed in this chapter.

The specimen configurations adopted for the withdrawal tests described in chapter 6 were numerically modelled (Figure 8-1). These models were used to determine the stress distribution of the self-tapping screws under the moisture content changes mentioned in Table 8-1.

Table 8-1: Finite element model configurations and moisture content changes

Wood Product	Wood Species	Self-tapping Screw Effective Penetration Length (mm)	Self-tapping Screw Nominal Outer Diameter (mm)	Moisture Content Change (Initial – Final)
160x170 mm CLT	Spruce-Pine-Fir	72	8	12% → 21%, 21% → 12%
260x270 mm CLT	Spruce-Pine-Fir	120	13	12% → 21%, 21% → 12%
80x160 mm Glulam	Douglas Fir-Larch	72	8	12% → 21%, 21% → 12%
130x260 mm Glulam	Douglas Fir-Larch	120	13	12% → 21%, 21% → 12%

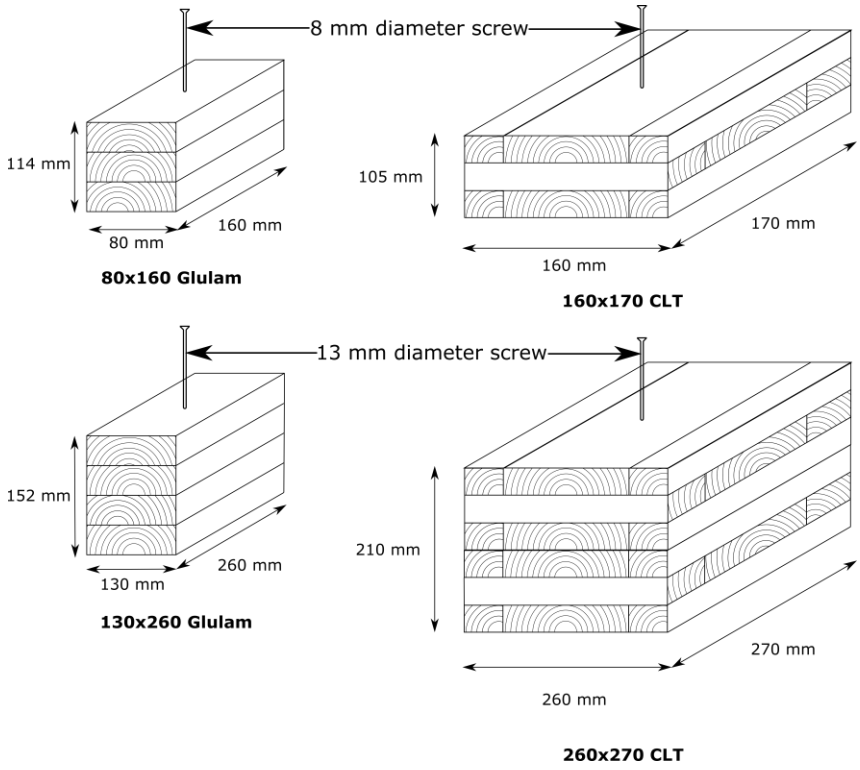

Figure 8-1: Small-scale test specimen configurations

8.2 Tests Conducted To Determine Finite Element Model Input Properties

The input material properties of the finite element model were derived from the series of tests performed on the self-tapping screw, CLT and glulam products described in chapters 3 to 6. The finite element model focused on the stress distribution of the self-tapping screw in the linear elastic regime. Moreover, the primary purpose of the finite element model was to validate the analytical model of chapter 7. Thus, only a basic finite element model with the elastic input properties determined from the tests was adequate. The determined properties in the series of tests conducted in chapters 3 to 6 and the material properties used in the finite element model are summarised below. Some of the determined properties are not used in the finite element model of this research, but their implementation in future research remains a possibility.

- **Tensile test of self-tapping screws:** Self-tapping screws of different configurations were tested under uniaxial tension. The average Young's modulus, yield strength, ultimate tensile strength, strain at failure and strain at ultimate tensile strength were determined from these tests. These properties have been described in chapter 3. However, only the average Young's modulus of the screws was used in the finite element model since that was the

only property needed to model the elastic behaviour of the screw apart from Poisson's ratio, which was not determined in the screw tensile tests. The other screw properties can be used in future research to encapsulate the behaviour of the screws in the post-elastic regime.

- **Moisture transport properties of CLT and glulam:** The diffusion coefficient of the laminates of CLT and glulam mentioned in Table 8-1 was determined in chapter 4. The analytical model developed in this research assumes uniform moisture content change throughout the CLT and glulam. Thus, the moisture content change in the finite element model is also considered uniform, for which the diffusion coefficient values are not required. However, a more sophisticated analytical model that considers non-uniform moisture content change throughout the CLT and glulam can be developed in the future. The diffusion coefficient of the laminates will be useful to model the moisture content change in the finite element model to find the non-uniform moisture content change distribution of the CLT and glulam.
- **Swelling test of CLT and glulam:** The swelling behaviour of the CLT and glulam products mentioned in Table 8-1 were investigated in chapter 5. The swelling coefficient of the laminates of the CLT and glulam was determined from the samples' swelling strain vs. moisture content change plots. These swelling coefficient values were used as finite element model input for the different layers of the CLT and glulam.
- **Withdrawal test of self-tapping screws in CLT and glulam:** Withdrawal tests were conducted on the identical specimens modelled in ABAQUS, as shown in Figure 8-1. Self-tapping screws of the two diameters (8 mm and 13 mm) were inserted centrically in CLT and glulam products at 10d penetration length, perpendicular to the wood's grain direction. The specimens were then conditioned in two separate stages. The two-stage conditioning was performed chronologically: to achieve the initial target equilibrium moisture content (EMC) – screw installation – conditioning to reach the final target EMC. The two-stage conditioning process was adopted to simulate the condition that the moisture content of timber members might change after screw installation in practical settings. As discussed in chapter 6, seven types of conditioning settings (depending on the initial and final conditioning stage EMC) with six specimens for each setting were adopted for each configuration of the withdrawal test. After achieving the final target EMC, the specimens were tested in displacement control under pull-push loading conditions. Withdrawal

displacement of the screw from the top wood surface was measured with two LVDTs. The load-displacement curve for each specimen was recorded, along with the withdrawal strength and stiffness. The withdrawal test results of five conditioning setting specimens were used in the finite element model as input parameters among the seven conditioning settings, as shown in Table 8-2.

Table 8-2: Different specimen groups and their conditioning EMCs in the two stages used in the finite element model

Wood products and self-tapping screw	Conditioning setting no.	Target initial EMC before screw installation	Target final EMC after screw installation
160x170 mm CLT, 8 mm Screw 260x270 mm CLT, 13 mm Screw 80x160 mm Glulam, 8 mm Screw 130x260 mm Glulam, 13 mm Screw	1 (constant EMC)	12%	12%
	2 (constant EMC)	16%	16%
	3 (constant EMC)	21%	21%
	4 (varying EMC)	12%	21%
	5 (varying EMC)	21%	12%

8.3 Finite Element Modelling Technique

The finite element modelling technique adopted here has been inspired by the work done by Avez et al. (2016), Bedon et al. (2020) and Feldt & Thelin (2018). The screw-wood composite model was created in ABAQUS/CAE (Simulia, 2020) and consisted of three parts: steel screw core, wood member and soft layer. The screw core represents the core of the self-tapping screw, excluding the screw threads, the wood member represents the CLT and glulam product, and the soft layer is representative of the screw thread and wood fibre interaction zone.

A 3D model is a practical choice for describing the orthotropic material properties of wood. However, the computational time required for numerical simulations with a 3D model is quite large. A 2D axisymmetric model, on the other hand, significantly reduces the simulation time. The steel material of the screw is isotropic, and both 2D and 3D models can describe it. It was shown by Feldt & Thelin (2018) that the difference in the predicted pull-out capacity and stiffness of glued-in rods embedded in wood members using a 3D and a 2D axisymmetric model was very

small. The 2D axisymmetric modelling technique was adopted to model the self-tapping screws inserted into CLT and glulam, considering the slight difference in the predicted capacity and stiffness between a 3D and a 2D axisymmetric model and the reduced computational time.

The 3D system of the self-tapping screw inserted centrically into CLT/glulam was reduced to an axisymmetric model, as shown in Figure 8-2. The radius of the axisymmetric model is defined by the minimum of the (edge distance + D/2) and (end distance + D/2) of the screw inside the CLT/glulam. In ABAQUS/CAE, an axisymmetric model was generated by revolving a 2D plane about a symmetry axis and is described by a cylindrical coordinate system, as illustrated in Figure 8-3. In Figure 8-3, the symmetry axis lies along the longitudinal centre line of the screw, which implies that the screw is placed centrically with the wood grain direction running along the cylinder's circumferential direction.

The thermal analysis formulation available in ABAQUS/CAE is analogous to the moisture-swelling process in wood. Thus, thermal analysis using the ABAQUS Standard solver was carried out to simulate the moisture-swelling process in CLT and glulam. In the thermal analysis, the temperature is analogous to the wood's moisture content, and the coefficient of thermal expansion is analogous to the wood's moisture swelling coefficient. The uniform moisture content in the wood member was specified as a predefined constant-temperature field. For example, the whole wood member was specified the 12% moisture content condition with a constant predefined temperature of 12 (unitless). The wood's moisture swelling coefficient along the three orthotropic directions was defined as the orthotropic coefficient of thermal expansion values in ABAQUS/CAE.

For simulating the screw pullout behaviour under moisture content variation, an axial load was applied to the top surface of the screw core in the finite element model under (1) displacement control and (2) force control, with proper support and moisture content (in terms of temperature) boundary conditions, described later in details. The displacement-controlled axial load was applied by specifying a displacement boundary condition. The force-controlled axial load was applied by specifying a concentrated force acting on the screw core.

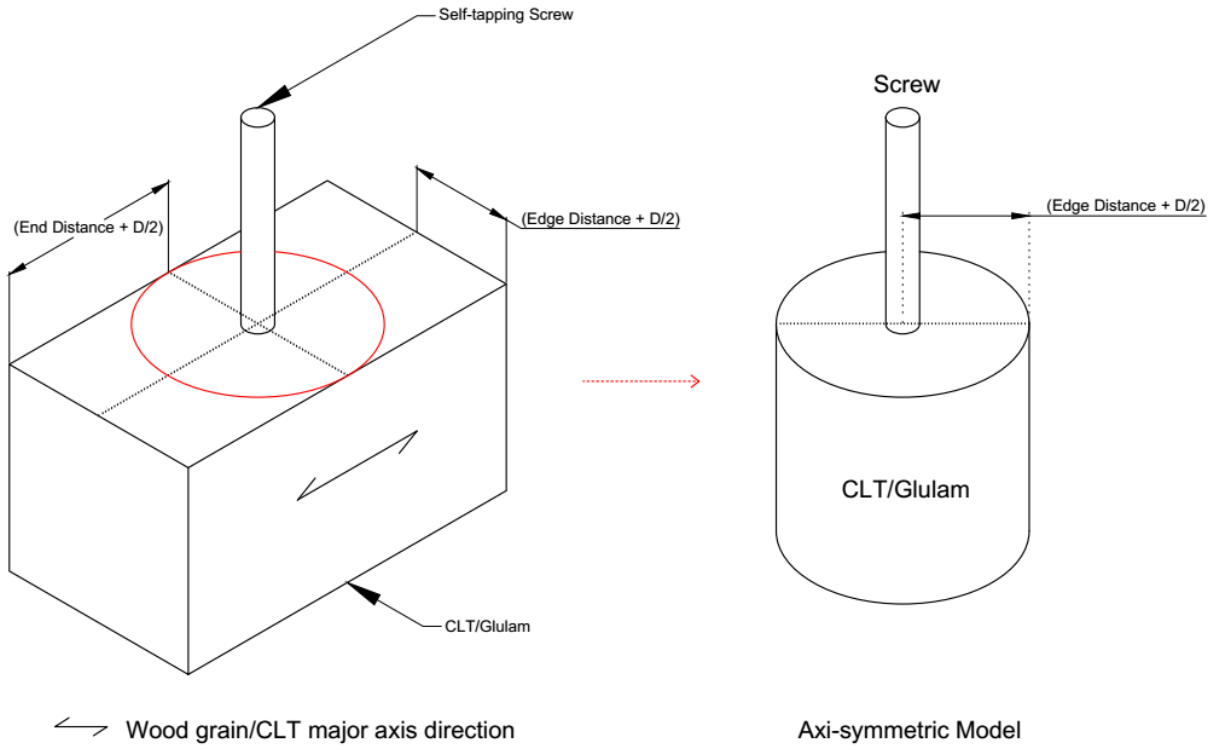

Figure 8-2: Reduction of the wood-screw 3D system to an axisymmetric system

8.4 Finite Element Material Model and Interactions

The screw core and wood were modelled as linear elastic materials, and the soft layer was assigned the same material properties as the wood member. The screw core was assigned isotropic material properties, and the wood was given orthotropic material properties. Local material orientation was assigned to the wood member, whose angular value was set per the average angle between the tangent to the annual rings and the horizontal direction of the CLT/glulam laminate's end grain. CAX4 elements of ABAQUS/CAE were used for all the parts in the finite element model.

The screw core and the soft layer were rigidly connected with the "tie" constraint in ABAQUS/CAE as the soft layer represents the integral threaded part of the screw embedded in the wood. A surface-based cohesive contact interaction was used to interconnect the external surface of the soft layer and the surrounding wood. In simpler terms, the soft layer was tied to the screw core on the inner side and cohesively bonded to the surrounding wood on the outer side, encapsulating the wood-screw thread interaction (Figure 8-3, right). The cohesive contact in

ABAQUS/CAE utilizes the cohesive zone modelling (CZM) approach based on nonlinear fracture mechanics. It does not require computationally expensive or complex meshing techniques (Bedon et al., 2020). The bottom end of the screw was modelled as a free edge, as it has a negligible effect on the stress distribution of the screw during axial loading (Feldt & Thelin, 2018).

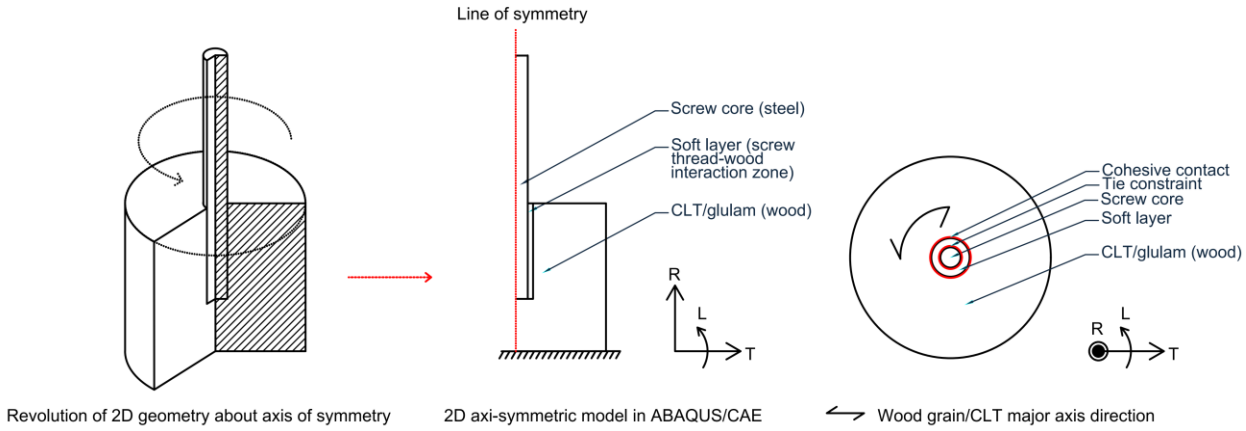

Figure 8-3: Axisymmetric model in ABAQUS/CAE

The CZM approach can adequately describe the pull-out behaviour of the screw during axial loading (Avez et al., 2016). The cohesive contact interaction in ABAQUS/CAE requires three input parameters: an elastic behaviour defined by the stiffness values, a damage initiation criterion and a damage evolution model. The stiffness values along three directions are required: the normal direction (K_{nn}), which is perpendicular to the screw longitudinal axis, and the two transverse (shear) directions (K_{ss} and K_{tt}), one parallel to the screw longitudinal axis and one parallel to the tangent to the cylindrical screw surface (Figure 8-4, right). The stiffness of the normal direction is less critical in this study as the axial loading conditions are focused here. This study took the stiffness along the two shear directions as equal. According to the traction separation law, the stiffness values relate the tractions (t_n, t_s, t_t) in the three directions to the separation ($\delta_n, \delta_s, \delta_t$) in the respective directions (Figure 8-4, left).

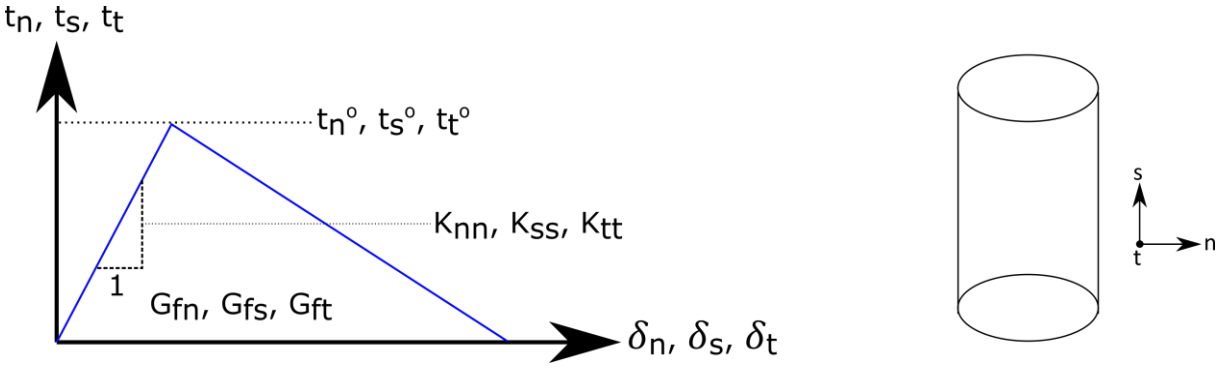

Figure 8-4: Traction separation law and the directions in the cylindrical coordinate system

The quadratic traction damage initiation criterion was used to determine the failure of the screw-wood interaction zone. The criterion is given by:

Equation 8-1

$$\left\{\frac{\langle t_n \rangle}{t_n^o}\right\}^2 + \left\{\frac{t_s}{t_s^o}\right\}^2 + \left\{\frac{t_t}{t_t^o}\right\}^2 = 1$$

Here, $\langle t_n \rangle$ is the normal tension traction, t_s and t_t are the tractions in the two shear directions, t_n^o, t_s^o and t_t^o are the maximum tractions in the three directions when the separation is either purely normal to the screw interface or acts purely in the shear directions. The symbol $\langle\ \rangle$ signifies that a purely compressive displacement or a purely compressive stress state does not initiate damage (Simulia, 2020).

Once the failure criterion is satisfied, the damage evolution model gives the stresses in the three directions. A linear energy-based softening model without considering mode-mixing was used as the damage evolution model. The total fracture energy per unit area (G_{fn}, G_{fs}, G_{ft}) in each mode was equal, and only one value of the total fracture energy was defined. The pressure-overclosure relationship type was set to "hard contact," and the default constraint enforcement method was used to describe the normal behaviour for the cohesive contact. For the tangential behaviour of cohesive contact, the "penalty" friction formulation with a friction coefficient of 0.2 was used (Murase, 1984). Finally, the small sliding formulation was used in ABAQUS/CAE to define the cohesive contact interaction for better convergence.

8.5 Finite Element Material Properties and Calibration

The screw core was assigned isotropic elastic material properties. The Young's modulus for the screw core was determined from the self-tapping screw tensile tests, and the Poisson's ratio was taken as 0.3, the usual for steel. The plastic material properties were not used since the goal of the finite element model was to verify the analytical model in the linear elastic range. The wood member (CLT/glulam) was assigned orthotropic material properties. The input elastic material properties used to model the two types of CLT and glulam were taken according to the stress grade of the laminates and published literature (Ross & USDA Forest Service., 2010). As the wood properties change significantly with the moisture content, the change in the elastic properties was considered by specifying temperature-dependent (temperature is analogous to the moisture content in ABAQUS/CAE's thermal analysis formulation) values of the elastic properties according to Gerhards (1982). The elastic properties at 20% EMC from Gerhards (1982) represented the 21% EMC condition.

CLT's longitudinal and transverse layers were made of lumber of different grades and material properties. Also, the wood grain direction of CLT's longitudinal and transverse layers are oriented in orthogonal directions. Thus, the wood member was partitioned into different layers to assign layer-specific material properties for CLT (Figures 8-5 and 8-6).

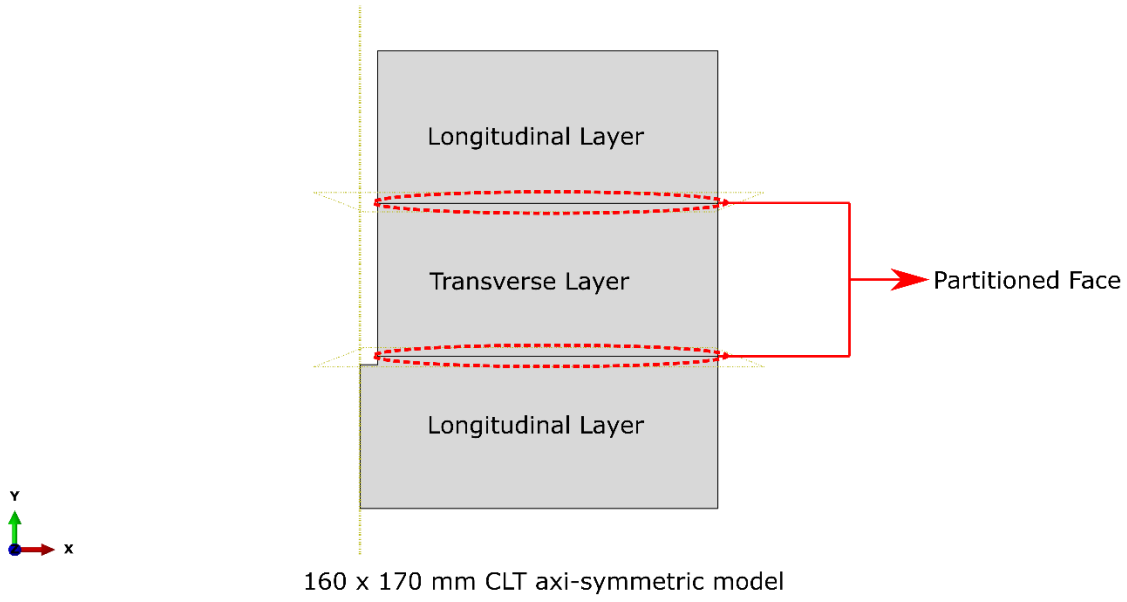

Figure 8-5: Partitioning method for 160x170 mm CLT

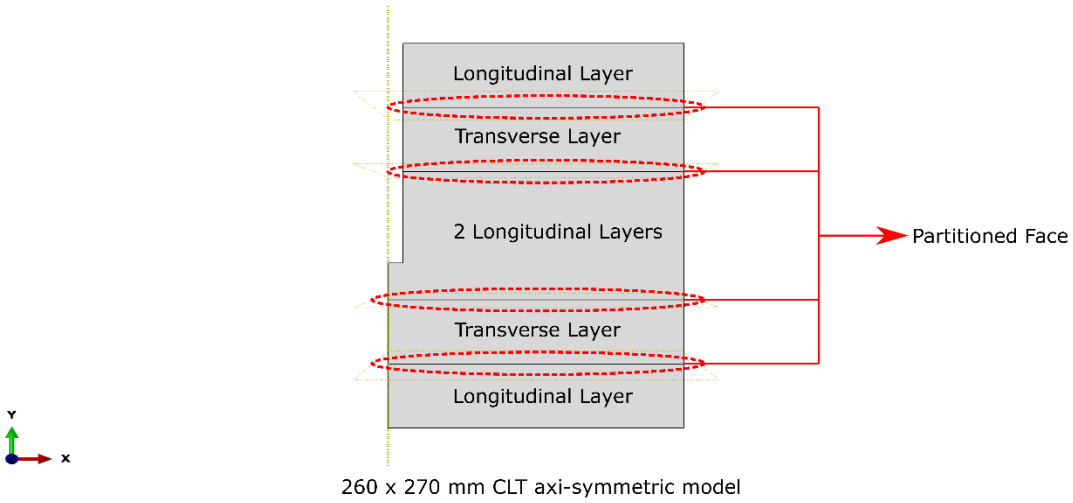

Figure 8-6: Partitioning method for 260x270 mm CLT

The lumber of all layers of glulam came from the same grade. The glulam was modelled as a single part without partitioning, and the same material properties were assigned to the whole glulam (Figures 8-7 and 8-8). The soft layer was assigned the same material properties as the wood member (Avez et al., 2016). The moisture-swelling coefficient of the different layers of CLT along the three orthotropic directions was determined from the swelling tests and assigned to the respective layers (longitudinal and transverse layers). On the other hand, since the glulam was modelled as a single whole part, the same swelling coefficient values along the three directions were used for the entire glulam. The screw core and the wood material properties are given in Tables 8-3, 8-4, 8-5, 8-6 and 8-7. Both types of glulam used in this study came from the same manufacturer and were of the same grade. Thus, the same material properties were used for them.

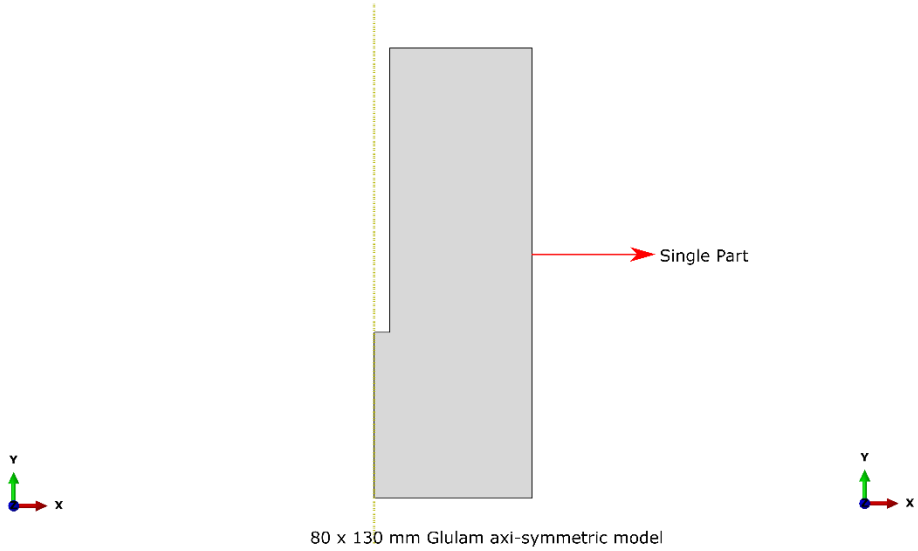

Figure 8-7: 80x160 mm Glulam part in ABAQUS

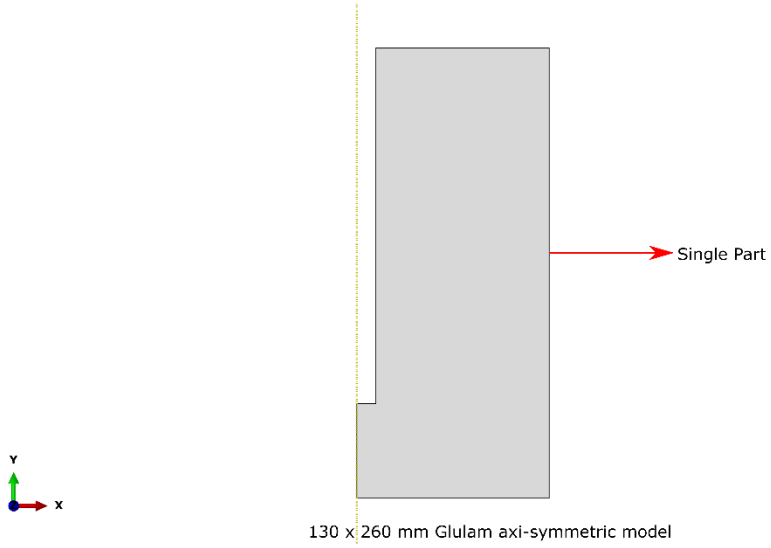

Figure 8-8: 130x260 mm Glulam part in ABAQUS

Table 8-3: Self-tapping Screw material properties

Screw Configuration	Mean Young's Modulus (GPa)	Poisson's Ratio
ASSY 8-160 (8 mm diameter screw)	208.2	0.3
VGS 13-200 (13 mm diameter screw)	226.6	0.3

Table 8-4: 160x170 mm CLT material properties

Longitudinal Layers			Transverse Layers		
Elastic property	12% EMC	21% EMC	Elastic property	12% EMC	21% EMC
E_L	11700 MPa	10179 MPa	E_L	9000 MPa	7830 MPa
E_R	1193.4 MPa	918.9 MPa	E_R	918 MPa	706.9 MPa
E_T	631.8 MPa	486.5 MPa	E_T	486 MPa	374.2 MPa
G_{LR}	731 MPa	584.8 MPa	G_{LR}	563 MPa	450.4 MPa
G_{TL}	608.4 MPa	486.7 MPa	G_{TL}	468 MPa	374.4 MPa
G_{RT}	73.1 MPa	58.5 MPa	G_{RT}	56.3 MPa	45 MPa
υ_{LR}	0.032	0.032	υ_{LR}	0.032	0.032
υ_{TL}	0.024	0.024	υ_{TL}	0.024	0.024
υ_{RT}	0.381	0.381	υ_{RT}	0.381	0.381

Table 8-5: 260x270 mm CLT material properties

Longitudinal Layers			Transverse Layers		
Elastic property	12% EMC	21% EMC	Elastic property	12% EMC	21% EMC
E_L	9500 MPa	8265 MPa	E_L	9500 MPa	8265 MPa
E_R	969 MPa	746.1 MPa	E_R	969 MPa	746.1 MPa
E_T	513 MPa	395 MPa	E_T	513 MPa	395 MPa
G_{LR}	570 MPa	456 MPa	G_{LR}	570 MPa	456 MPa
G_{TL}	494 MPa	395.2 MPa	G_{TL}	494 MPa	395.2 MPa
G_{RT}	57 MPa	45.6 MPa	G_{RT}	57 MPa	45.6 MPa
υ_{LR}	0.032	0.032	υ_{LR}	0.032	0.032
υ_{TL}	0.024	0.024	υ_{TL}	0.024	0.024
υ_{RT}	0.381	0.381	υ_{RT}	0.381	0.381

Table 8-6: 130x260 mm and 80x160 mm Glulam material properties

Elastic property	12% EMC	21% EMC
E_L	12400 MPa	10788 MPa
E_R	843.2 MPa	649.3 MPa
E_T	620 MPa	477.4 MPa
G_{LR}	793.6 MPa	634.9 MPa
G_{TL}	967.2 MPa	773.8 MPa
G_{RT}	86.8 MPa	69.4 MPa
υ_{LR}	0.036	0.036
υ_{TL}	0.029	0.029
υ_{RT}	0.39	0.39

Table 8-7: Swelling coefficient values for glulam and CLT

Type of wood product	Layer type	α_L	α_R	α_T
160x170 mm CLT	Longitudinal	0	0.0016	0.0024
	Transverse	0.0001	0.0017	0.0028
260x270 mm CLT	Longitudinal	0	0.0016	0.0027
	Transverse	0.0002	0.0019	0.0029
80x160 mm and 130x260 mm Glulam	-	0.0001	0.0017	0.0029

Specifying the proper local material orientation directions to accurately model wood to represent the withdrawal test specimens is essential. The average value of the angle between the tangent to the annual rings and the horizontal direction (θ in Figure 8-9) of the CLT/glulam laminate's end grain was measured by hand. For each type of CLT and glulam product, a constant average value of the angle θ was used as the direction of the local material orientation for all the layers for modelling simplicity (Table 8-8).

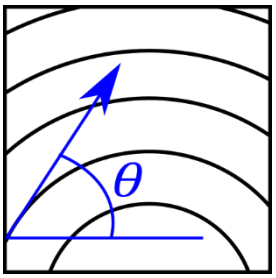

Figure 8-9: End-grain of the laminates of CLT/glulam

Table 8-8: Material orientation angle

Type of wood product	Material Orientation, θ (º)
160x170 mm CLT	49
260x270 mm CLT	33
80x160 mm Glulam	52
130x260 mm Glulam	65

Withdrawal tests were conducted on the specimen configurations mentioned in Table 8-2. The specimen under conditioning setting no. 1-3 (Table 8-2) were conditioned under constant EMC before and after screw installation. The test results from these specimens were used as the input properties for the CZM contact interaction between the screw core and the wood member.

The force-displacement curves of the withdrawal tests determined the withdrawal strength, stiffness, and fracture energy per unit area.

The withdrawal strength of the screws was determined with the following equation:

Equation 8-2

$$f_{ax} = \frac{F_{max}}{\pi d L_{eff}} \ [\mathrm{N/mm^2}]$$

Here, F_{max} is the maximum applied load, d is the outer thread diameter of the screw, L_{eff} is the effective penetration length of the screw inside the sample. The withdrawal stiffness was calculated according to the following formula:

Equation 8-3

$$k_{ax} = \frac{K_{ser}}{\pi d L_{eff}} \ [\mathrm{N/mm^3}]$$

Here, K_{ser} is the slope of the linear fit-line between 10 - 40% of the maximum load of the load-displacement curve. Finally, the fracture energy per unit area was calculated as:

Equation 8-4

$$G_f = \frac{\text{Total area under the force} - \text{displacement curve}}{\pi d L_{eff}} [\mathrm{N/mm}]$$

As mentioned in section 8.4, t_n^o, t_s^o and t_t^o are the maximum tractions in the normal and the two shear directions respectively. The maximum traction in the normal direction (t_n^o) is least critical for the finite element model for axial loading condition and was set to an arbitrary value of 100 N/mm^2. The maximum traction in the shear directions (t_s^o and t_t^o) was assigned the mean withdrawal strength value from the specimen's withdrawal test results under conditioning setting no. 1-3, for EMC 12%, 16% and 21%, respectively. Similarly, the withdrawal test was also used to determine the fracture energy per unit area per equation 8-4 for the linear energy-based softening model for the damage evolution. As mode-mixing of the different fracture modes was not considered, a constant fracture energy value ($G_{fn} = G_{fs} = G_{ft} = G_f$) was specified to describe the damage evolution and ultimate failure in all three directions.

The cohesive stiffness values, K_{nn}, K_{ss} and K_{tt} affect the possibility of convergence and the ultimate load-carrying capacity of the screw during axial loading. For modelling the cohesive contact, these parameters have to be adjusted appropriately to make the finite element model representative of the actual behaviour of screw-wood interaction. As the stiffness and traction of the normal direction are of the least importance in this study for axial loading conditions, the normal cohesive stiffness (K_{nn}) value was set as an arbitrary constant value. The cohesive stiffness in the two shear directions was considered equal ($K_{ss} = K_{tt}$). The value of the shear direction cohesive stiffness was changed until the ultimate load, and the slope of the force-displacement curves from the finite element analysis and the experimental withdrawal test results were very close. The normal cohesive stiffness was assigned a significantly higher value than the cohesive stiffness in the shear directions. The normal cohesive stiffness values chosen for the different specimen configurations are mentioned in Table 8-9.

Table 8-9: Normal cohesive stiffness values

Type of Wood Product	Normal Cohesive Stiffness (K_{nn}, N/mm^3)
160x170 mm CLT	400
260x270 mm CLT	100
80x160 mm Glulam	200
130x260 mm Glulam	100

The cohesive stiffness in the two shear directions was calibrated with the experimental withdrawal test results of the specimen under conditioning settings no. 1, 2, and 3 for EMC 12%, 16% and

21%, respectively. As a starting point, the input values for the cohesive stiffness were taken as the withdrawal stiffness from the experimental results. The withdrawal stiffness was taken as the reference value for the cohesive stiffness. The cohesive stiffness values were then scaled proportionately until a close match between the ultimate load and the slope of the initial linear portion of force-displacement curves from finite element analysis, and the experimental result was achieved (Figure 8-10).

Up to this point, the cohesive parameters (elastic behaviour defined by the stiffness values, damage initiation criterion defined by the maximum traction and damage evolution model defined by the fracture energy per unit area) at only constant EMC were considered. Once the cohesive stiffness values at constant EMC were calibrated, a temperature-dependent (temperature is analogous to the EMC) cohesive interaction was defined to capture the effect of change of the cohesive parameters with moisture content. Then, the process of EMC change was incorporated (in terms of temperature field) in the finite element model along with the axial load. The load-displacement curve under varying EMC from the finite element model was verified with the load-displacement curve of specimen groups 4-5, which had different EMC in the two conditioning stages. The calibration and the verification process of the finite element model are illustrated in Figure 8-11. Thus, in summary, two types of finite element models were created for each specimen:

- **FE model for calibration:** The purpose of this type of model was to calibrate the cohesive stiffness value. The effect of change of EMC on the material properties was not considered in this type of model. Also, the process of EMC change (in terms of temperature field) was not simulated in this model.
- **FE model for verification:** This type of model was aimed to verify the finite element model with the calibrated cohesive stiffness values and the analytical model proposed in chapter 7. The effect of change of EMC on the material properties was considered in this model type. Besides, the process of EMC change (in terms of temperature field) was simulated in this model by specifying two steps in ABAQUS, one with the initial conditioning EMC and the other with the final conditioning EMC.

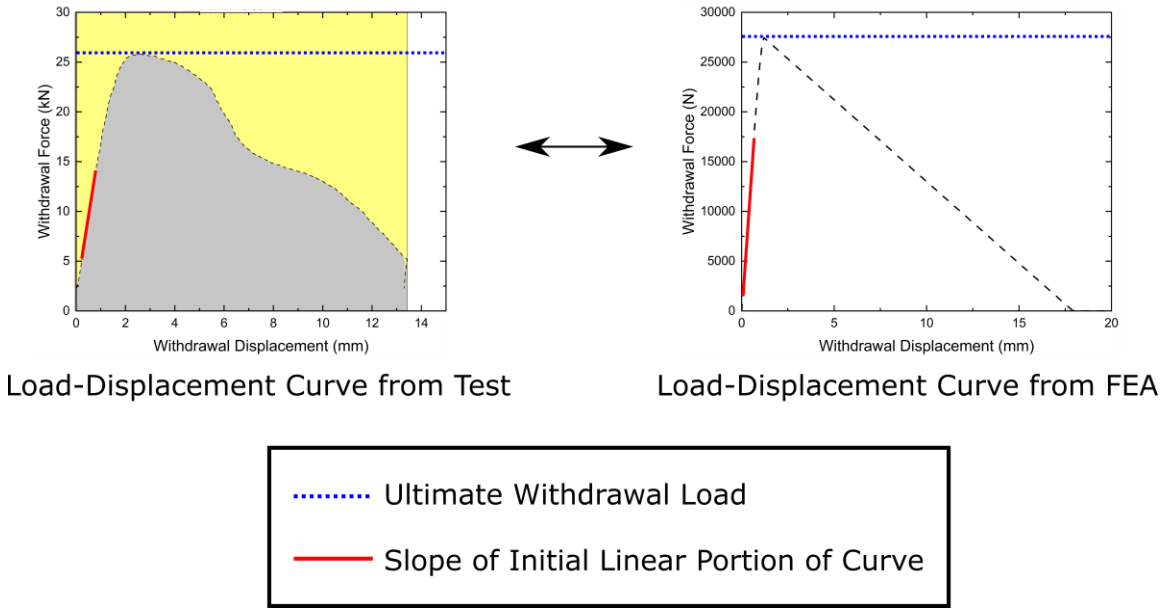

Figure 8-10: Comparison of the load-displacement curve from finite element analysis (FEA) and withdrawal test

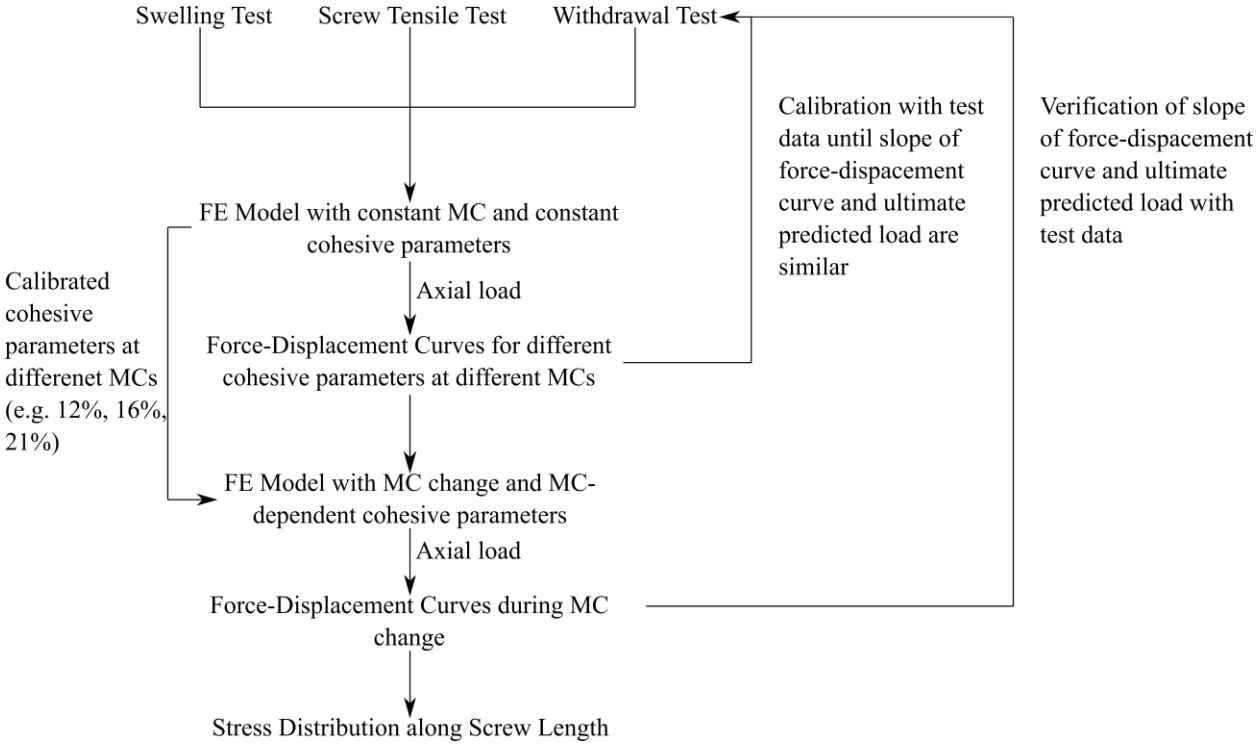

Figure 8-11: Finite element model calibration and verification process

The cohesive stiffness's exact calibration values are shown in Tables 8-10, 8-11, 8-12 and 8-13. As mentioned previously, the normal direction's cohesive stiffness (K_{nn}) was kept constant, and shear direction cohesive stiffness (K_{ss} and K_{tt}) was varied proportionately with the withdrawal

stiffness from the test. In Table 8-10, K_{ss} and K_{tt} value in the first row of a particular EMC is the withdrawal stiffness from the test result (1WS, which signifies one-time withdrawal stiffness from the test). The subsequent rows are scaled values (scaled by an integer value) of the withdrawal stiffness (2WS, 3WS etc.). The slope of the initial linear portion of the force-displacement curve (K_{ser}) and the maximum load capacity (F_{max}) from the withdrawal test and finite element analysis (FEA) were compared. The scaled value of the withdrawal stiffness, which gave the lowest percentage difference of K_{ser} and F_{max} between experimental and finite element results, was chosen as the calibrated value of the cohesive stiffness. The final calibrated value of the cohesive stiffness used for the different specimen configurations and used to model the varying EMC conditions is marked green in the following tables.

Table 8-10: 130x260 mm Glulam calibration values

EMC	Scaling Factor	K_{nn}, K_{ss} and K_{tt}	K_{ser} from withdrawal test	K_{ser} from FEA	Percentage Difference (%)	F_{max} from withdrawal test	F_{max} from FEA	Percentage Difference (%)
12% EMC	1WS	100, 5.33	26.13	16.64	36.31	43.28	42.77	1.17
	2WS	100, 10.66	26.13	24.55	6.04	43.28	42.75	1.22
	3WS	100, 15.99	26.13	28.5	9.08	43.28	42.83	1.03
16% EMC	1WS	100, 4.6	22.54	15.08	33.11	34.95	34.57	1.07
	2WS	100, 9.2	22.54	22.81	1.18	34.95	34.66	0.82
	3WS	100, 13.8	22.54	26.98	19.68	34.95	34.56	1.13
21% EMC	1WS	100, 4.17	20.46	14.09	31.12	27.63	27.45	0.63
	2WS	100, 8.34	20.46	21.65	5.83	27.63	27.46	0.62
	3WS	100, 12.5	20.46	26.22	28.17	27.63	27.43	0.73

Table 8-11: 80x160 mm Glulam calibration values

EMC	Scaling Factor	K_{nn}, K_{ss} and K_{tt}	K_{ser} from withdrawal test	K_{ser} from FEA	Percentage Difference (%)	F_{max} from withdrawal test	F_{max} from FEA	Percentage Difference (%)
12% EMC	1WS	200, 10.73	19.41	10.16	47.67	16.85	16.69	1.00
	3WS	200, 32.19	19.41	15.62	19.54	16.85	16.69	0.96
	5WS	200, 53.65	19.41	17.48	9.96	16.85	16.75	0.64
	7WS	200, 75.11	19.41	18.25	6.00	16.85	16.68	1.01
	8WS	200, 85.84	19.41	18.87	2.80	16.85	16.66	1.13
	10WS	200, 107.3	19.41	19.27	0.74	16.85	16.69	0.94
	11WS	200, 118	19.41	19.41	0.02	16.85	16.74	0.67
	12WS	200, 128.8	19.41	19.53	0.59	16.85	16.76	0.56
	13WS	200,139.5	19.41	19.64	1.16	16.85	16.75	0.60
16% EMC	10WS	200, 112.3	20.32	19.29	5.09	16.52	16.41	0.70
	11WS	200, 123.5	20.32	19.42	4.45	16.52	16.4	0.76
	12WS	200, 134.8	20.32	19.54	3.86	16.52	16.39	0.81
	13WS	200, 146	20.32	20.07	1.25	16.52	16.39	0.85
	14WS	200, 157.2	20.32	19.71	3.02	16.52	16.37	0.94
	16WS	200, 179.7	20.32	19.85	2.34	16.52	16.38	0.88
21% EMC	4WS	200, 38.49	17.41	16.37	5.98	13.96	13.86	0.71
	5WS	200, 48.11	17.41	17.08	1.90	13.96	13.82	0.99
	6WS	200, 57.73	17.41	17.56	0.86	13.96	13.90	0.45
	8WS	200, 76.97	17.41	18.17	4.36	13.96	13.87	0.63
	9WS	200, 86.59	17.41	18.38	5.57	13.96	13.86	0.71
	11WS	200, 105.8	17.41	18.67	7.24	13.96	13.84	0.81
	12WS	200, 115.5	17.41	18.78	7.87	13.96	13.84	0.85

Table 8-12: 260x270 mm CLT calibration values

EMC	Scaling Factor	K_{nn}, K_{ss} and K_{tt}	K_{ser} from withdrawal test	K_{ser} from FEA	Percentage Difference (%)	F_{max} from withdrawal test	F_{max} from FEA	Percentage Difference (%)
12% EMC	1WS	100, 4.51	22.09	14.91	32.51	30.31	30.06	0.83
	2WS	100, 9.02	22.09	22.61	2.34	30.31	30.20	0.37
	3WS	100, 13.52	22.09	27.26	23.38	30.31	30.20	0.34
16% EMC	1WS	100, 4.33	21.23	14.51	31.67	29.59	29.44	0.52
	2WS	100, 8.66	21.23	22.14	4.27	29.59	29.54	0.17
	3WS	100, 12.99	21.23	26.87	26.54	29.59	29.55	0.14
21% EMC	1WS	100, 3.17	15.55	11.6	25.39	23.13	23.02	0.48
	1.5WS	100, 4.76	15.55	15.89	2.20	23.13	23.10	0.13
	2WS	100, 6.34	15.55	18.53	19.19	23.13	23.08	0.22

Table 8-13: 160x170 mm CLT calibration values

EMC	Scaling Factor	K_{nn}, K_{ss} and K_{tt}	K_{ser} from withdrawal test	K_{ser} from FEA	Percentage Difference (%)	F_{max} from withdrawal test	F_{max} from FEA	Percentage Difference (%)
12% EMC	29WS	400, 366.41	22.86	22.6	1.15	16.99	16.84	0.89
	30WS	400, 379.05	22.86	22.96	0.42	16.99	16.85	0.83
	31WS	400, 391.68	22.86	22.67	0.85	16.99	16.86	0.77
16% EMC	4WS	400, 41.32	18.69	17.47	6.55	13.02	12.92	0.75
	5WS	400, 51.65	18.69	18.27	2.27	13.02	12.90	0.90
	6WS	400, 61.99	18.69	18.82	0.67	13.02	12.97	0.37
	7WS	400, 72.32	18.69	19.22	2.81	13.02	12.95	0.52
21% EMC	1WS	400, 7.73	13.98	8.6	38.48	11.67	11.57	0.88
	2WS	400, 15.45	13.98	12.49	10.65	11.67	11.57	0.88
	3WS	400, 23.18	13.98	14.67	4.94	11.67	11.62	0.45
	4WS	400, 30.9	13.98	15.93	13.96	11.67	11.57	0.88

The values of the other cohesive parameters (damage initiation criterion defined by the maximum traction and damage evolution model defined by the fracture energy per unit area) for the different specimen configurations are given in Tables 8-14, 8-15, 8-16, and 8-17.

Table 8-14: 130x260 mm Glulam damage initiation and evolution values

EMC	t_n^o (N/mm^2)	t_s^o and t_t^o (N/mm^2)	G_f (N/mm)
12% EMC	100	8.83	78.85
16% EMC	100	7.13	64.64
21% EMC	100	5.64	50.48

Table 8-15: 80x160 mm Glulam damage initiation and evolution values

EMC	t_n^o (N/mm^2)	t_s^o and t_t^o (N/mm^2)	G_f (N/mm)
12% EMC	100	9.31	59.14
16% EMC	100	9.13	53.6
21% EMC	100	7.71	51.62

Table 8-16: 260x270 mm CLT damage initiation and evolution values

EMC	t_n^o (N/mm^2)	t_s^o and t_t^o (N/mm^2)	G_f (N/mm)
12% EMC	100	6.18	44.6
16% EMC	100	6.04	49.95
21% EMC	100	4.72	40.8

Table 8-17: 160x170 mm CLT damage initiation and evolution values

EMC	t_n^o (N/mm^2)	t_s^o and t_t^o (N/mm^2)	G_f (N/mm)
12% EMC	100	9.39	55.42
16% EMC	100	7.19	52.73
21% EMC	100	6.45	47.3

8.6 Finite Element Analysis Steps, Loads, Boundary Conditions and Predefined Fields

The standard solver in ABAQUS/CAE was used for all analyses. As discussed in section 8.5, two types of models were created: (a) FE model for calibration and (b) FE model for verification. Only one analysis step was created for the FE model for calibration after the initial step in

ABAQUS/CAE. A displacement of 20 mm was applied on the top end of the screw in this step, and the top surface of the wood member was fixed (Figure 8-12) to create the pull-push loading condition (which is the boundary condition of the withdrawal test). For applying the displacement and ease of extracting the load-displacement curve, a reference point was defined on top of the screw (Figure 8-13). The reference point was tied with kinematic coupling to the top surface of the screw, and the displacement was applied to the reference point, yielding equal displacement at the top end of the screw and the reference point. The load-displacement curve of the top-end of the screw was also extracted from this reference point.

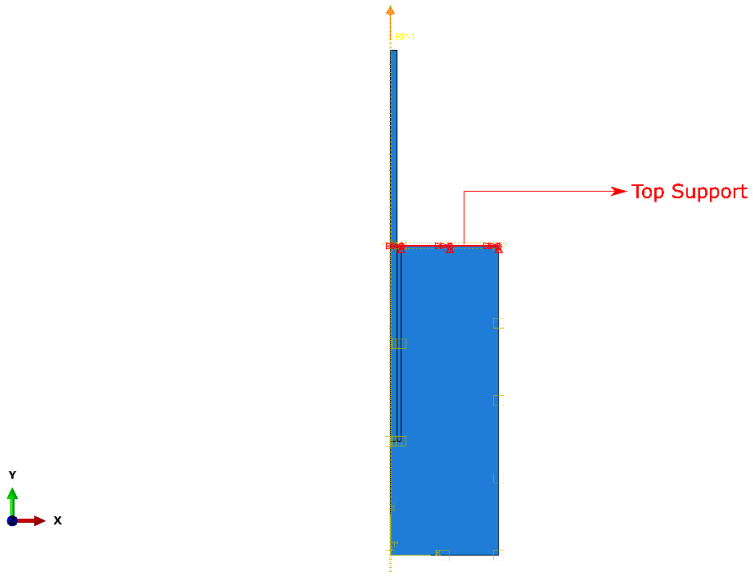

Figure 8-12: Top boundary condition

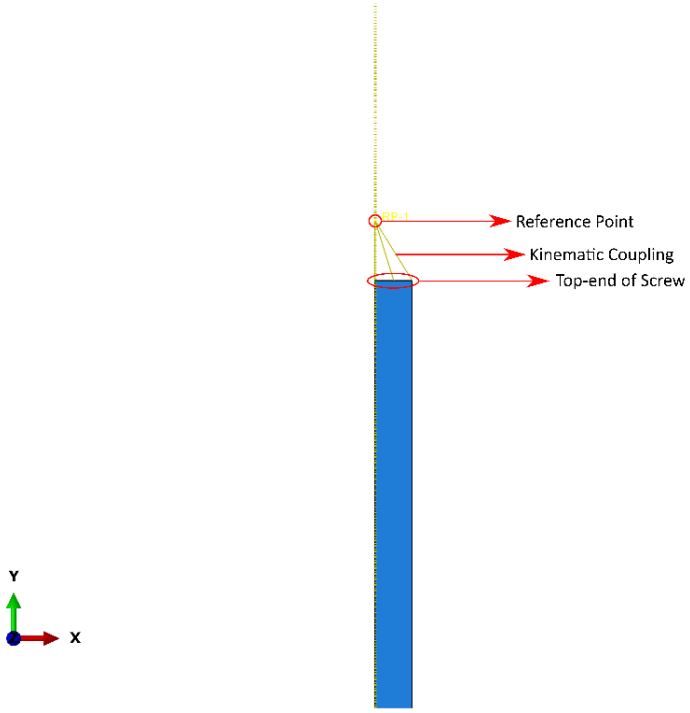

Figure 8-13: Reference point at the screw top

For the FE model for verification, two analysis steps were created after the initial step for the analysis. In the initial step, a constant predefined temperature (temperature is analogous to EMC of wood) field was specified throughout the wood member and the soft layer geometry. The moisture swelling/shrinkage of wood was simulated in the first step following the initial step by changing the value of the constant predefined temperature field specified in the initial step. Further, the bottom end of the wood member was kept fixed for stability and better convergence of the model, as shown in Figure 8-14 (Bedon et al., 2020). In the second step, a pull-out displacement of 20 mm was applied on the top surface of the screw through the reference point, as done in the FE model for calibration. In the second step after the initial step, the bottom boundary condition was deactivated, whose primary purpose was to achieve convergence of the finite element model during the moisture swelling/shrinkage step. In the second step, a fixed boundary condition was specified at the top surface of the wood member to simulate the pull-push loading condition. The predefined temperature fields used for simulating the moisture change of wood are shown in Table 8-18. Verification model no. 1 was verified against the withdrawal test data of specimen

conditioned under conditioning setting no. 4 (12% → 21% EMC), and verification model no. 2 was verified against specimen conditioned under conditioning setting no. 5 (21% → 12% EMC) (Table 8-2). The two models were aimed to investigate the case of wood wetting (an increase of EMC from 12% to 21%) and drying (a decrease of EMC from 21% to 12%), respectively. For verification of the FE model, the same process as before was followed, i.e., the slope of the initial linear portion of the force-displacement curve (K_{ser}) and the maximum load capacity (F_{max}) from the withdrawal test and finite element analysis (FEA) were compared.

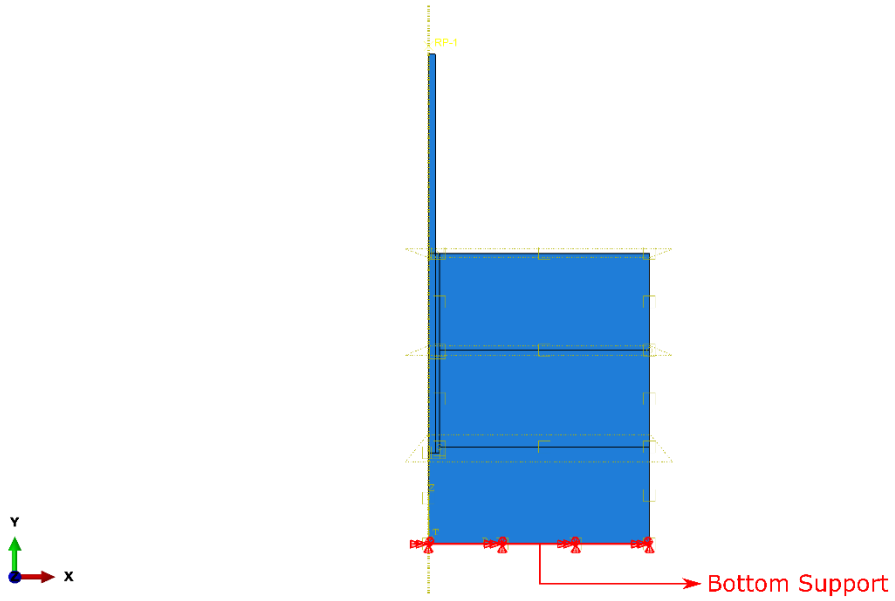

Figure 8-14: Bottom boundary condition

Table 8-18: Finite element verification models

FE Verification Model No.	EMC/Temp in Initial Step	EMC/Temp in First Step	Specimen Conditioing Setting No. Simulated
1	12	21	4
2	21	12	5

Finally, a slightly different approach was followed to verify the analytical model with the finite element model. The analytical model requires the axial load applied on the screw to be known. For this purpose, in the FE verification models 1 and 2, a load was applied through the reference point

instead of a displacement at the top of the screw in the second step of the analysis. The load values used for the different specimen configurations are given in Table 8-19. These load values were chosen to achieve convergence of the finite element model.

Table 8-19: Axial load applied to the finite element model for analytical model verification

Wood products and self-tapping screw	EMC in the Initial and First step	Applied Load (kN)
160x170 mm CLT, 8 mm Screw	12% → 21%	10
	21% → 12%	10
260x270 mm CLT, 13 mm Screw	12% → 21%	15
	21% → 12%	10
80x160 mm Glulam, 8 mm Screw	12% → 21%	15
	21% → 12%	10
130x260 mm Glulam, 13 mm Screw	12% → 21%	15
	21% → 12%	10

8.7 Finite Element Model Verification

The comparison between the load-displacement curve from the withdrawal test of specimen conditioned under conditioning settings no. 4 and 5 and verification models 1 and 2 are illustrated in Table 8-20. It can be observed that the slope of the initial linear portion of the slope-displacement curve (K_{ser}) for the drying cases (21% → 12% EMC change) from finite element analysis (FEA) is underpredicted compared to the test results. Reducing the wood moisture content by 3% around fully-threaded screws installed perpendicular to the wood's grain direction can lead to critical tensile stresses in the wood member. The critical tensile stresses can lead to moisture-induced cracks and alter the composite action between the wood material and the thread of the screw (Dietsch, 2017). This behaviour was not accounted for in the finite element model, which might have led to the discrepancy. Furthermore, the finite element model did not consider stress relaxation due to mechano-sorptive effects (Toratti & Svensson, 2000). These aspects are not investigated in the study and can be a topic for investigation in future research. The difference between the slopes from test results and FEA for the wetting cases (12% → 21% EMC change) was limited to about 20%. The ultimate load predicted from FEA and withdrawal tests deviated by a small amount, except for the wetting case of 80x160 mm glulam, 8 mm screw specimen.

However, since the domain of this study is within the linear elastic range, which is below ultimate load levels, the maximum load is less important. Thus, from the difference in the force-displacement behaviour of the different specimen configurations, it can be concluded that the finite element model is more representative of the composite action between the wood material and the thread of the screw for the wetting cases than in the drying cases. Since the primary goal of this project is to investigate the stress distribution of the screw during wood-wetting, the finite element model is adequate for that end.

Table 8-20: Finite element model verification comparison

Specimen Configuration	EMC Change	K_{ser} from withdrawal test	K_{ser} from FEA	Percentage Difference (%)	F_{max} from withdrawal test	F_{max} from FEA	Percentage Difference (%)
160x170 mm CLT, 8 mm Screw	12% → 21%	14.57	12.94	11.11	11.10	12.68	14.26
	21% → 12%	16.55	9.43	43.04	15.19	14.24	6.27
260x270 mm CLT, 13 mm Screw	12% → 21%	13.28	16.02	20.67	23.21	25.26	8.83
	21% → 12%	17.38	10.97	36.89	27.45	25.45	7.30
80x160 mm Glulam, 8 mm Screw	12% → 21%	13.40	13.53	0.98	11.33	15.80	39.48
	21% → 12%	18.36	9.10	50.44	15.38	14.37	6.59
130x260 mm Glulam, 13 mm Screw	12% → 21%	20.62	19.56	5.13	30.60	30.50	0.32
	21% → 12%	25.77	14.41	44.09	38.65	37.09	4.04

8.8 Verification of Analytical Model with Finite Element Analysis Results

The finite element model was created to predict the stress distribution along the length of the self-tapping screw under varying EMC conditions and to verify the analytical model proposed in chapter 7. The input parameters of the analytical model were carefully chosen to reflect the actual behaviour of the self-tapping screw in the mass timber products during axial loading. Also, the finite element and analytical model dimensions were consistent with the withdrawal test specimen dimensions.

8.8.1 Calculation of the Analytical Model Parameters

It is essential to choose representative values of the input parameters for the analytical model proposed in chapter 7 to model the screw stress distribution accurately. The equivalent shear stiffness parameter was found by solving equation 7-51 from the withdrawal stiffness values expressed in kN/mm (Table 6-4) for specimens with constant EMC conditioning before and after screw installation. The withdrawal stiffness values given in Table 6-4 were multiplied by $\pi d L_{eff}$ (d is the outer nominal diameter of the screw and L_{eff} is the effective penetration length) to determine the withdrawal stiffness in units of kN/mm. Solving equation 7-51 gave the equivalent shear stiffness parameter at 12%, 16% and 21% EMC. The equivalent shear stiffness parameter (Γ_e) for the different specimen configurations determined from the withdrawal stiffness (K_w) of the withdrawal test specimens are tabulated in Table 8-21.

Table 8-21: Equivalent shear stiffness parameters

Wood product and self-tapping screw	Specimen conditioning setting no.	Target initial EMC before screw installation	Target final EMC after screw installation	K_w (kN/mm)	Γ_e (MPa/mm)
160x170 mm CLT, 8 mm Screw	1 (constant EMC)	12%	12%	22.86	23.84
	2 (constant EMC)	16%	16%	18.69	19.01
	3 (constant EMC)	21%	21%	13.98	13.71
260x270 mm CLT, 13 mm Screw	1 (constant EMC)	12%	12%	22.09	6.62
	2 (constant EMC)	16%	16%	21.23	6.34
	3 (constant EMC)	21%	21%	15.55	4.55
80x160 mm Glulam, 8 mm Screw	1 (constant EMC)	12%	12%	19.41	20.21
	2 (constant EMC)	16%	16%	20.32	21.64
	3 (constant EMC)	21%	21%	17.41	18.03
130x260 mm Glulam, 13 mm Screw	1 (constant EMC)	12%	12%	26.13	8.15
	2 (constant EMC)	16%	16%	22.54	7.01
	3 (constant EMC)	21%	21%	20.46	6.29

Young's modulus of the different timber products in the direction parallel to the screw axis was determined with equations 7-56, 7-57 and 7-58. A constant value of θ was used for the laminates

of all layers of each CLT and glulam product to simplify the calculation of Young's modulus and swelling coefficient. The Young's modulus values at 12% and 20% EMC were determined from the product manufacturers' guides and published literature (Gerhards, 1982). Young's modulus at 20% EMC from the literature represented the 21% EMC condition. The Young's modulus values are summarised in Table 8-22. The swelling coefficient values along the radial and tangential anatomic direction of the laminates of CLT and glulam were determined experimentally from the swelling tests described in Chapter 5, and equations 7-54 and 7-55 were used to determine the swelling coefficient of the whole CLT/glulam in the direction parallel to the screw axis. The swelling coefficient values, along with the constant value of θ used for the laminates of all layers of each CLT and glulam product, are given in Table 8-23.

Table 8-22: Young's modulus of CLT and glulam

Mass timber product	Layer Type	Wood EMC	E_R (Mpa)	E_T (Mpa)	θ (º)	E_W (Mpa)
160x170 mm CLT	Longitudinal	12%	1193.4	631.8	49	647.2
	Transverse		918	486		
	Longitudinal	21%	918.9	486.5		
	Transverse		706.9	374.2		
260x270 mm CLT	Same property for all layers	12%	969	513	33	678.6
		21%	746.1	395		
80x160 mm Glulam	Same property for all layers	12%	843.2	620	52	609.9
		21%	649.3	477.4		
130x260 mm Glulam	Same property for all layers	12%	843.2	620	65	575.9
		21%	649.3	477.4		

Table 8-23: Effective swelling coefficient values

Mass timber product	θ (º)	α
160x170 mm CLT	49	0.0021
260x270 mm CLT	33	0.0020
80x160 mm Glulam	52	0.0025
130x260 mm Glulam	65	0.0027

The effective area of wood under axial stress during pulling in the pull-push loading condition ($A_{w,eff}$) and the effective area during wood swelling/shrinkage ($A_{w,eff2}$) were calculated with equations 7-5 and 7-25, respectively. The effective wood areas are given in Table 8-24.

Table 8-24: Wood effective areas

Wood products and self-tapping screw	$A_{w,eff}$ (mm^2)	$A_{w,eff2}$ (mm^2)
160x170 mm CLT, 8 mm Screw	32064	377
260x270 mm CLT, 13 mm Screw	60424	1036.7
80x160 mm Glulam, 8 mm Screw	16032	377
130x260 mm Glulam, 13 mm Screw	30212	1036.7

The core diameter of the screws (d_{core}) and the effective penetration length (L_{eff}) were determined from the screw manufacturer's guide, according to the geometry of the withdrawal test specimens. Young's modulus of the screws was determined from the screw tensile test and is already mentioned in Table 8-3.

Table 8-25: Core diameter and effective penetration length of the screws

Screw type	d_{core} (mm)	L_{eff} (mm)
8 mm diameter screw	5	72
13 mm diameter screw	9.6	120

Two moisture content changes were considered on par with the conditioning setting no. 4 and 5 (Table 8-2). In the analytical model, the actual value of the EMC is not required. Only the change in moisture content, Δu is necessary for the analytical model. Δu values (calculated as the final EMC – initial EMC) used in the analytical model are:

Table 8-26: Δu values

Conditioning setting no.	EMC change	Δu
4	12% → 21%	9
5	21% → 12%	-9

The other parameters of the analytical model, ω and K_s were calculated from equations 7-11 and 7-26 with the required values listed above.

8.8.2 Comparison of Screw Stress Distribution from Finite Element Analysis and Analytical Model

The average stress distribution of the screw along its length was determined from finite element verification models 1 and 2 (Table 8-18) at different load values (Table 8-19), which represented the case of axial loading of screw coupled with moisture content change of glulam/CLT. Paths were created in the screw core in the visualization module in ABAQUS/CAE to find the stress distribution. The starting point of the paths was at the entrant side of the screw, and the endpoint was at the bottom end of the screw (Figure 8-15). The stress distribution in the direction parallel to the screw (S22 in ABAQUS/CAE) was determined along these paths, and they were averaged to get the average stress distribution in the screw.

The stress distribution following the analytical model was found with equations 7-52 and 7-53 in MATLAB software with the parameters mentioned in section 8.8.1 (*MATLAB*, 2021). For the convenience of understanding and putting the stress distribution into perspective, Figure 8-16 illustrates the origin of the coordinate system for the screw stress distribution in a typical two-member connection with a self-tapping screw. As the pull-push loading condition is similar to the two-member connection where the side member is assumed to be sufficiently rigid to provide support to the top surface of the main wood member, the stress distribution given by the analytical and the finite element model represents the average stress distribution of the screw in the x-direction with the starting point at the top surface of the main member and ending point at the effective penetration length (L_{eff}). The stress distribution from finite element analysis (numerical) and analytical model (theoretical) are compared in Figures 8-17 and 8-18. The total average stresses in the screw along its length are shown in these figures. The total stress in the screw arises due to the superposition of two separate mechanisms, axial loading and wood swelling, as discussed in section 7.4 of chapter 7. The applied axial load for the different specimen configurations was different, which has been shown here again in Table 8-19.

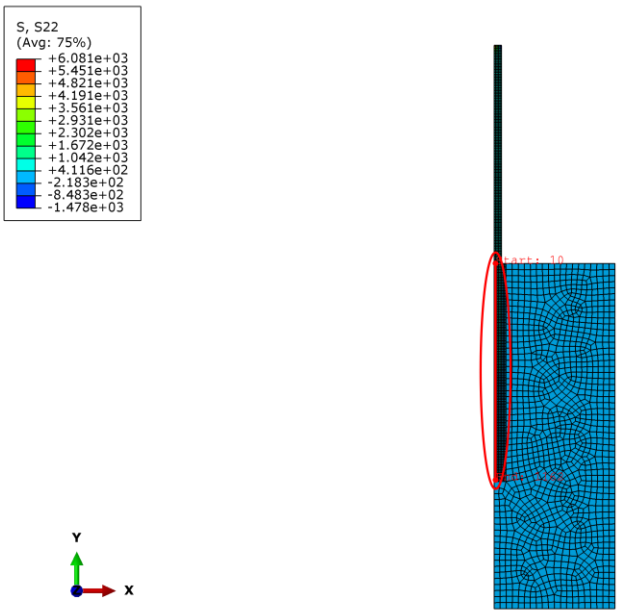

Figure 8-15: Path definition for extracting stress distribution in ABAQUS/CAE

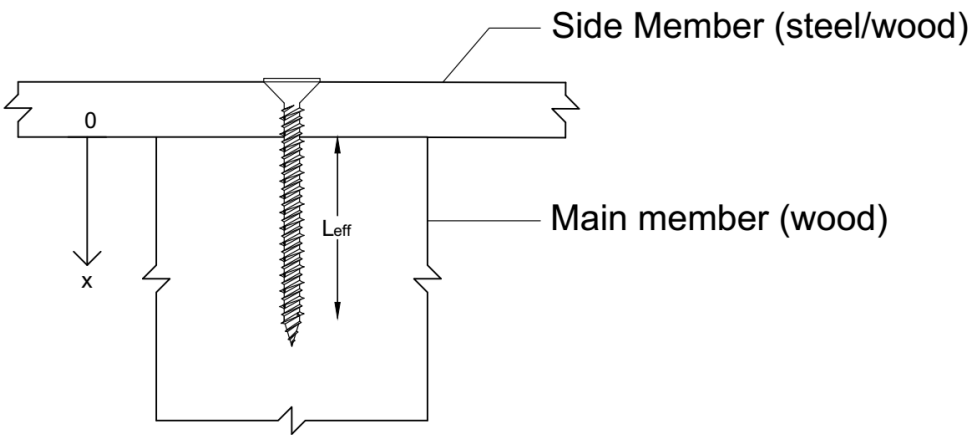

Figure 8-16: Coordinate system for screw stress distribution

Table 8-27: Axial load applied to the finite element model for analytical model verification

Wood products and self-tapping screw	EMC Change	Applied Load (kN)
160x170 mm CLT, 8 mm Screw	12% → 21%	10
	21% → 12%	10
260x270 mm CLT, 13 mm Screw	12% → 21%	15
	21% → 12%	10
80x160 mm Glulam, 8 mm Screw	12% → 21%	15
	21% → 12%	10
130x260 mm Glulam, 13 mm Screw	12% → 21%	15
	21% → 12%	10

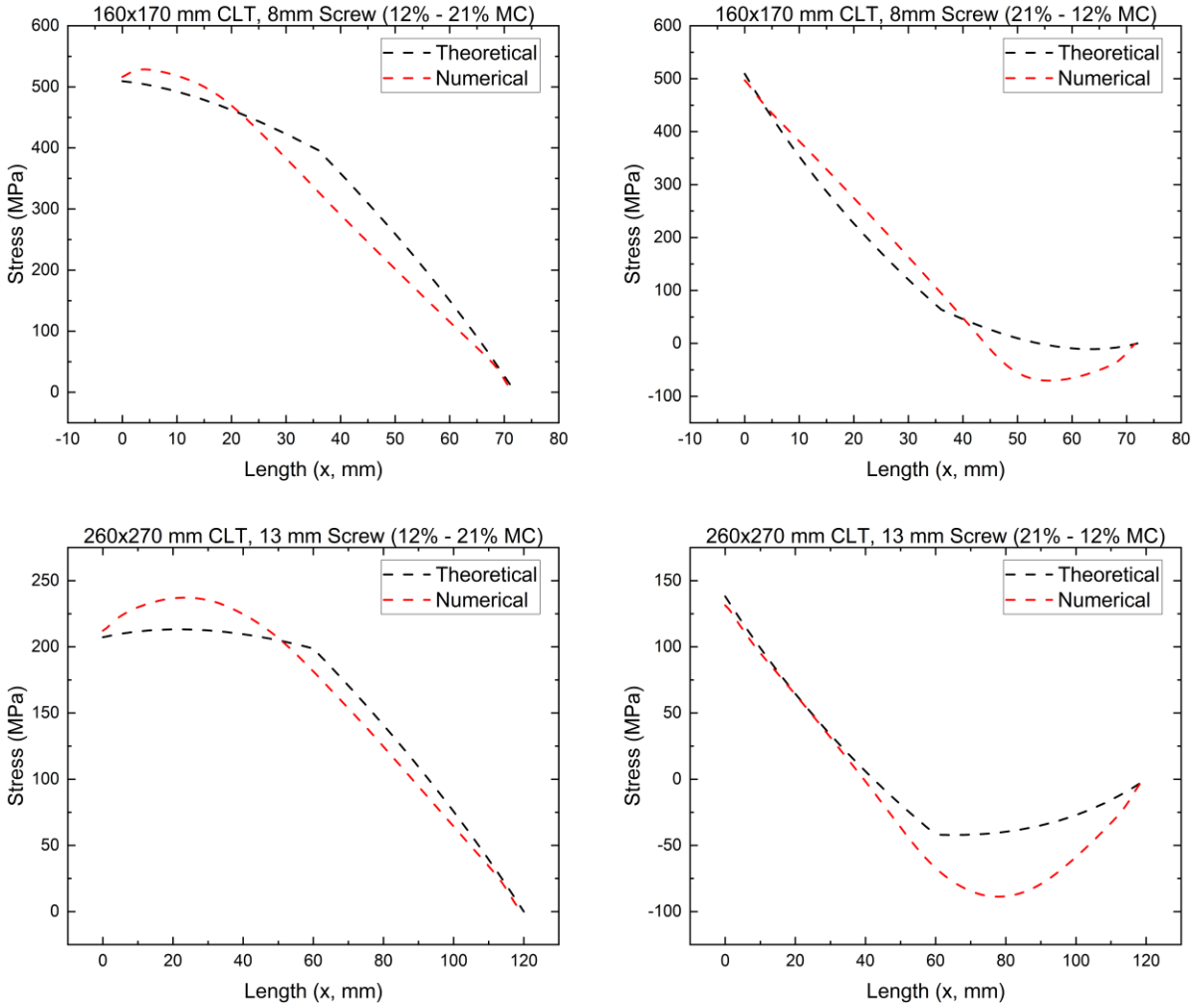

Figure 8-17: Comparison of stress distribution of screw in CLT

Figure 8-17 shows that the stress distribution prediction from the analytical model is very close to the stress distribution from finite element analysis for the wood wetting cases (12% → 21% EMC) for both CLTs. On the other hand, the stress distributions from the analytical and finite element model for the wood drying cases (21% → 12% EMC) for CLT deviated by a small amount. As mentioned earlier, the finite element model might not fully represent the wood drying cases, which can be investigated in future research.

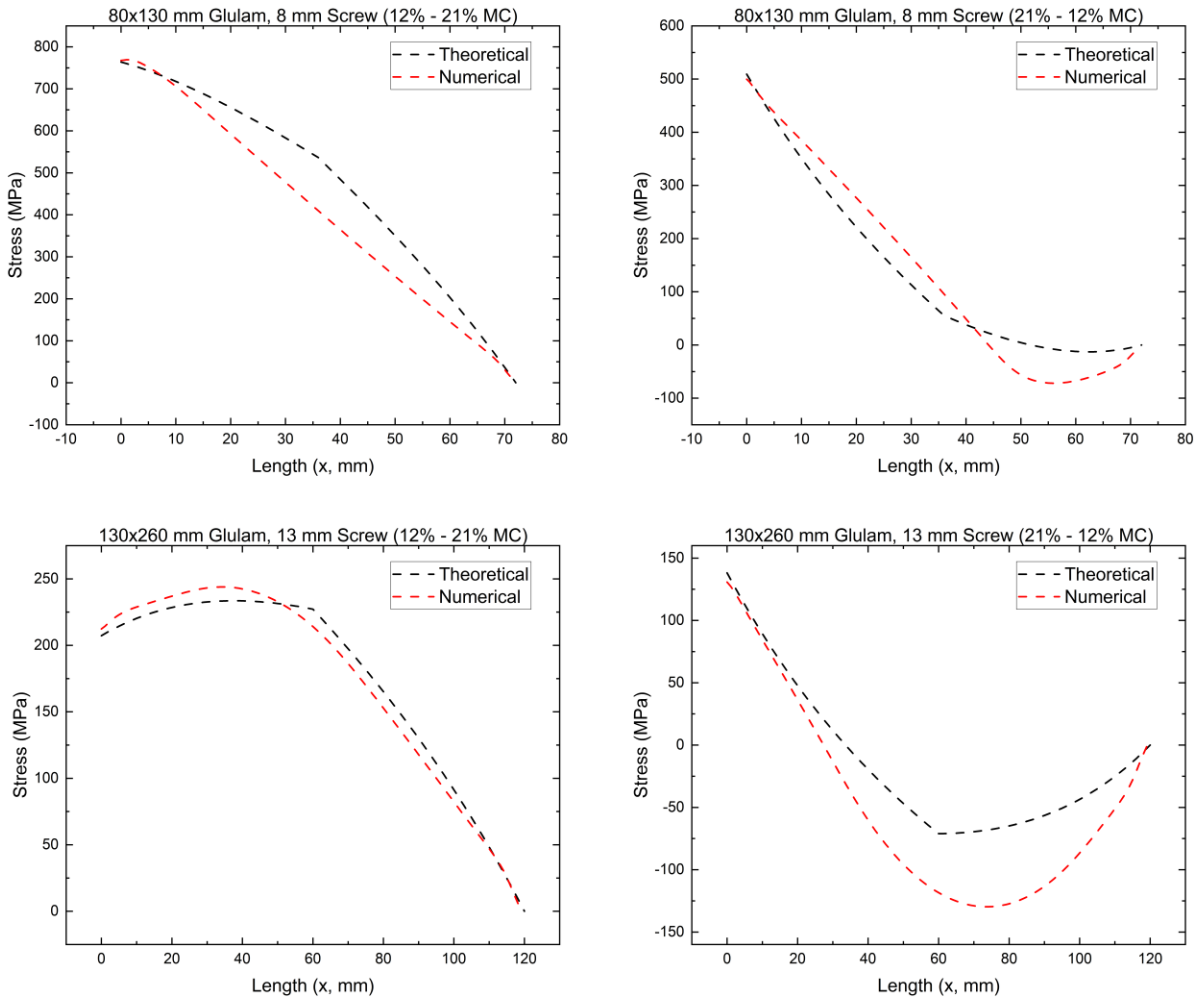

Figure 8-18: Comparison of stress distribution of screw in glulam

The same trend as that of CLT was observed for glulam. For the wood drying cases for CLT and glulam, it is seen that part of the stress in the screw is in compression (negative stress). The compression region might be due to stress relaxation in the screw during wood drying. The difference trend in the theoretical and numerical stress distribution of the screw during wood wetting for the CLT and glulam is slightly different, possibly due to the numerical modelling

simplifications and assumptions. One limitation of the analytical model is that it cannot describe the bump in the stress distribution near the left end of the curves for the wood-wetting cases and the near the right end for the wood-drying cases. Nevertheless, the analytical model can predict the stress distribution of the screw with fair accuracy.

Stress in the screw for both CLT and glulam was non-zero at the screw entrant side, gradually decreasing to zero at the inner end of the screw. The maximum stress was observed between the screw entrant side and the middle of the effective penetration length for the wood wetting cases. On the other hand, the maximum stress for the wood drying cases was observed between the middle of the effective penetration length and the inner end of the screw.

8.9 Analytical Model Implementation

Figures 8-17 and 8-18 show that the closest match between the theoretical and numerical prediction of the stress distribution of the self-tapping screw was found for 130x260 mm glulam with a 13 mm screw. For this specimen configuration, the total average stress distribution in the screw has been decomposed into the stress distributions from two separate mechanisms of axial loading and moisture swelling of the wood. The total stress distribution has been decomposed using equations 7-20, 7-45 and 7-46 from chapter 7. Figure 8-19 illustrates the total average stress decomposition. The applied axial load to the analytical model was 15 kN (Table 8-19). The stress distribution due to axial load (mechanism 1) will significantly increase with a higher axial load value. On the other hand, the stress distribution due to wood swelling (mechanism 2) would remain the same as long as the moisture content change is the same. Thus, the increase in axial load value would outweigh the effect of moisture swelling of the wood on the total average stress distribution in the screw. The total maximum stress in such cases might be close to the tensile strength of the self-tapping screw (>1100 MPa) and cause the tensile failure of the screw. Nevertheless, moisture swelling alone will not cause screw tensile failure in the self-tapping screw configurations investigated in this research. For example, the maximum stress caused by moisture swelling was between 100 and 150 MPa in Figure 8-19, which is a lot lower than the tensile strength of the screw.

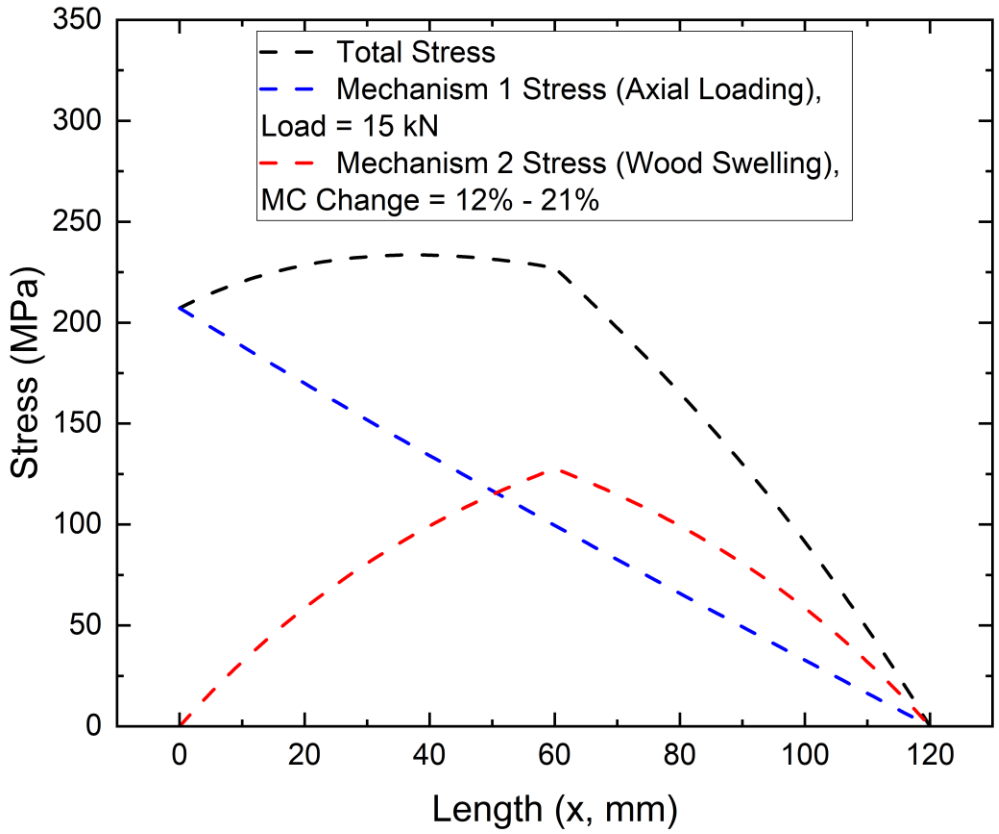

Figure 8-19: Total stress distribution decomposition for 130x260 mm glulam with a 13 mm screw

The combination of sufficiently high axial load value and moisture swelling of wood might cause the tensile failure of self-tapping screws. In two-member connections like the one shown in Figure 8-20, the high axial load values might arise if the screw is installed very tightly, at higher torque than required. In Figure 8-20, the side member is assumed to be sufficiently rigid to support the main member's top surface. This condition then becomes similar to screw withdrawal under the pull-push loading condition. The over-torque in the screw will induce axial load in the screw. Suppose the main wood member undergoes moisture swelling in this over-torqued condition. The analytical and numerical model can then predict the average axial stress distribution in the screw inside the main wood member due to the induced axial load and moisture swelling.

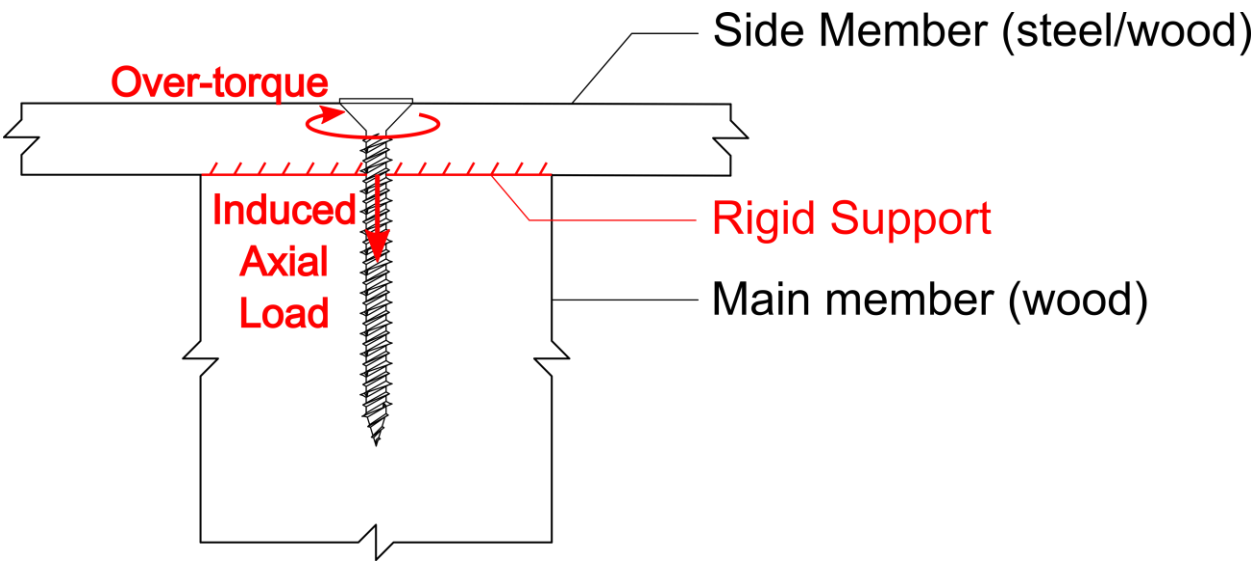

Figure 8-20: Model application in a two-member connection

It was noted in section 8.8.2 that the maximum stress in the screw was observed between the screw entrant side and the middle of the effective penetration length for the wood wetting cases. Now, the analytical model can be used to determine the maximum axial stress arising in screws of different effective penetration lengths (L_{eff}) under a combination of axial load and moisture swelling of the wood. The maximum axial stress arising in screws of 8 mm and 13 mm outer nominal diameter at different penetration lengths inserted into the glulam main member of the configuration shown in Figure 8-21 were determined from the analytical model. The maximum nominal stresses induced in a self-tapping screw at different penetration lengths due to assumed induced axial load of 1 kN, 5 kN and 10 kN from over-torquing of the screw and three moisture content changes of the main glulam member are shown in Figures 8-22 to 8-27. The moisture content changes cover a range from 6% EMC to 15% EMC of the main wood member. The induced axial load in the screw due to over-torquing can be estimated from the induced axial load and over-torque relationship, which can be investigated in future research. Curves similar to Figures 8-22 to 8-27 can be produced for the self-tapping screw of different nominal outer diameters, moisture content changes, induced axial load values and effective penetration lengths. Such curves can form the basis of guidelines for installing and storing self-tapping screws in terms of the initial torquing and moisture exposure during installation and service life.

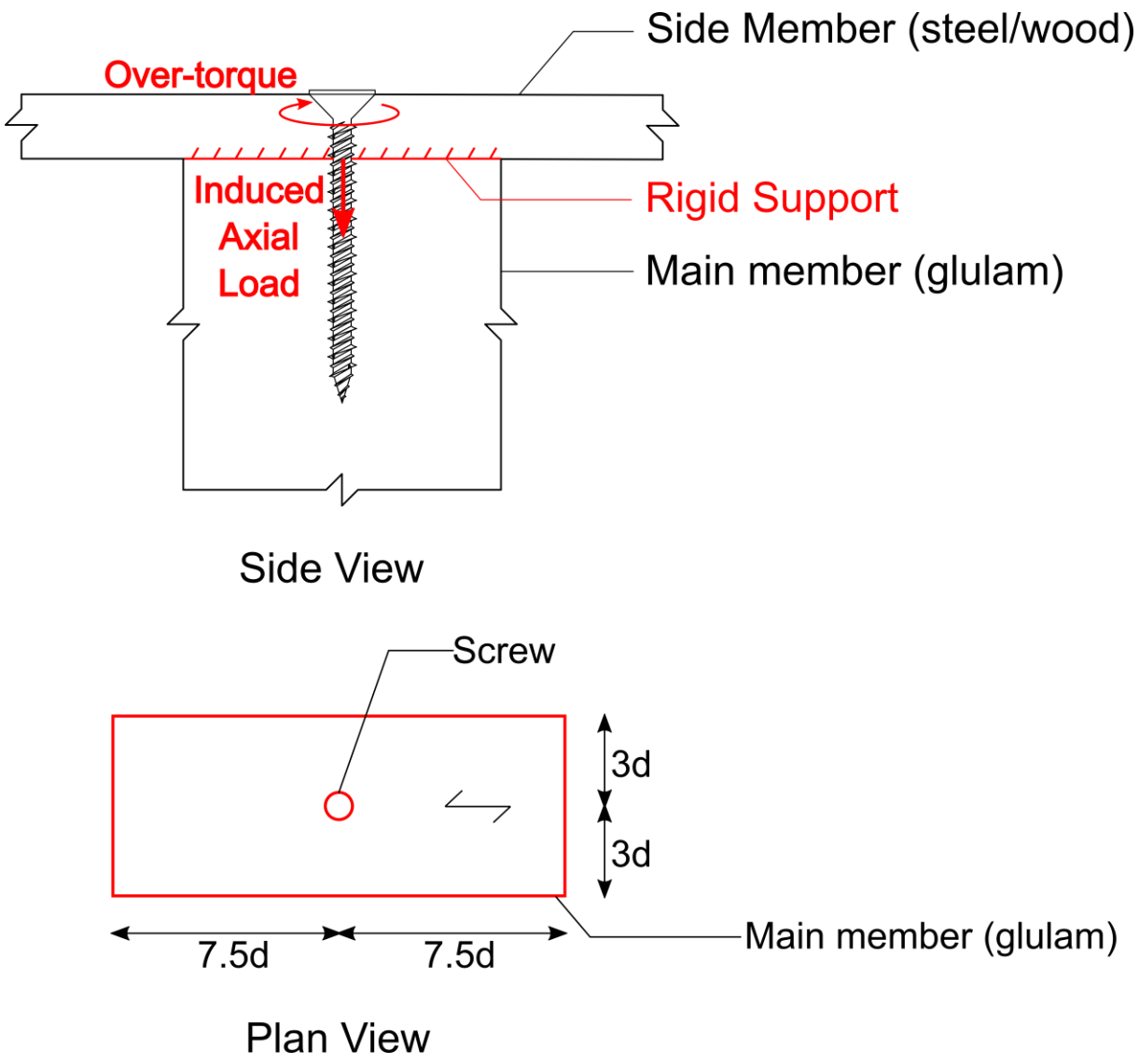

Figure 8-21: Two-member connection with Glulam as the main member

Figures 8-22, 8-23 and 8-24 show that the maximum stress in the 8 mm self-tapping screw exceeds the screw tensile strength (~1300 MPa, section 3.4.4) at an effective penetration length above approximately 200 mm, with an equilibrium moisture content change of 9%, from 6% to 15%. In Figures 8-22, 8-23 and 8-24, the green curves covering the equilibrium moisture content change from 6% to 9% indicate that the increase in maximum stress with the penetration length becomes less scarped at higher induced load levels. Thus, the effective penetration length has a small effect on the maximum stress of the screw at low equilibrium moisture content changes and high induced axial loads. Figures 8-25, 8-26 and 8-27 show that the maximum stress in the 13 mm self-tapping screw exceeds the screw tensile strength (~1200 MPa, section 3.4.4) at an effective penetration

length above approximately 400 mm, with an equilibrium moisture content change from 6% to 15%.

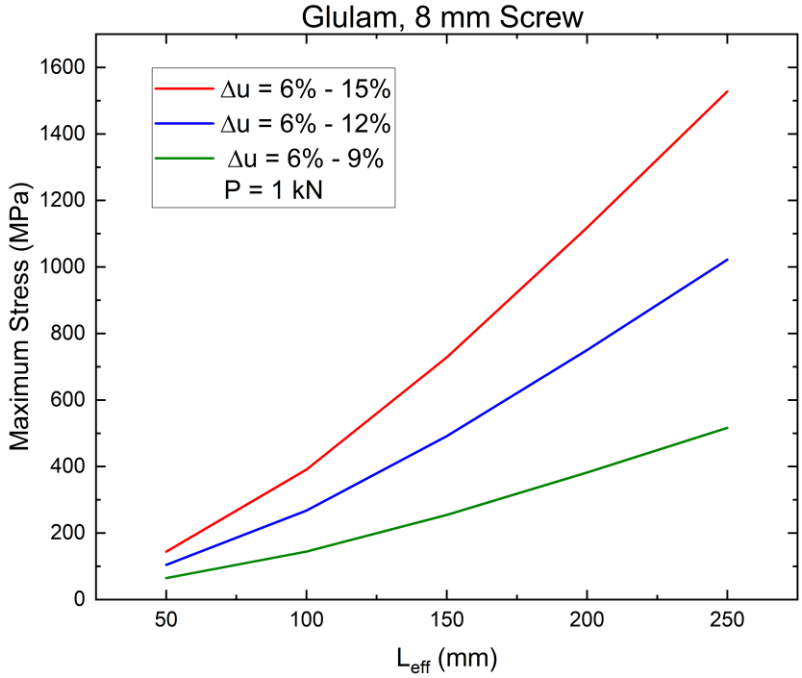

Figure 8-22: Maximum axial stress in 8 mm self-tapping screw at different penetration lengths and equilibrium moisture content changes (Δu) for an induced axial load of 1 kN

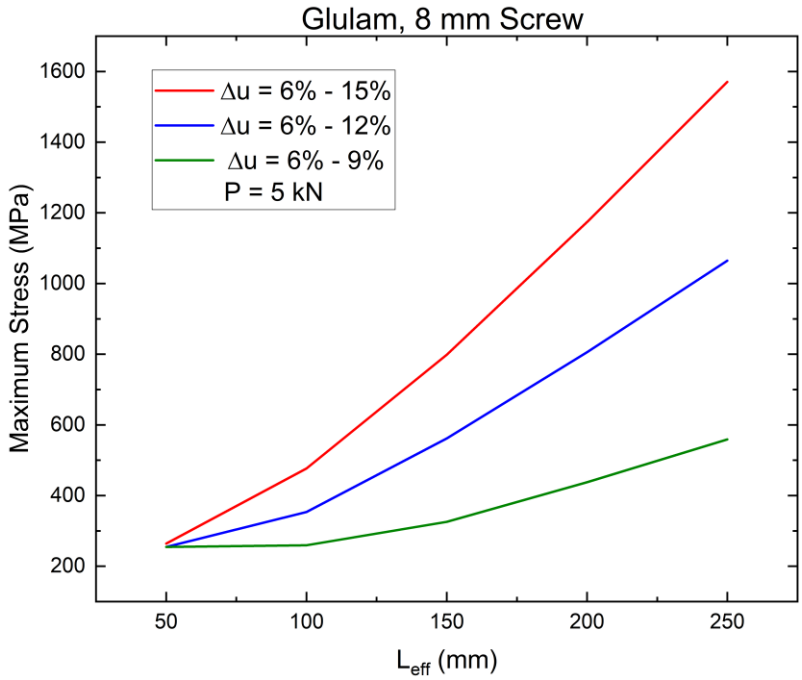

Figure 8-23: Maximum axial stress in 8 mm self-tapping screw at different penetration lengths and equilibrium moisture content changes (Δu) for an induced axial load of 5 kN

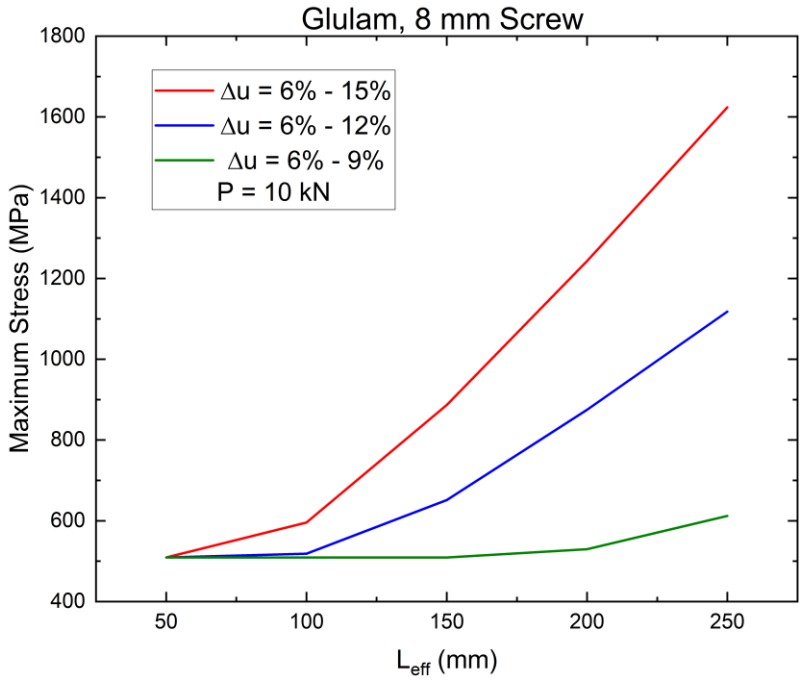

Figure 8-24: Maximum axial stress in 8 mm self-tapping screw at different penetration lengths and equilibrium moisture content changes (Δu) for an induced axial load of 10 kN

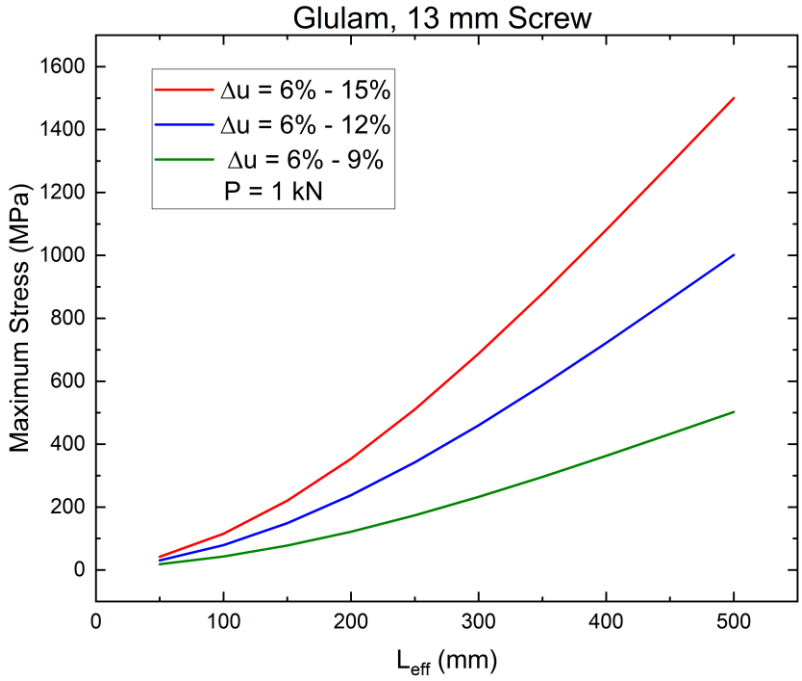

Figure 8-25: Maximum axial stress in 13 mm self-tapping screw at different penetration lengths and equilibrium moisture content changes (Δu) for an induced axial load of 1 kN

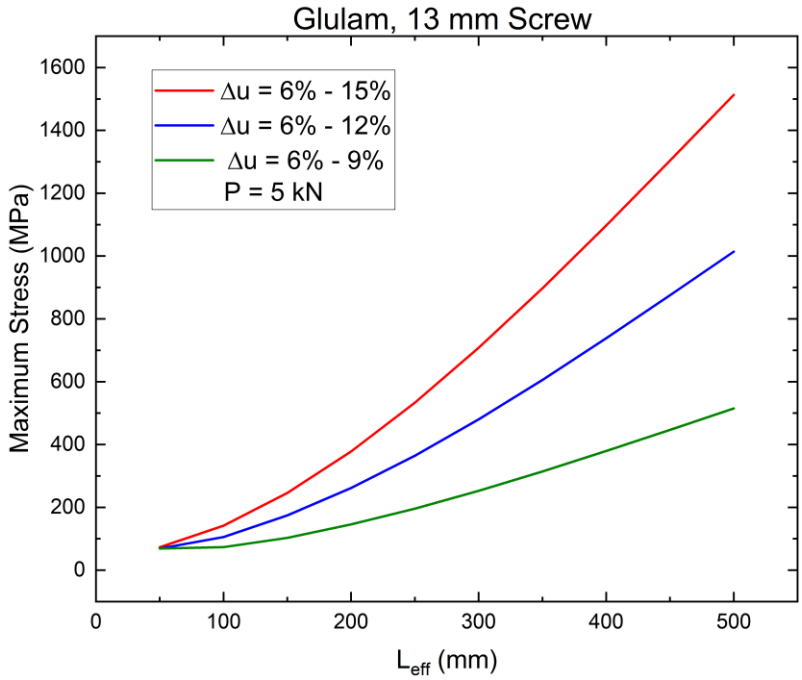

Figure 8-26: Maximum axial stress in 13 mm self-tapping screw at different penetration lengths and equilibrium moisture content changes (Δu) for an induced axial load of 5 kN

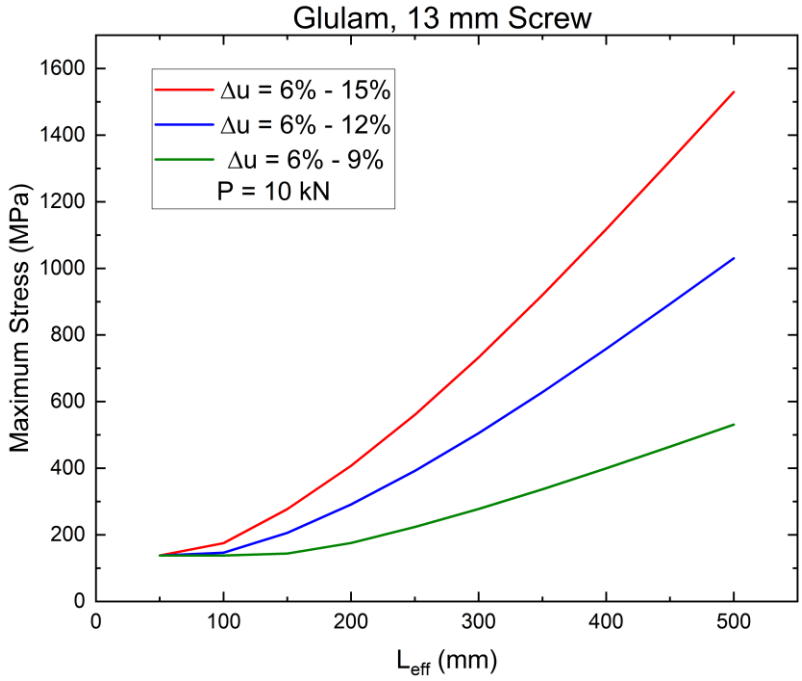

Figure 8-27: Maximum axial stress in 13 mm self-tapping screw at different penetration lengths and equilibrium moisture content changes (Δu) for an induced axial load of 10 kN

8.10 Extension of the Analytical Model to Non-Uniform Moisture Content Case

The analytical and finite element models laid the foundation for modelling the stress distribution of screws under uniform moisture content change throughout the wood member. A possible future work can focus on modelling the case of a non-uniform moisture content change along the length of the screw. For example, a glulam specimen subjected to a moisture content change might have a non-uniform moisture content change distribution. The moisture content change throughout the glulam is shown in the contour plot (Figure 8-28) and along the length of the screw (Figure 8-29). This case has been described in detail in section 4.7.3.

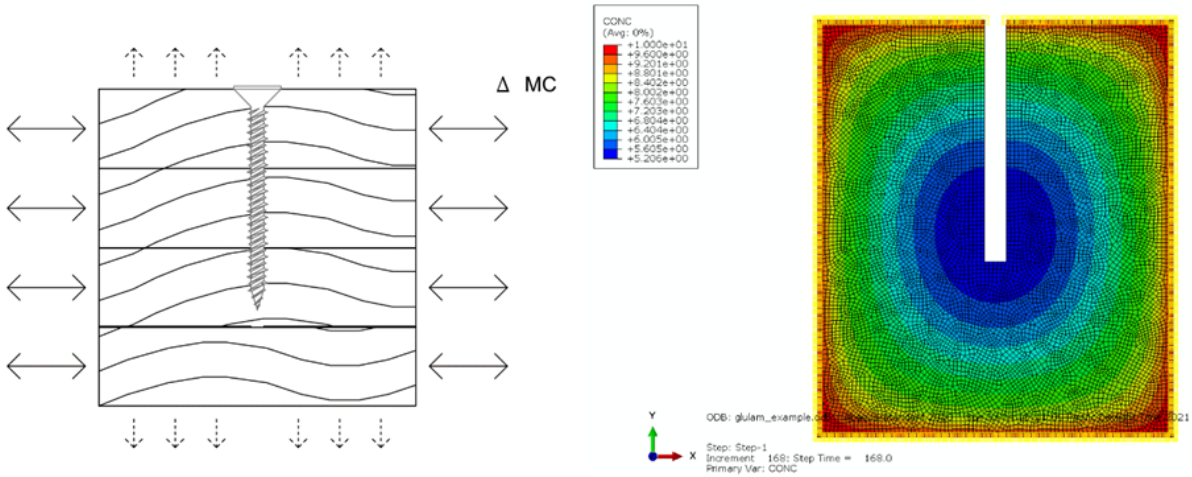

Figure 8-28: Glulam beam with self-tapping screw: schematic diagram (left), moisture content contour plot from ABAQUS analysis of the glulam (right)

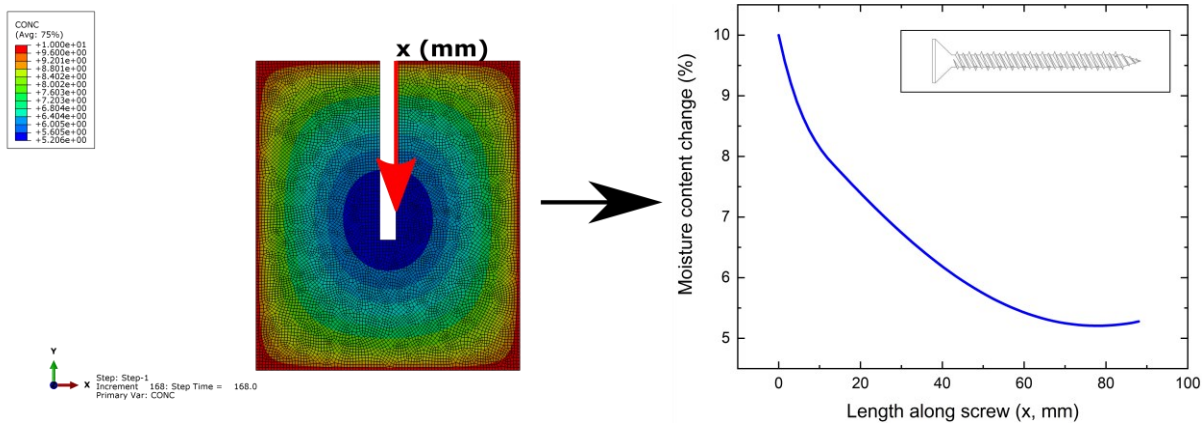

Figure 8-29: Moisture content change of glulam in the vicinity of the screw and parallel to the length of the screw

8.11 Summary

This chapter describes the finite element modelling technique to find the stress distribution in the self-tapping screw under moisture content change and axial load application. The input parameters of the finite element models came from the previous screw tensile tests, CLT and glulam swelling tests, and withdrawal tests. The finite element model was calibrated and verified with experimental withdrawal test results. Finally, the screw stress distributions from the finite element models were compared with the screw stress distributions from the analytical model. The finite element model results and the analytical model predictions of the screw stress distributions showed good agreement for the wood wetting cases. Moreover, the total stress distribution in the screw has been decomposed into the stress distribution under the two separate mechanisms. It is suggested that the moisture swelling of wood can only cause the tensile failure of the screw when a very high axial load in the screw accompanies it.

9 CONCLUSIONS AND RECOMMENDATIONS

9.1 Introduction

This study was focused on understanding the recently identified problem regarding the premature failure of self-tapping screws installed in mass timber products like CLT and glulam. The cause of this failure is suspected to be the additional stress exerted on the screw from the swelling of mass timber products due to an increase in the surrounding moisture content. For a better understanding of the behaviour and failure mechanism of STS, the research first looked into the material properties of STS and the mass timber products. It then investigated the properties of the STS-mass timber composite system.

The tensile properties of different self-tapping screw configurations, moisture transport and swelling properties of two types of CLT and glulam products, and finally, the withdrawal properties of self-tapping screws of two diameters installed into the two types of CLT and glulam products have been investigated and documented in this study. Then an analytical and numerical method of modelling the stress distribution in the self-tapping screw from these properties has been presented.

This study's documented properties and methods can form the basis for developing failure criteria and guidelines for installing and storing self-tapping screws in terms of the initial torquing and moisture exposure during installation and service life. Thus, the premature failure mechanism of self-tapping screws can be prevented based on failure criteria.

9.2 Conclusions

The conclusions drawn from this study are summarised below:

9.2.1 Tensile Properties of Self-tapping Screws

- The difference between the true and the engineering axial stress-strain curve for the self-tapping screw tensile tests was negligible.
- The self-tapping screws did not exhibit any distinct yield plateau or yield point under axial tensile load.
- The failure mode of the screws was brittle, and necking was not observed in the failure region.

- The failure location of the screw under axial tension moved closer to the head of the screw with the decrease of the screw diameter.
- The self-tapping screws exhibited high tensile strength (>1100 MPa), with slight variability in the data.
- The difference between the mean strain at ultimate tensile strength and the mean strain at failure was minimal.

9.2.2 Mass Transport Properties of CLT and Glulam

- The diffusion coefficient of CLT and glulam laminates decreased with the increase of moisture content during moisture adsorption.
- Numerical methods are convenient and reasonably accurate in predicting the moisture content distribution in CLT and glulam products during moisture adsorption, which have not been extensively implemented in practice.
- Although the adhesive between adjacent layers of CLT and glulam have different diffusion coefficient values, assuming the same diffusivity value for the adhesive and the laminates gave reasonably accurate numerical predictions of moisture content distribution inside the CLT and glulam.
- The natural in-grade variation of lumber impacts the moisture content prediction of CLT. This might be overcome by statistically analyzing a large dataset of the diffusion coefficient of different lumber grades over a moisture content range. The presence of gaps between adjacent laminates of the same layer of CLT is also suspected to influence the moisture diffusion process significantly.

9.2.3 Swelling Properties of CLT and Glulam

- The swelling coefficient of the laminates of CLT and glulam along the tangential direction of wood was almost two times the swelling coefficient along the radial direction. On the other hand, the swelling coefficient of the laminates along the longitudinal direction of the wood was negligible.
- Using an effective swelling coefficient to quantify the average swelling of CLT and glulam products in the out-of-plane direction is simple and convenient. It can be implemented judiciously in practical engineering settings. The effective swelling coefficient can be determined from the swelling coefficient values of the laminates of CLT and glulam.

9.2.4 Withdrawal Properties of Self-tapping Screws in CLT and Glulam During Moisture Swelling

- The withdrawal strength and stiffness of almost all samples with constant moisture content before and after screw installation decreased with increased moisture content.
- Wood wetting decreased the withdrawal strength and stiffness, and wood drying increased the withdrawal strength and stiffness.
- The variability of the withdrawal strength data was lower than the withdrawal stiffness data under varying moisture conditions.
- The decrease in withdrawal strength ranged from about 17% to 36% due to a change in moisture content from 12% to 21%.

9.2.5 Stress Distribution in Self-tapping Screws Due to Moisture Content Change and Axial Load Application

- The combination of sufficiently high axial load value and moisture swelling of wood might cause the tensile failure of self-tapping screws. Moisture swelling alone was not large enough to cause screw tensile failure in the self-tapping screw configurations investigated. The high axial load value in self-tapping screws might arise in connections where screws are tightened in over-torque conditions.
- Stress in the screw for both CLT and glulam was non-zero at the screw entrant side, gradually decreasing to zero at the inner end of the screw. The maximum stress was observed between the screw entrant side and the middle of the effective penetration length for the wood wetting cases. On the other hand, the maximum stress for the wood drying cases was observed between the middle of the effective penetration length and the inner end of the screw.

9.3 Original Contributions of the Thesis

The project had the following original contributions to the body of scientific knowledge:

- Implementing numerical methods to determine the diffusion coefficient and model the moisture content distribution of CLT and glulam
- Proposing an analytical approach to predict the swelling of CLT and glulam, verified with numerical and experimental methods

- Determining the withdrawal properties of self-tapping screws inserted into Canadian CLT and glulam products under varying moisture conditions
- Developing an analytical model for predicting the average axial stress distribution in self-tapping screws under axial load and moisture content change of wood
- Numerically predicting the axial stress distribution in self-tapping screws under axial load and moisture content change of wood from screw's withdrawal, screw's elastic, wood's swelling, and wood's elastic properties
- Implementation of the analytical model to determine the maximum stress arising in self-tapping screws under axial load and moisture content change of wood

9.4 Recommendations for Future Work

Further research is encouraged to expand the understanding of the behaviour of self-tapping screws installed in mass timber products. Due to project time constraints, some areas that could not be investigated in this thesis are left for future endeavours. Some areas that would benefit from further research are mentioned below:

- While investigating the moisture transport properties of CLT and glulam, the effects of in-grade variation of lumber grades and the presence of gaps between laminates were not investigated. A large dataset of the moisture diffusion coefficient of different lumber grades used in CLT and glulam can be statistically analyzed over a range of moisture contents. Further, the moisture diffusion process of CLT and glulam with various gap sizes can be investigated in the future.
- Although temperature affects the value of the diffusion coefficient, the effects of temperature were not investigated in this research. This is an aspect that can be explored in future research.
- This research investigated the withdrawal properties of self-tapping screws with only a 10d penetration length, inserted perpendicular to the wood's grain direction. Future research can examine the withdrawal properties of self-tapping screws at different penetration lengths and screws inserted to varying angles to the wood's grain direction.
- The analytical and finite element models laid the foundation for modelling the stress distribution of screws under uniform moisture content change throughout the wood member. A possible future work can focus on modelling the case of a non-uniform moisture

content change along the length of the screw. The methods proposed in chapter 4 can be utilized for modelling the moisture content change distribution of the wood member along the length of the screw.

- A constant value of equivalent shear stiffness parameter and the elastic properties of wood was considered in the analytical model. It is well established that wood properties change significantly with the moisture content of the wood. The change in the equivalent shear stiffness parameter and elastic properties of wood can be incorporated to develop a more sophisticated analytical model.
- The analytical model can be used to predict the stress distribution of the screw, which can pave the way for developing the failure criteria of self-tapping screws based on fracture mechanics concepts in the future. Two possible methods for developing the failure criteria are: (a) Weibull's weakest link theory and (b) the Maximum stress failure criterion. Weibull's weakest link theory states that even low-stress values occurring over a large area can cause failure. On the other hand, the Maximum stress failure criterion states that failure occurs when stress reaches a prescribed value (like the self-tapping screw tensile strength) at any single point.
- In the future, connection tests involving two-member wood-to-wood and wood-to-steel connections with self-tapping screws under moisture content change can be conducted to verify the screw failure criteria. Further, the connection tests can help understand how over-tightening the self-tapping screws in connections can induce axial load in the screws and cause premature failure during wood swelling of the main wood member.

REFERENCES

Abukari, M. H. (2012). *The performance of structural screws in Canadian Glulam*. McGill University.

Angst, V., & Malo, K. A. (2012a). Effect of self-tapping screws on moisture induced stresses in glulam. *Engineering Structures*, *45*, 299–306. https://doi.org/https://doi.org/10.1016/j.engstruct.2012.06.048

Angst, V., & Malo, K. A. (2012b). The effect of climate variations on glulam—an experimental study. *European Journal of Wood and Wood Products 2012 70:5*, *70*(5), 603–613. https://doi.org/10.1007/S00107-012-0594-Y

Arends, T., Pel, L., & Smeulders, D. (2018). Moisture penetration in oak during sinusoidal humidity fluctuations studied by NMR. *Construction and Building Materials*, *166*, 196–203. https://doi.org/https://doi.org/10.1016/j.conbuildmat.2018.01.133

ASTM International. (2017). *ASTM E111-17: Standard Test Method for Young's Modulus, Tangent Modulus, and Chord Modulus*.

ASTM International. (2021). *ASTM E8/E8M-21: Standard Test Methods for Tension Testing of Metallic Materials*.

Avez, C., Descamps, T., Serrano, E., & Léoskool, L. (2016). Finite element modelling of inclined screwed timber to timber connections with a large gap between the elements. *European Journal of Wood and Wood Products*, *74*(3), 467–471. https://doi.org/10.1007/s00107-015-1002-1

Avramidis, S., Hatzikiriakos, S. G., & Siau, J. F. (1994). An irreversible thermodynamics model for unsteady-state nonisothermal moisture diffusion in wood. *Wood Science and Technology*, *28*(5), 349–358. https://doi.org/10.1007/BF00195282

Avramidis, St., & Siau, J. F. (1987). An investigation of the external and internal resistance to moisture diffusion in wood. *Wood Science and Technology*, *21*(3), 249–256. https://doi.org/10.1007/BF00351396

Bedon, C., Sciomenta, M., & Fragiacomo, M. (2020). Mechanical Characterization of Timber-to-Timber Composite (TTC) Joints with Self-Tapping Screws in a Standard Push-Out Setup. In *Applied Sciences* (Vol. 10, Issue 18). https://doi.org/10.3390/app10186534

Beer, F. P., Johnston, E. R., DeWolf, J. T., & Mazurek, D. F. (2012). *Mechanics of materials* (6th ed.). McGraw-Hill Education.

Brandner, R., & Schickhofer, G. (2006). System effects of structural elements: determined for bending and tension. *9th World Conference on Timber Engineering (WCTE)*.

Canadian Standards Association. (2019). *CSA O86:19 Engineering design in wood*.

Chen, H.-T., Lin, J.-Y., Wu, C.-H., & Huang, C.-H. (1996). NUMERICAL ALGORITHM FOR ESTIMATING TEMPERATURE-DEPENDENT THERMAL CONDUCTIVITY. *Numerical Heat Transfer, Part B: Fundamentals*, *29*(4), 509–522. https://doi.org/10.1080/10407799608914995

Chen, W. T., & Nelson, C. W. (1979). Thermal Stress in Bonded Joints. *IBM Journal of Research and Development*, *23*(2), 179–188. https://doi.org/10.1147/rd.232.0179

Chiniforush, A. A., Akbarnezhad, A., Valipour, H., & Malekmohammadi, S. (2019). Moisture and temperature induced swelling/shrinkage of softwood and hardwood glulam and LVL: An experimental study. *Construction and Building Materials*, *207*, 70–83. https://doi.org/https://doi.org/10.1016/j.conbuildmat.2019.02.114

Chiniforush, A. A., Valipour, H., & Akbarnezhad, A. (2019). Water vapor diffusivity of engineered wood: Effect of temperature and moisture content. *Construction and Building Materials*, *224*, 1040–1055. https://doi.org/https://doi.org/10.1016/j.conbuildmat.2019.08.013

Chui, Y. H., & Craft, S. (2002). Fastener head pull-through resistance of plywood and oriented strand board. *Canadian Journal of Civil Engineering*, *29*(3), 384–388. https://doi.org/10.1139/l02-019

Dietsch, P. (2017). Effect of reinforcement on shrinkage stresses in timber members. *Construction and Building Materials*, *150*, 903–915. https://doi.org/https://doi.org/10.1016/j.conbuildmat.2017.06.033

Dietsch, P., & Brandner, R. (2015). Self-tapping screws and threaded rods as reinforcement for structural timber elements – A state-of-the-art report. *Construction and Building Materials*, *97*, 78–89. https://doi.org/https://doi.org/10.1016/j.conbuildmat.2015.04.028

European Committee for Standardization. (1999). *EN 1382:1999 Timber structures - Test methods - Withdrawal capacity of timber fasteners*.

European Committee for Standardization. (2004). *EN 1995-1-1:2004 Eurocode 5: Design of timber structures*.

European Committee for Standardization. (2015). EN 16351: Timber Structures - Cross Laminated Timber - Requirements. In *2015*.

Feldt, P., & Thelin, A. (2018). *Glued-in rods in timber structures: Finite element analyses of adhesive failure*. Chalmers University of Technology.

Gehloff, M. (2011). *Pull-Out Resistance of Self-Tapping Wood Screws*. University of British Columbia.

Gereke, T., & Niemz, P. (2010). Moisture-induced stresses in spruce cross-laminates. *Engineering Structures*, *32*(2), 600–606. https://doi.org/10.1016/J.ENGSTRUCT.2009.11.006

Gereke, T., Schnider, T., Hurst, A., & Niemz, P. (2008). Identification of moisture-induced stresses in cross-laminated wood panels from beech wood (Fagus sylvatica L.). *Wood Science and Technology*, *43*(3), 301. https://doi.org/10.1007/s00226-008-0218-1

Gerhards, C. C. (1982). Effect of Moisture Content and Temperature on the Mechanical Properties of Wood: An Analysis of Immediate Effects. *Wood and Fiber Science*, *14*(1), 4–36.

German Institute for Standardisation. (2008). *DIN 1052: 2008 DESIGN OF TIMBER STRUCTURES - GENERAL RULES AND RULES FOR BUILDINGS*.

Gutknecht, M. P., & MacDougall, C. (2019). Withdrawal resistance of structural self-tapping screws parallel-to-grain in common Canadian timber species. *Canadian Journal of Civil Engineering*, *46*(10), 952–962. https://doi.org/10.1139/cjce-2018-0374

Hukka, A. (1999). *The Effective Diffusion Coefficient and Mass Transfer Coefficient of Nordic Softwoods as Calculated from Direct Drying Experiments*. *53*(5), 534–540. https://doi.org/doi:10.1515/HF.1999.088

Jensen, J. L., Koizumi, A., Sasaki, T., Tamura, Y., & Iijima, Y. (2001). Axially loaded glued-in hardwood dowels. *Wood Science and Technology*, *35*(1), 73–83. https://doi.org/10.1007/s002260000076

Kain, G., Lienbacher, B., Barbu, M.-C., Senck, S., & Petutschnigg, A. (2018). Water vapour diffusion resistance of larch (Larix decidua) bark insulation panels and application considerations based on numeric modelling. *Construction and Building Materials*, *164*, 308–316. https://doi.org/https://doi.org/10.1016/j.conbuildmat.2017.12.212

Lee, S. S., Pan, S. J., & Jeong, G. Y. (2019). Effects of size, species and adjacent lamina on moisture related strain in glulam. *Wood and Fiber Science*, *51*(2), 101–118.

Liu, J. Y., Simpson, W. T., & Verrill, S. P. (2001). AN INVERSE MOISTURE DIFFUSION ALGORITHM FOR THE DETERMINATION OF DIFFUSION COEFFICIENT. *Drying Technology*, *19*(8), 1555–1568. https://doi.org/10.1081/DRT-100107259

Mack, J. J. (J. (1979). *The withdrawal resistance of plain steel nails and screws in Australian timbers / by J.J. Mack* (CSIRO. D. of B. Research, Ed.). CSIRO.

MATLAB (9.9.0 (R2020b Update 5)). (2021). The MathWorks Inc.

MTC Solutions. (2020). *Structural Screw Design Guide*.

Murase, Y. (1984). Friction of Wood Sliding on Various Materials. *Journal of the Faculty of Agriculture, Kyushu University*, *28*(4), 147–160.

Naderer, E., Franke, S., & Franke, B. (2016, August). Numerical simulation of reinforced timber structures perpendicualr to the grain. *WCTE 2016. Wien, Österreich.*

OriginLab Corporation. (2016). *OriginPro 2017* (9.4.0.220). OriginLab Corporation.

OriginLab Corporation. (2021). *Origin 2022* (9.9.0.225). OriginLab Corporation.

Pang, S.-J., & Jeong, G. Y. (2020). Swelling and shrinkage behaviors of cross-laminated timber made of different species with various lamina thickness and combinations. *Construction and*

Building Materials, *240*, 117924. https://doi.org/https://doi.org/10.1016/j.conbuildmat.2019.117924

Pirnbacher, G., Brandner, R., & Schickhofer, G. (2009). Base Parameters of self-tapping Screws. *WORKING COMMISSION W18 - TIMBER STRUCTURES*.

Plumb, O. A., Spolek, G. A., & Olmstead, B. A. (1985). Heat and mass transfer in wood during drying. *International Journal of Heat and Mass Transfer*, *28*(9), 1669–1678. https://doi.org/https://doi.org/10.1016/0017-9310(85)90141-3

Ringhofer, A., Brandner, R., & Schickhofer, G. (2015). Withdrawal resistance of self-tapping screws in unidirectional and orthogonal layered timber products. *Materials and Structures*, *48*(5), 1435–1447. https://doi.org/10.1617/s11527-013-0244-9

Ringhofer, A., Grabner, M., Silva, C. V., Branco, J., & Schickhofer, G. (2014). The influence of moisture content variation on the withdrawal capacity of self-tapping screws. *Holztechnologie*, *55*(3), 33–40.

Rosenkilde, A., & Arfvidsson, J. (1997). *Measurement and Evaluation of Moisture Transport Coefficients During Drying of Wood*. *51*(4), 372–380. https://doi.org/doi:10.1515/hfsg.1997.51.4.372

Ross, R. J., & USDA Forest Service., F. P. Laboratory. (2010). *Wood handbook : Wood as an engineering material*. Forest Products Laboratory. https://doi.org/10.2737/FPL-GTR-190

Salin, J.-G. (1996). Mass Transfer from Wooden Surfaces and Internal Moisture Non-Equilibrium. *Drying Technology*, *14*(10), 2213–2224. https://doi.org/10.1080/07373939608917204

Shi, S. Q. (2007). Diffusion model based on Fick's second law for the moisture absorption process in wood fiber-based composites: is it suitable or not? *Wood Science and Technology*, *41*(8), 645–658. https://doi.org/10.1007/s00226-006-0123-4

Silva, C., Branco, J. M., Ringhofer, A., Lourenço, P. B., & Schickhofer, G. (2016). The influences of moisture content variation, number and width of gaps on the withdrawal resistance of self tapping screws inserted in cross laminated timber. *Construction and Building Materials*, *125*, 1205–1215. https://doi.org/https://doi.org/10.1016/j.conbuildmat.2016.09.008

Simulia. (2020). *ABAQUS Software* (No. 2020). Dassault Systèmes.

Srpčič, S., Srpčič, J., Saje, M., & Turk, G. (2009). Mechanical analysis of glulam beams exposed to changing humidity. *Wood Science and Technology*, *43*(1), 9–22. https://doi.org/10.1007/s00226-008-0196-3

Stamatopoulos, H., & Malo, K. A. (2015). Withdrawal capacity of threaded rods embedded in timber elements. *Construction and Building Materials*, *94*, 387–397. https://doi.org/https://doi.org/10.1016/j.conbuildmat.2015.07.067

Stamatopoulos, H., & Malo, K. A. (2016). Withdrawal stiffness of threaded rods embedded in timber elements. *Construction and Building Materials*, *116*, 263–272. https://doi.org/https://doi.org/10.1016/j.conbuildmat.2016.04.144

Taylor, T. C., & Yuan, F. L. (1962). Thermal stress and fracture in shear-constrained semiconductor device structures. *IRE Transactions on Electron Devices*, *9*(3), 303–308. https://doi.org/10.1109/T-ED.1962.14987

Toratti, T., & Svensson, S. (2000). Mechano-sorptive experiments perpendicular to grain under tensile and compressive loads. *Wood Science and Technology*, *34*(4), 317–326. https://doi.org/10.1007/s002260000059

Uibel, T., & Blaß, H. J. (2007). Edge joints with dowel type fasteners in cross laminated timber. *CIB-W18 Meeting*.

Volkerson, O. (1938). Die Niektraftverteiling in Zugbeanspruchten mit Konstanten Laschquershritten. *Luftfahrforschung*, *48*.

Wu, Q., & Suchsland, O. (1996). PREDICTION OF MOISTURE CONTENT AND MOISTURE GRADIENT OF AN OVERLAID PARTICLEBOARD. *Wood and Fiber Science*, *28*(2), 227–239.

Zhou, J., Chui, Y. H., Gong, M., & Hu, L. (2017). Elastic properties of full-size mass timber panels: Characterization using modal testing and comparison with model predictions. In *Composites Part B: Engineering* (Vol. 112, pp. 203–212). https://doi.org/https://doi.org/10.1016/j.compositesb.2016.12.027

APPENDIX A – SCREW TENSILE TEST STRESS-STRAIN CURVES

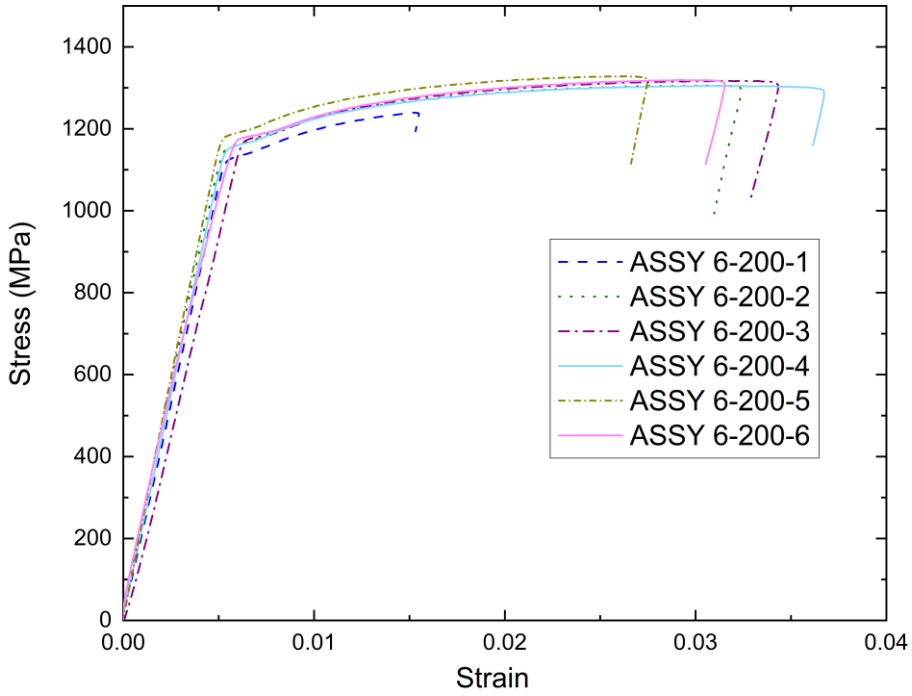

Appendix A 1: ASSY 6-200 screw configuration stress-strain curves

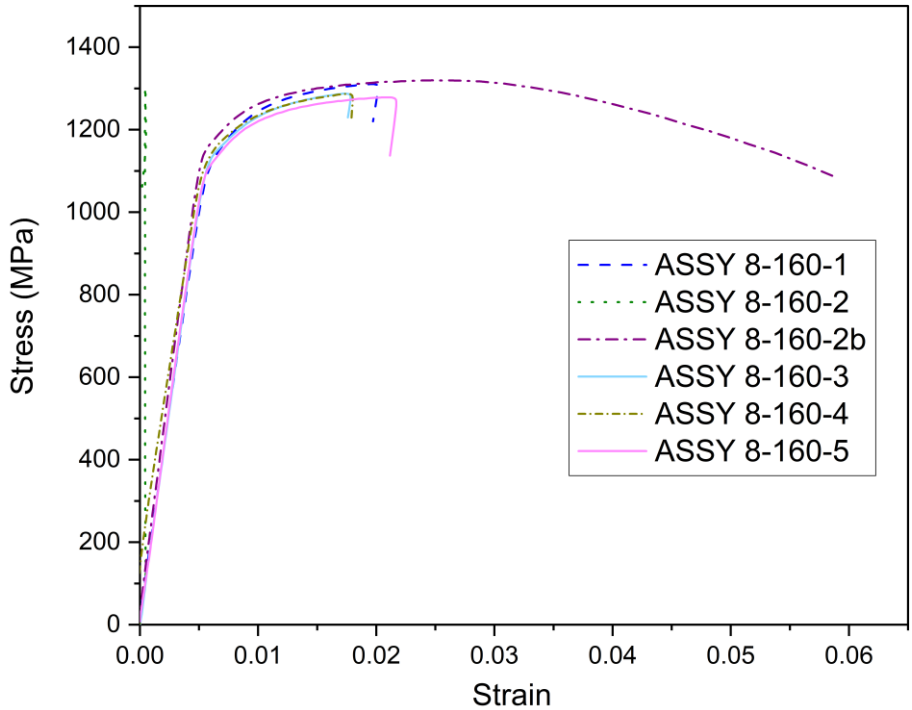

Appendix A 2: ASSY 8-160 screw configuration stress-strain curves

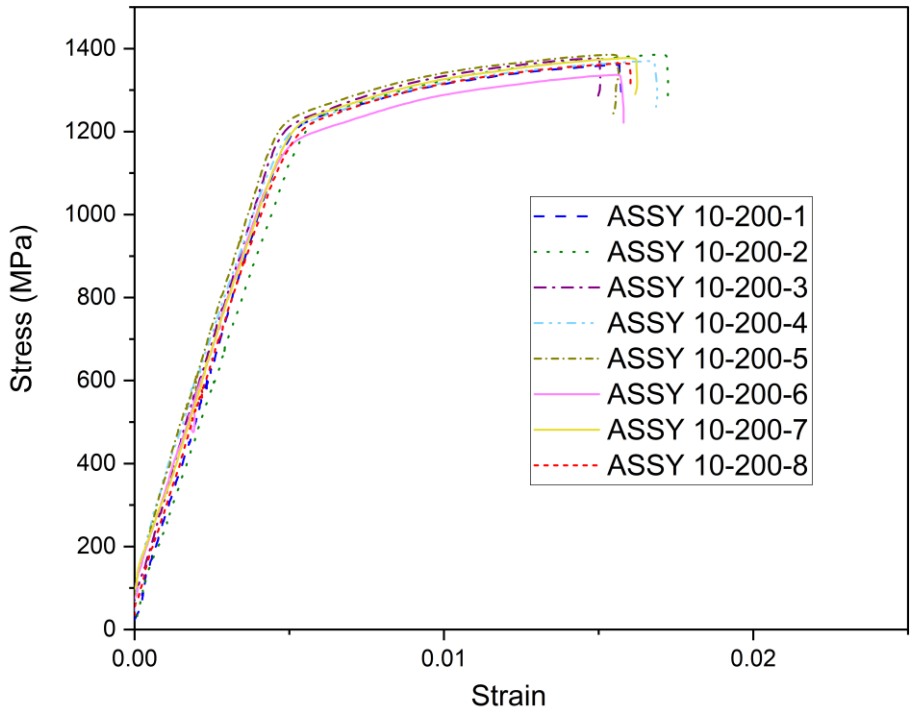

Appendix A 3: ASSY 10-200 screw configuration stress-strain curves

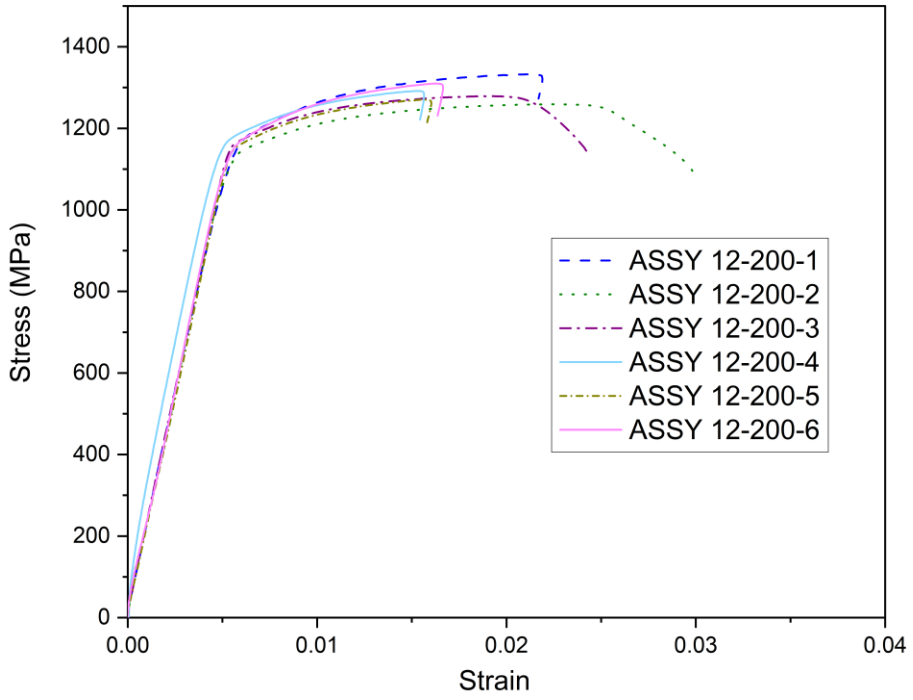

Appendix A 4: ASSY 12-200 screw configuration stress-strain curves

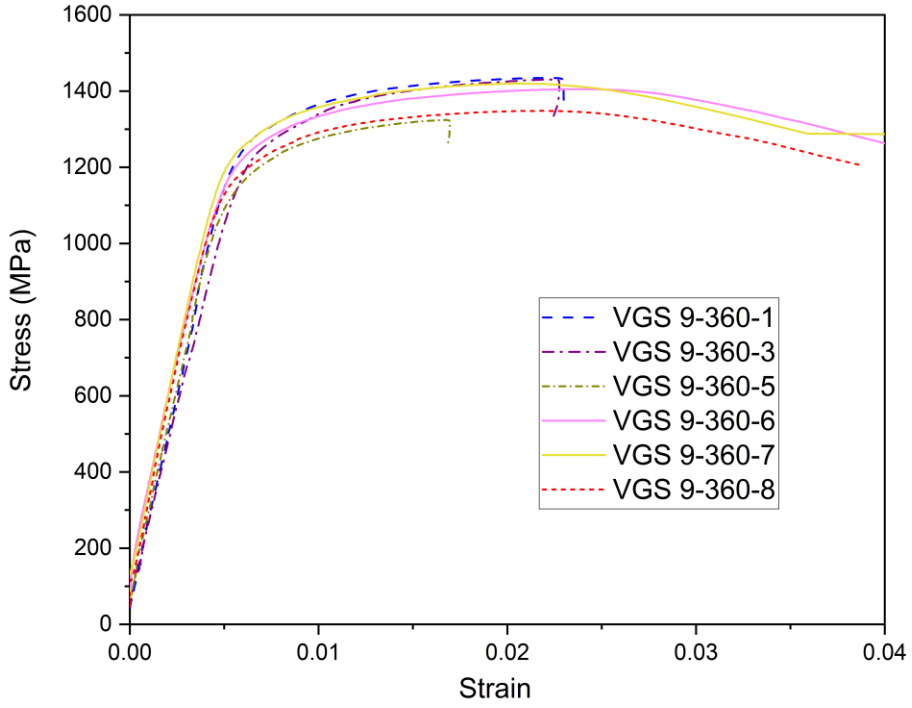

Appendix A 5: VGS 9-360 screw configuration stress-strain curves

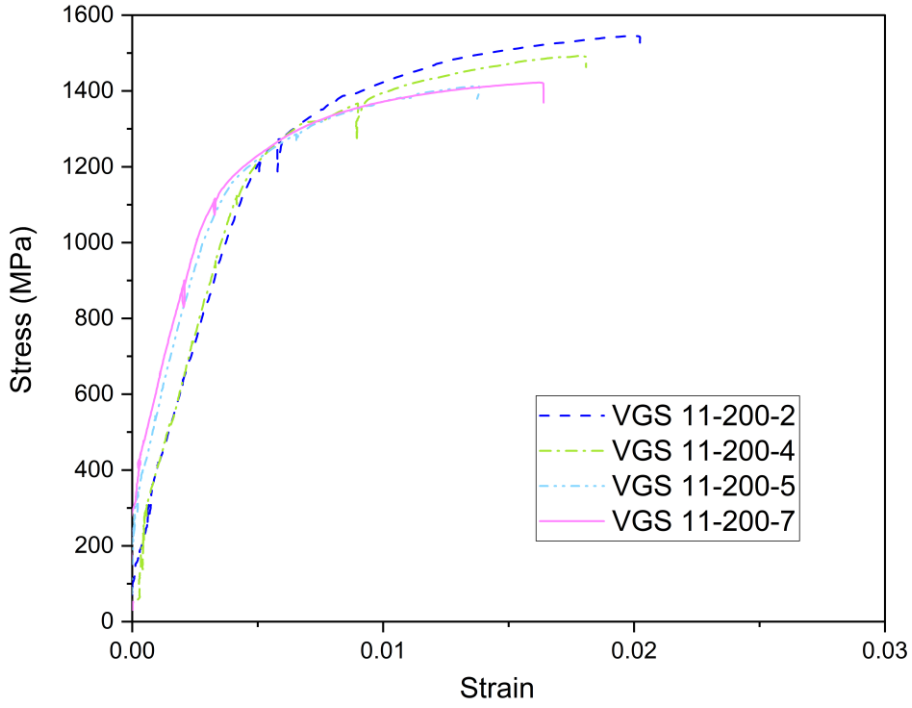

Appendix A 6: VGS 11-200 screw configuration stress-strain curves

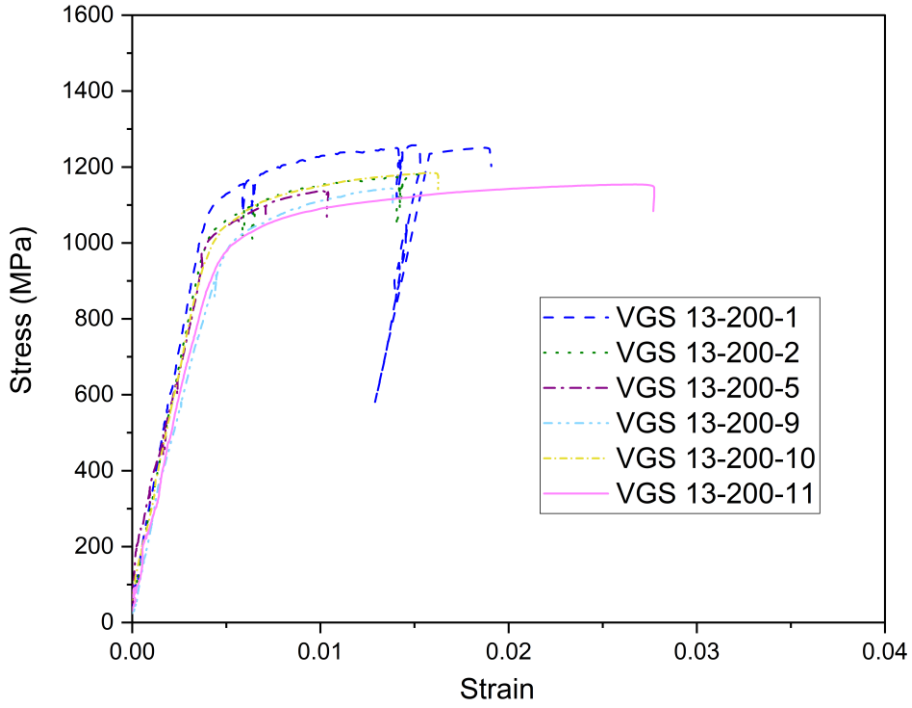

Appendix A 7: VGS 13-200 screw configuration stress-strain curves

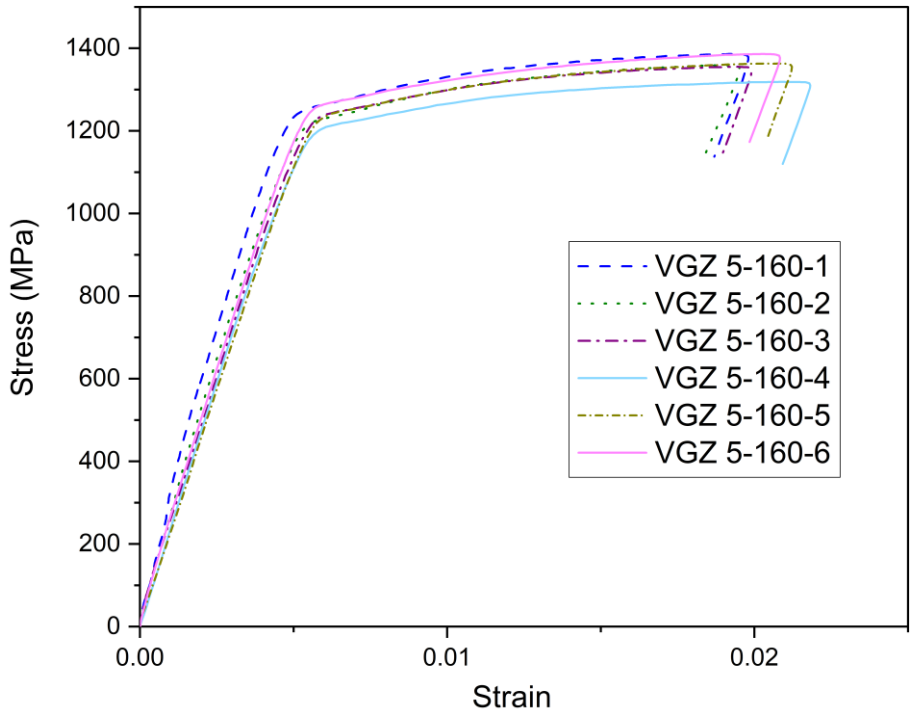

Appendix A 8: VGZ 5-160 screw configuration stress-strain curves

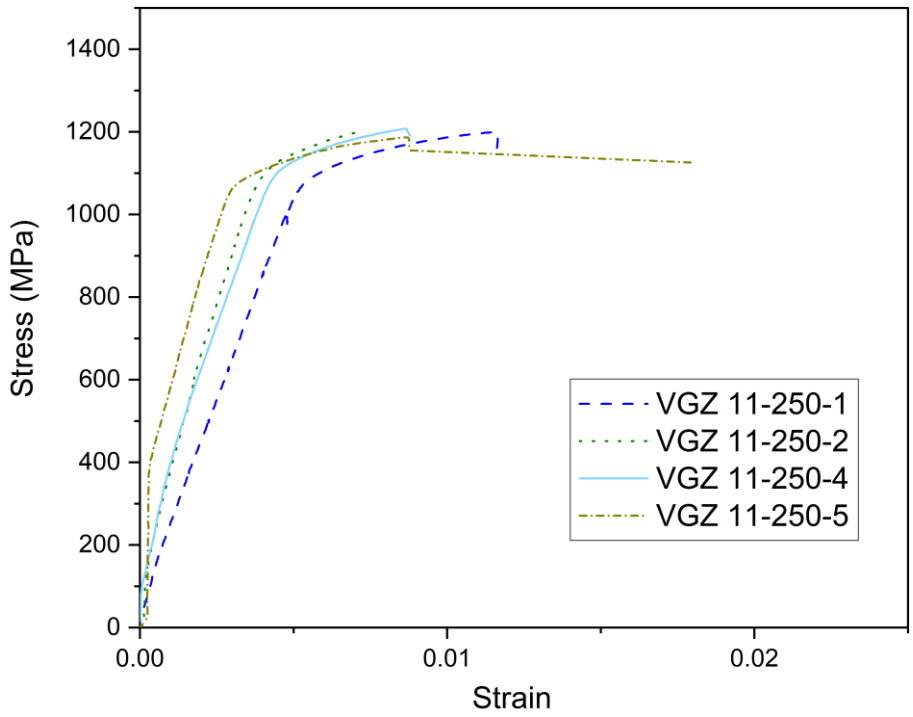

Appendix A 9: VGZ 11-250 screw configuration stress-strain curves

APPENDIX B – WITHDRAWAL TEST LOAD-DISPLACEMENT CURVES

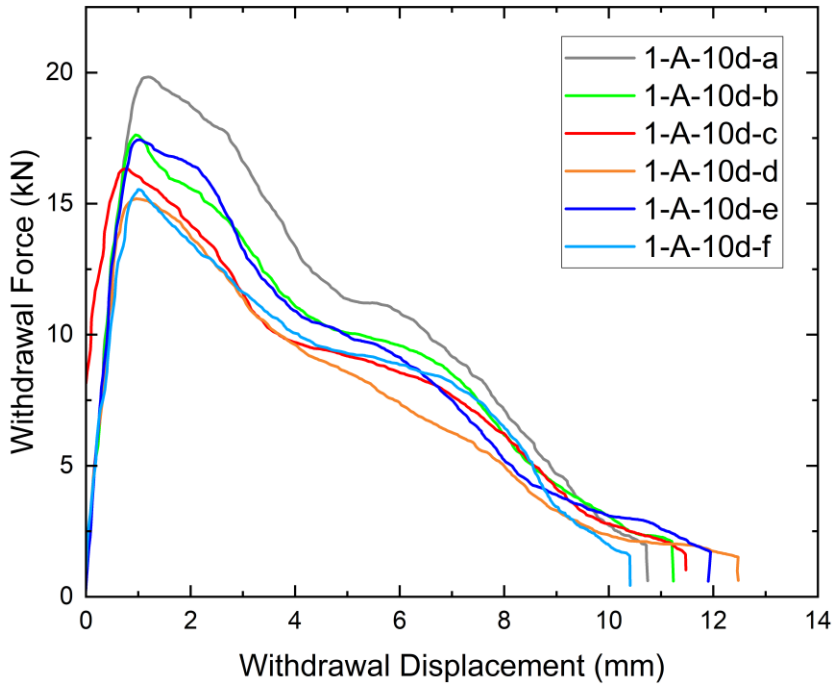

Appendix B 1: 160 mm x 170 mm SPF CLT with 8 mm diameter screw, 12% constant MC

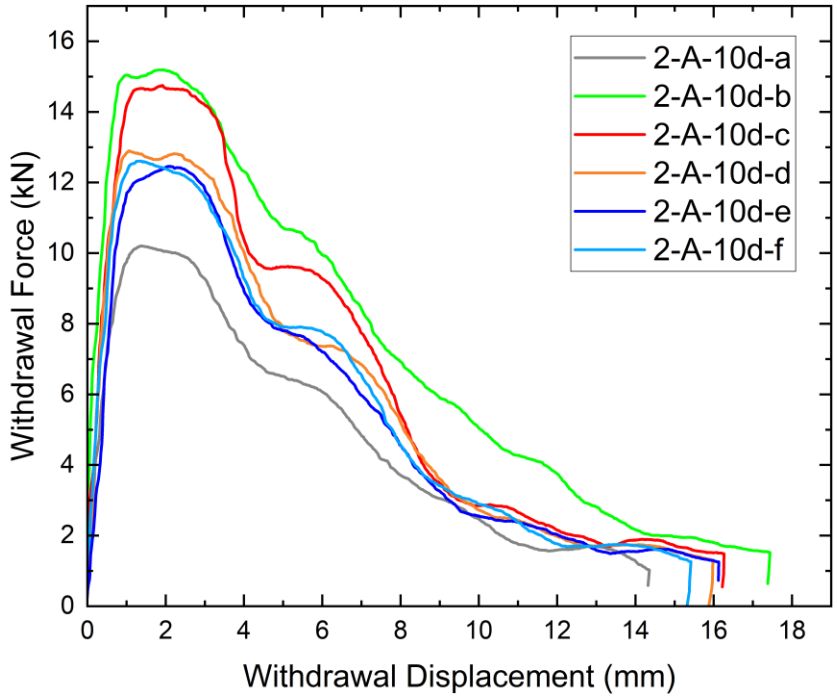

Appendix B 2: 160 mm x 170 mm SPF CLT with 8 mm diameter screw, 16% constant MC

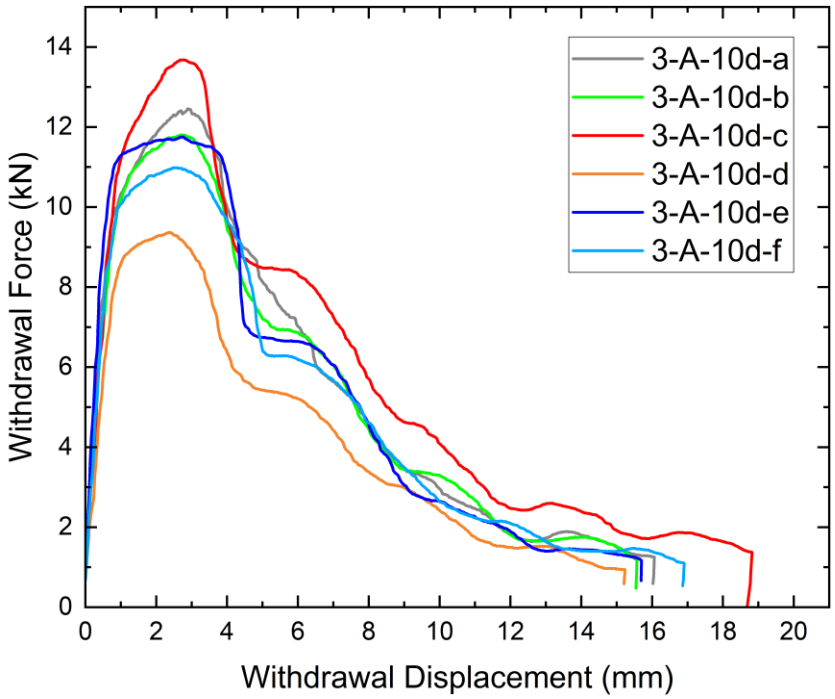

Appendix B 3: 160 mm x 170 mm SPF CLT with 8 mm diameter screw, 21% constant MC

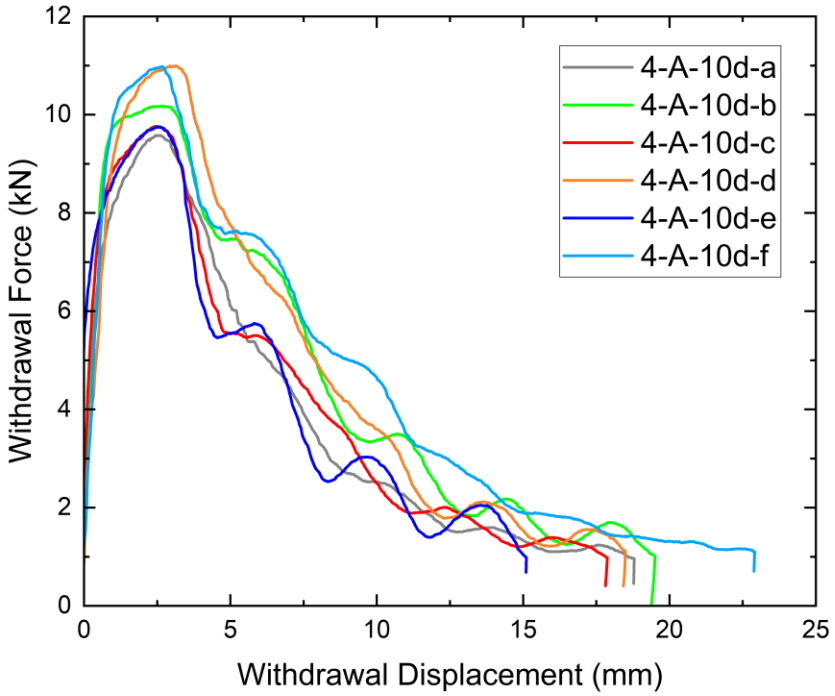

Appendix B 4: 160 mm x 170 mm SPF CLT with 8 mm diameter screw, Saturated constant MC

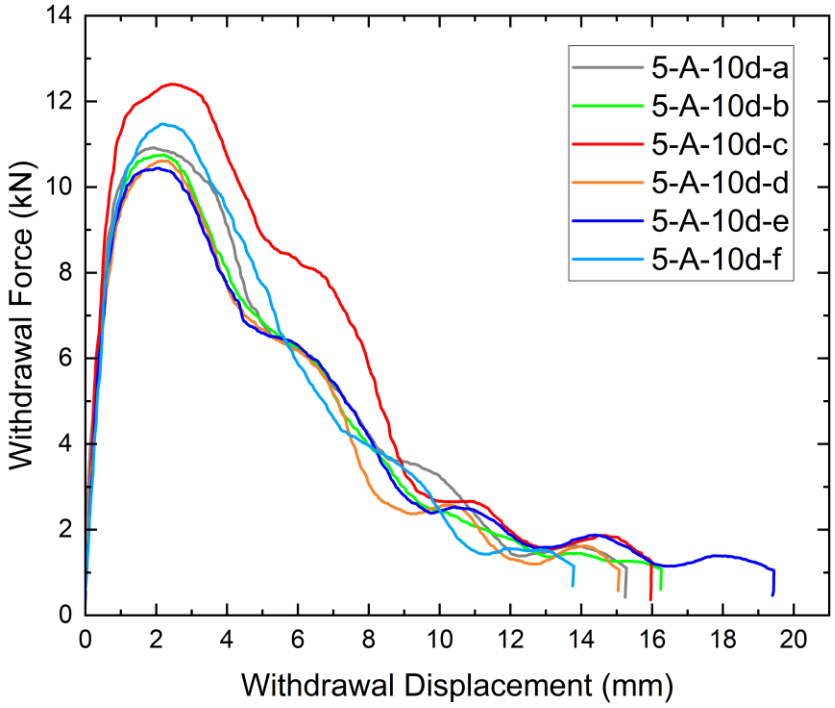

Appendix B 5: 160 mm x 170 mm SPF CLT with 8 mm diameter screw, 12% → 21% MC

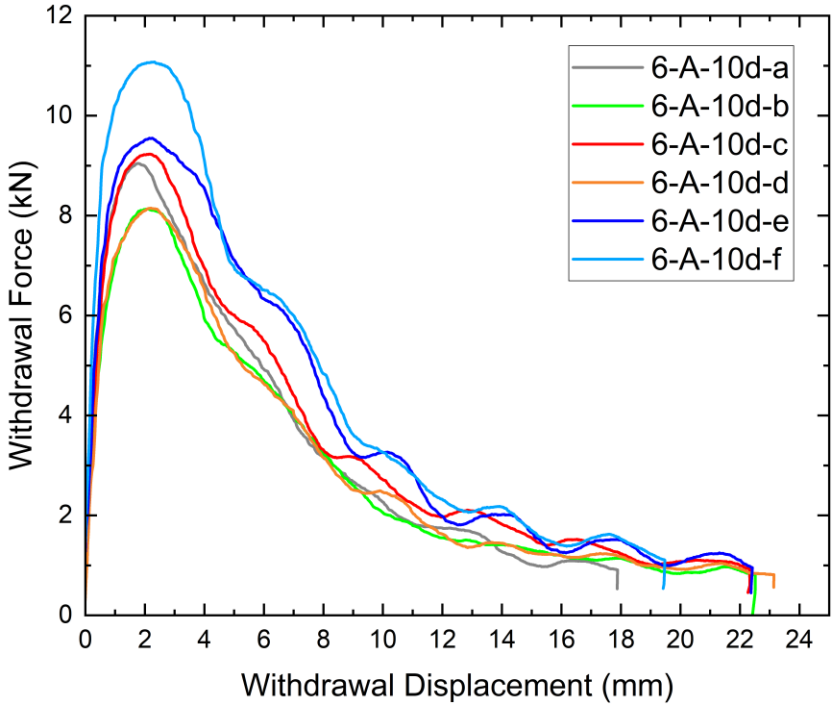

Appendix B 6: 160 mm x 170 mm SPF CLT with 8 mm diameter screw, 12% → Saturated MC

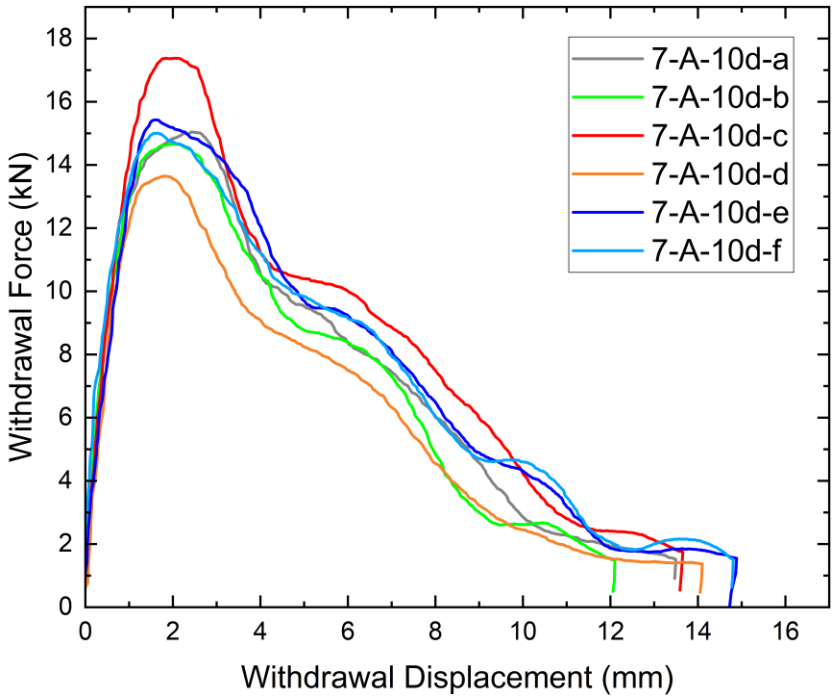

Appendix B 7: 160 mm x 170 mm SPF CLT with 8 mm diameter screw, 21% → 12% MC

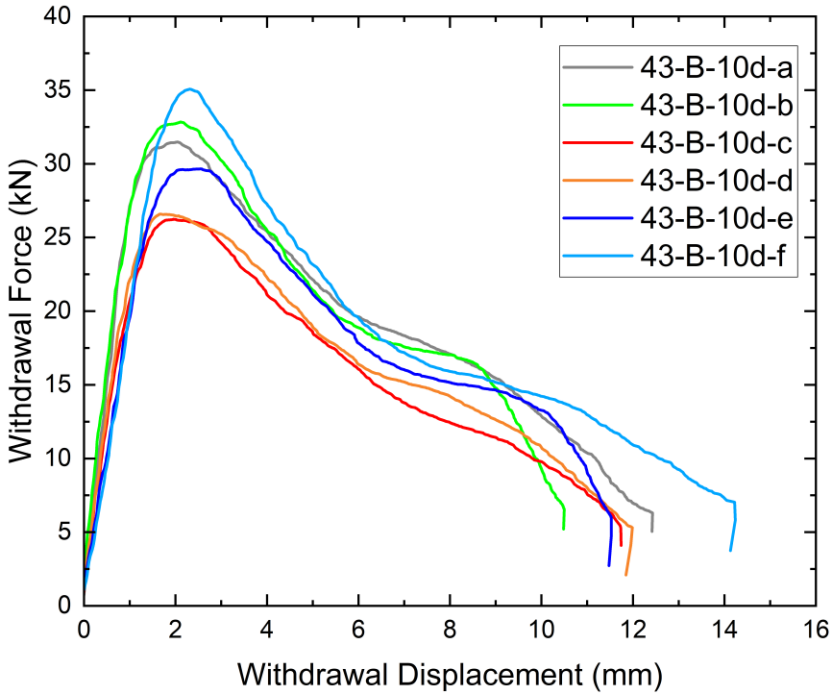

Appendix B 8: 260 mm x 270 mm SPF CLT with 13 mm diameter screw, 12% constant MC

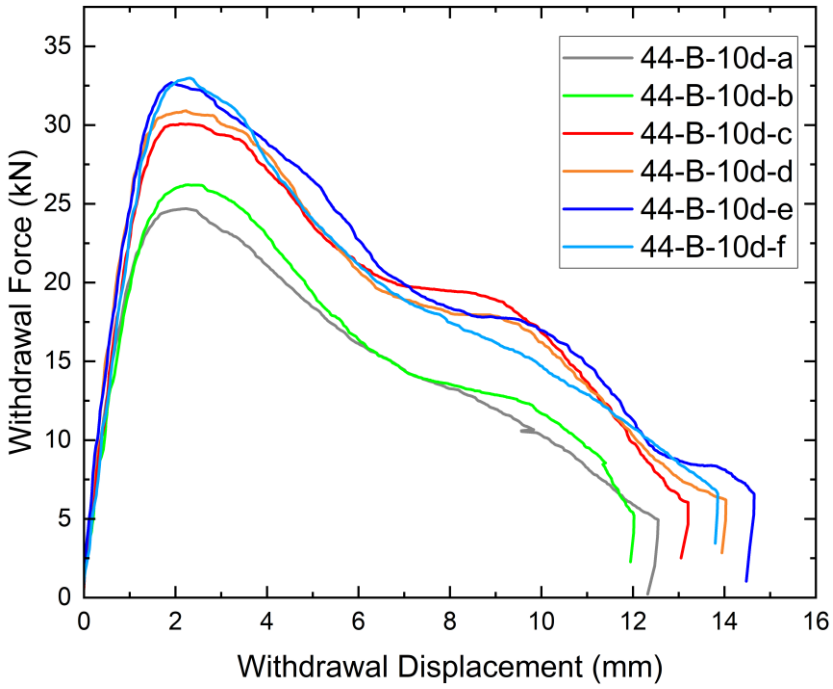

Appendix B 9: 260 mm x 270 mm SPF CLT with 13 mm diameter screw, 16% constant MC

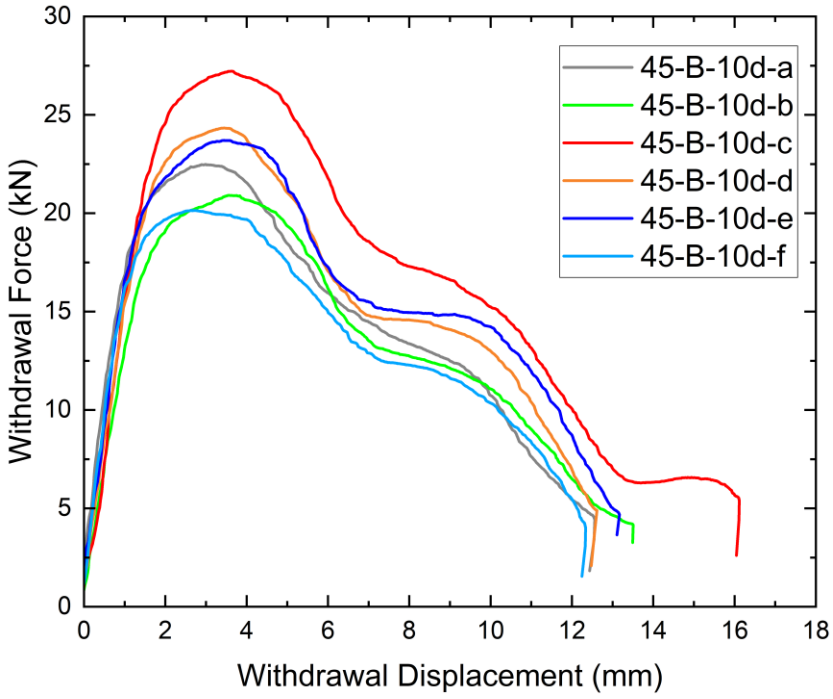

Appendix B 10: 260 mm x 270 mm SPF CLT with 13 mm diameter screw, 21% constant MC

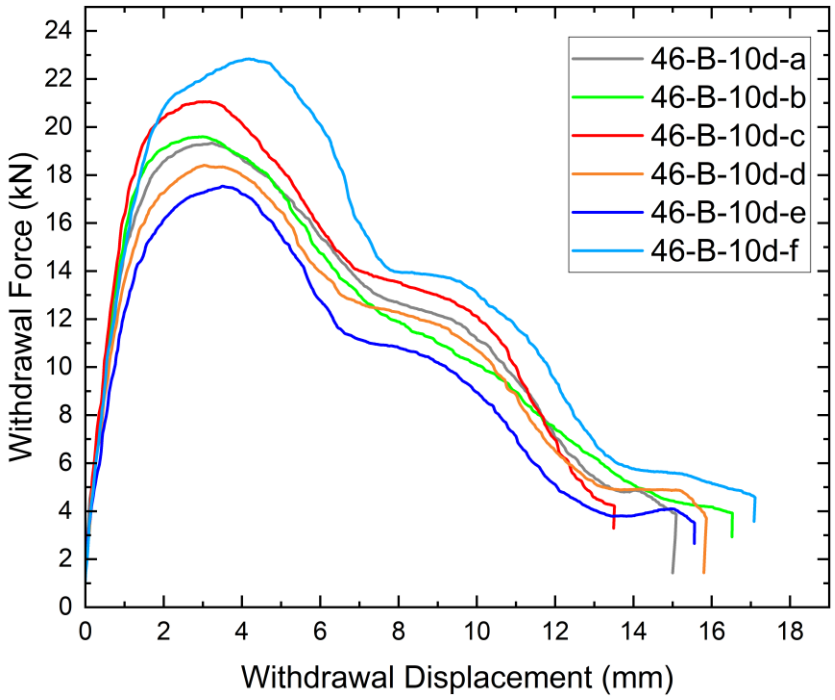

Appendix B 11: 260 mm x 270 mm SPF CLT with 13 mm diameter screw, Saturated constant MC

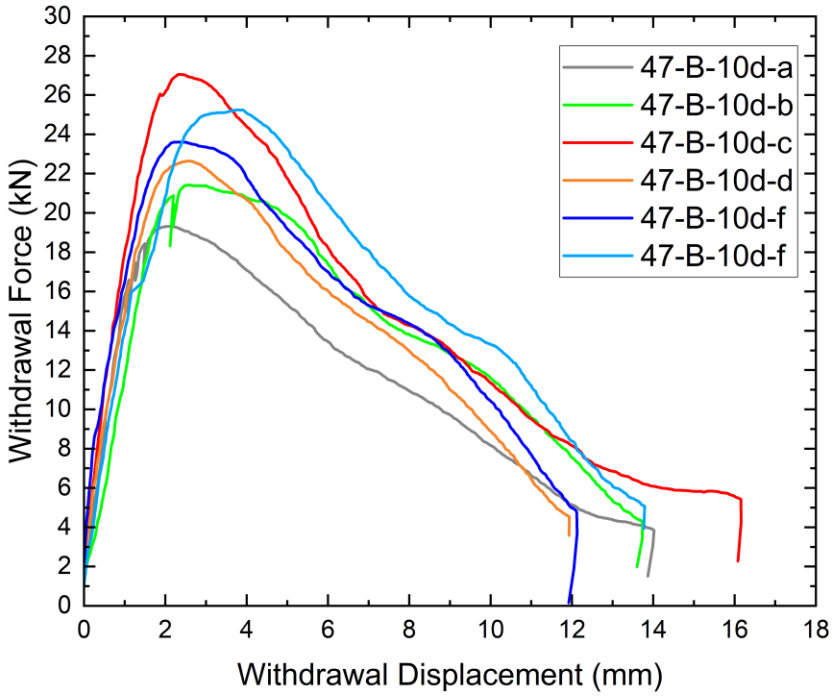

Appendix B 12: 260 mm x 270 mm SPF CLT with 13 mm diameter screw, 12% → 21% MC

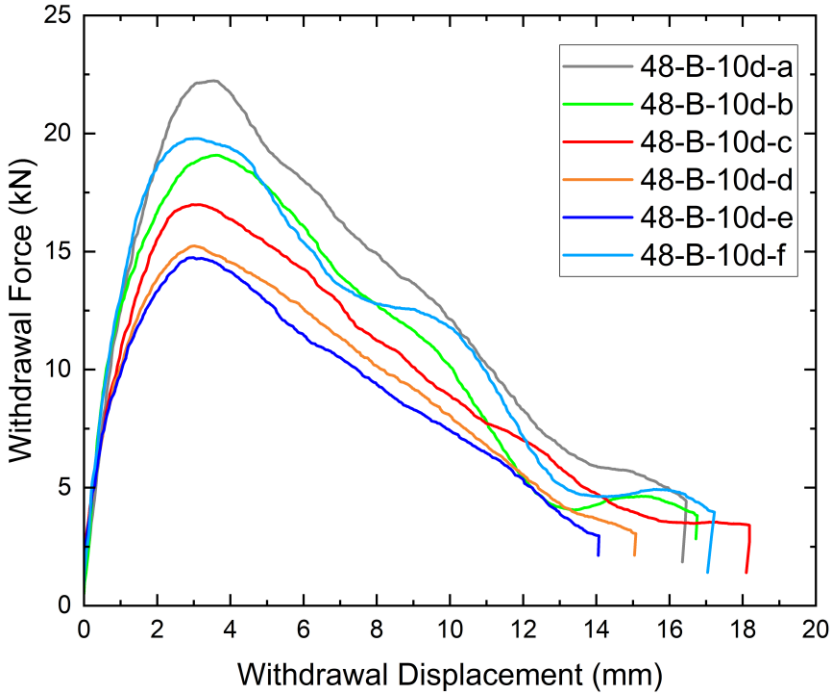

Appendix B 13: 260 mm x 270 mm SPF CLT with 13 mm diameter screw, 12% → Saturated MC

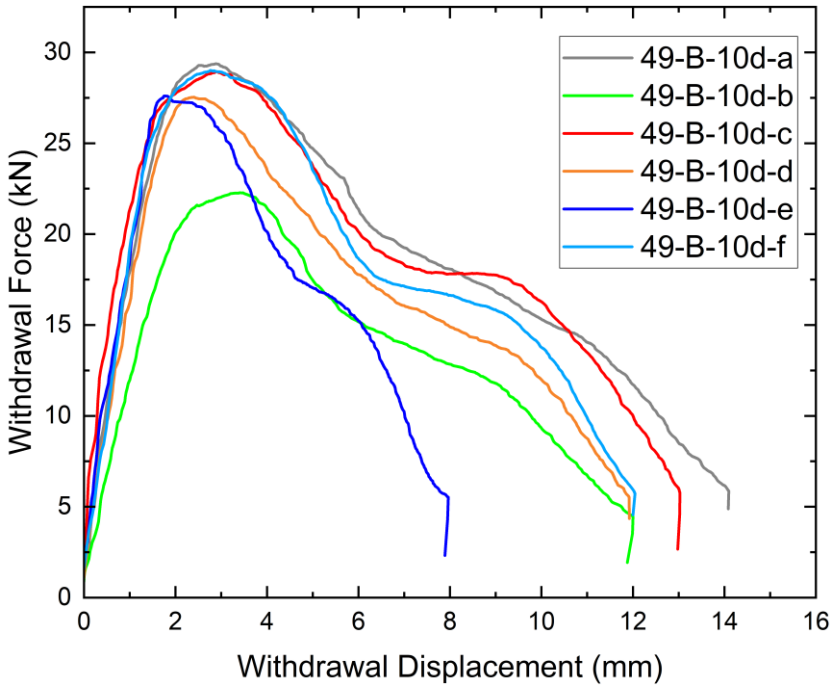

Appendix B 14: 260 mm x 270 mm SPF CLT with 13 mm diameter screw, 21% → 12% MC

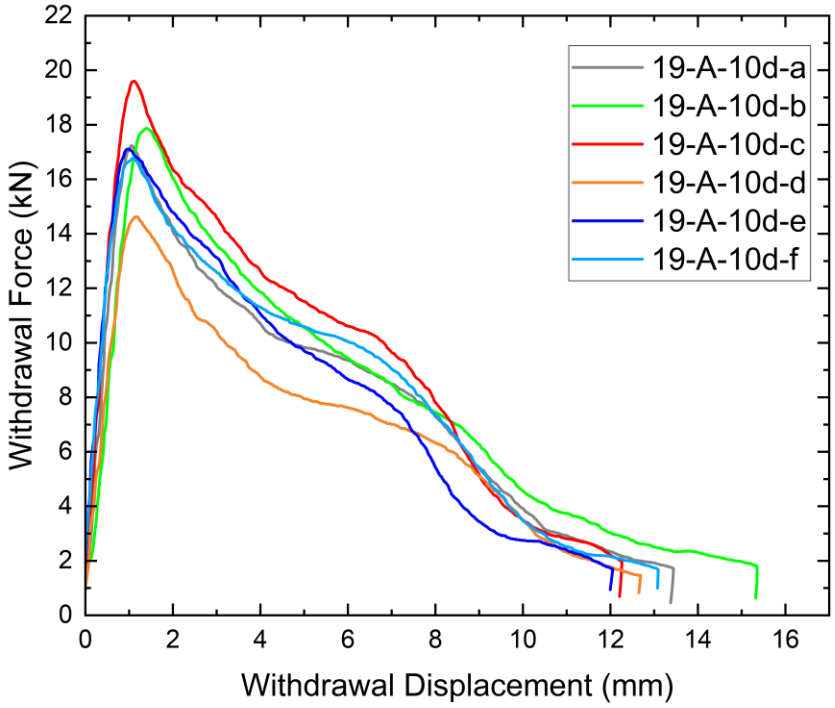

Appendix B 15: 80 mm x 160 mm D.Fir Glulam with 8 mm diameter screw, 12% constant MC

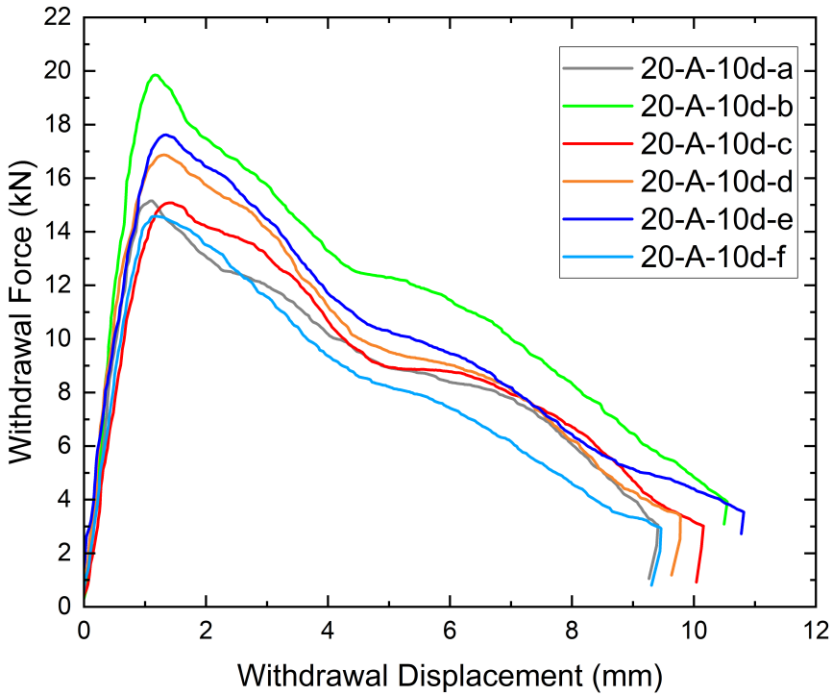

Appendix B 16: 80 mm x 160 mm D.Fir Glulam with 8 mm diameter screw, 16% constant MC

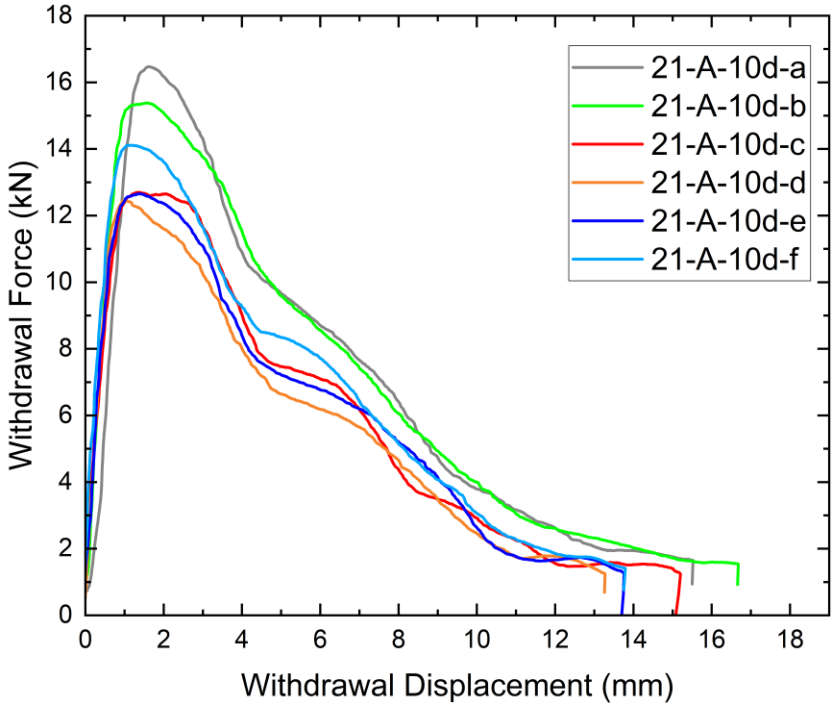

Appendix B 17: 80 mm x 160 mm D.Fir Glulam with 8 mm diameter screw, 21% constant MC

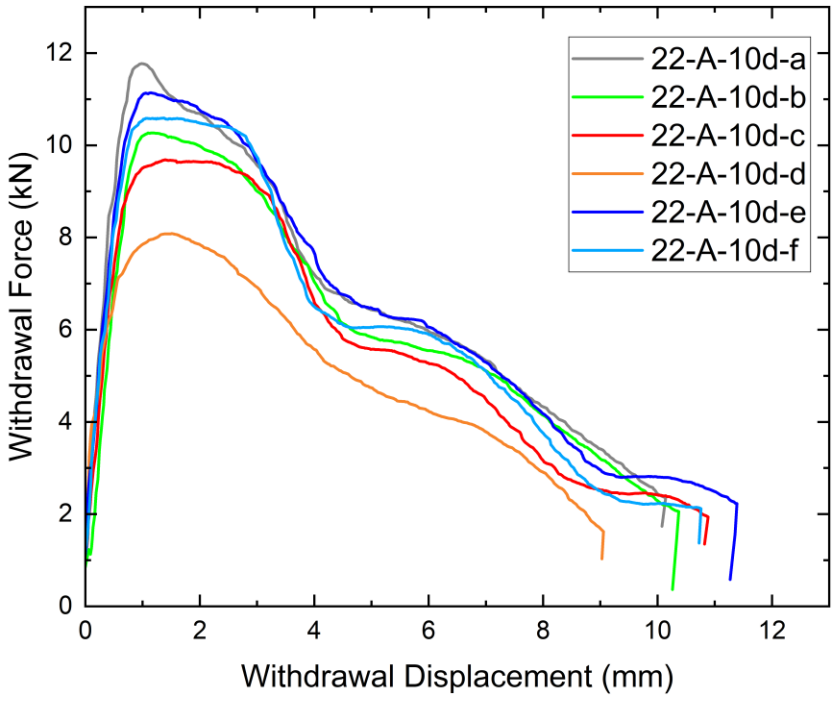

Appendix B 18: 80 mm x 160 mm D.Fir Glulam with 8 mm diameter screw, Saturated constant MC

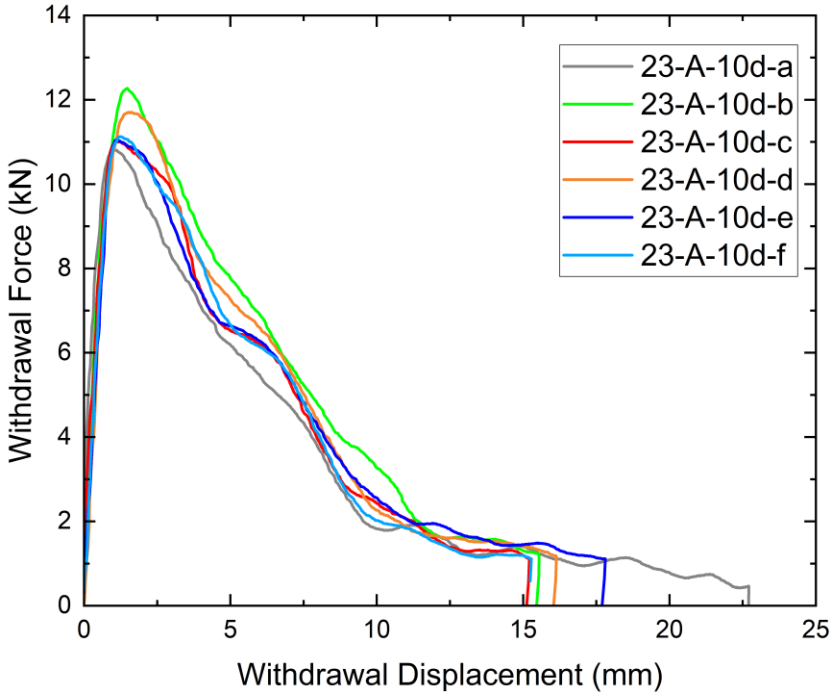

Appendix B 19: 80 mm x 160 mm D.Fir Glulam with 8 mm diameter screw, 12% → 21% MC

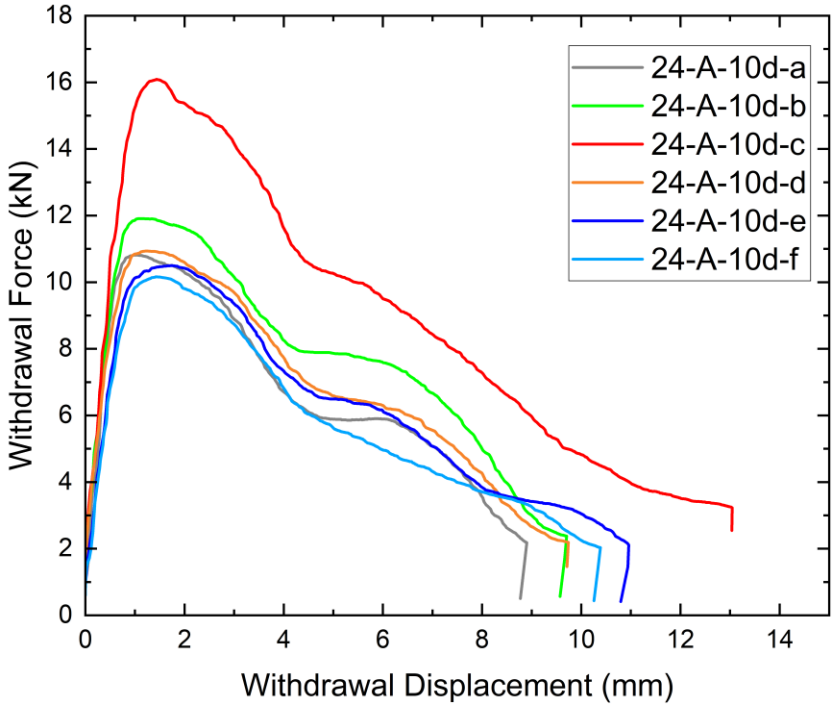

Appendix B 20: 80 mm x 160 mm D.Fir Glulam with 8 mm diameter screw, 12% → Saturated MC

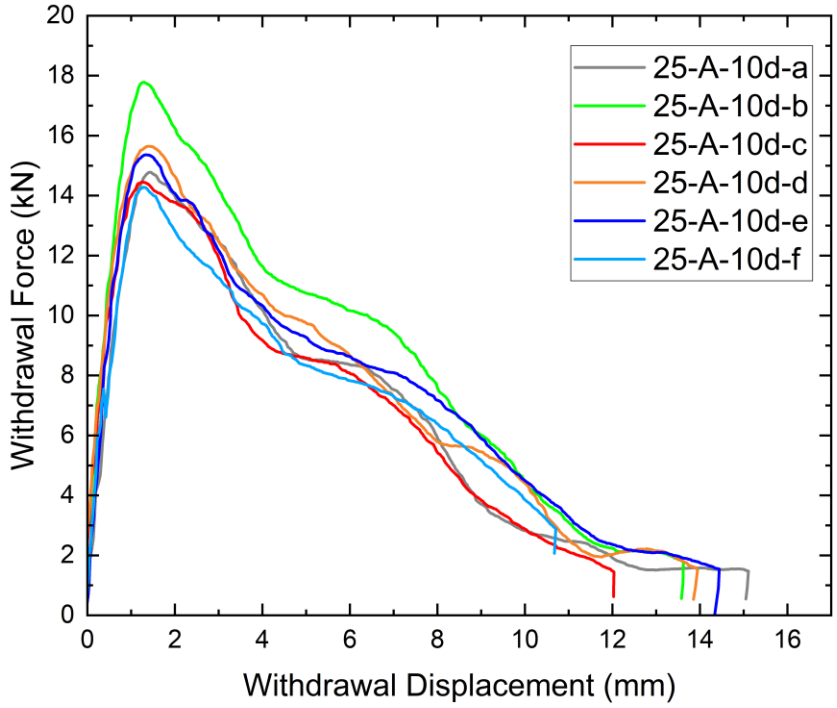

Appendix B 21: 80 mm x 160 mm D.Fir Glulam with 8 mm diameter screw, 21% → 12% MC

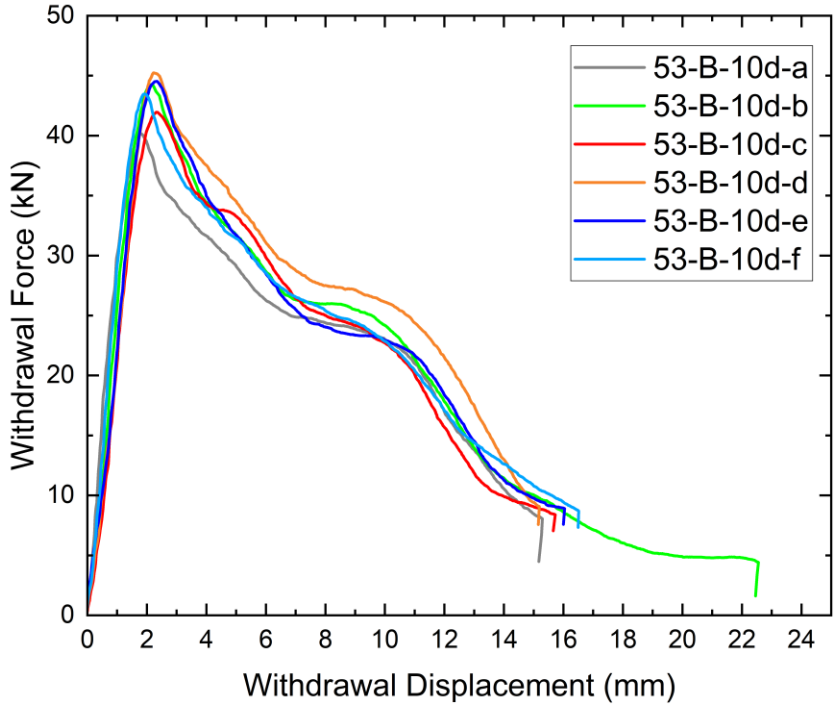

Appendix B 22: 130 mm x 260 mm D.Fir Glulam with 13 mm diameter screw, 12% constant MC

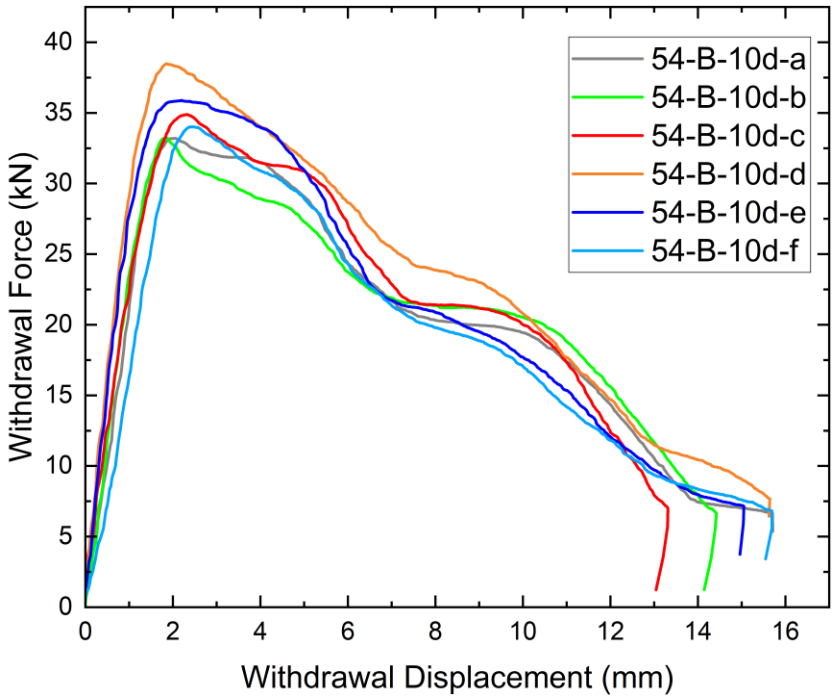

Appendix B 23: 130 mm x 260 mm D.Fir Glulam with 13 mm diameter screw, 16% constant MC

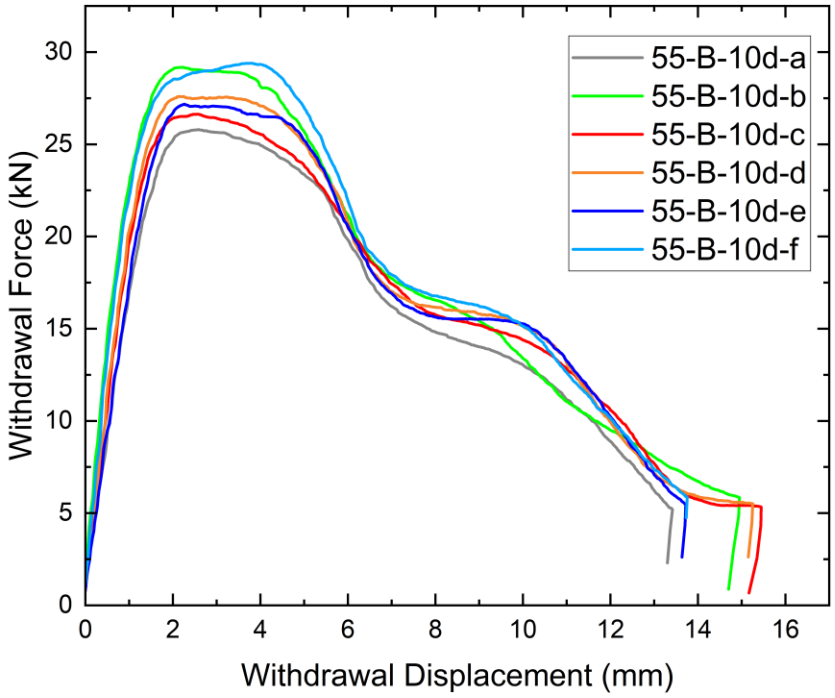

Appendix B 24: 130 mm x 260 mm D.Fir Glulam with 13 mm diameter screw, 21% constant MC

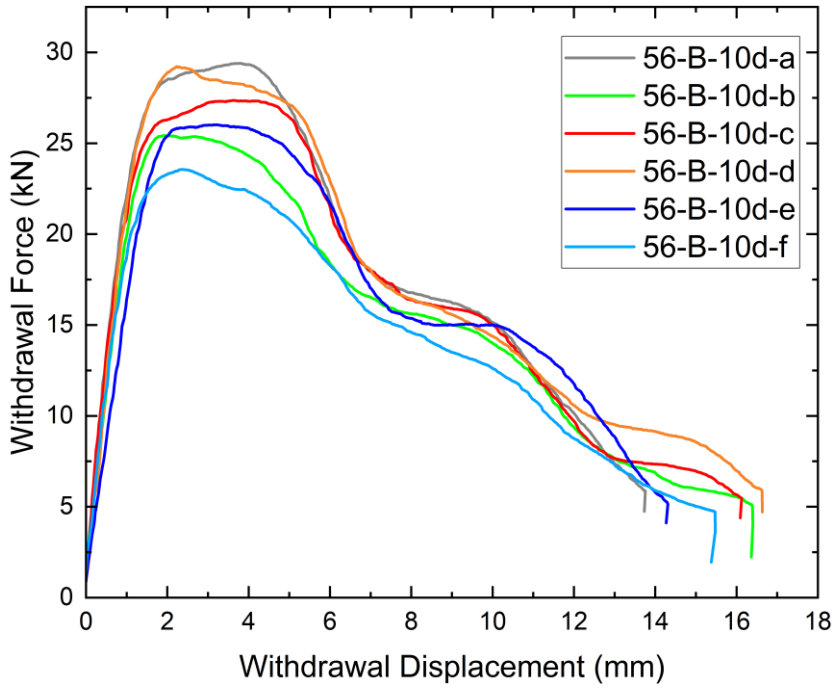

Appendix B 25: 130 mm x 260 mm D.Fir Glulam with 13 mm diameter screw, Saturated constant MC

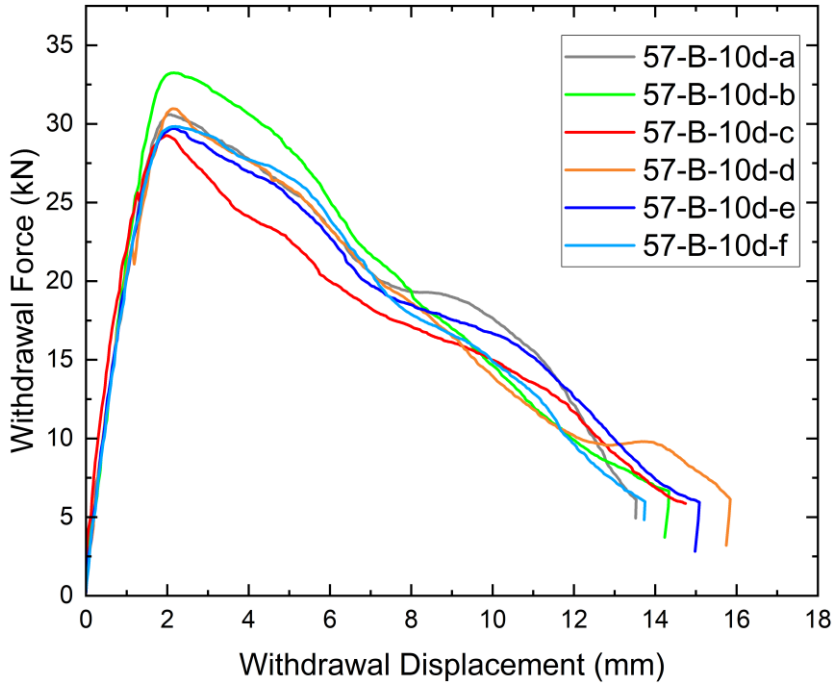

Appendix B 26: 130 mm x 260 mm D.Fir Glulam with 13 mm diameter screw, 12% → 21% MC

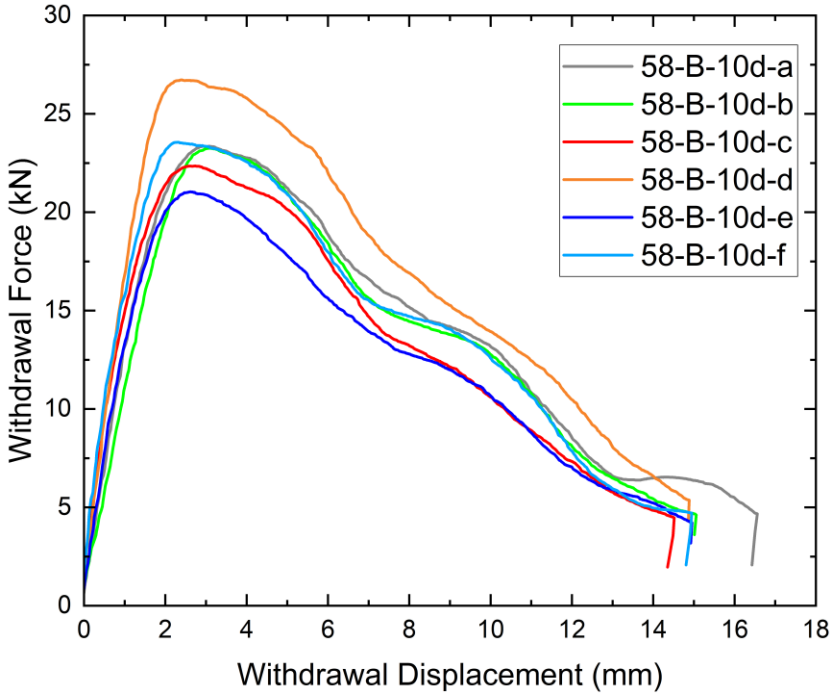

Appendix B 27: 130 mm x 260 mm D.Fir Glulam with 13 mm diameter screw, 12% → Saturated MC

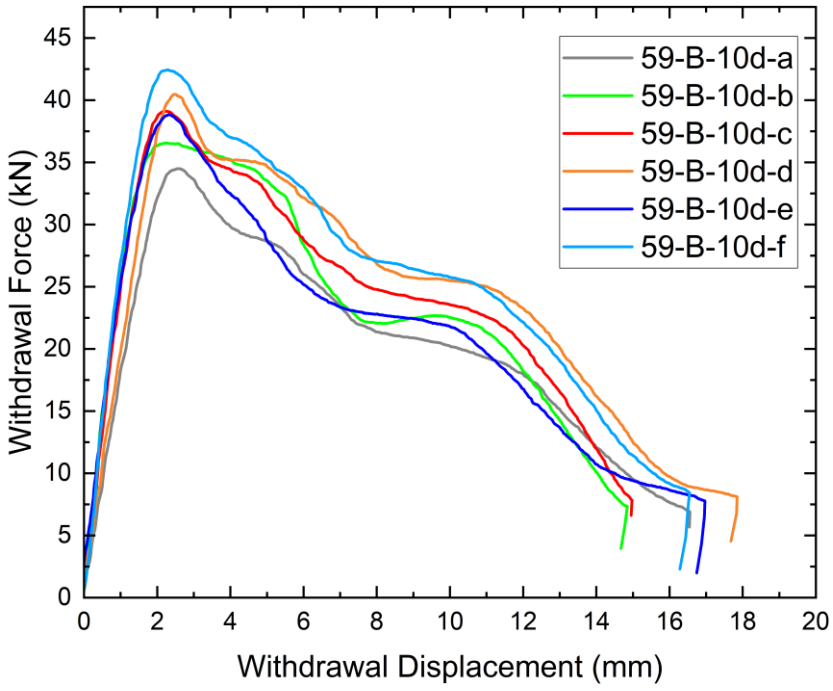

Appendix B 28: 130 mm x 260 mm D.Fir Glulam with 13 mm diameter screw, 21% → 12% MC